

Reducción de la Decoherencia Cuántica en Fotónica Integrada

*Una Disertación Presentada a
Universidad Autónoma de Madrid*



por
Joaquín Guimba Gaspar

*En Cumplimiento Parcial
de los Requerimientos del Programa de Doctorado de
Materiales Avanzados y Nanotecnología de la
Facultad de Ciencias UAM, Cantoblanco*

Instituto de Micro y Nanotecnología IMN-CNM, CSIC (CEI UAM+CSIC)

11/2022

a mi hermano Diego

Resumen

La fotónica cuántica integrada es un elemento indispensable para la miniaturización, estabilización y escalabilidad de las tecnologías cuánticas. El desarrollo de circuitos fotónicos integrados para aplicación en tecnologías cuánticas ayudará a traspasar el cuello de botella hacia niveles superiores de disponibilidad tecnológica y comercialización. La decoherencia cuántica supone uno de los retos técnicos a nivel fundamental con mayor relevancia para la realización de este desarrollo. En este contexto, el objetivo de este proyecto ha sido el de proporcionar herramientas teóricas para orientar la conceptualización y el diseño de los bloques fundamentales de los circuitos cuánticos integrados con vistas a la reducción de la decoherencia cuántica en estos sistemas. Los resultados obtenidos en forma de modelos teóricos, métodos numéricos de simulación y esquemas de optimización facilitan estas herramientas a través una serie de nuevos instrumentos matemáticos que sirven tanto para la caracterización de la decoherencia en diferentes componentes como para guías de diseño para su reducción: Expresiones analíticas que relacionan directamente los parámetros de diseño de estructuras fotónicas con el grado de decoherencia de la plataforma; Modelos para la simulación numérica de emisores cuánticos integrados en estructuras fotónicas que conectan la variación de los parámetros del diseño con el impacto en las figuras de mérito que caracterizan la decoherencia; Esquemas de optimización basados en métodos de Machine Learning para estructuras de fotónica cuántica integrada que ofrecen una reducción sin precedentes en términos de consumo de recursos computacionales; Interpretaciones físicas de las soluciones de los modelos desarrollados que contribuyen al avance del conocimiento del comportamiento de componentes de circuito en diferentes condiciones. El aparato matemático desarrollado ha sido evaluado a través de su aplicación en diferentes casos prácticos validando su fiabilidad y demostrando resultados prometedores: Identificación de los valores de los parámetros de diseño necesarios para la maximización de la indistinguibilidad y la eficiencia de extracción en emisores cuánticos acoplados a guías de onda dependiendo de las características del emisor, estimando incrementos en la indistinguibilidad de hasta un 30% para diseños optimizados; Optimización del diseño de una cavidad óptica para integración en chip de emisores cuánticos que garantiza valores de indistinguibilidad y eficiencia de extracción cercanos a la unidad con emisores fuertemente disipativos a temperatura ambiente; Relajación de los requisitos técnicos generales para cavidades ópticas a partir de una nueva plataforma propuesta basada en la integración de clústeres de emisores cuánticos acoplados que garantiza indistinguibilidad perfecta con emisores fuertemente disipativos a temperatura ambiente para las configuraciones óptimas. Esperamos que los resultados obtenidos en esta disertación contribuyan al avance del conocimiento para el desarrollo de la fotónica cuántica integrada y sirvan de hoja de ruta para la realización de nuevas demostraciones experimentales que incrementen su impacto en el estado del arte de las tecnologías cuánticas.

Contenidos

Capítulo 1. Introducción	2
Fotónica cuántica integrada	3
Decoherencia cuántica	5
Motivación y objetivos.....	10
Capítulo 2. Publicaciones.....	14
Enhancement of the Indistinguishability of Single Photon Emitters Coupled to Photonic Waveguides	14
Introduction	14
Methods,results and discussion	15
Conclusions	26
References	27
Numerical optimization of a nanophotonic cavity by machine Learning for Near Unity Single Photon Indistinguishability	32
Introduction	32
Methods	33
Results and discussion	38
Conclusions	43
References	44
Perfect Photon indistinguishability from a set of dissipative quantum emitters	50
Introduction	50
Methods	52
Results	54
Discussion	60
Conclusions	62
References	62
Capítulo 3. Resultados.....	68
Emisores acoplados a guías de onda	68
Emisores acoplados a cavidades ópticas	72
Clústeres de emisores integrados en cavidades ópticas	76
Conclusiones	80
Agradecimientos	82
Referencias	83
Anexo: Publicaciones completas.....	92

Capítulo 1. Introducción

El desarrollo de la mecánica cuántica (MC) a lo largo del siglo XX trajo consigo la revolución tecnológica que sostiene una buena parte del ecosistema industrial en la actualidad. Los avances en teoría de semiconductores junto con la evolución de las tecnologías CMOS permitieron el desarrollo de los micro-transistores, que proporcionaron por primera vez un candidato robusto para la manipulación de señales digitales en el procesamiento de información basado en lenguaje binario, haciendo posible el desarrollo de ordenadores e internet. En esta primera generación de tecnologías cuánticas jugó un rol esencial el tercer postulado de la MC que involucra a la ecuación de Schrödinger, la cual permite obtener el espacio discreto de estados energéticos de la función de onda (FO) para un potencial determinado. Este formalismo resultó clave para la descripción de la estructura de niveles electrónicos en materiales, dando lugar a la física de semiconductores.

En paralelo, el segundo postulado (postulado de la medida) centraba el debate sobre las interpretaciones filosóficas de la MC dentro de la comunidad de sus propios fundadores. A pesar de que en su formulación estándar la MC identifica del módulo de la FO con una densidad de probabilidad y a los observables como variables estocásticas, la aplicación de conceptos probabilísticos a la MC difiere sustancialmente del caso de una teoría clásica. En concreto, la noción de espacio de probabilidades junto con su correspondiente espacio de variables estocásticas no es compatible con las estructuras básicas en MC: el espacio de Hilbert de vectores estado y su correspondiente álgebra de operadores [1]. Como consecuencia, no es posible formular la MC como una teoría estadística en un espacio de probabilidad clásico [2]. Atendiendo estas inconsistencias, la exploración sobre las interpretaciones probabilísticas de la FO llevada a cabo a lo largo de la segunda mitad del siglo XX (von Neumann (1955) [3], J S Bell (1964) [4], JP Gordon (1962) [5], CW Helstrom. (1969) [6], AS Holevo (1973) [7], A Fine (1982) [8], JF Clauser (1969) [9]]) fue estableciendo lentamente los cimientos de la era de la información cuántica (IO). Este nuevo formalismo proporcionó un marco teórico en el contexto de la teoría de la información para los conceptos de superposición (i) y entrelazamiento (ii) introducidos previamente por la MC: (i) La correlación entre observables no comutables no admite su caracterización a través de una distribución de probabilidad conjunta [10]; (ii) La cantidad de entropía acumulada en un sistema compuesto es mayor que la almacenada en sus subsistemas por separado [11]. Pronto esta reinterpretación de ambos fenómenos dentro del nuevo marco despertó su potencial para la aplicación en los campos de la computación y el procesado de información.

La posibilidad de emplear superposiciones coherentes de estados entrelazados como soporte físico para la codificación y manipulación de registros de bits permite en principio la posibilidad de actuar simultáneamente sobre varios estados de un bit a través de la implementación de una única operación. De forma general, si un circuito cuántico dispone de un registro entrada de q-bits u , y un registro salida de q-bits todos en el estado $|0\rangle$, una computación arbitraria F produce la operación:

$$|u\rangle|0\rangle \rightarrow |u\rangle|F(u)\rangle \quad (1)$$

Si el registro u se compone de una cadena de N q-bits en una superposición de $|0\rangle$ y $|1\rangle$, este proceso deja cada salida de 2^N en un estado de superposición [12]. A lo largo de la década de los 90 una serie de trabajos teóricos demostraron la posibilidad de la explotación de este escalamiento exponencial para la reducción de la complejidad computacional de problemas de computación clásica moderna: Grover (1996), reducción de la complejidad del *problema de búsqueda desordenada* de N a \sqrt{N} (con N el número total de evaluaciones) [13]; Simons (1997), reducción del problema NP-complete de la *función vectorial periódica* a un problema lineal en N [14]; Shor (1994), reducción del problema NP-complete de la *factorización de números primos* a un problema tipo $P(N)$ [15]. Las aplicaciones potenciales de una tecnología capaz de operar en este nuevo paradigma de computación incluyen un gran número de problemas de optimización: Diseño eficiente de medicamentos para medicina personalizada [16-18]; Mejora de logística para protección de recursos naturales [19]; Gestión de carteras para optimización del beneficio/riesgo [20,21].

Fotónica cuántica integrada

A raíz de estas evidencias dio comienzo una escalada de inversiones público-privadas en tecnologías de información cuántica que se extendió a lo largo de Asia, Europa, Australia y Norte América con el objetivo del desarrollo de un hardware comercializable para la realización fiable de algoritmos cuánticos ($2^{\text{nd}} \text{ Quantum Revolution}$). Las tecnologías originalmente más extendidas fueron las basadas en q-bits superconductores y las Ion-Trapping, que demostraron la primera realización de una operación lógica con unos pocos q-bits en la década de los 90 [22,23]. En la actualidad existe una amplia variedad de alternativas para la realización de q-bits estables dentro de un extenso abanico de empresas privadas y público-privadas, entre las que destacan: **Q-bits superconductores** (IBM, Google, D-Wave, Intel, Qutech, Quantum circuits, Seeqc, Amazon, Quantware, UST of China, Bleximo, Alice and Bob, Origin Quantum, Raytheon BBN, Oxford Quantum Ciurcuits, IQM Quantum computers); **Ion-Trapping** (Quantinuum, IonQ, OXIONICS, Infineon, Qscout, Oxford Ionics, Alpine Quantum Technologies, Universal Quantum), **Quantum Dot (QD) q-bits** (Qutech, Intel, HRL laboratories, CEA-LETI, Quantum Motion, Riken Center for Quantum Computing); **Color center q-bits** (Qutech, SQC, Internacional Iberian Nanotech Lab, Quantum Brilliance); **Átomos neutros en pinzas ópticas** (Coldquanta, Atom Computing, Pasqal, Quera); **Topological q-bits** (Microsoft, Qutech); **Electrones en Helio** (EEROQ); y **q-bits ópticos** (Xanadu, PsiQuantum, Quix Quantum, Orca Computing, Quandela, UST of China). Para la realización de circuitos con profundidad computacional suficiente para ejecutar algoritmos que demuestran supremacía cuántica se estima que sería necesario un número de alrededor de 10^6 q-bits estables [24]. Esto es debido a que para garantizar la fidelidad en la aplicación de puertas lógicas es necesaria la implementación de circuitos de corrección de errores que involucran una serie de q-bits adicionales que funcionan cooperativamente como un único q-

bit lógico [25]. En el año 2022 las empresas que lideran el ranking en términos de número de q-bits disponen de ordenadores del orden de 10^2 q-bits: IBM (433 q-bits); Google (53 q-bits); Rigetti (80 q-bits); Coldquanta (100 q-bits); IonQ (32 q-bits); Pasqal (200 q-bits); Quera (256 q-bits). Las previsiones para el desarrollo de dispositivos con numero de q-bits del orden de 10^3 se sitúan a lo largo de la próxima década: IBM (2026); Google (2029); D-Wave (2024); Rigetti (2026) Psiquantum (2025); Coldquanta (2024); IonQ (2028); Silicon Quantum Computing (2029).

Por otro lado, resulta conveniente resaltar que la estimación de estas previsiones tiene como fuente la información ofrecida por las propias instituciones interesadas en la captación de fondos para el desarrollo de sus tecnologías. Aunque la consecución de estos hitos ha demostrado que el procesamiento de información a través de la superposición coherente de q-bits es tecnológicamente realizable, todas las tecnologías mencionadas previamente se enfrentan a una serie de retos comunes para los que no existe una solución única y fiable para el medio o largo plazo. Fundamentalmente, esta serie de retos involucran problemas relacionados con la robustez de los componentes y su escalabilidad. A modo de ejemplo, las tecnologías basadas en color-centers, QDS, o trampas de iones, requieren de sistemas sofisticados de control de pulsos láser para la creación o modificación de estados cuánticos [26]; En sistemas de q-bits superconductores, con transiciones en el régimen de microondas, el entrelazamiento entre distintos dispositivos se realiza a través del acoplamiento con fotones individuales en el espectro visible, para lo que se requieren fuentes coherentes de luz cuántica [27]; Para la generación de q-bits ópticos se utilizan resonadores cuya frecuencia de resonancia debe mantenerse estable frente a vibraciones para asegurar el acoplamiento con fuentes de fotones individuales [28]. La miniaturización y escalabilidad de este tipo de componentes supone un importante reto tecnológico para el que todavía es necesaria una fuerte inversión en investigación fundamental. En este punto juega un rol especialmente central el creciente desarrollo de las tecnologías de fotónica cuántica integrada (FCI).

La FCI se beneficia directamente del desarrollo en paralelo de la fotónica clásica integrada (FI), la cual dispone en la actualidad de un considerable grado de madurez. El crecimiento de las industrias de fibra óptica y sensores inteligentes ha motivado el esfuerzo para la miniaturización de componentes ópticos e integración a gran escala, siguiendo un camino similar al ya recorrido por la industria electrónica. Al igual que el proceso de manufacturación de componentes microelectrónicos, la fabricación de circuitos fotónicos integrados (CPI) se basa en tecnologías de escala de oblea, donde es posible integrar una gran cantidad de componentes ópticos sobre un único sustrato. El esfuerzo por la realización de una plataforma escalable de fabricación de CPI ha generado a lo largo de las últimas décadas un elevado número de soluciones que ya disponen de sus propios nichos de mercado: transceptores de alta velocidad para centros de procesamiento de datos; soluciones de sensado y monitorización para automatización industrial; sistemas microelectromecánicos). Pudiéndose beneficiar de este alcance, la FCI representa un candidato esencial para la miniaturización, estabilización y escalabilidad de las tecnologías cuánticas. El desarrollo de CPIs para aplicación en determinados dispositivos cuánticos puede ayudar a traspasar el cuello de botella hacia niveles superiores de disponibilidad tecnológica y comercialización: arquitecturas escalables y reconfigurables miniaturizadas [29,30]; alta estabilidad de sistemas ópticos [31]; co-integración on-chip de detectores de fotones individuales [32,33]; lectura electrónica CMOS complementaria y señal de compensación [34]. A pesar de su inmadurez, el desarrollo de la FCI muestra un crecimiento exponencial

desde la demostración de la primera puerta lógica funcional en 2008 [35]. Hasta la fecha, una buena parte de los componentes considerados como bloques fundamentales de la FCI han sido integrados en chips fotónicos clásicos con éxito: Fuentes laser y amplificadores a longitud de onda específica [36]; Estabilizadores de frecuencia [37]; transformadores de frecuencia [38]; Controladores de intensidad [39]; elementos de control de frecuencia, fase y amplitud para trampas de iones [40]; MEMS [41]; interruptores ópticos de alta velocidad [42]; Guías de onda de ultra-bajas pérdidas [43]; detectores de fotones individuales [44]; elementos de filtrado de polarización [45]; Cavidades ópticas de alto factor de calidad y volumen modal reducido [46]; Memorias cuánticas basadas en átomos o estado sólido [47]; Emisores cuánticos basados en confinamiento cuántico [48]; Convertidores de frecuencia cuánticos entre espectro visible y longitud de telecomunicación [49]; Elementos para operaciones de compensación de alta velocidad [50]. Al mismo tiempo, el impacto de la FCI en aplicaciones reales para diferentes áreas de tecnologías cuánticas muestra resultados altamente prometedores: **Comunicaciones cuánticas**: Sistema de distribución de claves cuánticas chip a chip basada en silicio a lo largo de 43 km de fibra óptica oscura (2018) [51]; Primera operación en red para computación cuántica distribuida (2021) [52]; **Computación cuántica**: Esquema de sampleado de bosones con 50 fotones para computación específica demuestra por primera vez ventaja cuántica basada en FCI (2020) [53]; **Simulación cuántica**: Plataforma para Eigensolver variacional para el cálculo del estado fundamental energético de moléculas de H₂ (2013) [54]; **Metrología cuántica**: Plataforma basada en defectos en diamante para detectores eficientes de campo magnético con una sensibilidad sin precedentes [55]. Como aliciente, en la actualidad se investigan diferentes plataformas basadas en FI con el potencial de materializarse en candidatos líderes para tecnologías de centros de datos y 5G. La FCI ha emergido sobre este ecosistema de desarrollos con previsión de corto plazo y ya existen sinergias que pueden explotarse para generar cadenas de suministro globales para tecnologías de FCI. Como consecuencia, la FCI atraviesa un periodo de fuerte captación de programas de inversión pública extendidos a lo largo de un gran número de países: **Europa**: Quantum Flagship (EU), QuantERA (ERA-NET), UK National Quantum Technologies Programme; **Australia**: EQUS, TMOS, CQC27; **Asia**: Programas de financiación por parte de Academia de Ciencias China, la Fundación de Ciencias Naturales de China y el Ministerio de Ciencia y Tecnología, con una inversión superior a 50 millones de Yuans; Tokyo QKD Network; Quantum Technology Innovation Strategy también en Tokio; **Norte América**: Quantum Internet Blueprint workshop (EEUU); Quantum Photonic Sensing and Security programme (Canadá); Quantum Encryption and Science Satellite (Canadá). Paralelamente, un amplio espectro desde grandes empresas hasta start-ups se encuentran involucradas activamente en el desarrollo y provisionamiento de CPIs para aplicación en FCI: Huawei, Baidu, Thales, Bosch, Atos, Telefonica, Teledyne, BAE Systems, BT, Optica Photonics, Vixar/OSRAM, OROLIA, FISBA, AUREA, LightOn, QuiX, QUANDELA, iPronics, LIGENTEC, VLC Photonics, IMASENIC, APE, VPIphotonics, IDQ, QUARTIQ, Single Quantum, MPD, SMART Photonics, LioniX, QZABRE, QNAMI, Element6, KETS, Qontrol.

En FCI la información del estado del q-bit viene codificada en un determinado grado de libertad del fotón (polarización, fase, momento angular, etc), y la implementación de operaciones lógicas sobre estos estados se realiza a través elementos básicos de óptica integrada, fundamentalmente *beam-splitters* y *phase-shifters*. En este contexto, la fidelidad de las puertas lógicas se ve comprometida por un lado por la precisión de las

especificaciones de estos elementos, y por un fenómeno de origen fundamental conocido como decoherencia cuántica.

Decoherencia cuántica

Al margen de los desafíos en términos de escalabilidad y estabilidad de componentes, toda tecnología basada en la creación y manipulación de estados cuánticos en q-bits, incluida la FCI, enfrenta un obstáculo común de naturaleza más fundamental. Basados en vectores de corriente en superconductores, spin de electrones de iones atrapados en trampas óptico-magnéticas, polarización de fotones en guías de onda, o en cualquiera de sus variantes, los q-bits representan sistemas cuánticos abiertos en interacción con entornos con un espectro continuo de grados de libertad. La interacción de un sistema cuántico abierto con sus alrededores genera correlaciones entre los estados del sistema reducido y los del entorno. Así, el entorno almacena información del sistema abierto en forma de estas correlaciones. Para cierto tipo de interacciones sistema-entorno, el efecto del entorno se traduce de forma efectiva en una serie de medidas indirectas sobre el sistema abierto [11]. Tras tomar la traza parcial sobre los grados de libertad del entorno, obtenemos un conjunto de estados del sistema abierto fuertemente estables, mientras que las superposiciones entre este conjunto de estados son destruidas de forma casi instantánea. A esta destrucción de superposiciones coherentes inducida por el entorno se le denomina decoherencia cuántica. A partir de este proceso las superposiciones de amplitudes de probabilidad se reducen a estados mixtos de probabilidad clásica produciendo una pérdida irreparable de información cuántica contenida en el estado del q-bit.

La propiedad característica de este tipo de interacciones se basa en que el sistema reducido afecta al entorno generando correlaciones sistema-reservorio, y sin embargo, el efecto de back-action por parte del reservorio sobre ciertos estados del sistema puede considerarse negligible. Como consecuencia, el decaimiento de las poblaciones de la matriz densidad reducida del sistema abierto es despreciable, mientras que las coherencias (elementos no diagonales de la matriz densidad) decaen en escalas temporales mucho más cortas que los tiempos de relajación típicos del sistema abierto. Así, tomamos el siguiente Hamiltoniano del proceso como punto de partida [11]:

$$H = H_s + H_B + H_I \quad , \quad H_I = \sum_n |n\rangle\langle n| \otimes B_n \quad (2)$$

Donde H_s , H_B y H_I son los Hamiltonianos del sistema abierto, reservorio e interacción respectivamente, $|n\rangle$ son los vectores base del sistema abierto, y B_n operadores arbitrarios del reservorio. Si asumimos que H_s commuta con los proyectores del sistema $|n\rangle$, la evolución temporal del estado combinado en función del tiempo se puede escribir como [11]:

$$|\psi(t)\rangle = \sum_n c_n |n\rangle \otimes |\phi_n(t)\rangle \quad (3)$$

Donde $|\phi_n(t)\rangle$ es un estado arbitrario del reservorio. El estado entrelazado (3) representa una correlación perfecta entre los estados del sistema y del reservorio, y al mismo tiempo, envuelve una superposición coherente de los estados $|n\rangle$ del sistema. Como consecuencia, las coherencias del sistema permanecen presentes en la matriz de densidad reducida [11]:

$$\rho_s(t) = \sum_{n,m} c_n c_m^* |n\rangle \langle m| (\phi_m(t)|\phi_n(t)\rangle) \quad (4)$$

Teniendo en cuenta que $\langle \phi_n(t) | \phi_n(t) \rangle = 1$, los elementos diagonales de $\rho_s(t)$ se mantienen constantes en el tiempo, sin embargo, los elementos no diagonales experimentan una evolución temporal. De esta forma, la dependencia temporal de las coherencias depende del overlap entre los diferentes estados del reservorio [11]:

$$|\langle \phi_m(t) | \phi_n(t) \rangle| = \exp [\Gamma_{nm}(t)] \quad (5)$$

La cantidad $\Gamma_{nm}(t)$ describe la evolución temporal de las coherencias y se denomina función de decoherencia. La dependencia con el tiempo de $\Gamma_{nm}(t)$ depende del tipo de acoplamiento entre el sistema y el reservorio, y en general, para sistemas dinámicos irreversibles tiene forma de decaimiento exponencial a un determinado ratio. De esta forma, considerando el caso extremo en el que el overlap entre distintos estados $|\phi_n(t)\rangle$ y $|\phi_m(t)\rangle$ decrece a 0 pasado un tiempo de coherencia τ_D [11]:

$$|\langle \phi_m(t) | \phi_n(t) \rangle| \rightarrow \delta_{nm} \quad (6)$$

La matriz densidad reducida del sistema vendrá dada por [11]:

$$\rho_s(t) \rightarrow \sum_n |c_n|^2 |n\rangle \langle n| \quad (7)$$

Después de tiempos de escalas superiores a τ_D las coherencias del sistema abierto han desaparecido y este se comporta como una mezcla incoherente de estados $|n\rangle$, por lo que los términos de interferencia para el cálculo del valor esperado del observable $\langle n | A | m \rangle$ ya no serán localmente observables a partir de medidas sobre el sistema reducido (i.e. el q-bit).

En caso específico de la FCI los principales mecanismos de decoherencia tienen lugar el proceso de generación de fotones individuales. Las plataformas para fuentes de fotones individuales (FFI) vienen típicamente constituidas por un emisor cuántico (EC) integrado en una cavidad óptica monomodal (ver Figura 1):

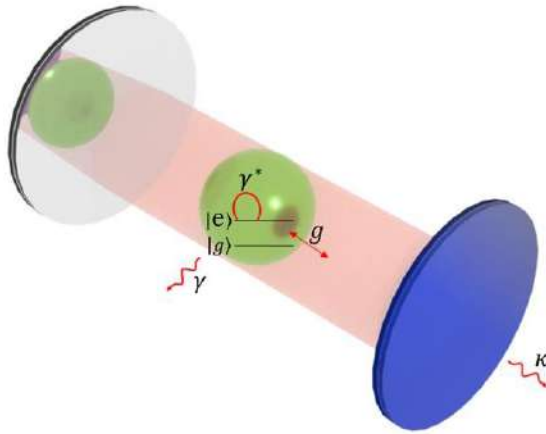


Figura 1. Esquema de un emisor cuántico con ratio de decaimiento γ y ratio de dephasing γ^* acoplado con una fuerza de acoplamiento g al monomodo de una cavidad óptica con ratio de decaimiento κ . El espacio de estados del emisor consiste en un sistema de dos niveles $|g\rangle$ y $|e\rangle$,

El EC viene descrito por un sistema de dos niveles $\{|f\rangle, |e\rangle\}$ (fundamental y excitado) y se encuentra acoplado con una constante de acoplamiento g al monomodo de la cavidad óptica con espacio de estados

en la base de Fock $\{|0\rangle, |1\rangle\}$ (vacío, ocupado). Si consideramos un detuning despreciable entre la energía de transición del EC y la frecuencia de resonancia de la cavidad, y asumimos como condición inicial la excitación instantánea del EC, la energía total del sistema se restringe al intercambio coherente de un único quanta entre el monomodo y el EC durante todo el proceso. En estas condiciones podemos truncar el espacio de Hilbert del sistema compuesto eliminando los estados no acoplados a la dinámica del sistema reduciéndolo al sistema 2-dimensional $\{|e 0\rangle, |f 1\rangle\}$. Después de aplicar la aproximación *rotating-wave*, el Hamiltoniano de interacción del sistema viene dado por [56]:

$$H = \begin{pmatrix} 0 & g \\ g & 0 \end{pmatrix} \quad (8)$$

Que describe la evolución unitaria del sistema compuesto sin tener en cuenta el acoplamiento con el entorno. Si consideramos que tanto el EC como la cavidad óptica se encuentran acoplados a un espacio continuo de modos electromagnéticos, la dinámica no unitaria de la matriz densidad del sistema vendrá descrita por la siguiente ecuación de Lindblad [56]:

$$\dot{\rho}_s = -i[H, \rho_s] + \mathcal{L}_{EC} + \mathcal{L}_{cav} + \mathcal{L}_{deph}, \quad \mathcal{L}_{EC} = -\gamma \begin{pmatrix} \rho_{ee} & \rho_{ec}/2 \\ \rho_{ce}/2 & 0 \end{pmatrix}, \quad \mathcal{L}_{cav} = -\kappa \begin{pmatrix} 0 & \rho_{ec}/2 \\ \rho_{ce}/2 & \rho_{cc} \end{pmatrix} \quad (9)$$

Donde ρ_{ee} y ρ_{cc} son las poblaciones del EC y la cavidad respectivamente y ρ_{ce} y ρ_{ec} son las coherencias del sistema compuesto. En este esquema los términos disipativos \mathcal{L}_{EC} y \mathcal{L}_{cav} vienen descritos bajo la aproximación de Born-Markov e introducen el efecto de disipación de energía por acoplamiento al continuo de modos electromagnéticos a través de un decaimiento exponencial de las poblaciones del EC y la cavidad a ratios γ y κ respectivamente. Adicionalmente, dependiendo del tipo de plataforma empleada para la integración de la FFI, el EC se encuentra acoplado a un entorno mesoscópico con un vasto número de grados de libertad. El sistema de dos niveles experimenta fluctuaciones aleatorias de su energía que pueden describirse mediante un proceso estacionario estocástico que viene introducido en la ecuación de Lindblad mediante el operador de colapso [56]:

$$\mathcal{L}_{deph} = -\gamma^* \begin{pmatrix} 0 & \rho_{ec}/2 \\ \rho_{ce}/2 & 0 \end{pmatrix} \quad (10)$$

El ratio disipativo γ^* , denominado dephasing puro, trae cuenta del decaimiento exponencial de las coherencias del sistema y por tanto del grado de decoherencia cuántica inducida por el acoplamiento del EC con su entorno mesoscópico. Dependiendo de la naturaleza de la plataforma para la integración del EC la magnitud de γ^* puede variar desde niveles comparables a γ , para el caso de emisores poco disipativos, hasta extremos de $10^4\gamma$ para el caso de emisores fuertemente disipativos, lo que la convierte en uno de los indicadores fundamentales de la calidad de la emisión de la FFI.

Este conjunto de definiciones para describir el grado de decoherencia en FCI establece medidas aplicables generales para determinar la calidad de estados cuánticos en q-bits ópticos. Sin embargo, no representan magnitudes directamente accesibles en el contexto de experimentos de coherencia óptica. En particular, existen funciones de correlación cuántica, directamente dependientes de los parámetros de decoherencia, más relevantes e indicados para evaluar resultados experimentales típicos. Uno de los experimentos más establecidos para la caracterización de estas funciones de correlación, conocido como HOM (de Hong, Ou

y Mandel) [57], se basa en el fenómeno de coalescencia de dos fotones independientes en un set-up de interferometría (ver Figura 2):

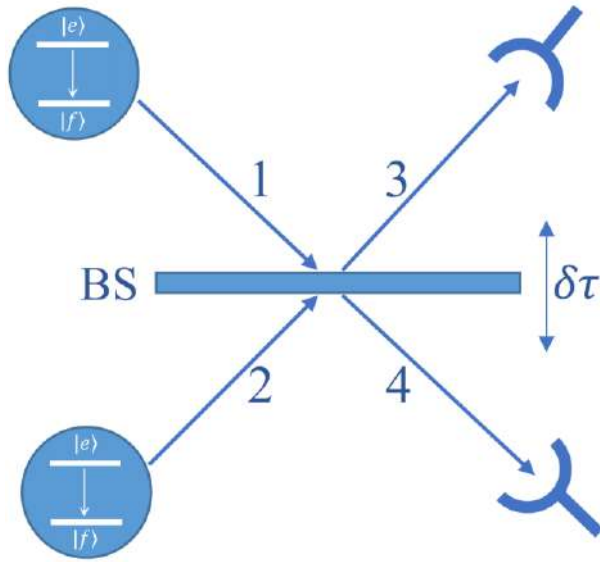


Figura 2. Esquema representativo de un experimento de interferometría HOM. Dos fotones independientes generados a partir de dos EC entran a través de los puertos 1 y 2 de un Beam Splitter (BS), abandonándolo por los puertos de salida 3 y 4, donde se colocan una pareja de detectores de fotones individuales. Mediante la regulación de la posición relativa del Beam Splitter con respecto a los EC es posible modificar la diferencia de caminos ópticos entre los dos haces introduciendo una diferencia de fase relativa $\delta\tau$.

En el esquema HOM dos fotones independientes generados a partir de dos EC llegan a los puertos de entrada 1 y 2 de un Beam Splitter (BS). Cada fotón abandona el BS con una cierta probabilidad por el puerto 3 o el puerto 4, la cual viene regulada por los parámetros de transmisión y reflectividad del BS. A la salida de los puertos 3 y 4 se colocan dos detectores de fotones individuales que generan pulsos eléctricos discretos con la detección de un fotón. En general se necesita considerar 4 caminos ópticos diferentes con 4 tiempos de propagación entre cada EC y cada detector. En la mayoría de set-ups experimentales 3 de estos caminos se mantienen fijos, mientras que se introduce un retardo ajustable en uno de los puertos de entrada para que las medidas puedan expresarse en función de ese retardo. Para nuestro propósito, resulta más conveniente considerar la situación en la que ambos EC y detectores se disponen simétricamente a cada lado del BS, de forma que los 4 tiempos de propagación son iguales. En esta configuración los desplazamientos del BS con respecto a la posición simétrica producen un retardo $\delta\tau$ afectando simultáneamente a los dos caminos ópticos simétricos. Las señales generadas por los fotodetectores registran, al mismo tiempo, el tiempo de llegada de cada fotón que abandona el BS, y se procesan mediante un contador de coincidencias que acumula los eventos en los que se detectan dos señales simultáneas. Los resultados del experimento vienen descritos por la función de correlación $g^{(2)}(\tau)$, que se relaciona con los operadores de campo mediante la expresión [58]:

$$g^{(2)}(\tau) = \frac{\langle\langle \hat{E}_3^\dagger(t)\hat{E}_4^\dagger(t+\tau)\hat{E}_4(t+\tau)\hat{E}_3(t)\rangle\rangle}{\langle\langle \hat{E}_3^\dagger(t)\hat{E}_3(t)\rangle\rangle\langle\langle \hat{E}_4^\dagger(t+\tau)\hat{E}_4(t+\tau)\rangle\rangle} \quad (11)$$

Donde el numerador indica la probabilidad de detección conjunta de un fotón en el puerto 3 a tiempo t y un fotón en el puerto 4 a tiempo $t + \tau$, mientras que el denominador permite la normalización con respecto a eventos descorrelacionados. Para el caso de EC ideales no disipativos, empleando un BS 50:50 y un retardo de $\tau = 0$, ambos fotones entran al BS simultáneamente y coalescen en un estado de Fock puro de dos fotones abandonando el BS por el mismo puerto. En este caso la probabilidad de detección conjunta es nula y $g^{(2)}(0) = 0$. Por el contrario, en presencia de mecanismos de dephasing los EC se encuentran descorrelacionados en fase debido a su acoplamiento a reservorios independientes. El desfase entre emisores genera una difusión de fases en los campos emitidos modificando el patrón de interferencia y destruyendo parcialmente la coalescencia. En este caso la función de correlación para $\tau = 0$ viene dada por [58]:

$$g^{(2)}(0) = 1 - \frac{\gamma}{\gamma + \gamma^*} \quad (12)$$

Por lo tanto, el grado de coalescencia viene regulado directamente por la magnitud del cociente $\frac{\gamma}{\gamma + \gamma^*}$. Dado que el grado de coalescencia describe en cierta medida la posibilidad de distinguir experimentalmente parejas de fotones independientes, a este cociente se le define como grado de indistinguibilidad (I), que de forma general para un sistema arbitrario viene dado por [56]:

$$I = \frac{\iint_0^\infty dt d\tau |\langle \hat{a}^\dagger(t+\tau) \hat{a}(t) \rangle|^2}{\iint_0^\infty dt d\tau \langle \hat{a}^\dagger(t) \hat{a}(t) \rangle \langle \hat{a}^\dagger(t+\tau) \hat{a}(t+\tau) \rangle} \quad (13)$$

Donde \hat{a}^\dagger y \hat{a} son los operadores creación y aniquilación del campo. La expresión (13) puede resolverse numéricamente vía teorema de regresión cuántica, y en algunos casos específicos admite solución analítica a través de métodos de funciones de Green fuera del equilibrio. De esta forma, la estimación teórica del grado de indistinguibilidad de una FFI para unos valores de γ , γ^* , g y κ específicos viene dada a partir de las soluciones de la ecuación de Lindblad (9) y el cálculo de (13). Dado que un extenso número de aplicaciones para esquemas de computación cuántica óptica se basan en el fenómeno de coalescencia (como la implementación de puertas CNOT), para el que se requieren fotones altamente indistinguibles, el grado de I representa una medida particularmente indicada de la calidad de los estados cuánticos de q-bits ópticos en presencia de fenómenos de decoherencia cuántica. Ya que, al mismo tiempo, se trata de una magnitud fácilmente extraíble experimentalmente, el valor de I se utiliza como figura de mérito para la caracterización de FFI.

Motivación y objetivos

En la actualidad existe un amplio espectro de plataformas viables como candidatas para FFI cuya integración en chip ha sido demostrada experimentalmente: III-V QDs [59], nanotubos de carbono [60], NV [61], centros SiV en diamante [62], defectos inducidos en materiales monocapa 2D [63], nanocubos de perovskitas [64] y dopantes en erbio [65], entre otros. Particularmente, las FFI basadas en QDs epitaxiales proporcionan control de posicionamiento durante el proceso de crecimiento [66] y la posibilidad de integración monolítica en nanoestructuras fotónicas [67,68]. Estas características facilitan significativamente la integración en cavidades ópticas en chip, permitiendo posicionar el EC en el punto de

máximo acople con el modo del resonador potenciando la calidad de la emisión. Como resultado, en los últimos años se ha reportado un gran número de demostraciones experimentales de QDs integrados en cavidades ópticas a temperatura (T) criogénica mostrando valores récord de I : $g^{(2)}(0) = 7 \cdot 10^{-3}$ e $I = 0.96$ con InAs/GaAs QDs integrados en micropilares a $T = 4.3$ K [69]; $g^{(2)}(0) = 1.2 \cdot 10^{-2}$ e $I = 0.97$ con InAs/GaAs QDs integrados en microcavidades DBR a 4.2 K [70]; $g^{(2)}(0) = 2.8 \cdot 10^{-3}$ e $I = 0.99$ con InAs/GaAs QDs integrados en micropilares DBR a 4 K [71]. Sin embargo, para T por encima del régimen criogénico el efecto de los mecanismos de dephasing puro reducen drásticamente la calidad de la coherencia en la emisión: $g^{(2)}(0) = 0.47$ con InAs/GaAs QDs a 120 K [72]; $g^{(2)}(0) = 0.34$ con InAs/InP QDs a 80 K [73]; $g^{(2)}(0) = 0.48$ con GaAs/GaAsP QDs a 160 K [74]. Para $T > 200$ K la máxima calidad reportada es de $g^{(2)}(0) = 0.34$ [75]. Como consecuencia, el valor de I se reduce a niveles impracticables para aplicación en tareas de procesamiento de información cuántica ($I > 0.8$ para la mayoría de esquemas propuestos [76]). En este contexto, la implementación de QDs en plataformas para FFI está restringida al régimen de T ultra-baja.

Con el objetivo de traspasar esta limitación existen diferentes estrategias de ingeniería de cavidades que recientemente han demostrado resultados prometedores. Una de las más extendidas consiste en maximizar el acople g por medio del confinamiento del modo óptico en una cavidad de volumen modal (V_{eff}) ultra-pequeño. En este aspecto las cavidades plasmónicas ofrecen una gran variedad de alternativas: El confinamiento de modos ópticos en huecos sub-nanométricos entre pares de nanopartículas plasmónicas (esferas de oro [77], nanohilos de oro [78], bowties metálicos [79]) generan los máximos confinamientos de campo alcanzando valores de hasta $g = 200$ meV [80], aunque al mismo tiempo, proporcionan bajos factores de calidad (Q) ($\sim 10^1$) y eficiencias de extracción (β) [81]. Existen diferentes propuestas para el incremento de Q y β en estos sistemas, algunas de ellas basadas en estructuras de núcleos dieléctricos con envolturas metálicas para el incremento de Q [82,83], o sistemas híbridos de Fabrit-Perot con nano-antenas para la maximización de β [84,85]. En general, las estructuras plasmónicas presentan una serie de desventajas en términos de pérdidas óhmicas en las plataformas metálicas que repercuten drásticamente tanto en la eficiencia de integración en chip como en el ajuste del valor de Q [86]. En contraposición, las cavidades dieléctricas basadas en tecnología del silicio ofrecen plataformas de pérdidas ultra-bajas, y al mismo tiempo, compatibles con las tecnologías CMOS para la integración con circuitos electrónicos complementarios. Además, los avances en las tolerancias de precisión en tecnologías de litografía por haz de electrones [87] sobre obleas de silicio y nitruro de silicio permiten la miniaturización de estructuras de elevada complejidad con detalles en el rango de las decenas de nanómetros [88]. A lo largo de la última década se ha demostrado con éxito la integración de varios tipos de EC en diferentes cavidades dieléctricas en chip, entre las que destacan: Cristales fotónicos 2D [89-91]; micro-pilares DBR [92]; nanobeams [93]; bullseye [94]; Bragg-Fabry-Perot en chip [95]. El diseño de cavidades con V_{eff} ultra-pequeños también es posible en las plataformas dieléctricas basadas en cristales fotónicos con slots. Los nanobeams con slots discretos [96,97] ofrecen V_{eff} del orden de $10^{-3}(\lambda/2n)^3$ manteniendo alto Q . Sin embargo, la introducción de slots discretos produce grandes perturbaciones en el modo óptico reduciendo β . Por otro lado, los diseños basados en slots continuos [98], o concatenaciones slot-anti-slot en nanobeams [99,100] consiguen mantener un V_{eff} reducido manteniendo alta β . En contraprestación, las cavidades dieléctricas con V_{eff} ultra-

pequeño dificultan significativamente la deposición del EC cuántico en la posición de máxima intensidad de campo eléctrico [101]. Por lo general, la realización experimental de la integración de un EC requiere de la fabricación de un elevado número de dispositivos y el chequeo de candidatos adecuados uno a uno. De esta forma, aunque estos esquemas puedan resultar útiles para la demostración experimental de determinados fenómenos cuánticos, se encuentran francamente lejos de convertirse en una tecnología escalable. Hasta la fecha, la realización de FFI de alta I con EC fuertemente disipativos (como QDs a alta T o defectos en materiales 2D tanto a alta como baja T) no ha sido demostrada experimentalmente. En este contexto, la exploración teórica sobre nuevas estrategias para la conceptualización y diseño de plataformas para FFI de alta I resulta especialmente relevante.

En general, el diseño de plataformas tanto para FFI como otros componentes de circuitos integrados pasa por la simulación computacional de la estructura integrada a través de métodos numéricos de resolución de las ecuaciones clásicas de Maxwell, como el FDTD [102-105]. A partir de la evaluación del rendimiento de la estructura en el entorno de simulación, se procede a la optimización de los diferentes grados de libertad de la geometría del diseño para la maximización de una determinada figura de mérito clásica (como Q o V_{eff}). La selección de estas figuras de mérito clásicas y sus valores objetivo vienen dados por los resultados de estudios teóricos basados en modelos cuánticos (como en (9)), que buscan ofrecer guías de diseño generales para el alcance de alta I [106-108]. En otras palabras, las estrategias de diseño actuales se construyen a partir de un proceso de dos etapas independientes: (i) Desarrollo de un modelo cuántico que determine cuales son los valores adecuados de figuras de mérito clásicas (Q o V_{eff}) para la obtención de alta I en una plataforma arbitraria; (ii) Diseño, simulación clásica FDTD y optimización de los parámetros geométricos de una plataforma específica para ajustar las figuras de mérito clásicas a los valores objetivo. Los trabajos citados previamente en las referencias del párrafo anterior representan ejemplos de aplicación de esta metodología. Bajo un punto de vista riguroso este enfoque presenta varias deficiencias. Como se ha demostrado en un número de trabajos teóricos previos [106-108], la dependencia de I con las figuras de mérito clásicas es altamente no-trivial, y se ve drásticamente afectada por los parámetros específicos del EC y otros parámetros clásicos no considerados en los modelos. Por otro lado, la electrodinámica presente en una estructura específica puede tener efectos en la interacción con el EC que tampoco están incorporados en el modelo cuántico, que considera una plataforma general descrita por unos pocos parámetros del campo. Como consecuencia, la extrapolación de las conclusiones del modelo teórico cuántico general a situaciones específicas con estructuras y EC concretos puede conducir a una descripción deficiente del proceso real, y una desviación significativa de los resultados de las simulaciones con los datos experimentales. En conclusión, para la búsqueda de estructuras de FCI con el objetivo de reducir de la decoherencia cuántica se hace indispensable el desarrollo de modelos teóricos híbridos que proporcionen expresiones analíticas que relacionen directamente los parámetros del diseño con las figuras de mérito de coherencia cuántica (i.e. I). A través de estas herramientas podremos llevar a cabo interpretaciones físicas intuitivas de los procesos que tienen lugar en cada dispositivo en concreto, obteniendo orientaciones mejor fundamentadas para el diseño.

En este contexto, la presente disertación tiene como objetivo principal el desarrollo de **modelos teóricos** para la obtención de expresiones analíticas que relacionen directamente los parámetros geométricos de estructuras fotónicas con el grado de I . Las soluciones proporcionadas por este esquema teórico permiten

la interpretación física del efecto directo de variaciones de los parámetros de la estructura sobre la decoherencia del sistema con un EC integrado. Al mismo tiempo, se han desarrollado **métodos numéricos para la simulación** de EC integrados en plataformas fotónicas basados en modelos híbridos que combinan la resolución de las ecuaciones de Maxwell con modelos cuánticos abiertos del tipo (9). Estos métodos permiten aplicar esquemas de optimización de estructuras donde la variación de los parámetros de la geometría tiene un impacto directo sobre el cálculo de la I en la plataforma, en lugar de parámetros indirectos como Q o V_{eff} , ofreciendo una estimación más fiable de su rendimiento en términos de las figuras de mérito objetivo. Adicionalmente, se ha llevado a cabo la realización de **esquemas Machine-Learning de optimización** para estructuras de FCI basados en arquitecturas híbridas de algoritmos genéticos (AG) con redes neuronales (RN). A partir de bancos de datos producidos por los modelos teóricos se han entrenado con éxito diferentes arquitecturas de RN les capaces de modelizar el comportamiento plataformas integradas y predecir el valor de I en función de una serie de inputs relacionados con la geometría de la estructura. Esta metodología novedosa ofrece una reducción significativa de los recursos computacionales para problemas de maximización permitiendo la optimización simultánea de un gran número de grados de libertad a partir de AG. En su aplicación para estructuras de FCI, el esquema híbrido RN-AG hace posible la optimización complementaria de varias figuras de mérito como β e I abarcando un enorme número de grados de libertad de la geometría del diseño simultáneamente.

Este análisis se estructura a partir de tres trabajos independientes, presentados en el Capítulo 2, cada uno de ellos dedicado a la exploración de un tipo específico de plataforma integrada: (i) EC integrados en guías de onda; (ii) EC integrados en cavidades ópticas; (iii) Clústeres de EC acoplados entre sí integrados en cavidades ópticas.

- (i) “Guimba, J., Weituschat, L. M., Montolio, J. L., & Postigo, P. A. (2021). Enhancement of the indistinguishability of single photon emitters coupled to photonic waveguides. *Optics Express*, 29(14), 21160-21173, <https://doi.org/10.1364/OE.422023> Journal 2021 Received 10 Feb 2021/ published 22 Jun 2021”
- (ii) “Guimba, J., Sanchis, L., Weituschat, L., Manuel Llorens, J., Song, M., Cardenas, J., & Aitor Postigo, P. (2022). Numerical Optimization of a Nanophotonic Cavity by Machine Learning for Near-Unity Photon Indistinguishability at Room Temperature. *ACS Photonics*. <https://doi.org/10.1021/acspophotonics.1c01651>, Received: October 27, 2021/ Published: May 11, 2022”
- (iii) “Guimba, J., Sanchis, L., Weituschat, L. M., Llorens, J. M., & Postigo, P. A. (2022). Perfect photon indistinguishability from a set of dissipative quantum emitters. *Nanomaterials*, 12(16), 2800, <https://doi.org/10.3390/nano12162800>, Received: 17 July 2022 / Published: 15 August”

Los resultados obtenidos en esta serie de publicaciones contribuyen al desarrollo del conocimiento de los mecanismos de decoherencia cuántica en circuitos de fotónica cuántica integrada y esperamos resulten de

utilidad para la búsqueda de nuevas estrategias de conceptualización y diseño para el avance de esta tecnología cuántica emergente.

Capítulo 2. Publicaciones

Enhancement of the Indistinguishability of Single Photon Emitters Coupled to Photonic Waveguides

Abstract: One of the main steps towards large-scale quantum photonics consists of the integration of single photon sources (SPS) with photonic integrated circuits (PICs). For that purpose, the PICs should offer an efficient light coupling and a high preservation of the indistinguishability of photons. Therefore, optimization of the indistinguishability through waveguide design is especially relevant. In this work we have developed an analytical model that uses the Green's Dyadic of a 3D unbounded rectangular waveguide to calculate the coupling and the indistinguishability of an ideal point-source quantum emitter coupled to a photonic waveguide depending on its orientation and position. The model has been numerically evaluated through finite-difference time-domain (FDTD) simulations showing consistent results. The maximum coupling is achieved when the emitter is embedded in the center of the waveguide but somewhat surprisingly the maximum indistinguishability appears when the emitter is placed at the edge of the waveguide where the electric field is stronger due to the surface discontinuity.

© 2020 Optical Society of America under the terms of the [OSA Open Access Publishing Agreement](#)

Introduction

Indistinguishability of single photons generated by point defects is the central topic of quantum photonic integrated circuits for quantum information applications like quantum simulation [1], quantum teleportation [2] or quantum networks [3]. Indistinguishable photons are usually generated by parametric down-conversion [4] or alternatively from a single two-level quantum emitter in a solid-state environment [5]. Over the last years several on-chip integration of different SPS material systems have been demonstrated: III-V quantum dots [6], carbon nanotubes [7], NV [8] or SiV centers in diamond [9] and 2D layered materials [10]. For most of those solid-state quantum emitters the intrinsic indistinguishability at room temperature is almost zero because pure dephasing rates are orders of magnitude larger than the population decay rate [11]. Improvement of the indistinguishability can be achieved by low temperature operation and by reducing the radiative lifetime of the SPS using an optical cavity that takes advantage of the Purcell effect [12]. The balance between dephasing and population decay rates varies significantly depending on the material system. Whereas for specific single self-assembled GaAs quantum dots the emission at low

temperature can be radiative lifetime limited [13], defects in 2D materials can exhibit several orders of magnitude of difference between radiative decay and pure dephasing rates [14]. Purcell enhancement using photonic resonators permits on-chip control of light–matter interaction to enhance collection efficiency and generation of indistinguishable photons [15] that can be used for on-chip processing of quantum information [16-18]. Therefore, it is important to explore the coupling of SPS to PICs and its effect on the indistinguishability. In this work we use an analytical treatment of light radiation from a point source placed at an arbitrary location and with arbitrary orientation on a waveguide. The refractive indexes of the waveguide correspond to materials commonly used in silicon photonics (SiO_2 , Si_3N_4 , Si) besides other high-index materials like WSe_2 or WO_3 [19]. It is worth to note that other specially designed nanomaterials with ultra high refractive index can be designed [20]. We explore how the position of the source and its orientation affects the coupling to the waveguide modes and the indistinguishability of the photons. We also explore how the dimensions of the waveguide impact the indistinguishability. We perform FDTD simulations to validate the analytical model and to calculate the Purcell effect. The results show remarkable differences depending on the orientation of the SPS and provide maximum indistinguishability when the source is placed at the edge of the waveguide, in contrast to the maximum coupling efficiency position at the center of the waveguide. The indistinguishability is expressed in terms of the pure dephasing value of the emitter, so that the effects of the waveguide can be compared between strong and weak dissipative emitters. Depending on the waveguide geometry and the position of the source the indistinguishability can either increase or decrease, showing non-negligible enhancements for weak dissipative emitters placed at optimum positions.

Several works deal with the radiation of a point source embedded in bounded dielectric slabs and square waveguides through Green's function methods [21-26]. Also, the problem of the unbounded dielectric slab is treated in [27] from a classical perspective and in [28] from a quantum perspective. However, in those cases the description of the source comes from the macroscopic expression of the dipole moment, without computing the Green's Dyadic. The Green's function of the unbounded 2D dielectric slab is covered in [29] and the same for the 3D cylindrical fiber in [30-32] through the development of a transform theory. As far as we know, the Green's Dyadic of a 3D unbounded rectangular waveguide has not been treated until this work. Here we develop a generalization of the transform theory from the 2D case [29] to obtain the solution of the 3D version of the problem for an unbounded rectangular waveguide. The obtention of the Green's Dyadic allows us to directly connect the value of the indistinguishability with the geometrical parameters of the waveguide, which also has not been covered neither in the previously mentioned works.

Methods, results and discussion

Indistinguishability for different SPS

In an isolated two-level system, the emission rate can be fully described by its population decay rate Γ_0 . However, a solid-state quantum emitter has an interaction with the mesoscopic environment. The two-level system is affected by random fluctuations of its energy that can be described by a stationary stochastic

process characterized by a dephasing rate Γ^* [33]. In this situation the indistinguishability (I) is reduced to [34]:

$$I = \frac{\Gamma_0}{\Gamma_0 + \Gamma^*}, \quad (1)$$

In general, for any practical implementation in quantum information processing $I \geq 0.5$ [33]. The pure dephasing rates at room temperature of solid-state quantum emitters like color centers, quantum dots or organic molecules are about 3 to 6 orders of magnitude larger than their radiative decay rates [34]. Improvement of this efficiency can be achieved by working at cryogenic temperatures. For example, for excitons weakly confined in GaAs quantum dots the dot ground-state transition at low temperature is near radiative life-time limited [13] which would provide a balance of about $\Gamma^*/\Gamma_0 \approx 1$ and $I \approx 0.5$. There are recent reports of even better performance with strain free GaAs/AlGaAs quantum dots without the need of Purcell enhancement [35]. For those highly efficient emitters the ratio $\Gamma^*/\Gamma_0 \rightarrow 0$ and the intrinsic indistinguishability tends to the unity. As an example of an intermediate situation, InAs quantum dots have decay and pure dephasing rates $\Gamma^*/\Gamma_0 = 2.6$ [36,37] and the indistinguishability is only $I \approx 0.19$. On the opposite side, strain-induced defects in 2D materials have typical radiative lifetimes in the order of nanoseconds with dephasing lifetimes in the order of picoseconds [14]. For those emitters the Γ^*/Γ_0 balance reaches 103 with almost zero indistinguishability. However, recent works related to defects created in transition metal dichalcogenides (like MoS₂) by local helium ion irradiation [38] show radiative lifetimes <150 ps. Also, a lifetime <100 ps has been observed recently in regular strain induced defects in WSe₂ layers deposited on metallic surfaces [39, 40]. More examples of quantum emission demonstrations in 2D materials can be found in [41]. Therefore, emitters with a certain Γ^*/Γ_0 ratio may enhance significantly their indistinguishability when properly integrated inside photonic waveguides due to the change in their radiative decay rate. We will show that for certain geometries and emitter positions I can be greatly reduced whereas optimal configurations can maintain or even enhance I significantly, especially for emitters with a certain Γ^*/Γ_0 ratio.

Analytic model for pure dephasing

We can assume that for a two-level emitter coupled to a waveguide the coupling (g) and the cavity decay rate (κ) are in the incoherent limit ($2g \ll \Gamma_0 + \Gamma^* + \kappa$) and “bad cavity” regime ($\kappa \gg \Gamma_0 + \Gamma^*$) [34]. In that limit the cavity can be adiabatically eliminated so the dynamics of the coupled system are described by an effective quantum emitter with decay rate ($\Gamma + R$) where R is the population transfer between the emitter and the cavity [34]:

$$I = \frac{(\Gamma_0 + R)}{(\Gamma_0 + R) + \Gamma^*} ; R = \frac{4g^2}{\Gamma_0 + \Gamma^* + \kappa}, \quad (2)$$

R is related to the Purcell enhancement (P_f) by $R = \Gamma_0 \cdot P_f$ [42]. Substituting in (2) we obtain:

$$I = \frac{(1+P_f)}{(1+P_f) + \frac{\Gamma^*}{\Gamma_0}}, \quad (3)$$

Here the Purcell enhancement is defined as Γ/Γ_0 where Γ is the population decay rate in the inhomogeneous environment. This ratio is related to the power emitted by the source [43]:

$$\frac{\Gamma}{\Gamma_0} = \frac{P}{P_0}, \quad (4)$$

With P and P_0 the power emitted in the inhomogeneous and homogeneous environment, respectively. The radiative decay rate enhancement can be obtained by FDTD simulations integrating the power emitted by the source inside the waveguide (P) and normalizing it with respect to the power in a homogeneous surrounding (P_0). In order to extract the maximum amount of physical information from the interaction between the quantum emitter and the photonic waveguide, we develop an analytic model of the system. We use the relation between Γ and the Green dyadic of the equation governing the interaction between the source and the waveguide. From (4) one can obtain the dependence of the decay rate with the imaginary part of the Green dyadic evaluated at the position of the source [43]:

$$\Gamma = \frac{4\omega^2}{\pi c^2 \hbar \epsilon_0} [\vec{\mu} \cdot \text{Im}\{\vec{G}(r_0, r_0)\} \cdot \vec{\mu}], \quad (5)$$

Where ω is the frequency of emission of the source, ϵ_0 is the vacuum dielectric constant, c the speed of light in vacuum, \hbar the reduced Planck constant, and μ the dipole moment of the source. Fig 1 shows a layout of a section of the waveguide used for our model. The waveguide (infinite in the z-axis) has a rectangular section filled with a linear homogeneous medium with refractive index n_1 . The surrounding environment has a refractive index $n_2=1$.

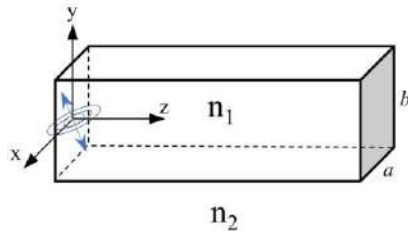


Fig. 1. Layout of the homogeneous infinite waveguide used for the analytical model.

The calculation of the Green's Dyadic is based on the development of a 3D transform theory applied to the unbounded Helmholtz equation. Details of the calculation and the explicit dependence with the waveguide width and the position/orientation of the source (for each contributing guided mode) can be found in the Supplementary material. Using the Green's dyadic we can obtain the Purcell enhancement as a function of the waveguide width for a point dipolar source that can be oriented parallel to the x-axis (s) or to the y-axis (p). The source is placed initially at the center of the waveguide cross-section ($x_0=0, y_0=0$). Initially, the waveguide thickness is arbitrarily fixed at $b=200$ nm and we will change the width (a) and the refractive index of the waveguide (n_1) using $n_1=1.44, 2$ and 3.4 corresponding to SiO₂, SiN and Si respectively. This will provide some initial hints on how the system actually behaves.

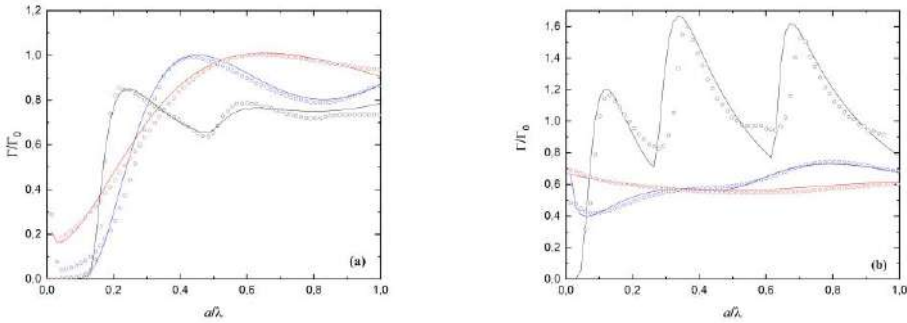


Fig. 2. Purcell enhancement of the radiative decay rate as a function of the wavelength-normalized waveguide width obtained from analytical calculations (lines) and FDTD simulations (open dots). $n_1=3.4$ (black), $n_1=2$ (blue), $n_1=1.44$ (red). (Left) Source orientation parallel to x-axis (s) (Right) Parallel to y-axis (p) .

Fig. 2 shows the value of the Purcell enhancement, Γ/Γ_0 , as a function of the normalized waveguide width, a/λ , for the mentioned values of n_1 (1.44, 2, 3.4). Solid lines show the calculation of Γ/Γ_0 using (5) and open dots show the values obtained through FDTD simulations. Details of the FDTD simulations can be found in the Supplementary material. Fig. 2.a shows the Purcell enhancement for the s-source. In general, it almost vanishes before the width reaches the cut-off of the TE10 mode, which happens for $a/\lambda = 0.13$, 0.1 and 0.05 for $n_1=3.4$, 2 and 1.44, respectively. Since the cut-off increases with n_1 , the vanishing threshold also increases with n_1 . After the cut-off, for increasing a/λ , The Purcell enhancement increases as the propagation constant decreases (with $1/a$) and the mode gets more confined. The maximum values for Γ/Γ_0 are 0.83, 1 and 1 when $a/\lambda=0.23$, 0.42 and 0.64 respectively and the light confinement is maximum. If the waveguide becomes wider the modes spread out with lower intensity at the position of the source producing a decrease in Γ/Γ_0 that scales with $1/a$, until the cut-off with the second order mode is reached at $a/\lambda=0.43$, 0.8 and 1.2 for the same values of n_1 . At this point, the same mechanism takes place showing the second maxima and second decay. The process is repeated for each contributing mode. We note that there is no contribution from the lowest TM00 mode because the components of the Green dyadic vanish at the position of the source for this orientation. This is expected since the x-components of the fundamental modes are antisymmetric with respect to the source when it is placed at the center. For the p-source (Fig. 2, Fig. 2.a) the situation is somewhat opposite and the components do not vanish at the position of the source for the lowest order TM00. Since $b=200$ nm, in the case of $n_1=2$ and $n_1=1.44$ the cut-off condition is already reached at $a/\lambda = 0$. For $n_1=3.4$ the cut-off is reached at $a/\lambda = 0.05$. The Purcell enhancement for the s-source shows maximum values of $\Gamma/\Gamma_0=1.2$, 0.51 and 0.6 when $a/\lambda=0.13$, 0.27 and 1 for the same values of n_1 than before. For both s and p orientations the Purcell enhancement decays asymptotically with the width, although in a different trend due to the different (m,n) values for each contributing mode. The maxima located at $a/\lambda=0$ are accidentally generated by the model due to the unphysical divergence of the Green function at the origin. The maximum values of Γ/Γ_0 for the s-source are about 40% higher than for the p-source with $n_1=2$ and $n_1=1.44$. The reason is the transverse electric field component of the TE10, which is higher than the TM00 at the position of the source ($x_0=0$, $y_0=0$) [44]. Nevertheless, for $n_1=3.4$ the maximum Γ/Γ_0 is about 40% higher for the p-source. This happens because when $n_1=2$ and $n_1=1.44$ the TE10 mode is well confined for $b=200$ nm, but when $n_1=3.4$ the TE10

mode is not optimally confined and the source has a better overlap with the TM00. Therefore, high modal confinement and good spatial overlapping to waveguide modes are key ingredients for Purcell enhancement, as one could intuitively expect. The indistinguishability should show its maximum value when the Purcell enhancement is maximum, according to (3). We note that a deviation in the optimal width of about 20 nm can decrease the Purcell enhancement, and therefore the indistinguishability, about 10%.

Since the position of the emitter is very relevant, we explore now its effect keeping fixed the waveguide widths in $a/\lambda=0.23, 0.42$ and 0.64 (respectively to the n_1 values as before) and for the s orientation. We change the position of the source along the x-axis, from the center of the waveguide ($x_0/a=0$) to far away from the edge ($x_0/a>\pm 1$).

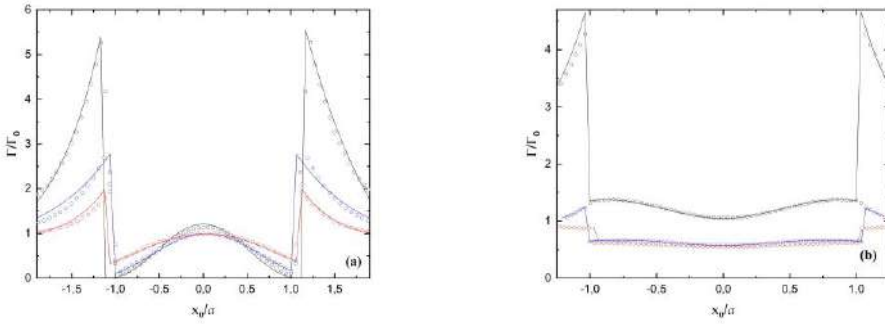


Fig. 3. Enhancement of the radiative decay rate as a function of the position of the point source (normalized with respect to the waveguide width, a) obtained from the analytical model (lines) and from FDTD simulations (open dots). The origin in the x-axis corresponds to the center of the waveguide and the edges to $x_0/a=\pm 1$. $n_1=3.4$ (black), $n_1=2$ (blue), $n_1=1.44$ (red). (Left) s-source (Right) p-source.

First we focus on the region inside the waveguide core ($x_0/a<\pm 1$). Fig. 3 (left panel) shows the Purcell enhancement depending on the position of the s-source. As the s-source is separated from the center the overlapping to symmetric modes decreases and the enhancement decreases. The maximum enhancement happens at the center of the waveguide. A deviation from that optimal position of about $x_0/a=\pm 0.5$ leads to a decrease of the Purcell enhancement of about 20%. The opposite behavior is obtained for a p-source (Fig. 3 right). In this case the minimum overlapping is obtained at the center of the waveguide and the maximum enhancement is for about $x_0/a=\pm 0.75$, where the overlap with the antisymmetric modes is maximum. FDTD simulations provide a maximum value for the enhancement of 1.42 matching the analytical calculations within an error of 0.2% for the Purcell enhancement and 0.3% for x_0 .

The variation of the coupling efficiency with the position of the source inside the waveguide follows a similar trend than the Purcell enhancement. Details of coupling definition and its calculation can be found in the Supplementary material. Fig. 4 shows the coupling efficiency depending on the position of the source for both s and p orientations. At the center of the waveguide, the s-source achieves a maximum coupling of $P_c/P_0 = 0.88, 0.6$ and 0.25 for $n_1=3.4, 2$ and 1.44 respectively, where P_c is the emitted power coupled to guided modes. As expected, the coupling decreases with decreasing n_1 . When the s-source is separated from the center, the coupling to symmetric modes decreases. Again, the opposite behavior is obtained for

the p-source, which shows minimum coupling at the center of the waveguide. Some discrepancies between analytic and FDTD results arise from the discretization of space in the FDTD simulations. Also, the slight asymmetries shown in the x_0/a dependence in Fig. 4b are due to small misalignments between the simulation cells and the dielectric waveguide.

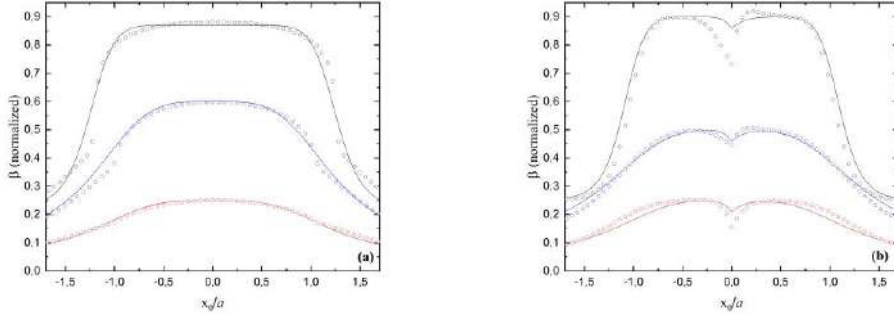


Fig. 4. Coupling efficiency versus normalized position of the source with respect to waveguide width a . The origin in the x-axis corresponds to the center of the waveguide. The edges of the waveguide correspond to $x_0/a=\pm 1$. Figure shows results from analytical model (lines) and from FDTD simulations (open dots). $n_1=3.4$ (black), $n_1=2$ (blue), $n_1=1.44$ (red). (Left) s-source, (Right) p-source.

Since there are recent experimental works that use heterogeneous integration of SPS and waveguides [45][46] it is worth to explore the dependence of the enhancement with the position of the source in the region outside the waveguide but close to its edge ($x_0/a > \pm 1$). Due to the index contrast between air and waveguide the electric field shows a strong discontinuity at the interface with an amount comparable to the square of the index ratio at the interface [47]. This effect can lead to a dramatic alteration of the mode profile in the vicinity of the edge that drastically increments the Purcell enhancement. This effect has been used, for example, to achieve ultrasmall cavity mode volumes of the order of $7 \cdot 10^{-5} \lambda^3$ that enable ultrastrong Kerr nonlinearities at the single-photon level [48]. When the source is placed at the edge the enhancement is $\Gamma/\Gamma_0=4.2, 2.6$ and 1.9 for the s-source, and $\Gamma/\Gamma_0=4.6, 1.2$ and 0.87 for the p-source. The cost of the increase in the Purcell enhancement is a decrease in the coupling efficiency, which for the position at the edge is about $P_c/P_0 = 0.5, 0.37$ and 0.15 for the s-source and about $P_c/P_0 = 0.5, 0.3$ and 0.12 for the p-source. Details about this calculation can be seen in the Supplementary material. At the points $x_0/a=\pm 1$ (i.e. the edges of the waveguide) the mode field shows its highest contrast according to $E_{clad} = (n_1/n_2)^2 E_{core}$ where E_{core} is the field inside the waveguide and E_{clad} is the field outside the waveguide. For that reason, the maximum value of the Purcell enhancement lies in the edges of the waveguide, especially for high n_1 . Since the Purcell enhancement is strictly dependent on the field value at the position of the source, its maximum value is achieved at the edge of the waveguide. On the other hand, the coupling is proportional to the guided-mode field value divided by the non-guided modes field value. Despite the guided-mode field value is maximum at the edge, the value of non-guided modes is also maximum at the edge. In consequence, the coupling at the edge is weaker than in the center of the core (where the coupling to non-guided modes is smaller).

Now that we have a better understanding of the physical meaning of the model we can explore simultaneously both degrees of freedom (i.e. a and b) in order to find the optimal configurations in terms

of the figures of merit. The source is placed initially at the center of the waveguide cross-section ($x_0=0$, $y_0=0$) in horizontal orientation (i.e. parallel to x -axis) but this time both a and b are varied from 0 to 0.7λ . The results are obtained for four different values of the refractive index of the waveguide $n_1=1.44, 2, 3.4$, and 4.

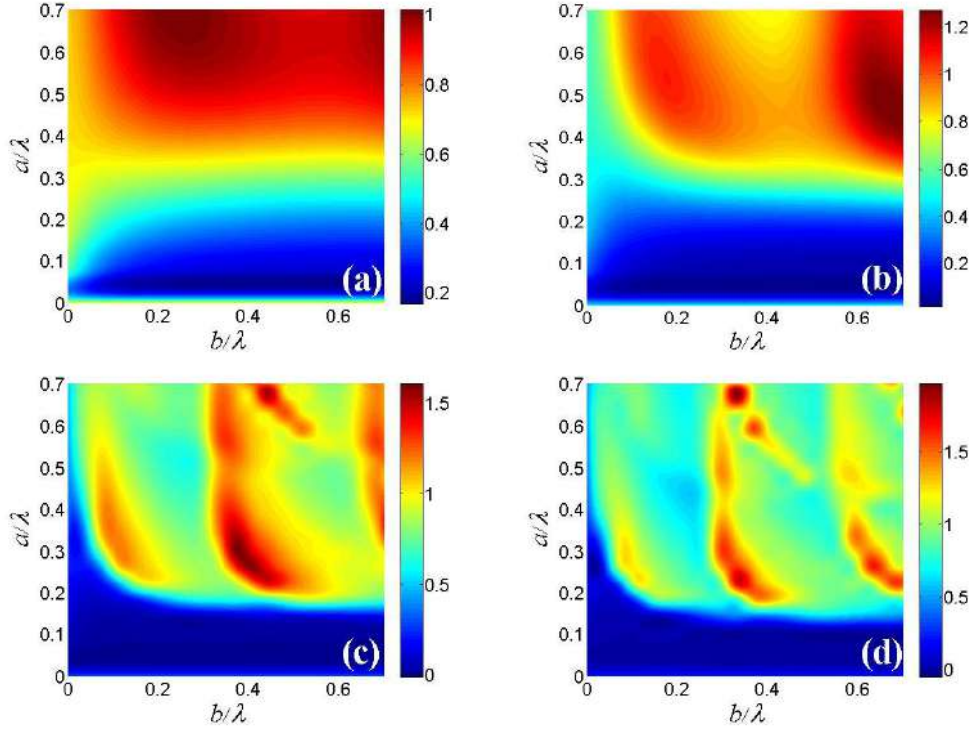


Fig. 5. Purcell enhancement as a function of the normalized width, a/λ , and thickness, b/λ , when the s-source is placed at the center of the waveguide calculated with the analytical model. (Top-left) $n_1=1.44$ (Top-right) $n_1=2$ (Bottom-left) $n_1=3.4$ (Bottom-right) $n_1=4$.

Fig. 5 shows the value of Γ/Γ_0 as a function of the normalized waveguide width, a/λ , and normalized thickness, b/λ , calculated for the four different refractive indexes. The blue areas in the plots correspond to values of a and b below the first cut-off. The subsequent maxima and minima correspond to the activation of the TE mn and TM mn modes. For low refractive indexes (i.e. $n_1=1.44, 2$) the two first modes appear. As the refractive index increases the source starts to overlap effectively with the rest of higher order modes. The absolute maxima of Γ/Γ_0 increases with the refractive index, since the area of the spatial distribution of the modes decreases with n_1 , so the field intensity gets higher at the position of the source. We obtain maximum values of $\Gamma/\Gamma_0=1, 1.1, 1.6$ and 1.9 for $n_1=1.44, 2, 3.4$ and 4 , respectively. Due to the symmetry of the system the plots for the vertical source show the same rotated 90 degrees (see the Supplementary material).

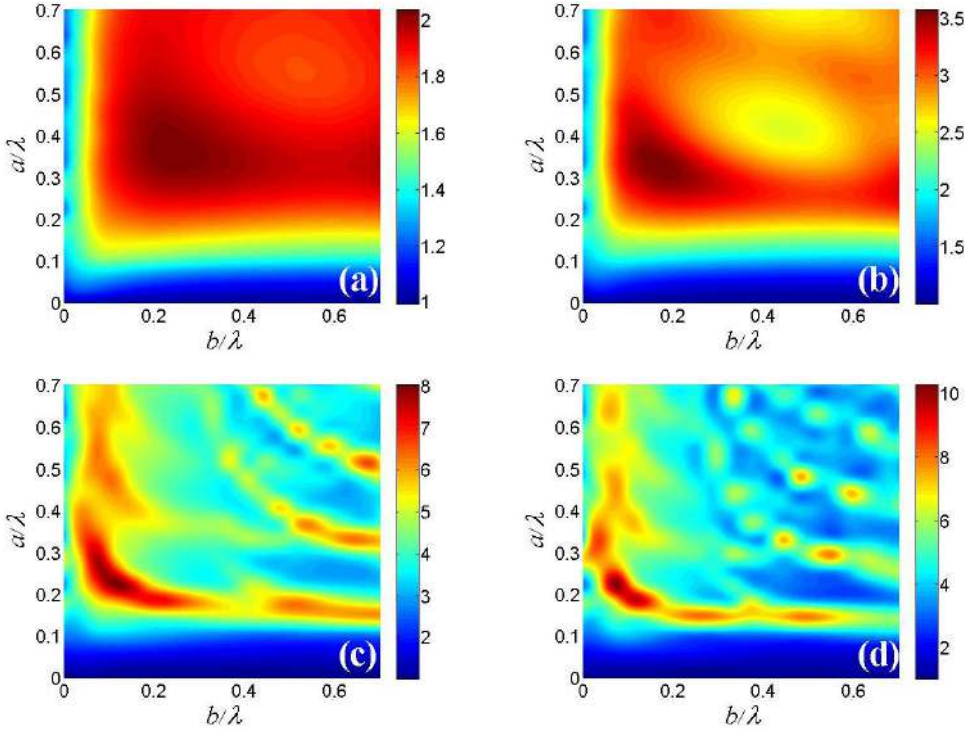


Fig. 6. Purcell enhancement as a function of a/λ and b/λ when the s-source is placed outside the core calculated with the analytical model. (Top-left) $n_1=1.44$ (Top-right) $n_1=2$ (Bottom-left) $n_1=3.4$ (Bottom-right) $n_1=4$.

Next, we place the source outside the waveguide, 10 nm away from the edge and oriented horizontally (i.e. parallel to x-axis). Fig. 6 shows the value of Γ/Γ_0 as a function of the normalized waveguide width, a/λ , and normalized thickness, b/λ , for different n_1 . As we saw before, the field discontinuity generates a dramatic enhancement when the source is placed near the evanescent region of the mode. We observe that in all of the cases the maxima are located in the bottom left region, where both a and b have reached the cut-off but the first mode has not reached the maximum confinement. For that geometry, the mode is not optimally confined inside the core and the field gets accumulated at the edges of the waveguide so the overlap is more efficient. We obtain maximum values of $\Gamma/\Gamma_0=2, 3.5, 8$ and 10 for $n_1=1.44, 2, 3.4$ and 4 respectively. At this time the orientation of the source matters, since we can arrange two different configurations: (a) Parallel to the larger side of the waveguide (i.e. parallel to the x-axis if the source is placed on top of the core, or parallel to the y-axis if the source is placed on one side of the core); (b) Perpendicular to the larger side of the waveguide (i.e. parallel to the y-axis if the source is placed on top of the core, or parallel to the x-axis if the source is placed on one side of the core). The plots in Fig. 6 correspond to the second case. When the source is parallel we obtain lower values for the maximum enhancements: $\Gamma/\Gamma_0=0.9, 1.5, 6.8$ and 7.1 for the different values of n_1 . For emitters with orientations other than s or p one should decompose the projection of the orientation on the x-axis and the y-axis and treat the emitter as two separated emitters with corresponding s and p contributions. The total enhancement is given by the addition of those two contributions.

The maximum enhancements obtained for the source at the edge can be used in (3) to obtain the maximum values for the indistinguishability. Fig. 7 shows I for an s-emitter placed at the edge of the waveguide versus

the intrinsic emitter normalized dephasing ratio, Γ^*/Γ_0 . Results for the p-source show an analogous behavior. From Fig. 7 we see that for low dissipative emitters with $\Gamma^*/\Gamma_0 \sim 1$ (like weakly confined GaAs dots of Ref. [13]) the expected indistinguishability can reach a value up to 0.8 when $n_1=4$, which makes an enhancement of I of about 30% with respect to the same dots without coupling to a waveguide. For InAs quantum dots with $\Gamma^*/\Gamma_0 = 2.6$ [36,37] we obtain $I \approx 0.6$, an enhancement of 40%. As the pure dephasing rate increases the indistinguishability decays asymptotically reaching 0.2 when $\Gamma^*/\Gamma_0 = 50$. Therefore, for strong dissipative systems with $\Gamma^*/\Gamma_0 > 50$ (like quantum emitters in 2D materials) the effect of the waveguide in the indistinguishability is very small. For emitters with lower dephasing ratio, $\Gamma^*/\Gamma_0 < 1$, and high intrinsic indistinguishability ($I > 0.5$) the effect of the waveguide becomes again negligible since $I \rightarrow 1$ when $\Gamma^*/\Gamma_0 \rightarrow 0$. As n_1 increases the maximum Γ^*/Γ_0 for $I > 0.5$ also increases reaching values up to 12 for $n_1=4$.

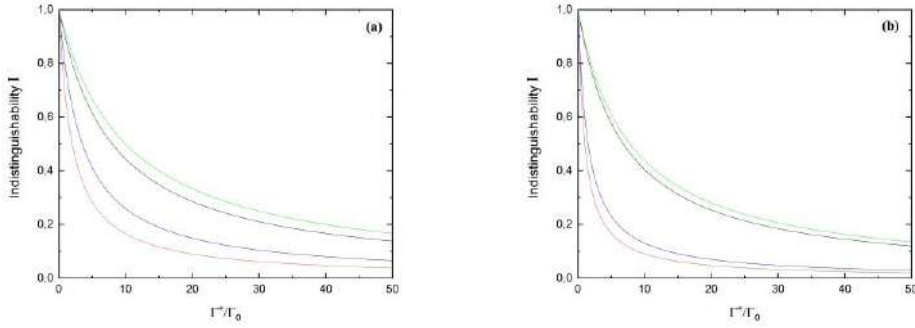


Fig. 7. Indistinguishability of an s-source quantum emitter placed at the edge of the waveguide versus its $\frac{\Gamma^*}{\Gamma_0}$ value. Green- $n_1=4$, Black- $n_1=3.4$, Blue- $n_1=2$, Red- $n_1=1.44$. (Left) Perpendicular-source (Right) Parallel-source.

Despite a SPS can achieve much stronger Purcell enhancements inside optical cavities [49], it is often required small mode volumes or high quality factors, or both. Small mode volumes difficult the deposition of the emitter at the field maxima [50], and on the other hand, high quality factors reduce the extraction efficiency [34]. In the case of waveguide integration, deposition at the field maxima (i.e. edge of the waveguide) becomes trivial, and as it has been shown, high extraction efficiency can be achieved. However, our results also reveal that for strong dissipative SPS integrated in a waveguide the indistinguishability does not reach the standard requirements for quantum information applications. For those cases the use of an optical cavity is mandatory.

From a practical perspective, the heterogeneous integration of the emitter with a waveguide may be performed by placing the emitter inside a material with non-unity refractive index (i.e. $n_2 \neq 1$) [45], it is worth to explore how the Purcell enhancement is affected by different index contrasts. As we mentioned above, the field discontinuity at the edge of the waveguide is proportional to $(n_1/n_2)^2$, so we can expect a significant reduction of the enhancement depending on n_2 .

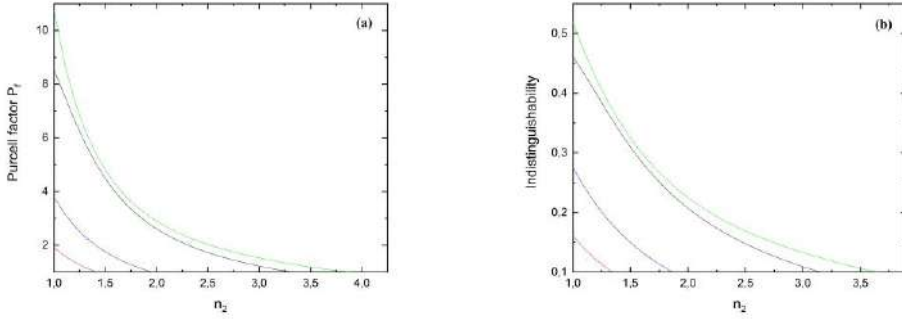


Fig. 8. (a) Purcell enhancement of an s-source at the edge of the waveguide as a function of n_2 . (b) Indistinguishability of an s-source at the edge of the waveguide as a function of n_2 .

Fig. 8a shows the dependence of the Purcell enhancement with n_2 for an s-source placed at the edge of the waveguide with optimal (a,b) geometry. Since the Purcell enhancement in the edge depends on the index contrast n_1/n_2 , it decreases asymptotically with n_2 . In the limit where $n_2 \sim 1$ the Purcell value approaches to that shown in Fig. 6, and when $n_2 \sim n_1$ we obtain the emitter decay rate corresponding to a homogeneous material (i.e. $P_f=1$). For cladding materials like SiO₂ ($n_2=1.44$) the Purcell enhancement is reduced about 50% with respect to the value with $n_2=1$. On the other hand, Fig. 8b shows the reduction in the indistinguishability due to this lower Purcell enhancement for an emitter with $\Gamma^*/\Gamma_0=10$. Similarly to what happened to the Purcell enhancement, when $n_2 \sim 1$ the indistinguishability approaches to that shown in Fig. 7, and when $n_2 \sim n_1$ we obtain the value corresponding to the specific Γ^*/Γ_0 ratio in a homogeneous material (i.e. $I=0.1$). Again, for $n_2 = n_{\text{SiO}_2}$ the indistinguishability is reduced about 15% with respect to $n_2 \sim 1$. Regarding the optimization sweep for finding the optimal waveguide height and width for the case of n_2 in the range (1-1.6) the results are almost equivalent to that shown in Fig. 6 (case of $n_1=1.44$). Therefore Fig. 6 can be used as a guide for waveguide design when n_2 is inside that range.

It is important to highlight that the positions for maximum indistinguishability differ from those of maximum coupling efficiency. Indistinguishability depends strongly on Purcell enhancement, which for the case of a waveguide achieves its maximum value at the edge, where the field is strongest. On the other side, the coupling efficiency on the edge is not as high as in the center, but still may have a value useful for some experiments or even some applications. An interesting figure of merit for the geometrical optimization of the waveguide is the $I \cdot \beta$ product (with β the coupling efficiency) that can be explored as a function of a and b . In the same way we did for the optimization of the Purcell enhancement, a and b change from 0 to 0.7λ , and the emitter is placed at the edge of the waveguide. We set $n_2=1.44$ this time and we vary $n_1=2, 3.4, 4$ and 4.4 . For the estimation of the indistinguishability we set $\Gamma^*/\Gamma_0=10$ as before.

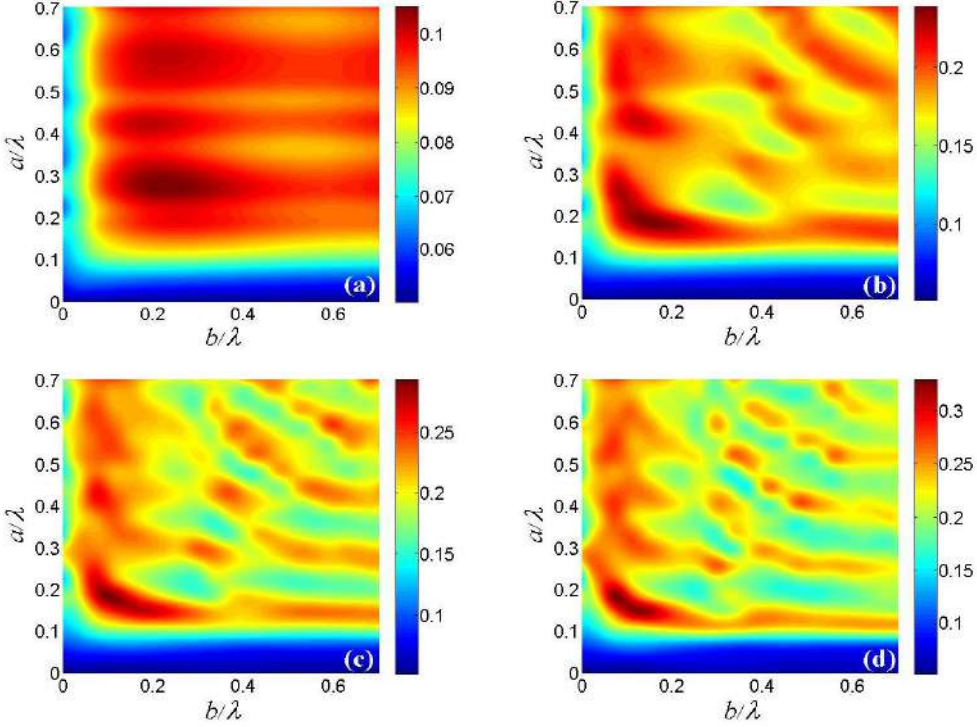


Fig. 9. $I\beta$ value as a function of the normalized width, a/λ , and thickness, b/λ , when the s-source is placed at the edge of the waveguide with $n_2=1.44$ calculated with the analytical model. (Top-left) $n_1=2$ (Top-right) $n_1=3.4$ (Bottom-left) $n_1=4$ (Bottom-right) $n_1=4.5$.

Fig. 9 shows the $I\beta$ value as a function of the normalized waveguide width, a/λ , and normalized thickness, b/λ , calculated for $n_1=2, 3.4, 4$ and 4.4 . As expected, for the four refractive indexes the highest $I\beta$ happens for the geometry that maximizes the Purcell enhancement. Maximum $I\beta = 0.35$ is found for the highest waveguide index ($n_1=4.5$) and minimum $I\beta = 0.15$ for $n_1=2$. Also, in the four cases the $I\beta$ product is significantly higher than the obtained when the source is at the center of the waveguide (0.06 for $n_1=2$, 0.09 $n_1=3.4$, and 0.13 for $n_1=4$).

Analytic model for spectral diffusion

We have explored so far the effect of pure dephasing in the indistinguishability. In addition, the effect of spectral diffusion needs to be treated separately. Whereas the dynamics of pure dephasing evolve at shorter time scales than the emitter decay rate Γ_0 , spectral diffusion is related to processes with significantly larger time scales [51] so it is characterized by a statistical average over the different center frequencies associated with the emitter [52]. In this context, the spectral broadening of the emission is given by $\Gamma_2 = \Gamma_0 + \Gamma'$, where Γ' represents the FWHM of the distribution associated with spectral diffusion. The indistinguishability reads $I = \Gamma_0/\Gamma_2$ [51]. Being $\Delta\omega$ the intrinsic width of each center frequency, and $\Delta\delta$ the extrinsic width due to the entanglement with the extrinsic environment, for a Lorentzian distribution the ratio $\theta = \Delta\delta/\Delta\omega$ is equal to $2\Gamma'/\Gamma_0$ [52]. The indistinguishability can be written in terms of θ as:

$$I = \frac{\Gamma/\Gamma_0}{\Gamma/\Gamma_0 + \frac{\theta}{2}}, \quad (6)$$

With Γ the enhanced decay rate due to Purcell effect. As we did in the previous section, we can use the maximum enhancements obtained for the source at the edge in (6) to obtain the maximum values for the indistinguishability.

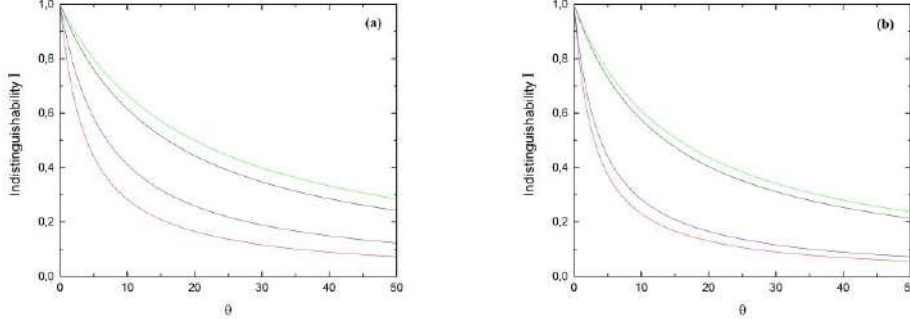


Figure 10. Indistinguishability of an s-source quantum emitter placed at the edge of the waveguide versus its θ -value. Green- $n_1=4$, Black- $n_1=3.4$, Blue- $n_1=2$, Red- $n_1=1.44$. (a) Parallel-source (b) Perpendicular-source.

Fig. 10 shows I for s- and p-emitters placed at the edge of the waveguide versus the normalized ratio θ . From Fig. 1 we see that for emitters with $\theta \sim 1$ [13] the expected indistinguishability is above 0.9 for the four refractive indexes. As the extrinsic width of the emitter increases respect to the intrinsic width the indistinguishability decays asymptotically reaching 0.3 when $\theta = 50$ for $n_1=4$ and $\theta = 10$ for $n_1=1.44$. Therefore, for emitters with extrinsic width much larger than intrinsic width the effect of the waveguide in the indistinguishability is negligible. As n_1 increases the maximum θ for $I > 0.5$ also increases reaching values up to 21 for $n_1=4$. We can say that in general we observe a similar behavior to pure dephasing although with a slower asymptotic decay of I .

Conclusions

We have calculated the indistinguishability of a point-source quantum emitter coupled to a waveguide because its technological implications in future quantum photonic integrated circuits. The emitter has arbitrary orientation and location with respect to the waveguide. We have obtained the results for different index of refraction of the waveguide (SiO_2 , Si_3N_4 , Si , and other high index materials like WeS_2 or WO_3). The analytical model used permits a fast computing of the indistinguishability from a set of simple expressions derived from the same solution of the dyadic Helmholtz equation. The model has been numerically evaluated through 3D-FDTD simulations with excellent agreement. Maximum indistinguishability for an optimal waveguide width is found for a source placed outside the core, at the edge of the waveguide, in contrast to maximum coupling efficiency position at the center of the waveguide. For strong dissipative emitters with $\Gamma^*/\Gamma_0 > 50$ (like transition metal dichalcogenides) the effects of the waveguide in the indistinguishability are negligible but for low dissipative emitters with $\Gamma^*/\Gamma_0 \approx 1$ (like GaAs quantum dots) the indistinguishability can be enhanced up to a 30% and reach values around $I \approx 0.8$ when dots are coupled to a waveguide. We hope this work can help for an optimized design of PIC waveguides in quantum photonic circuits.

Acknowledgments

We gratefully acknowledge financial support from the European Union's Horizon 2020 research and innovation program under grant agreement No. 820423 (S2QUIP).

Disclosures

The authors declare no conflicts of interest.

Data availability statement

All the data generated and analyzed in this work are available upon request.

See Supplement 1 for supporting content.

References

- [1] Aspuru-Guzik, A., & Walther, P. (2012). Photonic quantum simulators. *Nature physics*, 8(4), 285-291.
- [2] D. Fattal, E. Diamanti, K. Inoue, and Y. Yamamoto, *Phys. Rev. Lett.* 92, 037904 (2004).
- [3] H. Kimble, *Nature (London)* 453, 1023 (2008).
- [4] M. Eisaman, J. Fan, A. Migdall, and S. Polyakov, *Rev. Sci. Instrum.* 82, 071101 (2011).
- [5] Santori, C., Fattal, D., Vučković, J., Solomon, G. S., & Yamamoto, Y. (2002). Indistinguishable photons from a single-photon device. *Nature*, 419(6907), 594.
- [6] Chen, Y., Zhang, J., Zopf, M., Jung, K., Zhang, Y., Keil, R., ... & Schmidt, O. G. (2016). Wavelength-tunable entangled photons from silicon-integrated III-V quantum dots. *Nature communications*, 7(1), 1-7.
- [7] Khasminskaya, S. et al. Fully integrated quantum photonic circuit with an electrically driven light source. *Nat. Photon.* 10, 727–733 (2016).
- [8] Mouradian, S. L., Schröder, T., Poitras, C. B., Li, L., Goldstein, J., Chen, E. H., ... & Lipson, M. (2015). Scalable integration of long-lived quantum memories into a photonic circuit. *Physical Review X*, 5(3), 031009.
- [9] Sipahigil, A., Evans, R. E., Sukachev, D. D., Burek, M. J., Borregaard, J., Bhaskar, M. K., ... & Camacho, R. M. (2016). An integrated diamond nanophotonics platform for quantum-optical networks. *Science*, 354(6314), 847-850.
- [10] Peyskens, F., Chakraborty, C., Muneeb, M., Van Thourhout, D., & Englund, D. (2019). Integration of single photon emitters in 2D layered materials with a silicon nitride photonic chip. *Nature communications*, 10(1), 1-7.

- [11] Kiraz, A., Ehrl, M., Hellerer, T., Müstecaplıoğlu, Ö. E., Bräuchle, C., & Zumbusch, A. (2005). Indistinguishable photons from a single molecule. *Physical review letters*, 94(22), 223602.
- [12] Gérard, J. M., Sermage, B., Gayral, B., Legrand, B., Costard, E., & Thierry-Mieg, V. (1998). Enhanced spontaneous emission by quantum boxes in a monolithic optical microcavity. *Physical review letters*, 81(5), 1110.
- [13] Gammon, D., Snow, E. S., Shanabrook, B. V., Katzer, D. S., & Park, D. (1996). Homogeneous linewidths in the optical spectrum of a single gallium arsenide quantum dot. *Science*, 273(5271), 87-90.
- [14] Aharonovich, I., Englund, D., & Toth, M. (2016). Solid-state single-photon emitters. *Nature Photonics*, 10(10), 631-641.
- [15] Dusanowski, L., Köck, D., Shin, E., Kwon, S. H., Schneider, C., & Höfling, S. (2020). Purcell enhanced and indistinguishable single-photon generation from quantum dots coupled to on-chip integrated ring resonators. *Nano Letters*.
- [16] Qiang, X., Zhou, X., Wang, J., Wilkes, C. M., Loke, T., O'Gara, S., ... & Wang, J. B. (2018). Large-scale silicon quantum photonics implementing arbitrary two-qubit processing. *Nature photonics*, 12(9), 534-539.
- [17] Wang, J., Sciarrino, F., Laing, A., & Thompson, M. G. (2019). Integrated photonic quantum technologies. *Nature Photonics*, 1-12.
- [18] Slussarenko, S., & Pryde, G. J. (2019). Photonic quantum information processing: A concise review. *Applied Physics Reviews*, 6(4), 041303.
- [19] Chen, C. T., Pedrini, J., Gaulding, E. A., Kastl, C., Calafiore, G., Dhuey, S., ... & Schwartzberg, A. M. (2019). Very high refractive index transition metal dichalcogenide photonic conformal coatings by conversion of ALD metal oxides. *Scientific reports*, 9(1), 1-9.
- [20] He, Y., He, S., Gao, J., & Yang, X. (2012). Nanoscale metamaterial optical waveguides with ultrahigh refractive indices. *JOSA B*, 29(9), 2559-2566.
- [21] Huang, W., Yakovlev, A. B., Kishk, A. A., & Glisson, A. W. (2006, July). Dyadic Greens Function of the Hard Surface Rectangular Waveguide Verified Numerically by a Realistic Model. In 2006 IEEE Antennas and Propagation Society International Symposium (pp. 2249-2252). IEEE.
- [22] Huang, W., Yakovlev, A. B., Kishk, A. A., Glisson, A. W., & Eshrah, I. A. (2005). Green's function analysis of an ideal hard surface rectangular waveguide. *Radio science*, 40(05), 1-12.
- [23] Zhang, X., Xu, C., & Song, W. (2000, December). Calculating higher order mode characteristics of heteromorphic waveguide by operator theory. In 2000 Asia-Pacific Microwave Conference. Proceedings (Cat. No. 00TH8522) (pp. 970-974). IEEE.

- [24] Słobodzian, P. M. (2002). On the dyadic Green's function in the source region embedded in waveguides or cavities filled with a stratified medium. *Microwave and Optical Technology Letters*, 35(2), 93-97.
- [25] Klymko, V. A., Yakovlev, A. B., Eshrah, I. A., Kishk, A. A., & Glisson, A. W. (2005). Dyadic Green's function of an ideal hard surface circular waveguide with application to excitation and scattering problems. *Radio science*, 40(3), 1-16.
- [26] Liu, S., Li, L. W., Leong, M. S., & Yeo, T. S. (2000). Rectangular conducting waveguide filled with uniaxial anisotropic media: A modal analysis and dyadic Green's function. *Progress In Electromagnetics Research*, 25, 111-129.
- [27] Brueck, S. R. J. (2000). Radiation from a dipole embedded in a dielectric slab. *IEEE Journal of Selected Topics in Quantum Electronics*, 6(6), 899-910.
- [28] Creatore, C., & Andreani, L. C. (2008). Quantum theory of spontaneous emission in multilayer dielectric structures. *Physical Review A*, 78(6), 063825.
- [29] Santosa, F., & Magnanini, R. (2001). Wave propagation in a 2-D optical waveguide. *SIAM Journal on Applied Mathematics*, 61(4), 1237-1252.
- [30] Alexandrov, O., & Ciraolo, G. (2004). Wave propagation in a 3-D optical waveguide. *Mathematical Models and Methods in Applied Sciences*, 14(06), 819-852.
- [31] Ciraolo, G., Gargano, F., & Sciacca, V. (2013). A computational method for the Helmholtz equation in unbounded domains based on the minimization of an integral functional. *Journal of Computational Physics*, 246, 78-95.
- [32] Alexandrov, O. (2007). The far-field expansion of the Green's function in a 3-D optical waveguide. *Asymptotic Analysis*, 52(1-2), 157-171.
- [33] Bylander, J., Robert-Philip, I., & Abram, I. (2003). Interference and correlation of two independent photons. *The European Physical Journal D-Atomic, Molecular, Optical and Plasma Physics*, 22(2), 295-301.
- [34] Grange, T., Hornecker, G., Hunger, D., Poizat, J. P., Gérard, J. M., Senellart, P., & Auffèves, A. (2015). Cavity-funneled generation of indistinguishable single photons from strongly dissipative quantum emitters. *Physical review letters*, 114(19), 193601.
- [35] Schöll, E., Hanschke, L., Schweickert, L., Zeuner, K. D., Reindl, M., Covre da Silva, S. F., ... & Rastelli, A. (2019). Resonance fluorescence of gaas quantum dots with near-unity photon indistinguishability. *Nano letters*, 19(4), 2404-2410.
- [36] J.M. Gérard, O. Cabrol, B. Sermage, *Appl. Phys. Lett.* 68, 3123 (1996).

- [37] P. Borri, W. Langbein, S. Schneider, U. Woggen, R.L. Sellin, D. Ouyang, D. Bimberg, Phys. Rev. Lett. 87, 157401-1 (2001).
- [38] Klein, J., Lorke, M., Florian, M., Sigger, F., Sigl, L., Rey, S., ... & Zimmermann, P. (2019). Site-selectively generated photon emitters in monolayer MoS₂ via local helium ion irradiation. Nature communications, 10(1), 1-8.
- [39] Chakraborty, C., Vamivakas, N., & Englund, D. (2019). Advances in quantum light emission from 2D materials. Nanophotonics, 8(11), 2017-2032.
- [40] Tripathi, L. N., Iff, O., Betzold, S., Dusanowski, Ł., Emmerling, M., Moon, K., ... & Schneider, C. (2018). Spontaneous emission enhancement in strain-induced WSe₂ monolayer-based quantum light sources on metallic surfaces. ACS Photonics, 5(5), 1919-1926.
- [41] Chaudhary, R., Raghunathan, V., & Majumdar, K. (2020). Origin of selective enhancement of sharp defect emission lines in monolayer WSe₂ on rough metal substrate. Journal of Applied Physics, 127(7), 073105.
- [42] Wein, S., Lauk, N., Ghobadi, R., & Simon, C. (2018). Feasibility of efficient room-temperature solid-state sources of indistinguishable single photons using ultrasmall mode volume cavities. Physical Review B, 97(20), 205418.
- [43] Novotny, L., & Hecht, B. Principles of nano-optics. (2012, Cambridge university press), pp 58.
- [44] Chuang, S. L., & Chuang, S. L. (1995). Physics of optoelectronic devices.
- [45] Lombardi, P., Ovyan, A. P., Pazzagli, S., Mazzamuto, G., Kewes, G., Neitzke, O., ... & Toninelli, C. (2017). Photostable molecules on chip: integrated sources of nonclassical light. ACS Photonics, 5(1), 126-132.
- [46] Errando-Herranz, C., Schöll, E., Laini, M., Gyger, S., Elshaari, A. W., Branny, A., ... & Bonato, C. (2020). On-chip single photon emission from a waveguide-coupled two-dimensional semiconductor. arXiv preprint arXiv:2002.07657.
- [47] Majumder, S., & Chakraborty, R. (2013). Semianalytical method to study silicon slot waveguides for optical sensing application. Optical Engineering, 52(10), 107102.
- [48] Choi, H., Heuck, M., & Englund, D. (2017). Self-similar nanocavity design with ultrasmall mode volume for single-photon nonlinearities. Physical review letters, 118(22), 223605.
- [49] Pisanello, F., Qualtieri, A., Stomeo, T., Martiradonna, L., Cingolani, R., Bramati, A., & De Vittorio, M. (2010). High-Purcell-factor dipolelike modes at visible wavelengths in H1 photonic crystal cavity. Optics letters, 35(10), 1509-1511.

- [50] Hugall, J. T., Singh, A., & van Hulst, N. F. (2018). Plasmonic cavity coupling. *Acs Photonics*, 5(1), 43-53.
- [51] Choi, H., Zhu, D., Yoon, Y., & Englund, D. (2019). Cascaded cavities boost the indistinguishability of imperfect quantum emitters. *Physical review letters*, 122(18), 183602.
- [52] Sun, F. W., & Wong, C. W. (2009). Indistinguishability of independent single photons. *Physical Review A*, 79(1), 013824.

Numerical Optimization of a Nanophotonic Cavity by Machine Learning for near-Unity Photon Indistinguishability at Room Temperature

Abstract: Room-temperature (RT), on-chip deterministic generation of indistinguishable photons coupled to photonic integrated circuits is key for quantum photonic applications. Nevertheless, high indistinguishability (I) at RT is difficult to obtain due to the intrinsic dephasing of most deterministic single-photon sources (SPS). Here we present a numerical demonstration of the design and optimization of a hybrid slot-Bragg nanophotonic cavity that achieves theoretical near-unity I and high coupling efficiency (β) at RT for a variety of single-photon emitters. Our numerical simulations predict modal volumes in the order of $10^{-3}(\lambda/2n)^3$, allowing for strong coupling of quantum photonic emitters that can be heterogeneously integrated. We show that high I and β should be possible by fine-tuning the quality factor (Q) depending on the intrinsic properties of the single-photon emitter. Furthermore, we perform a machine learning optimization based on the combination of a deep neural network and a genetic algorithm (GA) to further decrease the modal volume by almost three times while relaxing the tight dimensions of the slot width required for strong coupling. The optimized device has a slot width of 20 nm. The design requires fabrication resolution in the limit of the current state-of-the-art technology. Also, the condition for high I and β requires a positioning accuracy of the quantum emitter at the nanometer level. Although the proposal is not a scalable technology, it can be suitable for experimental demonstration of single photon operation.

Keywords: Single-photon; Neural Network; Genetic Algorithm; Nanophotonics; nanocavity.

Introduction

Indistinguishable single photons are the leading candidates for quantum communication and quantum information processing technologies. They play a central role in a range of proposed schemes, including quantum simulation¹, quantum walks², boson sampling³, quantum teleportation⁴, and quantum networks⁵. However, the complex mesoscopic environment of solid-state sources entails fundamental barriers that restrict the operation to cryogenic temperature (T)⁶. Trying to overcome the thermal restrictions of quantum devices remains a challenge for the development of on-chip, on-demand SPS. A feasible approach for achieving efficient indistinguishable photon emission from a solid-state emitter consists of maximizing the emitter-field coupling (g) through the effective confinement of light in an ultra-small cavity mode-volume (V_{eff}) and reaching the strong coupling regime⁷. In this regime the transfer rate between the emitter and the cavity field exceeds the dephasing rate of the emitter, and the emitted photons are able to leave the cavity before being affected by decoherence⁷. Plasmonic cavities with sub-nanometer gaps between dimers like Au spheres⁸, Ag nanowires⁹, and surface plasmon-polariton systems¹⁰ or metallic bowties with CdSe/ZnS quantum dots¹¹ produce the highest g value up to 200 meV¹¹ and the lowest quality factors ($Q \sim 10$)⁹. There are different proposals to improve Q and β in these systems, some of them involving dielectric-core/metal-shell schemes for $Q^{10,12}$, or hybrid FP-nanoantenna cavities for $\beta^{13,14}$. However, using plasmonic cavities faces two obstacles¹⁵: (i) the placement of the emitter in the point with the strongest cavity field can be

challenging; (ii) ohmic and quenching losses can be very high. The use of dielectric cavities can avoid the latter limitation and strong coupling can happen using strategies to decrease the modal volume, like slotted photonic crystals. Discrete slotted nanobeams^{16,17} lead to volumes in the order of $10^{-3}(\lambda/2n)^3$ while keeping high Q . However, because introducing a finite slot causes a large perturbation to the optical mode, β values remain low. Continuous-slot designs improve β and Q ¹⁸, and more recently, slot-anti slot concatenations in 1D-PC^{19,20} have shown record Q/V_{eff} ratios with PC cavities. Also, designs based on cascaded cavities schemes have shown promising results with dielectric structures²¹. According to those works, a slotted dielectric cavity can provide sufficient small modal volume for strong coupling, thus a high I , avoiding at the same time the losses inherent to plasmonic cavities. However, for highly dissipative emitters, the dependence of I with g at RT is highly non-trivial⁷. With high g there is a high population transfer rate between the emitter and the cavity field, so the emitted photons must leave the cavity before getting dephased by the emitter. This can be accomplished by setting the right Q . As we will show, this trade-off between different rates (i.e. dephasing rate, g and Q) translates in to a complex dependence of I with the cavity figures of merit.

In this work, we show that achieving high I at RT requires a tuning of Q together with a small modal volume. That does not translate to a high Q , but a specific Q threshold depending on the emitter's intrinsic properties and the modal volume. From our calculations, none of the previously mentioned dielectric cavities can provide a high I for strong dissipative emitters despite achieving small modal volumes. Furthermore, the implementation of machine learning algorithms for the geometrical optimization of the cavity modal volume and Q has shown promising results in recent works²²⁻²⁵. Here we present a numerical demonstration of a design strategy for high indistinguishable SPS at RT strongly coupled to a hybrid slot-Bragg waveguide cavity. We vary the geometrical parameters of the waveguide cavity (i.e., the waveguide width, slot width, number of periods), and we obtain a theoretical estimation of the cavity performance for I , β , and the Purcell enhancement. We explore different types of promising SPS (InGaAs²⁶ and GaAs²⁷ quantum dots, single molecules²⁸, localized excitons in transition metal dichalcogenides TMDC monolayers²⁹, and diamond color centers³⁰), and we obtain theoretical near-unity I and high β simultaneously by parameter optimization. Finally, we develop a hybrid deep neural network-GA scheme that further reduces the modal volume for achieving near-unity I with a slot width of 20 nm. The optimized device presents strong challenges for current fabrication and quantum emitter (QE) positioning techniques. In this regard, we have developed a comparison of the design requirements with the state of the art demonstrations.

Methods

We can compute the value of I for a QE with radiative decay rate γ and pure dephasing rate γ^* coupled to a photonic cavity (with decay rate κ and electromagnetic coupling constant g) from the Lindblad equation and applying the quantum non-regression theorem. For each (g , κ , γ , γ^*) we have⁷:

$$I = \frac{\iint_0^\infty dt d\tau |\langle \hat{a}^\dagger(t+\tau) \hat{a}(t) \rangle|^2}{\iint_0^\infty dt d\tau \langle \hat{a}^\dagger(t) \hat{a}(t) \rangle \langle \hat{a}^\dagger(t+\tau) \hat{a}(t+\tau) \rangle} \quad (1)$$

Where \hat{a}^\dagger, \hat{a} are the creation/annihilation operators of the cavity mode. Details of the calculation can be found in the supplementary material. The values of g and κ are linked to Q and V_{eff} by $\kappa \sim 1/Q$ and $g \sim 1/\sqrt{V_{eff}}$.

Figure 1e shows the value of I for photons emitted by a high dissipative QE with $\gamma^* = 10^4 \gamma$ as a function of g and κ normalized to γ in the coherent strong-coupling regime (i.e. $g > \gamma^* + \gamma$). In this regime, the rate of photon transfer from the emitter to the cavity is $R = 4g^2/\kappa^7$, which exceeds the pure dephasing rate ($R > \gamma^*$) for certain values of κ . For high I the photon must escape out of the cavity before the emitter dephases it. In other words, $\kappa > \gamma^*$, which means that a small Q is needed. Specifically, for a QE with $\gamma^* = 10^4 \gamma$ one needs a value of κ/γ above $2 \cdot 10^4$ for $I > 0.9$. The region of high I in Figure 1e has a shape and area that depend on T through γ^* . For a QE at RT, $\gamma^* \sim 10^4 \gamma^7$ and the minimum value of g/γ to achieve $I > 0.9$ is $(g/\gamma)_{min} \sim 10^4$. As γ^*/γ decreases the area of high I grows and $(g/\gamma)_{min}$ decreases.

Figure 1g shows the contour maps of the region with high I ($I > 0.9$) as γ^* changes. For moderate dissipative emitters ($\gamma^* \sim 10^2 \gamma$), the minimum g/γ necessary for $I > 0.9$ is $(g/\gamma)_{min} = 10^3$. As γ^* increases (g/γ)_{min} grows monotonously, reaching 10^4 for $\gamma^* \sim 10^4 \gamma$. Similarly, the minimum $(\kappa/\gamma)_{min}$ increases from 10^3 for $\gamma^* \sim 10^2$, to $2 \cdot 10^4$ for $\gamma^* \sim 10^4 \gamma$. We can use this colormap to plot the cavities mentioned before, according to its performance for I . Plasmonic cavities⁸⁻¹⁰ can achieve $I > 0.9$ even for high dissipative emitters with $\gamma^* \sim 10^4 \gamma$. On the other hand, slotted dielectric cavities¹⁶⁻¹⁸ can achieve $I > 0.9$ for emitters with γ^* between $\sim 10^2 \gamma$ to $\sim 2 \cdot 10^2 \gamma$ and slot-anti slot concatenations in 1D-PC¹⁹ for emitters with $\gamma^* \sim 2 \cdot 10^2 \gamma$ to $\gamma^* \sim 4 \cdot 10^2 \gamma$. The cavity shown in²⁰ is the only one, in the group of dielectric structures, that can reach $I > 0.9$ when $\gamma^* > 2 \cdot 10^3 \gamma$. According to our calculations those dielectric cavities can potentially achieve the region with $I > 0.9$ for high dissipative emitters (i.e., QE at RT) just by increasing its cavity decay rate κ (i.e., deteriorating its quality factor Q). Figure 1b shows the dependence of the value $(g/\gamma)_{min}$ with T for $I > 0.9$, calculated for quantum dots of GaAs³¹ and InAs³², organic molecules^{33,34} and defects in 2D materials³⁵. The evolution of $(g/\gamma)_{min}$ with T shows a proportional increase with a different trend that depends on γ^* . We can obtain the $(g/\gamma)_{min}$ needed for $I > 0.9$ for a QE at an specific T from Figure 1g. It is interesting to observe that for the technologically relevant T of liquid nitrogen (77 K) the same value $(g/\gamma)_{min} = 490$ works for InAs and GaAs QDs and 2D materials.

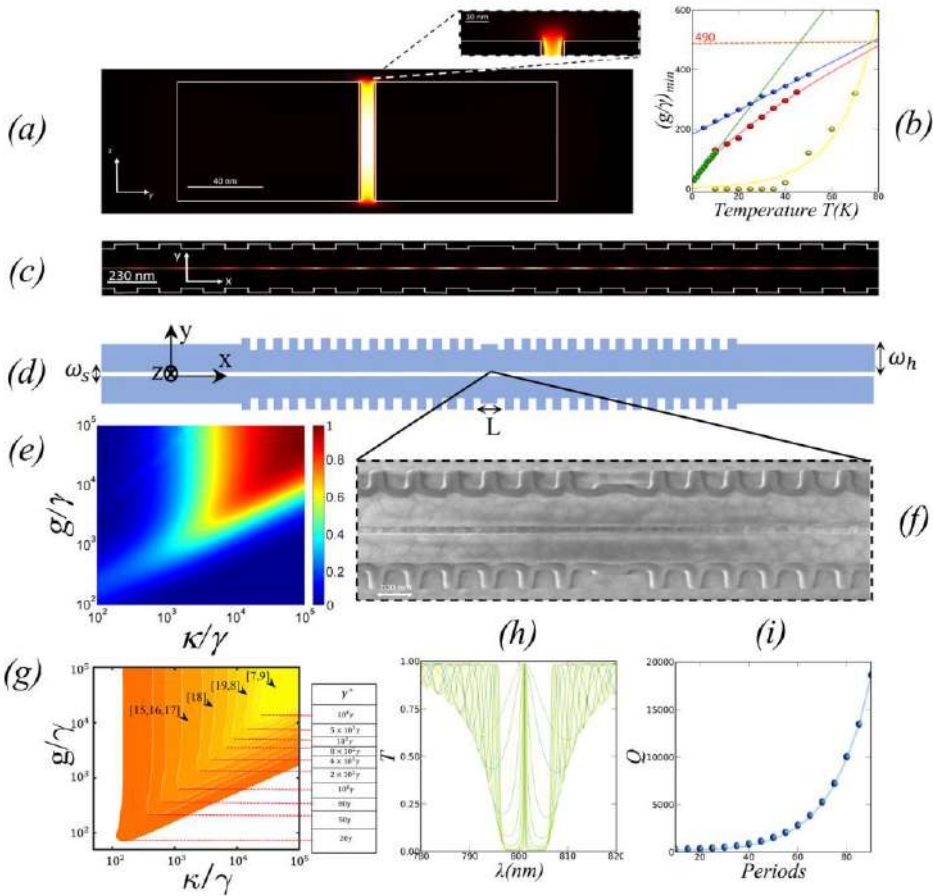


Figure 1. (a) $|E|^2$ field profile in the y-z plane. (b) Variation of the ratio $(g/\gamma)_{\min}$ with T for $I>0.9$ and different SPS: GaAs (red), S.molecules (green), 2D-materials (blue), InAs (yellow). (c) $|E|^2$ field profile of the cavity-mode in the x-y plane. (d) Layout of the proposed structure, where ω_h is the width of each waveguide, ω_s is the slot width, L is the cavity length, and Λ is the grating period. (e) Color map of I as a function of g/γ and κ/γ for photons emitted by a high dissipative QE with $\gamma^* = 10^4 \gamma$. (f) SEM image of the center of the cavity. (g) Contour map of regions with $I>0.9$ for different dephasing values ($\gamma^* = 20 \gamma, 50 \gamma, 80 \gamma, 10^2 \gamma, 2 \cdot 10^2 \gamma, 4 \cdot 10^2 \gamma, 8 \cdot 10^2 \gamma, 10^3 \gamma, 5 \cdot 10^3 \gamma$, and $10^4 \gamma$). (h) Transmission spectrum of the structure for different number of periods, the FWHM of the resonance scales exponentially with $\#p$. (i) Q versus number of periods.

Therefore, our goal is to keep the κ/g ratio inside the region with high I by increasing g and adjusting Q . Moreover, we look for an on-chip cavity that can be CMOS-compatible with photonic integrated circuits (PICs) used in silicon photonics. Slotted one-dimensional dielectric photonic crystal cavities¹⁶⁻²⁰ have been shown to fulfill most of our requirements in terms of compatibility and small modal volume. Nevertheless, to efficiently control Q , we choose a hybrid slot-Bragg cavity, where Q changes by the number of periods of the Bragg reflector section. Figure 1d shows a layout of our hybrid slot-Bragg photonic cavity aiming to achieve near-unity I and high β simultaneously. ω_h is the width of each waveguide, ω_s is the slot width, and $\#p$ is the number of periods. While this structure has been explored for sensing applications^{36,37,38}, it has never been proposed for SPS operation, as far as we know, neither calculated its performance in terms of the figures of merit (I, β). It consists of a phase-shifted corrugated Bragg grating situated at the sides of a Si_3N_4 ($n_1=2$) deposited on top of a SiO_2 substrate ($n_2=1.4$). The cavity length L corresponds to the central section between the two periodic regions and matches the wavelength of the zero-order Fabry-Perot mode

for the target wavelength λ . The Si_3N_4 thickness (t) is set for optimum field enhancement at the slot for the target λ . Each of the periodic regions behaves like a mirror with an effective reflectivity that depends on the number of periods ($\#p$), creating a Fabry-Perot structure. The grating period Λ matches the central frequency of the photonic bandgap at the target λ . In order to get information about the physical behavior of the device, we will set first $\lambda = 801$ nm to perform a general evaluation of the performance. After that, for each type of emitter the geometrical parameters of the device (i.e. t , L and Λ) are set to match the specific emission wavelength λ : $(\lambda, t, L, \Lambda) = (915 \text{ nm}, 900 \text{ nm}, 263 \text{ nm}, 263 \text{ nm})$ for InGaAs²⁶, $(916 \text{ nm}, 900 \text{ nm}, 263 \text{ nm}, 263 \text{ nm})$ for GaAs²⁷, $(728 \text{ nm}, 710 \text{ nm}, 210 \text{ nm}, 210 \text{ nm})$ for TMDC²⁸, $(785 \text{ nm}, 770 \text{ nm}, 225 \text{ nm}, 225 \text{ nm})$ for S.molecules²⁹ and $(685 \text{ nm}, 680 \text{ nm}, 195 \text{ nm}, 195 \text{ nm})$ for diamond color centers³⁰. Figure 1a show how the slotted cross-section of the cavity enhances the field of the zero-order TE mode in the gap showing an evanescent tail in the top of the waveguide. This field distribution provide advantages related to the coupling of the source when is heterogeneously integrated on top. The cavity provides strong coupling if the slot width is sufficiently small, and it also provides advantages in extraction efficiency (β) since (i) cavity and output waveguide share the same cross section, so the modes are perfectly matched; (ii) the integration of the QE (for example colloidal QDs) can be done by direct deposition on top of the cavity which avoids interferences by total internal reflection and enhances β ; (iii) the slot mode has the field maxima at the edges of the slot, which matches well with the region of maximum probability of having SPS in 2D materials deposited on top of waveguides³⁹. Finally, the cavity modal volumes are in the order of $10-3(\lambda/2n)^3$ along with the whole slot, increasing the probability of having one or several QE strongly coupled to the cavity mode. As a proof of concept, we have fabricated a specific design valid for diamond color center requirements. We selected $(\omega_s, \#p) = (38 \text{ nm}, 50)$ and added vertical grating couplers to the structure to collect the input and output light beams. Figure 1f shows an SEM image of the cavity fabricated by e-beam lithography and reactive ion etching on a layer of Si_3N_4 130 nm-thick deposited on top of a SiO_2 layer ($1 \mu\text{m}$ -thick) by plasma-enhanced chemical vapor deposition (PECVD). The obtained slot width is $\omega_s = 54 \text{ nm}$, and the grating period is 204 nm, with less than 5% of the error to the initial design for the grating period and 30% for ω_s . According to our simulations, the wider slot translates into a modal volume increase, $V_{eff} \sim 6 \cdot 10^{-2}(\lambda/2n)^3$, which slightly reduces the indistinguishability to $I = 0.81$. This issue can be solved by further optimization by machine learning, as we will show later. We can obtain the transmission spectrum $T(\lambda)$ shown in Figure 1h and the field profile (Figure 1c) of the cavity mode for a set $(\omega_s, \omega_h, \#p)$ using a fully vectorial, bi-directional, frequency-domain model for solving Maxwell's equations (3D-FD)⁴⁰. We obtain Q from $T(\lambda)$ by $Q = \frac{\lambda_0}{FWHM}$ and the cavity decay rate from $\kappa = \omega/2Q$. Details of the model appear in the supplementary material. There is a different effective index for each set $(\omega_s, \omega_h, \#p)$, so the values of Λ and L are changed to keep the cavity resonance at 801 nm. The volume of the cavity-mode V_{eff} is⁴¹:

$$V_{eff} = \frac{\iiint \epsilon(\vec{r}) |\vec{E}(\vec{r})|^2 d^3\vec{r}}{\max\{\epsilon|\vec{E}(\vec{r})|^2\}} \quad (2)$$

The value of g , when the QE is placed at the maximum cavity field and perfectly matches the polarization is⁴²:

$$g = \frac{\mu_{eg}}{\hbar} \sqrt{\frac{\hbar\omega}{2\varepsilon_M V_{eff}}} ; \mu_{eg} = \frac{3\hbar e^2 f}{2m_{eff}\omega} \quad (3)$$

Where μ_{eg} is the electric dipole moment of the excitonic transition, ω is the frequency of the transition, e is the electron charge, ε_M is the dielectric constant in the source region, \hbar is the reduced Planck constant, m_{eff} the exciton effective mass, and f the oscillator strength. Once we have g and κ , we obtain I according to the procedure outlined in Figure 2a. For the computation of the Purcell enhancement (Γ_p) and the coupling efficiency β , we perform 3D-Finite Difference Time Domain (3D-FDTD) simulations⁴⁰ by placing a dipole point source emitting at 801 nm with position x_0, y_0 at the center of the slot and z_0 4 nm above the top of the waveguides. We obtain Γ_p by integrating the power P emitted by the source and normalizing it to the power inside a homogeneous environment P_0 ⁴³. Finally, we calculate β by measuring the fraction of light coupled to guided modes at the output waveguide. Details of the simulations appear in the supplementary material.

Our design strategy can be further enhanced using machine-learning techniques, especially to keep critical fabrication parameters, like the slot width ω_s , experimentally accessible and far from too narrow and unrealistic values. Recently, the optimization of nanophotonic structures by deep learning techniques has been reported²²⁻²⁵. The two main advantages are: (i) further improved performance beyond the time-consuming method of sweeping the $(\omega_s, \omega_h, \#p)$ parameters; (ii) we can introduce a vast number of new parameters for the optimization, like the width of each of the Bragg corrugations, as shown in Figure 2b.

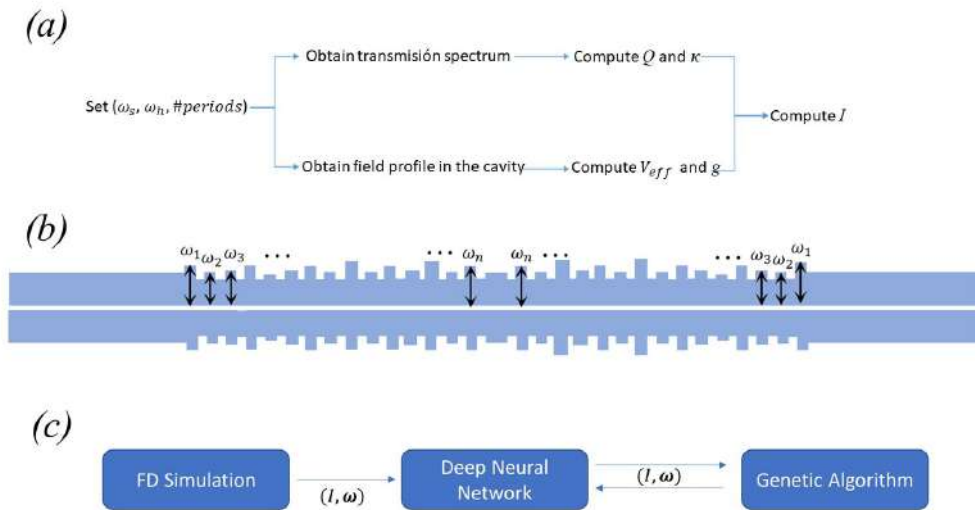


Figure 2 (a) Outline of the computation algorithm for the calculation of I . (b) Parametrization of the Bragg corrugations for machine learning optimization. Each ω_i represents the width of the corresponding Bragg corrugation. (c) Routine for the hybrid NN-GA optimization of the Bragg corrugations.

For that purpose we can use a vector $\omega = (\omega_1, \omega_2, \omega_3, \dots, \omega_n)$, where each entry ω_i with $i=1, \dots, 20$ representing the width of each Bragg corrugation. For each configuration ω we obtain I using the two-step method described in Figure 2c. We use a GA to create a random vector ω and the fitness function obtains I from the 3D-FD simulation (Figure 2a). Through the iteration of cross-over and mutation, the GA should find the optimal configuration for maximizing I after a certain number of generations. Details of the code appear in the Supplementary material. However, this procedure faces a critical issue. Typically, in a GA optimization one needs to generate about 10^5 pairs (ω, I) and the generation of each pair (ω, I) involves a 3D-FD simulation that may take several minutes, making the whole optimization process unfeasible in terms of time and computational resources. To solve this issue, we take a different approach: (i) we generate 5000 pairs (ω, I) through 3D-FD simulations; (ii) with these data, we train a deep neural network (NN) which learns to estimate the outcome of I for any possible ω . Now we can use the NN to calculate I for the fitness function of the GA optimization. In this way, the calculation of the fitness function for each ω takes just a few seconds; (iii) We perform the GA optimization by calculating the fitness function for each individual of the population through the NN. With this scheme, we reduce by two orders of magnitude the number of actual numerical simulations for the dataset from 10^5 to 10^3 with the aid of the NN.

Results and discussion

We first assess the performance of the cavity by sweeping the main geometrical parameters and setting a target $\lambda = 801$ nm. t , L and Λ are set to $(t, L, \Lambda) = (800$ nm, 230 nm, 230 nm). Figure 3 shows how I changes with (ω_s, ω_h) and $\#p$ when $\gamma^* = 10^4$ γ (a typical ratio for many QE at RT as we have seen before). Figure 3a shows I versus ω_h and ω_s for $\#p=10$ with ω_s varying between 10 to 50 nm and ω_h between 150 to 220 nm (required for single-mode operation). With $\#p$ fixed, Q remains constant ($Q=50$), while the field profile of the cavity mode varies for each (ω_h, ω_s) . Therefore, the variation of I follows the variation of g with ω_h and ω_s . As ω_s increases, the cavity mode spreads out from the slot and gets confined at each waveguide core separately. That results in an exponential decay of the field intensity in the slot region⁴⁴, increasing V_{eff} exponentially with ω_s . Since $g \sim 1/\sqrt{V_{eff}}$, g decreases, driving the system to the weak coupling regime (i.e., going downwards in Figure 1a) and inducing an exponential decay of I . For small enough ω_s (<20 nm) the system remains in the strong coupling regime and I becomes independent of g ⁷. Therefore, we can observe that for $\omega_s < 20$ nm I shows a weak variation with ω_h . When $\omega_s > 20$ nm, the cavity starts to perform away from the strong coupling regime and I shows an evident change with ω_h , which we will further analyze later. A slot width $\omega_s < 10$ nm produces a maximum value of $I=0.96$, decaying with ω_s at a rate of $5 \cdot 10^{-3}$ nm⁻¹. Figure 3d shows the dependence of I with $\#p$, with $\#p$ in the range from 10 to 100 and fixed $\omega_h = 140$ nm and $\omega_s = 15$ nm so we keep the strong coupling regime. As $\#p$ increases, the effective reflectivity also increases, and the Q factor grows exponentially (see Figure 1i). Consequently, κ decreases exponentially with $\#p$. Therefore, the time that the photon stays in the cavity increases exponentially with $\#p$ and when $\kappa < \gamma^*$ the photon is dephased by the emitter (i.e., going in the left direction in Figure 1a). The result is that I decreases with $\#p$ giving $I=0.4$ for $\#p=100$. Figure 3b shows Γ_p versus (ω_s, ω_h) when $\#p=10$, ω_s in the range 10-100 nm and ω_h between 110 nm to 600 nm. Since $\Gamma_p \sim 1/V_{eff}$, Γ_p changes with ω_s in a similar way

than I does. As the slot mode spreads over the waveguide cores, the field's intensity at the source's position decreases and Γ_p shows an exponential decay. The change with ω_h displays a more complex structure, shown more clearly in Figure 3e. For $\omega_s = 15$ nm and $\omega_h = 80$, Γ_p increases monotonically as the zero-order cosine/even⁴⁵ slot mode gets more efficiently confined in the waveguide. Γ_p is maximum ($\Gamma_p = 11$) when $\omega_h = 125$ nm and the strongest light confinement in the waveguide happens. For higher ω_h the mode spreads over the structure producing a decay of the overlapping with the source that scales with $1/\omega_h$. The decay interrupts abruptly when the zero-order sin-type/odd mode cut-off is reached at $\omega_h = 155$ nm. From there, the same pattern reproduces until the activation of the subsequent mode, and so on. The same behavior happens for ω_s . However, as ω_s increases the dependence of Γ_p with ω_h shifts to lower values of ω_h . This is because the ω_h cut-off value of the zero-order sine mode/odd decreases monotonically with ω_s ⁴⁵. Therefore, the activation of the second mode shifts to lower values of ω_h as ω_s increases.

Figure 3c shows β versus ω_s and ω_h for the same values of $\#p$, ω_s and ω_h used in Figure 3b. While Γ_p is a measure of the field enhancement due to the overlapping of all available modes, β accounts just for the overlapping with guided modes. Therefore, we expect a similar dependence and, in fact, β shows an exponential decay with ω_s similarly to I and Γ_p . The dependence with ω_h shows the same "mode jumps" found for Γ_p , giving a maximum $\beta=75\%$ at $\omega_h = 128$ nm. In this case, the regions of high β become bigger for higher ω_h , as the number of available modes increases with ω_h .

The position of the QE inside the cavity plays a relevant role⁴⁶. To explore the effect of the position of the QE in Γ_p we have performed 3D-FDTD simulations changing the position (y_0) of the QE along the cavity cross-section (y-axis) at $z_0=4$ nm above the top of the cavity. Figure 3f shows Γ_p versus y_0 varying from -225 nm to +225 nm when $\omega_h = 200$ nm, $\omega_s = 30$ nm and $\#p=10$. Since Γ_p is proportional to the field of the available modes for each spatial position, the plot reproduces the field profile of the zero-order mode of the slot waveguide. The maximum Γ_p happens in the region inside the slot, with maxima at the edges of the waveguides. The enhancement falls abruptly inside the waveguide, with values reduced by one order of magnitude. For a QE located away from the outer edges of the waveguide cores, the evanescent coupling increases the enhancement slightly. In summary, even for a strong dissipative emitter with $\gamma^* = 104 \gamma$, we can achieve $I > 0.9$ by adjusting the number of periods and reducing the slot width ω_s below 10 nm. At the same time, high Purcell enhancement ($\Gamma_p = 45$) and good extraction efficiency ($\beta=0.7$) can be obtained for the same ω_s . On the other hand, we need an accurate positioning of the emitter inside the slot region.

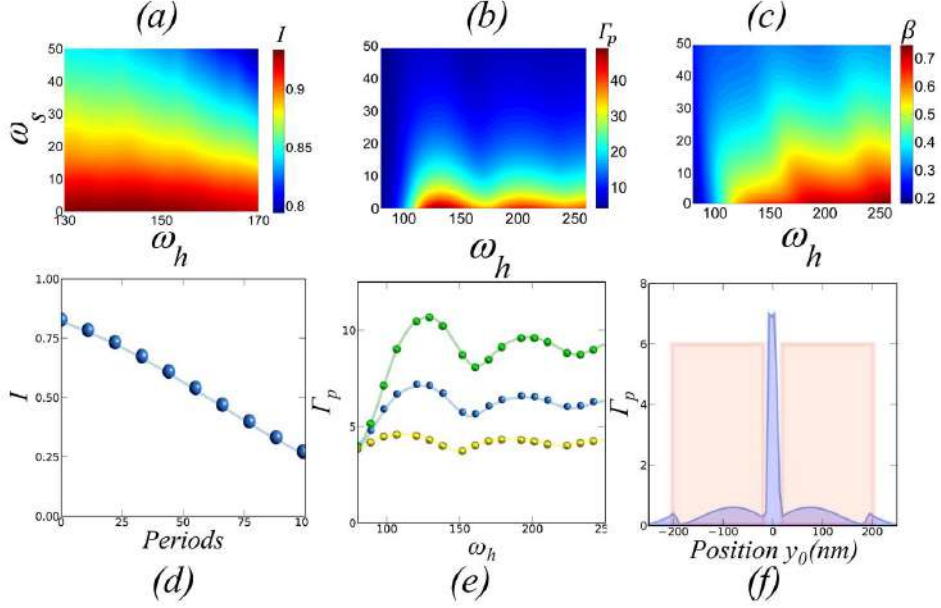


Figure 3. (a) Cavity-induced I when $\gamma/\gamma^*=10^4$ versus waveguide width (ω_h) and slot width (ω_s) for $\#p=10$. (b) Purcell enhancement (Γ_p) versus waveguide width (ω_h) and slot width (ω_s). (c) Coupling efficiency (β) versus waveguide width (ω_h) and slot width (ω_s) for $\#p=10$. (d) I versus number of grating periods ($\#p$) for $(\omega_s, \omega_h) = (5 \text{ nm}, 140 \text{ nm})$. (e) Γ_p versus ω_h for three ω_s (green- $\omega_s = 15 \text{ nm}$, blue- $\omega_s = 20 \text{ nm}$, yellow- $\omega_s = 25 \text{ nm}$). (f) Γ versus source position y_0 along the y-axis.

	$\gamma^* = 10^2\gamma$	$\gamma^* = 10^3\gamma$	$\gamma^* = 10^4\gamma$
InGaAs	(43,100)	(36,50)	(15,10)
GaAs	(41,100)	(30,50)	(9,10)
TMDC	(36,120)	(25,60)	(5,12)
S.molecules	(40,120)	(28,60)	(8,12)
Diamond	(45,100)	(38,50)	(15,10)

Table 1. Maximum (ω_s (nm), $\#p$) for $I>0.9$ using InGaAs QD, GaAs QD, TMDCs and single molecules as QE.

We further explore the performance of the device and the design requirements for different types of QE with different dephasing rates. For each type of emitter the geometrical parameters of the device (i.e. t , L and Λ) are set to match the specific emission wavelength λ . Table 1 shows the values of the pairs $(\omega_h, \#p)$ needed for $I>0.9$ for five different γ^*/γ values corresponding to each emitter. The values of the oscillation strengths are extracted from InGaAs⁴⁷, GaAs⁴⁸, TMDC^{49,50}, single molecules^{28,51} and diamond⁵². We observe that as γ^* increases (i.e., T increases) the cavity demands smaller ω_s (i.e., narrower slot). For the highest oscillator strength (~ 5 in InGaAs QD and diamond color centers) (g/γ)_{min} is easily reached when $\omega_s < 44 \text{ nm}$ and $\gamma^* = 102 \gamma$. A TMDC QE with oscillator strength ~ 0.1 demands $\omega_s < 38 \text{ nm}$ on the opposite side. In an intermediate situation, the oscillator strength of the GaAs QD (~ 1) gives $\omega_s < 42 \text{ nm}$. From this, we can find the optimal design for each emitter at high T. InGaAs at 300 K have a pure dephasing of 600γ ⁵³, so $(\omega_s, \#p) = (36 \text{ nm}, 50)$ are needed for $I>0.9$. GaAs at 300 K has 1450γ ⁵⁴ and needs of the same values $(\omega_s, \#p) = (36, 50)$. High dissipative emitters with dephasing of $\sim 104 \gamma$ at 300 K, like TMDC⁵⁵

and single molecules, demand narrower slot widths (ω_s , #p) = (5 nm, 10). For color centers in diamond, with $\gamma^* = 103 \gamma$ at room T⁵⁶, the optimal configuration is (ω_s , #p) = (38 nm, 50).

As we have shown, for high dissipative emitters with $\gamma^* = 104 \gamma$ the width of the cavity slot must be $\omega_s < 10$ nm for $I > 0.9$. Similarly, $\omega_s < 10$ nm is needed for $\beta > 0.7$. At the same time, the emitter's position plays a critical role, giving very low coupling when the emitter is outside the slot region. These requirements make complex both the fabrication and the emitter integration. Achieving slot widths below 10 nm is beyond the state of the art of almost any fabrication technology and deterministic deposition of a QD with that accuracy can be complicated. To reduce those limitations, we need to optimize the geometry of the cavity further. We have performed a hybrid GA-NN optimization of the Bragg corrugation geometry. The GA-NN optimization must deal with the trade-off between reducing the cavity modal volume (to increase g) and maintaining the appropriate Q to achieve $I > 0.9$ with $\gamma^* = 104 \gamma$. With this aim, we set $\omega_s = 20$ nm and the number of periods to #p=20. The structure without optimization has a modal volume of about $10^{-2}(\lambda/2n)^3$, which gives $I = 0.82$ with $\gamma^* = 10^4 \gamma$. Figure 4a shows the GA-NN optimized geometry. Somehow surprisingly to us, the GA-NN found that it is enough to change the widths of the most external Bragg corrugations, leaving the others unperturbed. This geometry provides the best confinement of the cavity mode in the center of the structure, significantly reducing the modal volume while maintaining the correct Q.

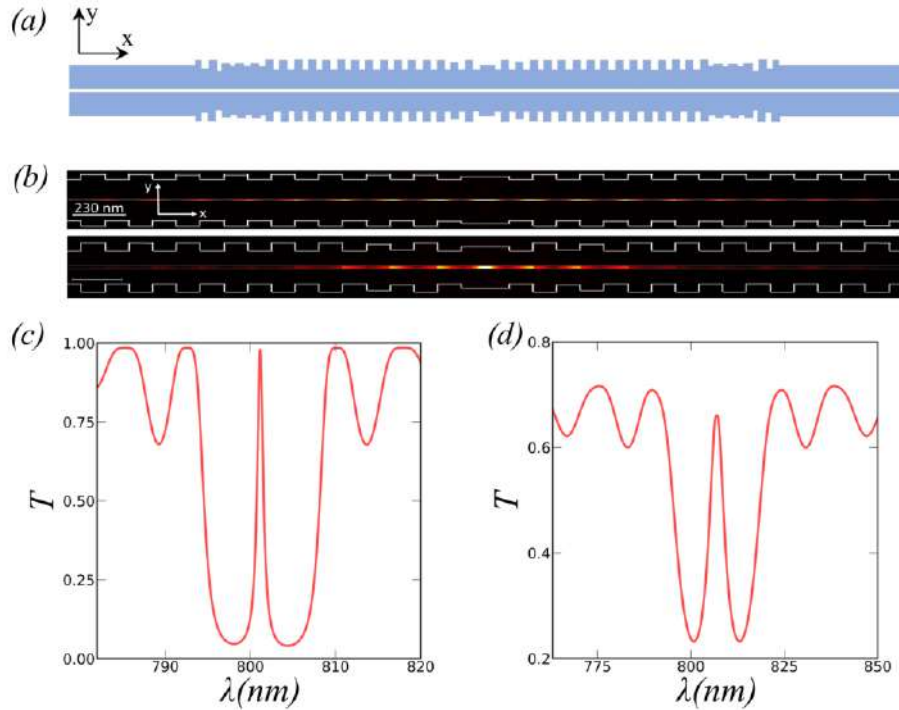


Figure 4. (a) Optimized structure for fixed (ω_s , #p) = (20,20). Cavity-mode field profile in the XY plane inside the cavity region for (b) Cavity mode profiles of the non-optimized structure (up) and optimized structure (down); Transmission spectra for (c) Structure without optimization; (d) GA-NN optimized structure.

Figure 4 b,c,d show the cavity-mode profile and the transmission spectrum for the structure with and without optimization. It is easy to appreciate how the cavity mode is significantly more confined in the central region of the optimized cavity. The modification of the widths of the external Bragg corrugations creates a tapered section that connects the cavity with the input/output slot waveguides and increases the confinement of the cavity mode. The modal volume is reduced from $7 \cdot 10^{-3}(\lambda/2n)^3$ to $2.5 \cdot 10^{-3}(\lambda/2n)^3$, a factor of 2.8. At the same time, the *FWHM* has been increased to $Q=50$, keeping the system in the region of high I . The reduction in the modal volume, and the Q adjustment, improve the indistinguishability from $I=0.82$ to $I=0.91$. In conclusion, we obtain that for the optimized structure, we can achieve $I>0.9$ for $\gamma^*=10^4\gamma$ with a slot width of $\omega_s=20$ nm, relaxing the tight requirements for the fabrication of the slot to more realistic values. The resulting transmission spectra of the optimized device reveals that there is a 7 nm shift of the resonance wavelength. This results from the discontinuous alteration of the periodicity of the Bragg reflectors. The λ -Bragg condition for total reflection changes along the corrugations, giving rise to a small modification of the spectra. This resonance displacement could be reduced through a second optimization process involving the maximization of I together with the minimization of the λ -shift, which will be covered in future works.

Although simulations results show a promising device performance, potential difficulties related to fabrication have to be considered according to CMOS compatible processes. Realization of vertical slots widths below 80 nm can be difficult with standard lithography techniques. For emitters with $\gamma^*=10^2\gamma$ slots between 36 nm and 45 nm are needed (see Table 1). Despite achieving these widths can be challenging, there are many experimental demonstrations reporting the fabrication of sub-100 nm slots (between 30 nm and 80 nm) using e-beam lithography (EBL)⁵⁷⁻⁶⁴. On the other hand, strong dissipative emitters with $\gamma^*=10^4\gamma$ require slot widths between 5 nm and 15 nm. Defining sub-10 nm structures with EBL is a great challenge, requiring simultaneous control of several factors like resist contrast, beam diameter, resist development mechanics, and limitations in metrology⁶⁵. A novel fabrication procedure with EBL was reported⁶⁵ which allows to achieve slots widths down to 8 nm in Si substrates. Also, recent works⁶⁶ experimentally demonstrate a different fabrication approach achieving slots with 10 nm width in Si waveguides. In this context, the relaxation up to 20 nm width achieved through the ML optimization is especially relevant, since it reduces the fabrication requirements from the limit of the technology (5 nm) to a more accessible value (20 nm). Still, we must emphasize that achieving such ultra-narrow slots presents a significant challenge which require top-state-of-the-art resolution technology.

Another key aspect to consider for the experimental realization is the nanoscale positioning approach for the deposition of the QE in the 20 nm slot region of the cavity. Recently, several nanoscale positioning techniques compatible with nanofabrication processes have shown promising results, achieving positioning accuracy at the nanometer level⁶⁷. Atomic force microscopy-based positioning approaches with 30 nm positioning accuracy have been reported with GaAs QDs strongly coupled to a nano-cavity⁶⁸. Confocal micro-photoluminescence techniques also showed 10 nm positioning accuracy with GaAs QDs inside a photonic structure⁶⁹. Bi-chromatic photoluminescence approaches with 5 nm position accuracy was recently achieved through a novel image analysis software implementation in the positioning setup⁷⁰. Also, In Situ lithographic techniques, where the QD position extraction and the nanostructure definition are

developed in the same setup have improved position accuracy down to 30 nm⁷¹. Pick-and-place techniques, which are the most suitable approach for our specific structure, have also shown significant progress⁷². Recently, Si vacancy centers were transferred to AlN waveguides achieving 98% coupling efficiency⁷³, the placement mean error was about 38 nm. According to this, for a pick and place deposition, assuming a normal distribution we would have a standard deviation of 38 nm with a target of 20 nm, which leads to 34% probability of successful deposition. Therefore, the positioning accuracy required for our structure lies close to the limit of the technology depending on the positioning approach. An experimental realization of a QE coupling requires fabricating many devices and looking for good candidates one by one. This approach allows the experimental demonstration of certain quantum effects for quantum information applications, but is still far from a scalable technology.

Conclusions

We explored a hybrid slot-Bragg nanophotonic cavity for the generation of indistinguishable photons at RT from various quantum emitters through a combination of numerical methods. We obtain the values of the theoretical indistinguishability, efficiency and Purcell enhancement for each configuration (i.e. waveguide width, slot width, number of periods). We obtained theoretical near-unity indistinguishability and high efficiency simultaneously by parameter sweep optimization. To relax the fabrication requirements (slot width) for near-unity indistinguishability, we have developed a machine learning algorithm that provides the optimal geometry of the cavity. According to our simulations, the optimized structure shows high indistinguishability ($I>0.9$) with slot widths about 20 nm. The geometrical features of the optimized design present significant challenges from the perspective of fabrication process. Although the device may be far from a real scalable technology it can be suitable for experimental demonstration of single photon operation. Also, the developed ML approach may provide insights for the optimization of different photonic structures for quantum information applications.

Acknowledgments

We gratefully acknowledge financial support from the European Union's Horizon 2020 research and innovation program under grant agreement No. 820423 (S2QUIP) and CSIC Quantum Technology Platform PT-001. JML acknowledges the Agencia Estatal de Investigación (AEI) grant PID2019-106088RB-C31.

Disclosures

The authors declare no conflicts of interest.

Data availability statement

Details underlying the results presented in this paper are available in the Supplement 1 file.

Funding sources

This work has been funded by the European Union's Horizon 2020 research and innovation program under grant agreement No. 820423 (S2QUIP).

Supplement information

This material is available free of charge via the internet at <http://pubs.acs.org>. Details of the computation of the indistinguishability; details of the numerical simulation; details of the machine learning algorithm; Information about the fabrication process.

References

- [1] Aspuru-Guzik, A., & Walther, P. (2012). Photonic quantum simulators. *Nature physics*, 8(4), 285-291.
- [2] Aharonov, D., Ambainis, A., Kempe, J. & Vazirani, U. in Proc. 33rd Annual ACM Symposium on Theory of Computing 50–59 (ACM, 2001).
- [3] Broome, M. A., Fedrizzi, A., Rahimi-Keshari, S., Dove, J., Aaronson, S., Ralph, T. C., & White, A. G. (2013). Photonic boson sampling in a tunable circuit. *Science*, 339(6121), 794-798.
- [4] Fattal, D., Diamanti, E., Inoue, K., & Yamamoto, Y. (2004). Quantum teleportation with a quantum dot single photon source. *Physical review letters*, 92(3), 037904.
- [5] Kimble, H. J. (2008). The quantum internet. *Nature*, 453(7198), 1023-1030.
- [6] Aharonovich, I., Englund, D., & Toth, M. (2016). Solid-state single-photon emitters. *Nature Photonics*, 10(10), 631.
- [7] Grange, T., Hornecker, G., Hunger, D., Poizat, J. P., Gérard, J. M., Similar, P., & Affixes, A. (2015). Cavity-funneled generation of indistinguishable single photons from strongly dissipative quantum emitters. *Physical review letters*, 114(19), 193601.
- [8] Chikara, R., De Nibs, B., Benz, F., Barrow, S. J., Sucherman, O. A., Rosa, E., ... & Blumberg, J. J. (2016). Single-molecule strong coupling at room T in plasmonic nanocavities. *Nature*, 535(7610), 127-130.
- [9] Russell, K. J., & Hu, E. L. (2010). Gap-mode plasmonic nanocavity. *Applied Physics Letters*, 97(16), 163115.
- [10] Seo, M. K., Kwon, S. H., E, H. S., & Park, H. G. (2009). Full three-dimensional subwavelength high-Q surface-plasmon-polariton cavity. *Nano letters*, 9(12), 4078-4082.
- [11] Santhosh, K., Button, O., Chitonid, L., & Haran, G. (2016). Vacuum Rabi splitting in a plasmonic cavity at the single quantum emitter limit. *Nature communications*, 7(1), 1-5.

- [12] Kang, J. H., No, Y. S., Kwon, S. H., & Park, H. G. (2011). Ultrasmall subwavelength nanorod plasmonic cavity. *Optics letters*, 36(11).
- [13] Peng, P., Liu, Y. C., Xu, D., Cao, Q. T., Lu, G., Gong, Q., & Xiao, Y. F. (2017). Enhancing coherent light-matter interactions through microcavity-engineered plasmonic resonances. *Physical review letters*, 119(23), 233901.
- [14] Burle, B., Sandoghdar, V., & Martín-Cano, D. (2018). Manipulation of quenching in nanoantenna-emitter systems enabled by external detuned cavities: a path to enhance strong-coupling. *ACS Photonics*, 5(2), 456-461.
- [15] Hugall, J. T., Singh, A., & van Hulst, N. F. (2018). Plasmonic cavity coupling. *Acs Photonics*, 5(1), 43-53.
- [16] Robinson, J. T., Manolatou, C., Chen, L., & Lipson, M. (2005). Ultrasmall mode volumes in dielectric optical microcavities. *Physical review letters*, 95(14), 143901.
- [17] Seidler, P., Lister, K., Drechsler, U., Hofrichter, J., & Stöferle, T. (2013). Slotted photonic crystal nanobeam cavity with an ultrahigh quality factor-to-mode volume ratio. *Optics express*, 21(26), 32468-32483.
- [18] Ryckman, J. D., & Weiss, S. M. (2012). Low mode volume slotted photonic crystal single nanobeam cavity. *Applied Physics Letters*, 101(7), 071104.
- [19] Hu, S., & Weiss, S. M. (2016). Design of photonic crystal cavities for extreme light concentration. *ACS photonics*, 3(9), 1647-1653.
- [20] Choi, H., Heuck, M., & Englund, D. (2017). Self-similar nanocavity design with ultrasmall mode volume for single-photon nonlinearities. *Physical review letters*, 118(22), 223605.
- [21] Saxena, A., Chen, Y., Ryou, A., Sevilla, C. G., Xu, P., & Majumdar, A. (2019). Improving indistinguishability of single photons from colloidal quantum dots using nanocavities. *ACS Photonics*, 6(12), 3166-3173.
- [22] Sanchis, L., Cryan, M. J., Pozo, J., Craddock, I. J., & Rarity, J. G. (2007). Ultrahigh Purcell factor in photonic crystal slab microcavities. *Physical Review B*, 76(4), 045118.
- [23] Sanchis, L., Håkansson, A., López-Zanón, D., Bravo-Abad, J., & Sánchez-Dehesa, J. (2004). Integrated optical devices design by genetic algorithm. *Applied Physics Letters*, 84(22), 4460-4462.
- [24] Morgado-León, A., Escuín, A., Guerrero, E., Yáñez, A., Galindo, P. L., & Sanchis, L. (2011, June). Genetic algorithms applied to the design of 3D photonic crystals. In *International Work-Conference on Artificial Neural Networks* (pp. 291-298). Springer, Berlin, Heidelberg.

- [25] Marques-Hueso, J., Sanchis, L., Cluzel, B., de Fornel, F., & Martínez-Pastor, J. P. (2010). Genetic algorithm designed silicon integrated photonic lens operating at 1550 nm. *Applied Physics Letters*, 97(7), 071115.
- [26] Tomm, N., Javadi, A., Antoniadis, N. O., Najer, D., Löbl, M. C., Korsch, A. R., ... & Warburton, R. J. (2021). A bright and fast source of coherent single photons. *Nature Nanotechnology*, 16(4), 399-403.
- [27] Schnauber, P., Singh, A., Schall, J., Park, S. I., Song, J. D., Rodt, S., ... & Davanco, M. (2019). Indistinguishable photons from deterministically integrated single quantum dots in heterogeneous GaAs/Si₃N₄ quantum photonic circuits. *Nano letters*, 19(10), 7164-7172.
- [28] Iff, O., Buchinger, Q., Moczała-Dusanowska, M., Kamp, M., Betzold, S., Davanco, M., ... & Schneider, C. (2021). Purcell-enhanced single photon source based on a deterministically placed WSe₂ monolayer quantum dot in a circular Bragg grating cavity. *Nano letters*, 21(11), 4715-4720.
- [29] Toninelli, C., Gerhardt, I., Clark, A. S., Reserbat-Plantey, A., Götzinger, S., Ristanović, Z., ... & Orrit, M. A. J. G. (2021). Single organic molecules for photonic quantum technologies. *Nature Materials*, 20(12), 1615-1628.
- [30] Dolan, P. R., Adekanye, S., Trichet, A. A. P., Johnson, S., Flatten, L. C., Chen, Y. C., ... & Smith, J. M. (2018). Robust, tunable, and high purity triggered single photon source at room temperature using a nitrogen-vacancy defect in diamond in an open microcavity. *Optics express*, 26(6), 7056-7065.
- [31] Fan, X., Takagahara, T., Cunningham, J. E., & Wang, H. (1998). Pure dephasing induced by exciton–phonon interactions in narrow GaAs quantum wells. *Solid state communications*, 108(11), 857-861.
- [32] Jakubczyk, T., Delmonte, V., Fischbach, S., Wigger, D., Reiter, D. E., Mermilliod, Q., ... & Rodt, S. (2016). Impact of phonons on dephasing of individual excitons in deterministic quantum dot microlenses. *ACS photonics*, 3(12), 2461-2466.
- [33] Kummer, S., & Basche, T. (1995). Measurement of optical dephasing of a single terrylene molecule with nanosecond time resolution. *The Journal of Physical Chemistry*, 99(47), 17078-17081.
- [34] Hesselink, W. H., & Wiersma, D. A. (1980). Optical dephasing and vibronic relaxation in molecular mixed crystals: A picosecond photon echo and optical study of pentacene in naphthalene and p-terphenyl. *The Journal of Chemical Physics*, 73(2), 648-663.
- [35] Moody, G., Dass, C. K., Hao, K., Chen, C. H., Li, L. J., Singh, A., ... & Li, X. (2015). Intrinsic homogeneous linewidth and broadening mechanisms of excitons in monolayer transition metal dichalcogenides. *Nature communications*, 6(1), 1-6.
- [36] Wang, X., Grist, S., Flueckiger, J., Jaeger, N. A., & Chrostowski, L. (2013). Silicon photonic slot waveguide Bragg gratings and resonators. *Optics express*, 21(16), 19029-19039.

- [37] Bera, A., Kuitinen, M., Honkanen, S., & Roussey, M. (2018). Silicon slot waveguide Fano resonator. *Optics Letters*, 43(15), 3489-3492.
- [38] Wang, X., Flueckiger, J., Schmidt, S., Grist, S., Fard, S. T., Kirk, J., ... & Chrostowski, L. (2013). A silicon photonic biosensor using phase - shifted Bragg gratings in slot waveguide. *Journal of biophotonics*, 6(10), 821-828.
- [39] Errando-Herranz, C., Schöll, E., Picard, R., Laini, M., Gyger, S., Elshaari, A. W., ... & Jöns, K. D. On-chip single photon emission from a waveguide-coupled two-dimensional semiconductor. 2020, August. In *Quantum Nanophotonic Materials, Devices, and Systems 2020* (Vol. 11471, p. 1147105). International Society for Optics and Photonics.
- [40] Lumerical Inc. <https://www.lumerical.com/products/>. (accessed 2022-02-21)
- [41] Kristensen, P. T., Van Vlack, C., & Hughes, S. (2011). Effective mode volumes and purcell factors for leaky optical cavities. 2011-7-22. *Optics Letters*, Vol. 37, Issue 10, pp. 1649-1651
- [42] Vuckovic, J. Quantum optics and cavity QED with quantum dots in photonic crystals. In *Quantum Optics and Nanophotonics*. Oxford University Press. (2017).
- [43] Novotny, L., & Hecht, B. (2012). *Principles of nano-optics*. Cambridge university press.
- [44] Almeida, V. R., Xu, Q., Barrios, C. A., & Lipson, M. (2004). Guiding and confining light in void nanostructure. *Optics letters*, 29(11), 1209-1211.
- [45] Liu, Y., Kong, M., & Jiang, Y. (2015). Transverse magnetic modes in planar slot waveguides. *JOSA B*, 32(10), 2052-2060.
- [46] Guimba, J., Weituschat, L. M., Montolio, J. L., & Postigo, P. A. (2021). Enhancement of the indistinguishability of single photon emitters coupled to photonic waveguides. *Optics Express*, 29(14), 21160-21173.
- [47] Stoleru, V. G., & Towe, E. (2003). Oscillator strength for intraband transitions in (In, Ga) As/GaAs quantum dots. *Applied physics letters*, 83(24), 5026-5028.
- [48] Hatami, F., Grundmann, M., Ledentsov, N. N., Heinrichsdorff, F., Heitz, R., Böhrer, J., ... & Kop'ev, P. S. (1998). Carrier dynamics in type-II GaSb/GaAs quantum dots. *Physical Review B*, 57(8), 4635.
- [49] Schneider, C., Glazov, M. M., Korn, T., Höfling, S., & Urbaszek, B. (2018). Two-dimensional semiconductors in the regime of strong light-matter coupling. *Nature communications*, 9(1), 1-9.
- [50] Lundt, N., Maryński, A., Cherotchenko, E., Pant, A., Fan, X., Tongay, S., ... & Schneider, C. (2016). Monolayered MoSe₂: a candidate for room T polaritonics. *2D Materials*, 4(1), 015006.

- [51] Zhao, H., Zhao, Y., Song, Y., Zhou, M., Lv, W., Tao, L., ... & Wang, X. (2019). Strong optical response and light emission from a monolayer molecular crystal. *Nature communications*, 10(1), 1-9.
- [52] Saani, M. H., Vesaghi, M. A., & Esfarjani, K. (2004). Oscillator strength calculations in color centers of diamond and the role of spin. *The European Physical Journal B-Condensed Matter and Complex Systems*, 39(4), 441-446.
- [53] Borri, P., Langbein, W., Schneider, S., Woggon, U., Sellin, R. L., Ouyang, D., & Bimberg, D. (2001). Ultralong dephasing time in InGaAs quantum dots. *Physical Review Letters*, 87(15), 157401.
- [54] Bayer, M., & Forchel, A. (2002). T dependence of the exciton homogeneous linewidth in In 0.60 Ga 0.40 As/GaAs self-assembled quantum dots. *Physical Review B*, 65(4), 041308.
- [55] Huang, L., Krasnok, A., Alu, A., Yu, Y., Neshev, D., & Miroshnichenko, A. Enhanced Light-Matter Interaction in Two-Dimensional Transition Metal Dichalcogenides. (2022-03-08). *Reports on Progress in Physics*. Volume 85 (4).
- [56] Albrecht, R., Bommer, A., Deutsch, C., Reichel, J., & Becher, C. (2013). Coupling of a single nitrogen-vacancy center in diamond to a fiber-based microcavity. *Physical review letters*, 110(24), 243602.
- [57] Häyrinen, M., Roussey, M., Säynätjoki, A., Kuittinen, M., & Honkanen, S. (2015). Titanium dioxide slot waveguides for visible wavelengths. *Applied optics*, 54(10), 2653-2657.
- [58] Raza, A., Van Daele, M., Wuytens, P., Dendooven, J., Detavernier, C., Clemmen, S., & Baets, R. (2018, May). E-beam-lithography free plasmonic slot waveguides for on-chip Raman spectroscopy. In *CLEO: Science and Innovations* (pp. SW3L-6). Optical Society of America.
- [59] Wang, Y., He, S., Gao, X., Ye, P., Lei, L., Dong, W., ... & Xu, P. (2022). Enhanced optical nonlinearity in a silicon–organic hybrid slot waveguide for all-optical signal processing. *Photonics Research*, 10(1), 50-58.
- [60] Lin, S., Hu, J., & Crozier, K. B. (2011). Ultracompact, broadband slot waveguide polarization splitter. *Applied Physics Letters*, 98(15), 151101.
- [61] Hochberg, M., Baehr-Jones, T., Wang, G., Huang, J., Sullivan, P., Dalton, L., & Scherer, A. (2007). Towards a millivolt optical modulator with nano-slot waveguides. *Optics Express*, 15(13), 8401-8410.
- [62] Wang, J., Cheng, Z., Chen, Z., Wan, X., Zhu, B., Tsang, H. K., ... & Xu, J. (2016). High-responsivity graphene-on-silicon slot waveguide photodetectors. *Nanoscale*, 8(27), 13206-13211.
- [63] Lin, C. Y., Wang, X., Chakravarty, S., Lee, B. S., Lai, W., Luo, J., ... & Chen, R. T. (2010). Electro-optic polymer infiltrated silicon photonic crystal slot waveguide modulator with 23 dB slow light enhancement. *Applied Physics Letters*, 97(9), 194.

- [64] Zhang, H., Zhang, J., Chen, S., Song, J., Kee, J. S., Yu, M., & Lo, G. Q. (2011). CMOS-compatible fabrication of silicon-based sub-100-nm slot waveguide with efficient channel-slot coupler. *IEEE Photonics Technology Letters*, 24(1), 10-12.
- [65] Cord, B. M. (2009). Achieving sub-10-nm resolution using scanning electron beam lithography (Doctoral dissertation, Massachusetts Institute of Technology).
- [66] Debnath, K., Khokhar, A. Z., Reed, G. T., & Saito, S. (2017). Fabrication of arbitrarily narrow vertical dielectric slots in silicon waveguides. *IEEE Photonics Technology Letters*, 29(15), 1269-1272.
- [67] Liu, S., Srinivasan, K., & Liu, J. (2021). Nanoscale Positioning Approaches for Integrating Single Solid-State Quantum Emitters with Photonic Nanostructures. *Laser & Photonics Reviews*, 15(10), 2100223.
- [68] Hennessy, K., Badolato, A., Winger, M., Gerace, D., Atatüre, M., Gulde, S., ... & Imamoğlu, A. (2007). Quantum nature of a strongly coupled single quantum dot–cavity system. *Nature*, 445(7130), 896-899.
- [69] Thon, S. M., Rakher, M. T., Kim, H., Gudat, J., Irvine, W. T., Petroff, P. M., & Bouwmeester, D. (2009). Strong coupling through optical positioning of a quantum dot in a photonic crystal cavity. *Applied Physics Letters*, 94(11), 111115.
- [70] Liu, J., Davanço, M. I., Sapienza, L., Konthasinghe, K., De Miranda Cardoso, J. V., Song, J. D., ... & Srinivasan, K. (2017). Cryogenic photoluminescence imaging system for nanoscale positioning of single quantum emitters. *Review of Scientific Instruments*, 88(2), 023116.
- [71] Gschrey, M., Schmidt, R., Schulze, J. H., Strittmatter, A., Rodt, S., & Reitzenstein, S. (2015). Resolution and alignment accuracy of low-temperature *in situ* electron beam lithography for nanophotonic device fabrication. *Journal of Vacuum Science & Technology B, Nanotechnology and Microelectronics: Materials, Processing, Measurement, and Phenomena*, 33(2), 021603.
- [72] Elshaari, A. W., Pernice, W., Srinivasan, K., Benson, O., & Zwiller, V. (2020). Hybrid integrated quantum photonic circuits. *Nature photonics*, 14(5), 285-298.
- [73] Wang, J., Sciarrino, F., Laing, A., & Thompson, M. G. Integrated photonic quantum technologies. (2020). *Nature Photonics*, 14(5), 273-284.

Perfect Photon Indistinguishability from a Set of Dissipative Quantum Emitters

Abstract: Single photon sources (SPS) based on semiconductor quantum dot (QD) platforms are restricted to low temperature (T) operation due to the presence of strong dephasing processes. Although the integration of QD in optical cavities provides an enhancement of its emission properties, the technical requirements for maintaining high indistinguishability (I) at high T are still beyond the state of the art. Recently, new theoretical approaches have shown promising results by implementing two-dipole-coupled-emitter systems. Here, we propose a platform based on an optimized five-dipole-coupled-emitter system coupled to a cavity which enables perfect I at high T . Within our scheme the realization of perfect I single photon emission with dissipative QDs is possible using well established photonic platforms. For the optimization procedure we have developed a novel machine-learning approach which provides a significant computational-time reduction for high demanding optimization algorithms. Our strategy opens up interesting possibilities for the optimization of different photonic structures for quantum information applications, like the reduction of quantum decoherence in clusters of coupled two-level quantum systems.

Keywords: Single-photon; Quantum Optics; Photonic Integrated Circuits; Quantum Decoherence.

Introduction

Over the last decade, milestones achieved in integrated quantum photonics (IQP) have led to promising results. While other quantum technologies (QT) like ion trapping or superconducting systems were used to demonstrate their first logical operations in the 1990s [1,2], the first functioning IQP gate was only developed in 2008 [3]. Yet, despite its immaturity, IQP has become established in a wide range of proposed schemes: (Quantum Communications) Si-based chip to chip quantum key distribution (QKD) over 43 km dark fiber was demonstrated in 2018 [4]; network operation for distributed quantum computation (i.e. quantum internet) was reported in 2021 [5]; (Quantum Computation) Gaussian boson sampling scheme with 50 photons for specific quantum computing demonstrated quantum advantage for the first time in 2020 [6]; (Quantum simulation) A IQP based variational eigensolver for calculation of the ground state energy of H₂ molecules was developed in 2013 [7]; (Quantum Metrology) A IQP platform based on defects in diamond was used for extremely efficient detectors of magnetic fields with unprecedent sensitivity [8]. In contrast to other QT platforms, IQP leverage commercially available systems from the integrated photonics industry, which provide reliable devices for on-chip integration [9] and metamaterial systems for broadband operation [10,11]. In this context, IQP shows a new leading candidate for the future q-bit in QT: the indistinguishable single photon.

Integrated photonics offer different approaches for the modulation of photon emission [12,13]. Suitable platforms for indistinguishable SPS are epitaxially grown semiconductor QDs. QDs enable site control during growth [14] and the possibility of monolithic integration into photonic nanocavities [15,16], providing enhanced quantum emission. As a result, many recent experimental demonstrations have reported

record I with cavity-integrated QDs at cryogenic T: $g(2)(0) = 7 \times 10^{-3}$ and $I = 0.96$ was reported with InAs/GaAs QDs embedded in a micropolar cavity at 4.3 K [17]; $g(2)(0) = 1.2 \times 10^{-2}$ and $I = 0.97$ with InAs/GaAs QDs integrated in a DBR microcavity at 4.2 K [18]; $g(2)(0) = 2.8 \times 10^{-3}$ and $I = 0.99$ with InGaAs/GaAs QDs inside DBR micropillars at 4 K [19]. However, for T above the cryogenic regime, QDs are subject to pure dephasing mechanisms which reduce the coherence of the emission [20-22]: $g^{(2)}(0) = 0.47$ with InGaAs/GaAs QDs at 120 K [23]; $g^{(2)}(0) = 0.34$ with InAs/InP QDs at 80 K [24]; $g^{(2)}(0) = 0.48$ with GaAs/GaAsP QDs at 160 K [25]. For $T > 200$ K the best reported value is $g_{(2)}(0) = 0.34$ [26]. As a consequence, I is reduced to non-practical values for quantum information tasks: $I > 0.79$ for most quantum information processing schemes and $I > 0.5$ for QKD protocols [27]. In this regard, QDs for SPS operation are restricted to low T. In an attempt to overcome this limitation, a variety of cavity-engineering approaches have been conducted [28,29]. However, several theoretical works [30-32] indicate that cavity quality factors (Q) above 4×10^7 are required for QDs to function at room T, while, to date, the highest reported Q coupled to a quantum emitter is about $Q = 55000$ [33]. In this regard, the theoretical exploration over new strategies for enhancing I in the presence of dephasing processes is especially relevant.

Recently, theoretical studies [34-38] have shown that the enhancement and tunability of single photon emission are possible through interfaces based on two-emitter systems coupled to a cavity mode. In their scheme, tunable bandwidth and Purcell enhancement are achieved by dynamical control of the collective states of the two emitters coupled by dipolar interaction. The results open up interesting possibilities for application in single photon generation for quantum information processing. At the same time, deterministic positioning required for dipole-dipole coupling between emitters has been experimentally demonstrated on several SPS platforms: organic molecules [39], color centers in h-BN [40] and diamond [41], terylene molecules [42] and QDs [43-46]. The potential applications of these cluster systems for the enhancement of I have not been studied neither theoretically nor experimentally. As we will show, the cooperative dynamics of these cluster systems can be exploited to maintain high I with arbitrary low Q cavities by tuning the energy transfer rates between the emitters.

In this work, we present a theory for estimating I in a two-emitter system with strong dephasing coupled to a single-mode cavity. We derived an analytical expression of I as a function of the distance between the emitters, cavity decay rate, and pure dephasing rate. The results show how the requirements of the cavity for high I change with the strength of the dipolar interaction. Taking the model further, we propose a new interpretation of the I value, which allows us to estimate its behavior with larger systems (i.e., systems with more than two emitters). We performed numerical simulations of a system of five dipole-coupled emitters to find the optimal configuration for maximum I . For the optimization process, we developed a novel machine-learning (ML) scheme based on a hybrid neural network (NN)-genetic algorithm (GA) to find the position of each emitter to maximize I . The optimization procedure provides perfect I (i.e., $I = 1$) in arbitrary low Q cavities, offering unprecedent advantages for relaxing the cavity requirements and favoring the use of QDs as SPS at room T.

Materials and methods

Dipole-dipole coupling model

After rotating the wave approximation, the Hamiltonian for the two-QE system coupled to the single-mode cavity reads [35]:

$$H = \Omega_{12}(\sigma_1^\dagger\sigma_2 + \sigma_1\sigma_2^\dagger) + ig(a^\dagger(\sigma_1 + \sigma_2) - a(\sigma_1^\dagger + \sigma_2^\dagger)), \quad (1)$$

where $\sigma_i/\sigma_i^\dagger$ are the lowering/rising operators of the QEs and a/a^\dagger the annihilation/creation operators of the cavity field. The terms associated with γ, γ^* and κ are described under Born-Markov approximation, so the evolution of the density matrix follows the Lindblad equation [34]:

$$\begin{aligned} \frac{\partial\rho}{\partial t} = & -i[H,\rho] + \sum_n(D_n\rho D_n^\dagger - \frac{1}{2}(D_n^\dagger D_n\rho + \rho D_n^\dagger D_n)) \\ & + 2\gamma\sum_{i\neq j}(\sigma_i\rho\sigma_j^\dagger - \frac{1}{2}(\sigma_j^\dagger\sigma_i\rho + \rho\sigma_j^\dagger\sigma_i)) \end{aligned} \quad (2)$$

where the D_n denotes the collapse operators: $\sqrt{\kappa}a$, and $\sqrt{\gamma^*}\sigma_i^\dagger\sigma_i$. We have assumed $kd \ll 1$ so the modified radiative decay rate is 2γ and $\Omega_{12} = \frac{3\gamma}{4(kd)^3}$. Without detuning between the QEs there is no coherent coupling between any state but the $\{|gg\rangle, |+\rangle\}$ set, so the Hamiltonian and Lindblad equation can be written as:

$$\begin{aligned} H = & \Omega_{12}|+\rangle\langle+| + i\sqrt{2}g(a^\dagger\sigma_+ - a\sigma_+^\dagger) \\ \frac{\partial\rho}{\partial t} = & -i[H,\rho] + \sum_n(D_n\rho D_n^\dagger - \frac{1}{2}(D_n^\dagger D_n\rho + \rho D_n^\dagger D_n)) \end{aligned} \quad (3)$$

Where $\sigma_+ = \frac{\sigma_1 + \sigma_2}{\sqrt{2}}$ and now the D_n denotes the collapse operators: $\sqrt{\kappa}a$, $\sqrt{2\gamma}\sigma_+$ and $\sqrt{\gamma^*}\sigma_+^\dagger\sigma_+$ [34]. The equations in (14) corresponds to the evolution of a system with a single effective QE with decay rate 2γ coupled to a single-mode cavity field with $\sqrt{2}g$. The degree of I is defined as [30]:

$$I = \frac{\int_0^\infty dt d\tau |\langle a^\dagger(t+\tau)a(t)\rangle|^2}{\int_0^\infty dt d\tau \langle a^\dagger(t)a(t)\rangle \langle a^\dagger(t+\tau)a(t+\tau)\rangle} \quad (4)$$

Which can be computed numerically via Quantum Regression Theorem (QRT). Alternatively, to derive an explicit formula for I we start from the following expressions of the master equation:

$$\begin{aligned} \frac{\partial\rho_{ee}}{\partial t} = & ig(\rho_{ec} - \rho_{ce}) - \gamma\rho_{ee} \\ \frac{\partial\rho_{cc}}{\partial t} = & ig(\rho_{ce} - \rho_{ec}) - \kappa\rho_{cc} \\ \frac{\partial\rho_{ec}}{\partial t} = & ig(\rho_{ee} - \rho_{cc}) - (\frac{\Gamma}{2} + \frac{3\gamma}{4(kd)^3})\rho_{ec} \end{aligned} \quad (5)$$

In the incoherent regime we can apply adiabatic elimination of the coherences by setting $\frac{\partial\rho_{ec}}{\partial t} = 0$ [30]. Substituting in (5) we obtain the rate equations (14) with the corresponding transfer rate R shown in (13). We can now obtain the numerator of (8) by calculating the ne-G of the system from the equations of motion:

$$i\frac{\partial}{\partial t}\hat{G}^R(\tau) = i\delta(\tau)\hat{I} + [\hat{H} - i\hat{\Sigma}^R(0)]\hat{G}^R(\tau), \quad \hat{\Sigma}^R = \begin{pmatrix} (\gamma + \frac{\gamma^*}{2}) & 0 \\ 0 & \kappa/2 \end{pmatrix} \quad (6)$$

Where $\hat{G}^R(\tau)$ is the retarded $\hat{G}^R(\tau)$ and $\hat{\Sigma}^R$ the retarded self-energy. Following a similar procedure as in [30], the numerator in (4) can be substituted by:

$$|\langle a^\dagger(t + \tau)a(t) \rangle|^2 = P_c^2(t)e^{-\tau(\kappa+4g^2\Gamma/(\Gamma^2+\frac{\gamma^2}{(kd)^2}))} \quad (7)$$

Solving equation (14) for P_c we can analytically solve (4), which gives the expression shown in (13).

Larger systems

We first obtain the characteristic polynomial of (14): $P(\lambda) = \lambda^2 + (\kappa + 2R + 1)\lambda + (\kappa R + \kappa + R)$, where we have set $\gamma = 1$. Then we set the iterative process $\lambda_{n+1} \rightleftharpoons P(\lambda_n)$ (from $\lambda = 0$) and check the stability in the parameter space (κ, R) . Fig 2.a shows the κ -parameter space of the stability of $P(\lambda)$ for a fixed R . Black dots in the complex plane correspond to κ values whose iteration stays bounded and doesn't diverge to infinity. White dots correspond to values whose iteration diverges to infinity at a maximum speed. Gradient colors correspond to values whose iteration diverges to infinity at different speeds. Our region of interest is the positive real line $\kappa \in \mathbb{R}^+$. In this region the iteration diverges to infinity for all κ . We want to measure the speed of the divergence θ for each κ and R (i.e. the number of iterations that takes the process to infinity). A good candidate to characterize this value is the slope of $P(\lambda)$ at $\lambda = 0$ (i.e. $P'(0)$). Since $P'(\lambda)$ grows monotonically with λ , $P'(0)$ uniquely determines θ . In Figure 2.b we show the value of $P(\lambda)$ (blue line) for specific (κ, R) . The arrows indicate consecutive λ_n values of the iteration process. In order to express θ in the decay rate units (λ units), we draw the tangent line to $P(\lambda)$ at $\lambda = 0$ (red line in Figure 2.b) and take the cut with the x-axis, which gives $\frac{P(0)}{P'(0)}$. With this definition θ reads:

$$\theta = \frac{P(0)}{P'(0)} = \frac{\kappa R + \kappa + R}{\kappa + 2R + 1} \quad (8)$$

In order to normalize θ , we need to divide (8) by its maximum value θ_{max} . θ is maximum when $\kappa, R \ll 1$, and therefore from (8) we have that $\theta_{max} = \kappa + R$. Then the normalized speed of divergence $\bar{\theta}$ is given by:

$$\bar{\theta} = \frac{\theta}{\theta_{max}} = \frac{\gamma + \frac{\kappa R}{\kappa + R}}{\kappa + 2R + \gamma} = I \quad (9)$$

which matches the expression for I [30]. If we apply the same definition of $\bar{\theta}$ for the cascaded cavity system (equation (15)) we obtain:

$$\bar{\theta} = \frac{\kappa_1/2 + \frac{\kappa_2 R_2}{2(\kappa_2 + R_2)}}{\kappa_1/2 + \kappa_2 + \frac{3}{2}R_2} = I \quad (10)$$

which again matches the expression for I [31] after applying the same approximations. In the same way, for the two-emitter system $\bar{\theta}$ matches the I value shown in (13). Note that in general the $\frac{P(0)}{P'(0)}$ is equal to $\frac{\Delta}{\tau}$, where Δ is the determinant and τ is the trace of the rate equations matrix. Therefore, with this method we

are able to obtain the analytic expression of I for any system from trivial operations in the rate equations, without the need of calculating the ne-G.

Machine Learning scheme

The Hamiltonian for the 5-QEs system coupled to a single-mode cavity field can be written as:

$$H = \sum_{i \neq j} \Omega_{ij} (\sigma_i^\dagger \sigma_j + \sigma_i \sigma_j^\dagger) + ig \sum_{i \neq j} (a^\dagger (\sigma_i + \sigma_j) - a (\sigma_i^\dagger + \sigma_j^\dagger)) \quad (11)$$

with $i, j = (1, \dots, 5)$. The modified radiative decay rates γ_{ij} and the dipolar interaction strengths Ω_{ij} can be obtained from the Green's tensor of the system leading to [38]:

$$\begin{aligned} \gamma_{ij} &= \frac{3}{2} \left\{ \sin(kd_{ij})/kd_{ij} - 2(\cos(kd_{ij})/kd_{ij}^2) - \sin(kd_{ij})/kd_{ij}^2 \right\} \\ \Omega_{ij} &= \frac{3}{4} \left\{ -\cos(kd_{ij})/kd_{ij} - 2(\sin(kd_{ij})/kd_{ij}^2) - \cos(kd_{ij})/kd_{ij}^2 \right\} \end{aligned} \quad (12)$$

The evolution of the density matrix follows the Lindblad equation (2) substituting γ by γ_{ij} and adding the corresponding $\sqrt{\gamma^*} \sigma_i^\dagger \sigma_i$ operators. For each iteration the value of I is calculated by solving (2) numerically and computing (8) by QRT. As in each iteration a 12x12 matrix is diagonalized, the total time of each function evaluation can take several minutes. At the same time, a GA optimization may require 105 evaluations of the fitness function. If we directly use QRT for each evaluation, the optimization would require excessive computational times. Instead, in our approach we first generate a data set (ω, I) with the results obtained from 2000 iterations. With these data, we train a deep NN which learns to estimate the outcome of I for any possible set of random positions $\vec{\omega}$. Now, each time the GA creates a random vector ω , the evaluation of the fitness function obtains I from the estimation of the NN. This way, each evaluation takes just a few seconds. Through the iteration of cross-over and mutation, the GA finds the optimal configuration for maximizing I after a certain number of generations. Therefore, with our NN-GA scheme we reduce the number of actual numerical simulations for the dataset by two orders of magnitude.

The NN consists of a sequential layer model implemented in Keras module with the corresponding settings: Number of layers = 4; Neurons per layer = 200; input-dimension = 10; output dimension = 1; loss = mean square error; Epochs = 200; learning rate = 0.001; Batch size = 100; Number of samples = 2000. After the training with 2000 samples both loss and validation-loss converged to 10-3, giving enough accuracy for the estimation of I and the optimization model. The Genetic Algorithm uses decimal representation for the genes, one-point crossover and uniform mutation. The total initial population was set to 5000, the number of parents matings = 2500, number of weights = 1000. Using these values, we needed over 216 generations to find each optimal geometry.

Results

Indistinguishability of dipole coupled emitters

We consider a system of two quantum emitters (QE) coupled to a single-mode cavity field. Each QE is described by a Two-Level-System $\{|g\rangle, |e\rangle\}$ with a decay rate γ and a pure dephasing rate γ^* . The QEs

interact with each other by direct dipole-dipole coupling with a strength $\Omega_{12} = \frac{3\gamma}{4(kd)^3}$, where k is the wave vector of the emission and d is the distance between the QEs [34]. The cavity field in the Fock basis $\{|0\rangle, |1\rangle\}$ has a decay rate κ and is coupled to the QEs with a coupling constant g . Assuming $kd \ll 1$ and no detuning between the QEs this system is equivalent to a single effective QE $\{|gg\rangle, |+\rangle\}$ (e-QE) with a decay rate 2γ [34]. Fig 1.a shows a layout of the proposed system where Fig 1.a (top) shows the two interacting QEs with γ coupled to the cavity field with g , and Fig 1.a (bottom) shows the equivalent single effective QE system coupled to the same cavity. Here $|+\rangle$ represents the superradiant state $|+\rangle = \frac{|eg\rangle - |ge\rangle}{\sqrt{2}}$.

The e-QE is coupled to the cavity field with $\sqrt{2}g$ and a cavity detuning $\delta = \Omega_{12}$ [35]. In Fig 1.b, c we report the numerical calculation of I for the e-QE as a function of the cavity parameters (g and κ) for fixed d , γ and $\gamma^* = 10^4\gamma$. Fig 1.b shows the region of high I in the incoherent regime (i.e. $g \ll \kappa + \gamma + \gamma^*$) while Fig 1.c corresponds to the region in the coherent regime ($g \gg \kappa + \gamma + \gamma^*$). The plots shows a color map with the indistinguishability of the effective QE versus the normalized parameters of the cavity κ and g .

Within the incoherent regime the dynamics can be approximated to a population transfer between the e-QE and the cavity field with an effective transfer rate R [30]. From the non-equilibrium Green's function (ne-G) of the system we obtain (see methods):

$$R = \frac{4g^2\Gamma}{\Gamma^2 + \frac{\gamma^2}{(kd)^6}}, \quad I = \frac{\gamma\kappa[\Gamma^3 + \Omega_{12}] + [4g^2(\gamma + 1) + \Omega_{12}\frac{\kappa\gamma}{\Gamma}][\Gamma^2 + \Omega_{12}]}{[\Gamma^2 + \Omega_{12} + 8g^2] \cdot [\kappa\Gamma^2 + \Omega_{12} + 4g^2\Gamma]} \quad (13)$$

where $\Gamma = \gamma + \gamma^* + \kappa$. In this regime the cavity behaves as an effective emitter pumped by the e-QE, and the conditions for high I are $\kappa < \gamma$ and $R < \gamma$ [30], as shown in Fig 1.b. As the distance between the QEs decreases the R of the e-QE reduces, so I remains high for higher g values. This effect is easily visualized in Fig 1.d, where we plot the iso-contours of $I = 0.9$ versus the normalized parameters of the cavity κ and g for different values of d . Each color region in Fig 1.d shows the $I > 0.9$ area for a specific value of d , which ranges from $d = 6.9 \cdot 10^{-2}\lambda$ to $d = 8.5 \cdot 10^{-2}\lambda$. Whereas the maximum g for $I > 0.9$ is about $g = 10\gamma$ when $d = 8.5 \cdot 10^{-2}\lambda$, this value increases to $g = 20\gamma$ when $d = 6.9 \cdot 10^{-2}\lambda$. In other words, the requirement for Q (i.e., $\kappa < \gamma$) remains unchanged and the R -reduction effect just enables high I for higher g values, which is not particularly interesting. Therefore, the implementation of the two-QE system does not provide any practical advantages (in terms of Q and g) with respect to the single-QE. For the three distances, Fig. 1.f confirms the excellent agreement for I values obtained from equation (1) and from numerical simulations of the two-QE system (see methods).

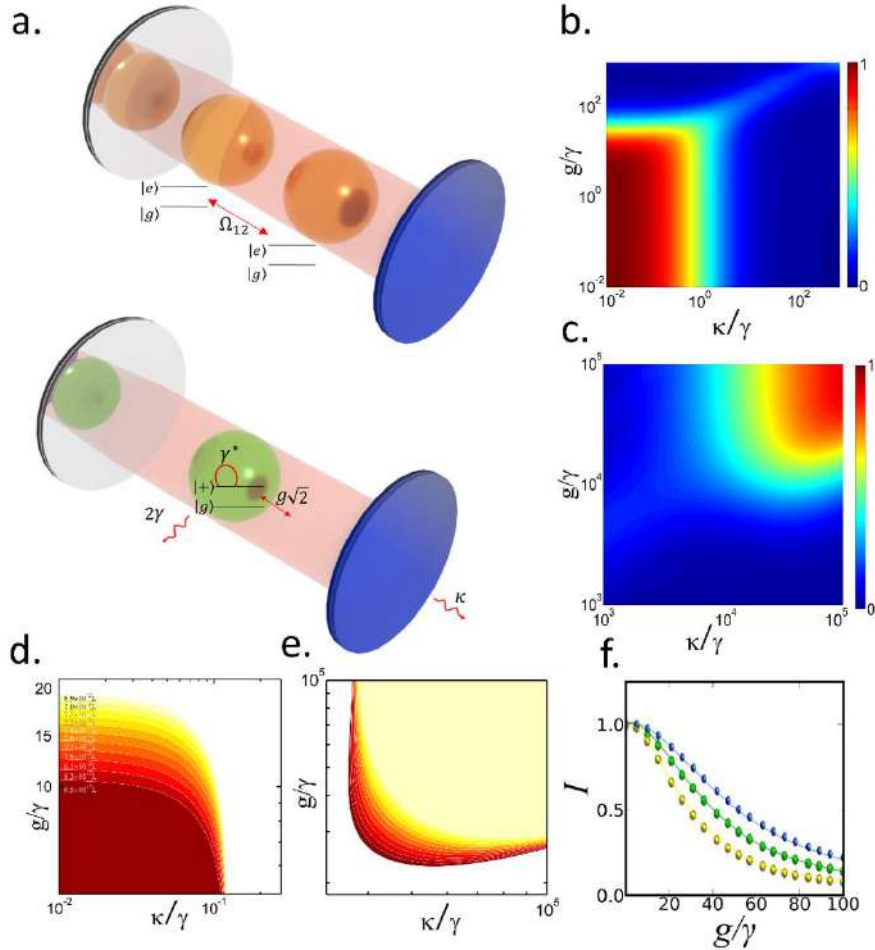


Figure 1. (a) The two interacting QEs with γ coupled to the cavity field with g are equivalent to a single QE with 2γ coupled to the cavity with $\sqrt{2}g$, each sphere represents a single two-level-system. Indistinguishability of the effective QE versus the normalized κ and g in the (b) incoherent regime, and (c) coherent regime. Contour map of regions with $I>0.9$ for different distances between the emitters from $d = 6.9 \cdot 10^{-2}\lambda$ to $d = 8.5 \cdot 10^{-2}\lambda$ (d) incoherent regime and ϵ coherent regime. (f) Indistinguishability versus normalized g for $d = 7.2 \cdot 10^{-2}\lambda$ (yellow), $d = 7 \cdot 10^{-2}\lambda$ (green) and $d = 6.9 \cdot 10^{-2}\lambda$ (blue); solid lines calculated using equation (1); colored dots obtained from numerical integration of the Lindblad equation with two QEs.

In the coherent regime the conclusions are roughly similar. Within the range where g is close to the strong coupling condition, the (e-QE)-cavity system is equivalent to an effective emitter [30] with decay rate $2\gamma + R$. Here the condition for high I is $R > \gamma^*$ [30], as shown in Fig 1.c. Same as before, reducing d decreases R , requiring higher g for high I . Fig 1.e shows the same iso-contours as Fig 1.d in the coherent regime. The $I > 0.9$ region narrows upwards as d decreases due to the same R reduction effect. Thus, in the coherent regime the two-QE system impose stronger restrictions than the single QE, since it demands higher g values for getting high I . Therefore, the two-QE interface does not provide any advantage for high I in terms of cavity requirements, in the incoherent or coherent regimes. However, an extended exploration over systems with larger number of coupled emitters can be relevant. As we will show next, exploiting the cooperative behavior of optimized systems with more than 2 emitters can provide benefits in terms of I .

Larger systems

We showed before that for a set of interacting 2-level quantum systems in the incoherent regime the dynamics are described by a population transfer between the subsystems with effective transfer rates R . As an example, for a single QE coupled to a single-mode cavity field the evolution of the system reduces to the following rate equations [30]:

$$\begin{pmatrix} \dot{P}_{QE} \\ \dot{P}_C \end{pmatrix} = \begin{pmatrix} -(\gamma + R) & R \\ R & -(\kappa + R) \end{pmatrix} \begin{pmatrix} P_{QE} \\ P_C \end{pmatrix} \quad (14)$$

Where P_{QE} is the population of the QE, P_C is the population of the cavity and $R = \frac{4g^2}{\Gamma}$. As it is described in the Methods section, I is obtained from the solution of (14) via the QRT. Since QRT computation is an iterative process, it may be useful to study the dynamic stability of the characteristic equation of (14) to find any kind of relation with I . For this purpose, we have defined the degree of stability ($\bar{\theta}$) by measuring the speed of divergence of the characteristic equation of (14) (see methods). After some algebra, we have found a direct relationship between $\bar{\theta}$ and I (see equations (9) and (10) in Methods). This means that we can derive analytic expressions of I for arbitrary large system without having to compute the ne-G. Instead, we obtain I from the determinant Δ and the trace τ of (14), which significantly simplifies the problem, especially for more complicated systems (like the ones with more than 2 emitters). This finding can be expressed as:

$$\bar{\theta} = I = \frac{\bar{\Delta}}{\tau} = \frac{\gamma + \frac{\kappa R}{\kappa + R}}{\kappa + 2R + \gamma} \quad (15)$$

where $\bar{\Delta}$ is the normalized determinant (see Methods). In the same way as I , if κ increases, $\bar{\theta}$ decays at different rates depending on R . The alternative interpretation of I shown in Eq (15) provides some hints to find a way of keeping high I with higher κ values (i.e. to reduce the Q of the cavity). For the case of a single QE-cavity system the decay of $\bar{\theta}$ with κ can be tuned by changing R . If we include more QEs (or, in general, more subsystems) we have additional transfer rates that may help even more to reduce the cavity Q . The additional transfer rates will show up in the off-diagonal terms of the rate equations, giving additional terms in Δ which can lead to new paths to improve the reduction of $\bar{\theta}$ with κ . This approach can be illustrated with the cascaded-cavities scheme [31]. This system considers a single QE coupled to a cavity which at the same time is coupled to a second cavity. In the incoherent regime the dynamics follows the rate equations [31]:

$$\begin{pmatrix} \dot{P}_{QE} \\ \dot{P}_{C1} \\ \dot{P}_{C2} \end{pmatrix} = \begin{pmatrix} -(\gamma + R_1) & R_1 & 0 \\ R_1 & -(\kappa_1 + R_1 + R_2) & R_2 \\ 0 & R_2 & -(\kappa_2 + R_2) \end{pmatrix} \begin{pmatrix} P_{QE} \\ P_{C1} \\ P_{C2} \end{pmatrix} \quad (16)$$

where P_{C1} is the population of the first cavity, P_{C2} is the population of the second cavity, κ_1 is the decay rate of the first cavity, κ_2 is the decay rate of the second cavity, R_1 is the transfer rate between the QE and the first cavity, and R_2 is the transfer rate between the first and second cavity. In this case we have one more degree of freedom (R_2) than in the single QE-cavity system. Therefore, by adjusting R_1 and R_2 we can tune the decay of the stability with κ in a more efficient way. Fig 2.c shows a quantitative example of this improvement. The plot shows the indistinguishability versus the normalized second-cavity parameter

κ_2 for three different values of normalized first-cavity parameter $g_1 =$ (green), 2γ (red) and 3γ (yellow). While with the single QE-cavity system I decreases below 0.5 for $\kappa = \gamma$, the cascaded-cavities scheme can maintain $I > 0.5$ up to $\kappa_2 = 100\gamma$ when setting the right R_1 and R_2 values (i.e. setting the cavity mode volume, V_{eff} , and Q).

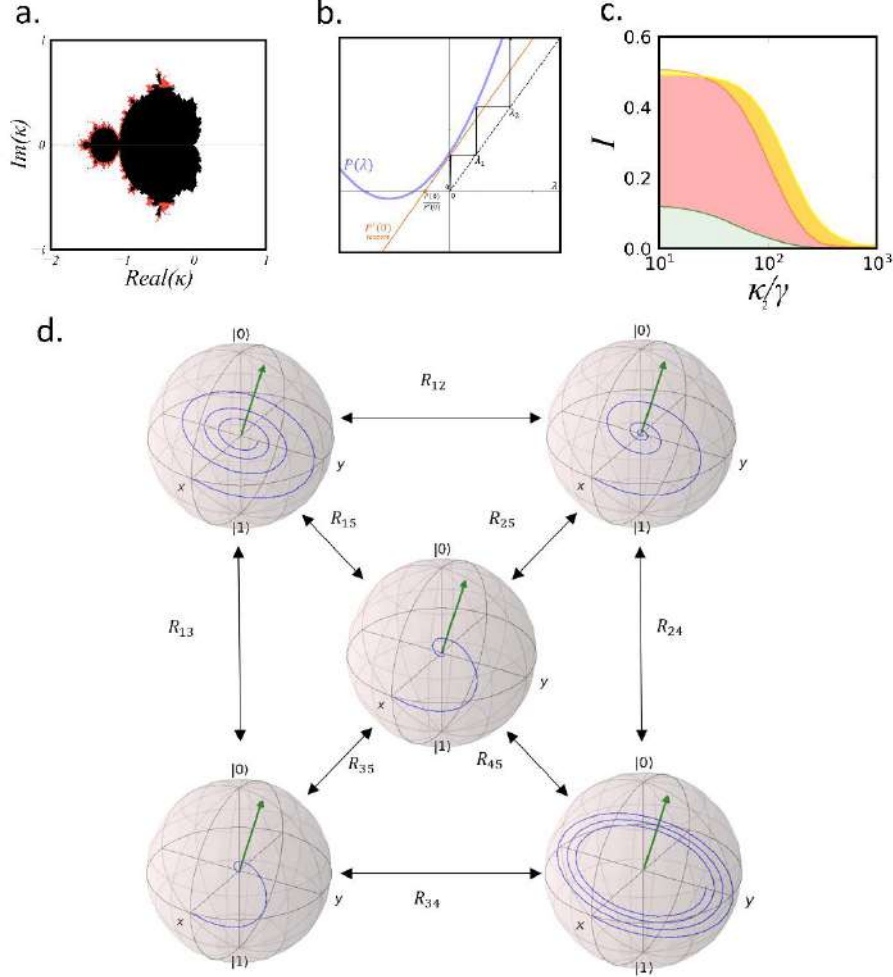


Figure 2. (a) κ -parameter space of the stability of rate equations of a single QE system coupled to a cavity. Black dots correspond to bounded points while the gradient colors represent the degree of stability. (b) Characteristic equation of (2) (blue line); tangent line with slope $P'(0)$. The cut of the tangent line with the x-axis is given by $\frac{P(0)}{P'(0)}$. The arrows indicate consecutive λ_n values of the iteration process. (c) Indistinguishability versus normalized κ_2 for $g_1 =$ (green), 2γ (red) and 3γ (yellow). (d) Bloch-spheres of the five-QE system with population rate transfers R_{ij} between each subsystem.

Therefore, adding more subsystems (emitters and/or cavities) provides additional paths to maintain the stability and, therefore, relax the cavity requirements for high I . Accordingly, we study now the case of a cluster of five QEs coupled to a single-mode cavity field. With this scheme, we have 10 transfer rates (R_{ij}) that can be tuned by setting the relative distances between the QEs, so we have enough parameters to perform a sufficiently complex optimization. Fig 2.d shows a layout of the system where each Bloch-sphere represents the time evolution of each QE_i, and each arrow represents the specific transfer rate between the QE_i and QE_j. Our aim now is to find the geometrical configuration of the QEs that provides the optimal set

of R_{ij} that keep high I for high κ values. This goal involves an optimization task with 10 degrees of freedom, which is a highly non-trivial problem and computationally very time-consuming. Nevertheless, similar optimization problems have been recently solved using machine-learning methods [28,47-50]. Employing a similar approach, we developed a machine-learning scheme based on a hybrid NN-GA algorithm which is able to solve the optimization problem in very short computational times providing the best geometrical configuration for the emitters.

Machine Learning optimization

We consider five QEs with γ^* randomly positioned in a 2D-grid. All of them are coupled to a single-mode cavity field with the same coupling constant g and cavity decay rate κ . Each relative distance d_{ij} ($i,j = 1,\dots,5$) between QEs leads to a dipolar interaction strength Ω_{ij} and modified decay rate γ_{ij} . Since this scheme requires solving a system of 144 coupled differential equations, we are not able to derive an analytic expression for I like in the 2-QE case. Instead, we numerically solve the Lindblad equation of the system and compute I via QRT. At each iteration we generate a vector ω with 5 random positions for the QEs and we calculate I via QRT for a fixed g and κ . The data set (ω, I) is then used to train the NN-GA algorithm which finds the optimal positions for maximum I for that g and κ . In Fig 3.a,b,c,d,e we report the obtained optimal geometries for $g = \gamma$ and $\kappa = 10\gamma, 50\gamma, 100\gamma, 500\gamma$ and 1000γ respectively. All these geometries provide perfect I ($I = 1$) with minimum distances $d_{ij} \sim 0.1\lambda$, a value compatible with experimental realizations [34-41]. Each geometry leads to the right transfer rates R_{ij} between the subsystems for keeping the stability at the specific rates g and κ . For a fixed geometry, small changes in g and κ drastically reduce I . This is displayed in Fig 3.f, which shows I versus normalized g/γ and κ/γ for the optimal geometry obtained for $g = \gamma, \kappa = 10\gamma$. The plot shows a small “bubble” of high I at the $(g/\gamma, \kappa/\gamma) = (1, 10)$ point, while in the neighbor regions of the bubble I reduces to 0. Fig 3.a,b,c,d,e also show the positioning tolerances for each QE for getting $I > 0.9$. The tolerances for the accuracy in the position depend on the specific QE and the (g, κ) values.

Within our scheme the realization of perfect I SPS with strong dissipative QEs is possible using well established photonic platforms. To verify this claim we performed 3D-FDTD simulations [51] of a point source placed at the antinode of a cavity-mode in a standard 2D-hexagonal SiN photonic crystal cavity (PCc). The V_{eff} and Q were obtained from the field profile (see Fig 3.g) and frequency analysis of the resonance. For a QE with $(\gamma, \gamma^*, \omega) = (160 \text{ MHz}, 400 \text{ GHz}, 400 \text{ THz})$ like color centers in diamond [52] we obtained $(g, \kappa) \approx (1, 100)$. The radius and distances between the holes of the PCc were set to 120 nm and 50 nm respectively, which is compatible with most fabrication techniques [53-55]. To highlight the benefits of our strategy we have contrasted the obtained performance with standard single-emitter-cavity systems [30] for different QEs at high T. Diamond color centers, InGaAs QDs, GaAs QDs and single molecules at 300 K has a pure dephasing of $1000\gamma, 600\gamma, 1450\gamma$ and $10^4\gamma$ respectively [52,20,21,56]. Considering the same standard PCc with $(g, \kappa) \approx (1, 100)$, a single-emitter-cavity system leads to $I \sim 0.01$ for all these emitters, whereas the 5-QEs optimized platform provides $I=1$. For these emitters, obtaining $I=1$ with a single-emitter-cavity at room T would require at least a cavity with Q above 4×10^7 , which is beyond the state of the art for most current fabrication technologies.

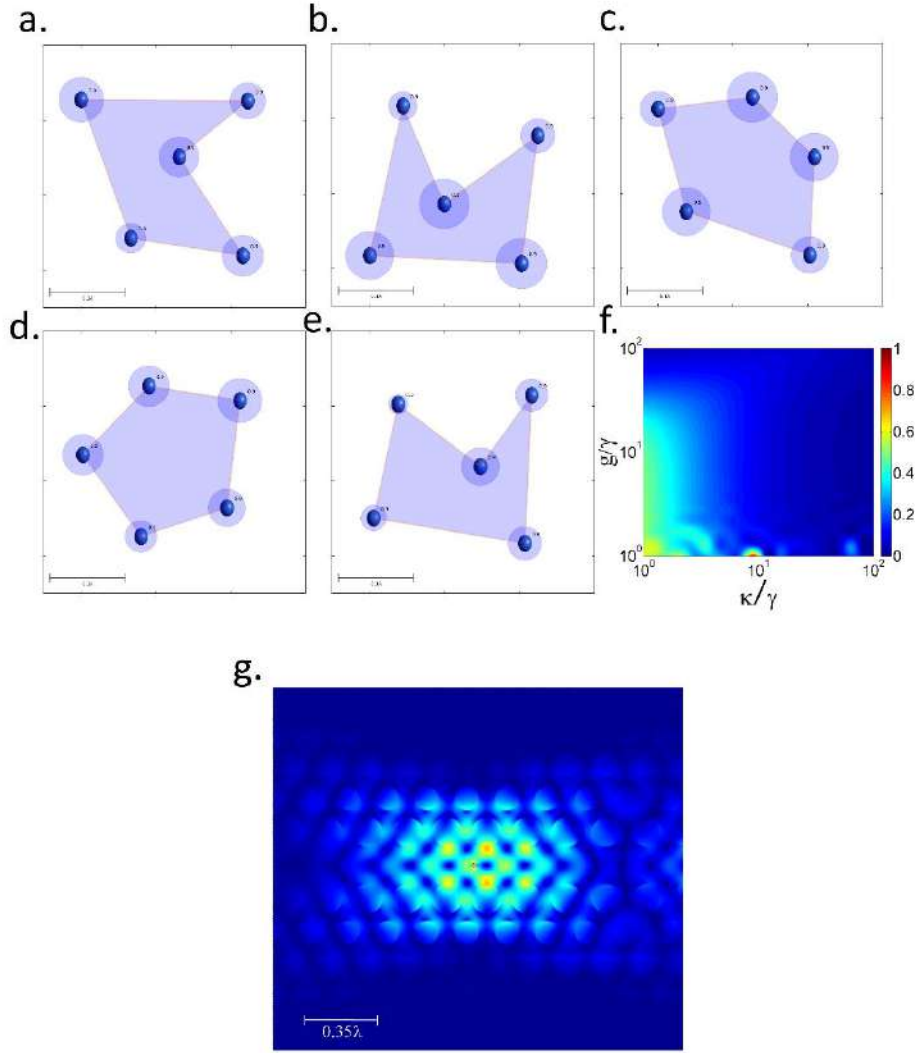


Figure 3. (a) Optimal configuration of the 5-QEs system in a 2D plane for (a) $\kappa = 10\gamma$, (b) $\kappa = 50\gamma$, (c) $\kappa = 100\gamma$, (d) $\kappa = 500\gamma$, (e) $\kappa = 1000\gamma$. The circles around each QE position corresponds to the positioning tolerance for having $I > 0.9$. (f) Indistinguishability versus normalized κ and g for the optimized system shown in (a). (g) Field profile $|E|^2$ of the hexagonal PC-cavity-mode with a point source placed at the antinode.

Discussion

A key point to evaluate for the experimental realization of our scheme is the nanoscale positioning approach for the deposition of the cluster of QDs. Novel positioning technologies have recently shown positioning accuracy at the nanometer level [57]. 30 nm positioning accuracy with GaAs QDs has been reported using atomic force microscopy [58]. Confocal micro-photoluminescence can provide 10 nm positioning accuracy also with GaAs QDs as it has been shown in [59]. 5 nm position accuracy has been achieved recently with Bi-chromatic photoluminescence through a new image analysis software implementation [60]. In-situ lithography approaches have also shown promising results improving its position accuracy down to 30 nm [61]. Pick-and-place approaches have shown 38 nm positioning accuracy for Si vacancy centers transference to aluminum nitride waveguides, achieving 98% coupling efficiency [62,63]. Therefore,

according to tolerances shown in Figure 3.b, for the case of point defects in diamond, using pick-and-place positioning we would have a standard deviation of 38 nm with a target of about 30 nm. This leads to 81% probability of successful deposition for a single QD. Successful deposition of the five QDs in place would have a probability of 32%. An experimental realization should require the fabrication of a large number of devices and checking for suitable candidates one by one. According to this, although our scheme could enable the experimental demonstration of certain quantum phenomena, it is still far from a high-scalable technology.

So far, we have explored the theoretical performance of our scheme considering identical QDs without detuning Δ between the emitters. However, a more realistic analysis involves the evaluation of the effect of mismatching between the emission frequencies of the QDs. With this aim, we have incorporated a statistical detuning distribution to the system of 5 QDs in the configuration shown in Figure 3.b. We consider a normal distribution setting the mean equal to 0 and standard deviation $\sigma_n = n\gamma$, as shown in Figure 4.a. The Δ of each QD is set randomly according to the normal distribution. We start with the distribution $\sigma_1 = \gamma$, we set five random Δ for the QDs and compute I . Then we reset the random Δ according to the same distribution and compute again I , repeating this process 200 times and computing the average of all obtained values of I . We obtained the average value of I for the 20 different probability distributions $\sigma_n = n\gamma$ with $n = 1 \dots 20$, as shown in Figure 4.b.

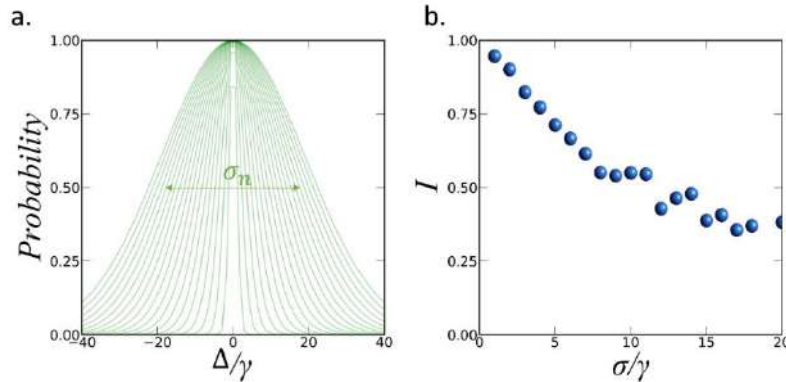


Figure 4. (a) Probability distributions with standard deviation σ_n for $n=1 \dots 20$ for the normalized detuning values Δ/γ . At each iteration we set a random Δ value for each QD according to the corresponding distribution. (b) Average value of the indistinguishability obtained for each of the 20 probability distributions.

As expected, the value of I reduces as the standard deviation of the distribution increases. For the distribution $\sigma_1 = \gamma$ the possible values for the Δ between the QDs range from -5γ to 5γ , leading to a negligible reduction of I . On the opposite side, with $\sigma_{20} = 20\gamma$ the possible values of Δ range from -60γ to 60γ , giving a reduction of I of about 70%. According to these results, our scheme is able to maintain high $I > 0.75$ for normal distributions of emitters with standard deviation below 5γ , which includes frequency mismatching between the QEs of about 20γ . Therefore, the proposed system is a relatively robust platform for distributions of non-identical QDs according to recent experimental demonstrations [64].

Conclusions

We have developed an analytical model for estimation of the indistinguishability with two-QE interfaces with dephasing integrated in optical cavities. The model provides an analytical expression that relates the indistinguishability to the distance between the QEs and the parameters of the cavity. Through an alternative interpretation of the indistinguishability, we can estimate the behavior of systems including more QEs. Finally, we performed a numerical optimization of a 5-QE system coupled to a single cavity by a machine learning scheme. The results predict perfect indistinguishability with strong dissipative QEs in arbitrary low Q cavities. The proposed method provides a strategy for the realization of a source of perfect indistinguishable single photons at room temperature. The strategy presents significant challenges from the perspective of QD positioning process. Although the required accuracy in positioning may be still far from a real scalable technology it can be suitable for experimental demonstration of single photon operation with high indistinguishability. The ML approach may provide insights for optimizing different photonic structures for quantum information applications, like the reduction of quantum decoherence in clusters of coupled two-level quantum systems.

Author Contributions: Conceptualization, J.G.; methodology, J.G.; software, J.G and L.S.; validation, P.A.P. and J.M.L.; formal analysis, J.G. and L.W.; investigation, J.G.; resources, P.A.P.; data curation, J.G.; writing—original draft preparation, J.G; writing—review and editing, J.G and P.A.P.; supervision, P.A.P.; project administration, P.A.P.; funding acquisition, P.A.P. All authors have read and agreed to the published version of the manuscript.

Funding: European Union's Horizon 2020 research and innovation program under grant agreement No. 820423 (S2QUIP) and CSIC Quantum Technology Platform PT-001y Agencia Estatal de Investigación (AEI) grant PID2019-106088RB-C31.

Data Availability Statement: Data underlying the results of this paper are available from the corresponding author upon request.

Acknowledgments: We gratefully acknowledge financial support from the European Union's Horizon 2020 research and innovation program under grant agreement No. 820423 (S2QUIP) and CSIC Quantum Technology Platform PT-001y Agencia Estatal de Investigación (AEI) grant PID2019-106088RB-C31. We also thanks Dr. Ian Shlesinger for his contribution in the development of this work.

Conflicts of Interest: The authors declare no conflict of interest

References

- [1] Monroe, C., Meekhof, D. M., King, B. E., Itano, W. M., & Wineland, D. J. (1995). Demonstration of a fundamental quantum logic gate. *Physical review letters*, 75(25), 4714.
- [2] Makhlin, Y., Scöhn, G., & Shnirman, A. (1999). Josephson-junction qubits with controlled couplings. *nature*, 398(6725), 305-307.

- [3] Politi, A., Cryan, M. J., Rarity, J. G., Yu, S., & O'Brien, J. L. (2008). Silica-on-silicon waveguide quantum circuits. *Science*, 320(5876), 646-649.
- [4] Bunandar, D., Lentine, A., Lee, C., Cai, H., Long, C. M., Boynton, N., ... & Englund, D. (2018). Metropolitan quantum key distribution with silicon photonics. *Physical Review X*, 8(2), 021009.
- [5] Lago-Rivera, D., Grandi, S., Rakonjac, J. V., Seri, A., & de Riedmatten, H. (2021). Telecom-heralded entanglement between multimode solid-state quantum memories. *Nature*, 594(7861), 37-40.
- [6] Zhong, H. S., Wang, H., Deng, Y. H., Chen, M. C., Peng, L. C., Luo, Y. H., ... & Pan, J. W. (2020). Quantum computational advantage using photons. *Science*, 370(6523), 1460-1463.
- [7] Peruzzo, A., McClean, J., Shadbolt, P., Yung, M. H., Zhou, X. Q., Love, P. J., ... & O'Brien, J. L. (2014). A variational eigenvalue solver on a photonic quantum processor. *Nature communications*, 5(1), 1-7.
- [8] Acosta, V. M., Bauch, E., Ledbetter, M. P., Santori, C., Fu, K. M., Barclay, P. E., ... & Budker, D. (2009). Diamonds with a high density of nitrogen-vacancy centers for magnetometry applications. *Physical Review B*, 80(11), 115202.
- [9] Pelucchi, E., Fagas, G., Aharonovich, I., Englund, D., Figueira, E., Gong, Q., ... & Jöns, K. D. (2022). The potential and global outlook of integrated photonics for quantum technologies. *Nature Reviews Physics*, 4(3), 194-208.
- [10] Zhang, H., Zhang, H. F., Liu, G. B., & Li, H. M. (2019). Ultra-broadband multilayer absorber with the lumped resistors and solid-state plasma. *Results in Physics*, 12, 917-924.
- [11] Cheben, P., Halir, R., Schmid, J. H., Atwater, H. A., & Smith, D. R. (2018). Subwavelength integrated photonics. *Nature*, 560(7720), 565-572.
- [12] Zhang, Y., Wang, Z., Su, Y., Zheng, Y., Tang, W., Yang, C., ... & Zhao, Y. (2021). Simple vanilla derivatives for long-lived room-temperature polymer phosphorescence as invisible security inks. *Research*, 2021.
- [13] Wu, S., Xia, H., Xu, J., Sun, X., & Liu, X. (2018). Manipulating luminescence of light emitters by photonic crystals. *Advanced Materials*, 30(47), 1803362.
- [14] Juska, G., Dimastrodonato, V., Mereni, L. O., Gocalinska, A., & Pelucchi, E. (2013). Towards quantum-dot arrays of entangled photon emitters. *Nature Photonics*, 7(7), 527-531.
- [15] Gérard, J. M., Sermage, B., Gayral, B., Legrand, B., Costard, E., & Thierry-Mieg, V. (1998). Enhanced spontaneous emission by quantum boxes in a monolithic optical microcavity. *Physical review letters*, 81(5), 1110.
- [16] Hennessy, K., Badolato, A., Winger, M., Gerace, D., Atatüre, M., Gulde, S., ... & Imamoglu, A. (2007). Quantum nature of a strongly coupled single quantum dot–cavity system. *Nature*, 445(7130), 896-899.
- [17] Wang, H., Duan, Z. C., Li, Y. H., Chen, S., Li, J. P., He, Y. M., ... & Pan, J. W. (2016). Near-transform-limited single photons from an efficient solid-state quantum emitter. *Physical Review Letters*, 116(21), 213601.

- [18] He, Y. M., He, Y., Wei, Y. J., Wu, D., Atatüre, M., Schneider, C., ... & Pan, J. W. (2013). On-demand semiconductor single-photon source with near-unity indistinguishability. *Nature nanotechnology*, 8(3), 213-217.
- [19] Somaschi, N., Giesz, V., De Santis, L., Loredo, J. C., Almeida, M. P., Hornecker, G., ... & Senellart, P. (2016). Near-optimal single-photon sources in the solid state. *Nature Photonics*, 10(5), 340-345.
- [20] Borri, P., Langbein, W., Schneider, S., Woggon, U., Sellin, R. L., Ouyang, D., & Bimberg, D. (2001). Ultralong dephasing time in InGaAs quantum dots. *Physical Review Letters*, 87(15), 157401.
- [21] Bayer, M., & Forchel, A. (2002). Temperature dependence of the exciton homogeneous linewidth in In 0.60 Ga 0.40 As/GaAs self-assembled quantum dots. *Physical Review B*, 65(4), 041308.
- [22] Berthelot, A., Favero, I., Cassabois, G., Voisin, C., Delalande, C., Roussignol, P., ... & Gérard, J. M. (2006). Unconventional motional narrowing in the optical spectrum of a semiconductor quantum dot. *Nature Physics*, 2(11), 759-764.
- [23] Mirin, R. P. (2004). Photon antibunching at high temperature from a single InGaAs/GaAs quantum dot. *Applied physics letters*, 84(8), 1260-1262.
- [24] Dusanowski, Ł., Syperek, M., Misiewicz, J., Somers, A., Hoefling, S., Kamp, M., ... & Sek, G. (2016). Single-photon emission of InAs/InP quantum dashes at $1.55 \mu m$ and temperatures up to 80 K. *Applied Physics Letters*, 108(16), 163108.
- [25] Yu, P., Li, Z., Wu, T., Wang, Y. T., Tong, X., Li, C. F., ... & Wang, Z. M. (2019). Nanowire quantum dot surface engineering for high temperature single photon emission. *ACS nano*, 13(11), 13492-13500.
- [26] Arakawa, Y., & Holmes, M. J. (2020). Progress in quantum-dot single photon sources for quantum information technologies: A broad spectrum overview. *Applied Physics Reviews*, 7(2), 021309.
- [27] Bylander, J., Robert-Philip, I., & Abram, I. (2003). Interference and correlation of two independent photons. *The European Physical Journal D-Atomic, Molecular, Optical and Plasma Physics*, 22(2), 295-301.
- [28] Guimba, J., Sanchis, L., Weituschat, L., Manuel Llorens, J., Song, M., Cardenas, J., & Aitor Postigo, P. (2022). Numerical Optimization of a Nanophotonic Cavity by Machine Learning for Near-Unity Photon Indistinguishability at Room Temperature. *ACS Photonics*.
- [29] Guimba, J., Weituschat, L. M., Montolio, J. L., & Postigo, P. A. (2021). Enhancement of the indistinguishability of single photon emitters coupled to photonic waveguides. *Optics Express*, 29(14), 21160-21173.
- [30] Grange, T., Hornecker, G., Hunger, D., Poizat, J. P., Gérard, J. M., Senellart, P., & Auffèves, A. (2015). Cavity-funneled generation of indistinguishable single photons from strongly dissipative quantum emitters. *Physical review letters*, 114(19), 193601.
- [31] Choi, H., Zhu, D., Yoon, Y., & Englund, D. (2019). Cascaded cavities boost the indistinguishability of imperfect quantum emitters. *Physical review letters*, 122(18), 183602.

- [32] Saxena, A., Chen, Y., Ryou, A., Sevilla, C. G., Xu, P., & Majumdar, A. (2019). Improving indistinguishability of single photons from colloidal quantum dots using nanocavities. *ACS Photonics*, 6(12), 3166-3173.
- [33] Ota, Y., Iwamoto, S., Kumagai, N., & Arakawa, Y. (2011). Spontaneous two-photon emission from a single quantum dot. *Physical review letters*, 107(23), 233602.
- [34] Shlesinger, I., Senellart, P., Lanco, L., & Greffet, J. J. (2021). Time-frequency encoded single-photon generation and broadband single-photon storage with a tunable subradiant state. *Optica*, 8(1), 95-105.
- [35] Shlesinger, I., Senellart, P., Lanco, L., & Greffet, J. J. (2018). Tunable bandwidth and nonlinearities in an atom-photon interface with subradiant states. *Physical Review A*, 98(1), 013813.
- [36] Schilder, N. J., Sauvan, C., Sortais, Y. R. P., Browaeys, A., & Greffet, J. J. (2020). Near-resonant light scattering by a subwavelength ensemble of identical atoms. *Physical review letters*, 124(7), 073403.
- [37] Ficek, Z., Tanas, R., & Kielich, S. (1986). Cooperative effects in the spontaneous emission from two non-identical atoms. *Optica Acta*, 33(9), 1149-1160.
- [38] Lehmberg, R. H. (1970). Radiation from an N-atom system. I. General formalism. *Physical Review A*, 2(3), 883.
- [39] Hettich, C., Schmitt, C., Zitzmann, J., Kühn, S., Gerhardt, I., & Sandoghdar, V. (2002). Nanometer resolution and coherent optical dipole coupling of two individual molecules. *Science*, 298(5592), 385-389.
- [40] ogl, T., Campbell, G., Buchler, B. C., Lu, Y., & Lam, P. K. (2018). Fabrication and deterministic transfer of high-quality quantum emitters in hexagonal boron nitride. *ACS Photonics*, 5(6), 2305-2312.
- [41] Schröder, T., Trusheim, M. E., Walsh, M., Li, L., Zheng, J., Schukraft, M., ... & Englund, D. (2017). Scalable focused ion beam creation of nearly lifetime-limited single quantum emitters in diamond nanostructures. *Nature communications*, 8(1), 1-7.
- [42] Hail, C. U., Höller, C., Matsuzaki, K., Rohner, P., Renger, J., Sandoghdar, V., ... & Eghlidi, H. (2019). Nanoprinting organic molecules at the quantum level. *Nature communications*, 10(1), 1-8.
- [43] Bayer, M., Hawrylak, P., Hinzer, K., Fafard, S., Korkusinski, M., Wasilewski, Z. R., ... & Forchel, A. (2001). Coupling and entangling of quantum states in quantum dot molecules. *Science*, 291(5503), 451-453.
- [44] Kim, H., Kyhm, K., Taylor, R. A., Kim, J. S., Song, J. D., & Park, S. (2020). Optical shaping of the polarization anisotropy in a laterally coupled quantum dot dimer. *Light: Science & Applications*, 9(1), 1-10.
- [45] Takagahara, T. (2002). Excitonic Structures and Optical Properties of Quantum Dots. *Semiconductor Quantum Dots*, 59-114.
- [46] Senellart, P., Solomon, G., & White, A. (2017). High-performance semiconductor quantum-dot single-photon sources. *Nature nanotechnology*, 12(11), 1026-1039.

- [47] Sanchis, L., Cryan, M. J., Pozo, J., Craddock, I. J., & Rarity, J. G. (2007). Ultrahigh Purcell factor in photonic crystal slab microcavities. *Physical Review B*, 76(4), 045118.
- [48] Sanchis, L., Håkansson, A., López-Zanón, D., Bravo-Abad, J., & Sánchez-Dehesa, J. (2004). Integrated optical devices design by genetic algorithm. *Applied Physics Letters*, 84(22), 4460-4462.
- [49] Morgado-León, A., Escuín, A., Guerrero, E., Yáñez, A., Galindo, P. L., & Sanchis, L. (2011, June). Genetic algorithms applied to the design of 3D photonic crystals. In *International Work-Conference on Artificial Neural Networks* (pp. 291-298). Springer, Berlin, Heidelberg.
- [50] Marques-Hueso, J., Sanchis, L., Cluzel, B., de Fornel, F., & Martínez-Pastor, J. P. (2010). Genetic algorithm designed silicon integrated photonic lens operating at 1550 nm. *Applied Physics Letters*, 97(7), 071115.
- [51] Lumerical Inc.
- [52] Neu, E., Hepp, C., Hauschild, M., Gsell, S., Fischer, M., Sternschulte, H., ... & Becher, C. (2013). Low-temperature investigations of single silicon vacancy colour centres in diamond. *New Journal of Physics*, 15(4), 043005.
- [53] Englund, D., Faraon, A., Zhang, B., Yamamoto, Y., & Vučković, J. (2007). Generation and transfer of single photons on a photonic crystal chip. *Optics Express*, 15(9), 5550-5558.
- [54] Chang, W. H., Chen, W. Y., Chang, H. S., Hsieh, T. P., Chyi, J. I., & Hsu, T. M. (2006). Efficient single-photon sources based on low-density quantum dots in photonic-crystal nanocavities. *Physical review letters*, 96(11), 117401.
- [55] Clark, A. S., Husko, C., Collins, M. J., Lehoucq, G., Xavier, S., De Rossi, A., ... & Eggleton, B. J. (2013). Heralded single-photon source in a III-V photonic crystal. *Optics letters*, 38(5), 649-651.
- [56] Huang, L.; Krasnok, A.; Alu, A.; Yu, Y.; Neshev, D.; Miroshnichenko, A. Enhanced Light-Matter Interaction in TwoDimensional Transition Metal Dichalcogenides. *Rep. Prog. Phys.* 2022, 85, No. 046401Liu, S., Srinivasan, K., & Liu, J. (2021). Nanoscale Positioning Approaches for Integrating Single Solid-State Quantum Emitters with Photonic Nanostructures. *Laser & Photonics Reviews*, 15(10), 2100223.
- [57] Liu, S., Srinivasan, K., & Liu, J. (2021). Nanoscale Positioning Approaches for Integrating Single Solid-State Quantum Emitters with Photonic Nanostructures. *Laser & Photonics Reviews*, 15(10), 2100223.
- [58] K. Hennessy, A. Badolato, M. Winger, D. Gerace, M. Atatürke, S. Gulde, S. Fält, E. L. Hu, A. Imamoglu, *Nature* 2007, 445, 7130 896.
- [59] S. M. Thon, M. T. Rakher, H. Kim, J. Gudat, W. T. M. Irvine, P. M. Petroff, D. Bouwmeester, *Appl. Phys. Lett.* 2009, 94, 11 1.
- [60] J. Liu, M. I. Davanco, L. Sapienza, K. Konthasinghe, J. V. De Miranda Cardoso, J. D. Song, A. Badolato, K. Srinivasan, *Rev. Sci. Instrum.* 2017, 88, 023116.

- [61] M. Gschrey, R. Schmidt, J.-H. Schulze, A. Strittmatter, S. Rodt, S. Reitzenstein, *J. Vac. Sci. Technol. B* 2015, 33, 2 021603.
- [62] Elshaari, A. W., Pernice, W., Srinivasan, K., Benson, O., & Zwiller, V. (2020). Hybrid integrated quantum photonic circuits. *Nature photonics*, 14(5), 285-298.
- [63] Wan, N. H. et al. Large-scale integration of near-indistinguishable artificial atoms in hybrid photonic circuits. Preprint at <https://arxiv.org/abs/1911.05265> (2019).
- [64] Arakawa, Y., & Holmes, M. J. (2020). Progress in quantum-dot single photon sources for quantum information technologies: A broad spectrum overview. *Applied Physics Reviews*, 7(2), 021309.

Capítulo 3. Resultados

A continuación se muestra una exposición resumida de los resultados y conclusiones extraídos de los tres trabajos compendiados en esta tesis. Es conveniente resaltar que, habiendo sido descritos previamente en el Capítulo 2, tanto la metodología como la interpretación de datos que fundamentan esta discusión de resultados no se encuentran presentes en las siguientes secciones, que exclusivamente recogen de forma ordenada sus aspectos más fundamentales. Tal y como se describe en el Capítulo 1, la estructura de esta tesis se basa en la aplicación de la metodología teórica desarrollada a tres casos prácticos de integración de EC en plataformas fotónicas ordenados de menor a mayor complejidad: (i) EC integrados en guías de onda; (ii) EC integrados en cavidades ópticas; (iii) Clústeres de EC integrados en cavidades ópticas. De esta forma, cada una de las subsecciones del Capítulo 3 se focaliza independientemente en la discusión de resultados de cada caso por separado.

Emisores acoplados a guías de onda

En este trabajo se llevó a cabo la derivación de la diádica de Green de una guía rectangular infinita 3D en un entorno homogéneo no-acotado. Para ello se realizó una generalización de la teoría de transformadas desarrollada previamente en [109] para el caso 2D, permitiendo obtener por primera vez una representación explícita del campo generado por una fuente puntual 3D en un entorno dieléctrico con contornos no-acotados. Las expresiones obtenidas permiten la separación de las energías de campos emitidos entre cada uno de los modos guiados y no-guiados, y describen la dependencia con los parámetros geométricos de la guía y la posición y orientación de la fuente. En contraposición a otros trabajos previos basados en el formalismo del vector de Hertz [110], la representación de la fuente puntual a partir de la diádica de Green permite introducir los efectos de campo cercano en el modelo, lo que resulta de especial utilidad para la descripción de EC integrados en guías de onda, donde la separación entre la fuente y la guía se encuentra en el rango de nanómetros. A partir de las soluciones del modelo es posible extraer ecuaciones que relacionan directamente los parámetros de ancho de guía (a), espesor (b), índice de refracción (n_1), posición de la fuente (x_0, y_0), orientación de la fuente, γ , y γ^* con las figuras de mérito de factor de Purcell (P_f), β e I . Estas herramientas facilitan la interpretación física del efecto de los parámetros de diseño en los mecanismos de decoherencia cuántica de EC integrados en guías de onda.

El modelo analítico considera una fuente puntual 3D con posición y orientación arbitrarias en una guía rectangular infinita de índice n_1 , anchura a y espesor b en un entorno homogéneo no-acotado de índice n_2 (ver Figura 1). De esta forma los elementos diagonales de la diádica del vector potencial \vec{G}_A vienen dados por la siguiente ecuación:

$$\nabla^2 G_{Avv}(\mathbf{r}, \mathbf{r}') + n(x, y) k^2 G_{Avv}(\mathbf{r}, \mathbf{r}') = -\delta(\mathbf{r} - \mathbf{r}') \quad (1)$$

Donde la fuente puntual viene representada por la delta $\delta(\mathbf{r} - \mathbf{r}')$. Mediante el desarrollo de una teoría de transformadas basado en [109], se pudo realizar una expansión parcial de \vec{G}_A en el espacio completo de soluciones guiadas y no-guiadas $v_j^\nu(x, y, \lambda)$ de la ecuación de Helmholtz homogénea asociada a (1), obteniendo las siguientes expresiones para las componentes de radiación libre G_{Avv}^{rad} y radiación guiada G_{Avv}^g :

$$G_{Avv}^{rad}(x, y, z, \mathbf{x}_0, \mathbf{y}_0, \mathbf{z}_0) = \sum_{j \in \{s, a\}} \int_{d^2}^{\infty} \frac{e^{i|z-z_0|\sqrt{k^2 n_1^2 - \lambda}}}{2i\sqrt{k^2 n_1^2 - \lambda}} v_j^\nu(x, y, \lambda) v_j^\nu(\mathbf{x}_0, \mathbf{y}_0, \mathbf{z}_0) \frac{\sigma_j^\nu(\lambda)}{\sqrt{\lambda - d^2}} d\lambda \quad (2)$$

$$G_{Avv}^g(x, y, z, \mathbf{x}_0, \mathbf{y}_0, \mathbf{z}_0) = \sum_{j \in \{s, a\}} \sum_{m=0} \sum_{n=0} \frac{e^{i|z-z_0|\sqrt{k^2 n_1^2 - \lambda}}}{2i\sqrt{k^2 n_1^2 - \lambda}} v_j^\nu(x, y, \lambda_{mn}^j) v_j^\nu(\mathbf{x}_0, \mathbf{y}_0, \lambda_{mn}) \quad (3)$$

$$r_{mn}^{j\nu} = \left[\iint_{-\infty}^{+\infty} v_j^\nu(x, y, \lambda_{mn})^2 dx dy \right]^{-1} = \frac{\sqrt{d^2 - \lambda_{mn}^j}}{\sqrt{d^2 - \lambda_{mn}^j} \int_{-a}^a \int_{-b}^b \phi_{mn}^{j\nu} dx dy + \phi_{mn}^{j\nu}(a, b)^2} \quad (4)$$

$$\sigma_j^\nu(\lambda) = \frac{\lambda - d^2}{(\lambda - d^2) \phi_j^\nu(a, b, \lambda)^2 + \phi_j^{\nu'}(a, b, \lambda)^2} \quad (5)$$

Donde λ la longitud de onda del emisor, m y n los órdenes de los modos guiados, k la constante de propagación del modo y $d = k^2(n_1^2 - n_2^2)$. Los índices s y a indican la simetría o antisimetría del modo respectivamente.

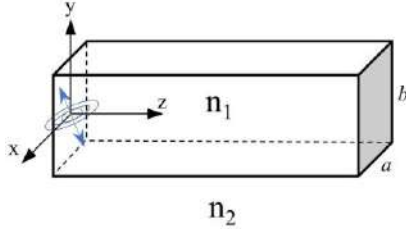


Figura 1. Esquema de una fuente puntual 3D en una guía de onda rectangular infinita de índice n_1 , anchura a y espesor b en un entorno homogéneo no-acotado de índice n_2 .

A partir de (2) y (3) se pueden obtener las expresiones para los campos eléctricos y magnéticos emitidos por la fuente de acuerdo con [111]:

$$\vec{G}_e(\mathbf{r}, \mathbf{r}') = (\vec{I} + \frac{1}{k^2} \nabla \nabla) \cdot \vec{G}_A(\mathbf{r}, \mathbf{r}') \quad (6)$$

$$\vec{G}_m(\mathbf{r}, \mathbf{r}') = \nabla \times \vec{G}_A(\mathbf{r}, \mathbf{r}') \quad (7)$$

Las expresiones obtenidas fueron validadas a partir de simulaciones computacionales FDTD mostrando una correspondencia perfecta entre los campos derivados del modelo teórico y los obtenidos por integración numérica de las ecuaciones de Maxwell. Tomando la componente z del vector de Pointing, integrando sobre la sección transversal de la guía de onda y normalizando con respecto a la potencia emitida por la fuente en un entorno homogéneo, extraemos el valor de β . Por otro lado, el P_f puede obtenerse a partir de la relación entre la modificación de γ y la componente imaginaria de \vec{G}_e [111]:

$$P_f = \frac{4\omega^2}{\pi c^2 \hbar \epsilon_0} [\vec{\mu} \cdot \text{Im}\{\vec{G}(r_0, r_0)\} \cdot \vec{\mu}] \quad (8)$$

Donde ω es la frecuencia de emisión de la fuente, ϵ_0 la constante dieléctrica en el vacío, c la velocidad de la luz, \hbar la constante de Planck reducida y $\vec{\mu}$ el momento dipolar eléctrico de la fuente. Del mismo modo, el valor de I vendrá dado por su relación con la modificación de γ :

$$I = \frac{(1+P_f)}{(1+P_f)+\frac{\gamma^*}{\gamma_0}} \quad (9)$$

Donde γ_0 indica el ratio de decaimiento espontáneo del emisor en un entorno homogéneo.

A partir del comportamiento de (2) y (3) en función de los parámetros normalizados a/λ , b/λ , x_0/λ e y_0/λ podemos extraer información de cómo se modifican las figuras de mérito en función del diseño de la guía y de posición y orientación relativas del EC. Como ejemplo ilustrativo fijaremos un espesor $b = 200$ nm y $n_2 = 1$ y analizamos la dependencia de P_f con la anchura normalizada de la guía a/λ para el caso de un EC integrado en el centro del núcleo ($x_0 = 0$, $y_0 = 0$) con orientación en el eje x . Para n_1 utilizaremos valores típicos de materiales utilizados en plataformas para guías de onda (SiO₂: $n_1 = 1.44$; SiN: $n_1 = 2$; Si: $n_1 = 3.4$). En general, con independencia de n_1 , P_f se mantiene nulo hasta que a/λ alcanza el umbral de activación modo fundamental TE₁₀, cuyo valor crece con n_1 desde $a/\lambda = 0.05$ para $n_1 = 1.44$ hasta $a/\lambda = 0.13$ para $n_1 = 3.4$. A partir de este valor umbral, P_f se incrementa monótonamente con a/λ conforme k disminuye y el modo mejora la calidad de su confinamiento. El incremento de P_f alcanza un máximo en el punto de a/λ de óptimo confinamiento del modo, cuyo valor también crece con n_1 . Para valores de ancho de guía superiores a este valor de a/λ de confinamiento óptimo el modo se extiende a lo largo de la sección transversal de la guía disminuyendo el valor de intensidad máxima situado en la posición del EC. Como consecuencia, a partir de este punto la fuerza de acoplamiento disminuye produciendo un decaimiento de P_f con a/λ a escala de $1/a$. Este decaimiento se prolonga hasta que a/λ alcanza el valor umbral de activación del modo de segundo orden. A partir de aquí el comportamiento de P_f repite el mismo patrón creciendo monótonamente hasta alcanzar un máximo en el punto de a/λ de óptimo confinamiento para el modo de segundo orden, seguido de un decaimiento asintótico conforme el modo se expande. Este proceso se repite indefinidamente conforme se van alcanzando las anchuras umbrales de activación de los subsecuentes modos. Los valores máximos obtenidos para P_f con el modo fundamental crecen con n_1 desde $P_f = 0.83$ para $n_1 = 1.44$ hasta $P_f = 1$ para $n_1 = 3.4$. Así, para el caso de EC enterrados en el interior del núcleo de la guía, la calidad del confinamiento del modo y el overlap del momento dipolar del EC con el modo son ingredientes esenciales, tal y como cabría esperar. De acuerdo con (9), la I mostrará máximos para los mismos valores de ancho de guía con confinamiento óptimo.

Por otro lado, el sistema muestra un comportamiento más interesante para el caso del EC posicionado en el exterior del núcleo de la guía en las proximidades de su eje, situación que se reproduce en la integración heterogénea de emisores en CPIs. Debido al contraste de índices n_1 - n_2 el campo eléctrico muestra una fuerte discontinuidad en la superficie de contacto entre los dos medios. Esta discontinuidad es proporcional al cuadrado del cociente entre índices $(\frac{n_1}{n_2})^2$. Este efecto da lugar a una alteración drástica del perfil del

modo en las regiones cercanas al eje de la guía que se traduce en un incremento significativo de P_f . Cuando el emisor se encuentra posicionado próximo al eje de la guía los valores máximos de P_f crecen con n_l desde $P_f = 1.9$ para $n_l = 1.44$ hasta $P_f = 4.2$ para $n_l = 3.4$. El coste de este incremento es una reducción de β , cuya valor también cambia con n_l desde $P_f = 0.15$ para $n_l = 1.44$ hasta $P_f = 0.5$ para $n_l = 3.4$. Dado que P_f depende estrictamente del valor de intensidad de campo en la posición de la fuente, su valor máximo se alcanza en esta región de máxima discontinuidad próxima al eje de la guía. Por el contrario, β es proporcional al ratio cociente entre el valor de intensidad del modo guiado y los modos no guiados. A pesar de que en esta región próxima al eje el modo guiado muestra su valor de intensidad máximo, la intensidad de los modos no guiados es también máxima para posiciones fuera del núcleo de la guía. Como consecuencia β es significativamente más débil en esta región en comparación que con el emisor integrado en el interior del núcleo.

Tomando estas conclusiones podemos llevar a la optimización de la anchura y espesor de una guía con un EC integrado heterogéneamente posicionado en el exterior del núcleo de la guía en las proximidades del eje. A partir de un barrido de los parámetros a/λ y b/λ observamos que el P_f alcanza valores máximos en el rango en que a y b han alcanzado el valor umbral de activación del modo fundamental, pero el confinamiento no ha llegado a su valor óptimo. Para estas geometrías el modo fundamental no se encuentra perfectamente confinado en el interior del núcleo y el campo se acumula en los ejes de la guía, produciendo un overlap más eficiente con el emisor. Los valores máximos alcanzados de P_f crecen con n_l desde $P_f = 2$ para $n_l = 1.44$ hasta $P_f = 8$ para $n_l = 3.4$. En esta situación, la orientación del dipolo eléctrico del emisor juega un papel más relevante, pudiendo diferenciar dos configuraciones: (i) Orientado paralelamente al eje con el parámetro más largo de la guía (x si $a > b$, y si $a < b$). En este caso los valores de P_f se corresponden con los máximos descritos anteriormente; (ii) Orientado perpendicularmente al eje con el parámetro más largo de la guía. Para esta configuración los máximos de P_f se reducen hasta $P_f = 0.9$ para $n_l = 1.44$ hasta $P_f = 7.1$ para $n_l = 3$. Para emisores con orientaciones en combinaciones lineales de estos dos ejes, podemos descomponer la proyección en cada uno de los dos ejes y tratar al emisor como dos emisores independientes cada uno con su correspondiente contribución. El valor de P_f total vendrá dado por la suma de estas dos contribuciones.

Los valores máximos de P_f obtenidos pueden utilizarse en (9) para la estimación del rendimiento de la plataforma en términos de los valores de I . Los resultados muestran que para emisores poco disipativos con valores de γ^* del orden de γ , como QDs basados en GaAs débilmente confinados [112], el valor de I alcanza un valor de 0.8 para $n_l = 4$ con el emisor orientado en la posición óptima. Para emisores con γ^* del orden de $2.6 \cdot \gamma$, como QDs InAs [113,114] se obtiene un valor de $I = 0.6$. A medida que el valor de γ^* aumenta la I decrece asintóticamente reduciéndose a 0.2 con γ^* del orden de $50 \cdot \gamma$. De esta forma, para emisores fuertemente disipativos con $\gamma^* > 50 \cdot \gamma$, como emisores basados en defectos en materiales 2D [115], el efecto de la guía de onda en la I se hace despreciable.

Como conclusión, las predicciones del modelo indican que la maximización de I requiere de la integración heterogénea el emisor lo más próximo posible al eje de la guía, con unos parámetros de anchura y espesor

en el rango entre la activación del modo fundamental y la maximización del confinamiento en el núcleo. En contraposición, la maximización de β requiere de la integración monolítica en el centro del núcleo de la guía con los parámetros de anchura y espesor ajustados a los valores de máximo confinamiento del modo fundamental. Por otro lado, Para emisores fuertemente disipativos con $\gamma^* > 50 \cdot \gamma$ los efectos de la guía sobre el valor de I son negligibles mientras que para emisores con γ^* comparable a γ la I puede incrementarse hasta un 30% alcanzando valores de 0.8 con materiales para el núcleo de la guía con valores de índice de refracción alto.

Emisores acoplados a cavidades ópticas

En este trabajo se demuestra un ejemplo de aplicación de un modelo teórico híbrido clásico-cuántico integrado en el algoritmo de aprendizaje automático de un esquema Machine Learning basado en redes neuronales profundas (RNP) en cooperación con algoritmos genéticos (AG). El modelo teórico describe la dinámica de EC acoplados a cavidades ópticas para la estimación de I a través de la combinación de simulaciones clásicas FDTD de los campos electromagnéticos presentes en la cavidad con la resolución numérica de la ecuación de Lindblad para el sistema cuántico abierto del EC acoplado a estos campos y a diferentes reservorios. Este modelo se implementó en el proceso de entrenamiento de una RNP que aprendió a estimar el valor de I a partir de los parámetros del diseño de la cavidad. A través del esquema cooperativo entre la RNP entrenada y un AG se llevó a cabo la optimización del diseño de la cavidad óptica para la maximización simultánea de I y β con EC fuertemente disipativos (i.e. $\gamma^* = 10^4 \cdot \gamma$). Los resultados demuestran la posibilidad de alcanzar valores de I y β cercanos a la unidad con emisores integrados a temperatura ambiente con especificaciones de diseño asequibles en el contexto del estado del arte de las tecnologías de fabricación y deposición de EC.

Como punto de partida tomamos una de las estrategias de diseño más extendidas para la maximización de I en EC acoplados a cavidades ópticas: maximización del acople g por medio del confinamiento del modo óptico en una cavidad de V_{eff} ultra-pequeño, trasladando la dinámica del sistema al régimen de acoplamiento-fuerte ($g > \gamma + \gamma^*$). En este régimen el ratio de transferencia de fotones entre el EC y el modo de la cavidad (R) supera a γ^* para ciertos valores de κ [56]. La condición para alta I en esta situación implica que los fotones emitidos escapen de la cavidad antes de ser reabsorbidos por el EC y se vean afectados por γ^* , lo que implica la necesidad de ajustar κ . En otras palabras, para obtener alta I en una cavidad con V_{eff} ultra-pequeño, se ha de ajustar el parámetro κ a un rango de valores que depende del valor específico de g alcanzado con ese V_{eff} y de los parámetros del EC γ y γ^* . Es conveniente recordar que el ajuste del parámetro κ se traduce en el ajuste del factor de calidad Q de la cavidad, ya que $Q \sim 1/\kappa$. En primer lugar, se realizó un estudio bibliográfico en donde se recogieron los valores de V_{eff} y Q de diferentes propuestas de cavidades para FFI y se evaluó su rendimiento en términos de I introduciendo estos parámetros en nuestro modelo. Como conclusión se determinó que ninguna de las estrategias de diseño evaluadas resulta en unos valores suficientes para alcanzar alta I con EC de alto γ^* . Sin embargo, se observó que muchas de las cavidades examinadas cumplen parcialmente los requisitos en términos de V_{eff} , y que por lo tanto son potencialmente válidas para asegurar alta I si se introducen las modificaciones necesarias para

el ajuste de Q al rango adecuado. En concreto, se puso especial atención a las cavidades dieléctricas basadas en cristales fotónicos con slot. Siguiendo este razonamiento, el diseño de partida utilizado para la implementación de nuestro modelo de optimización fue el descrito en el esquema de la Figura 2:

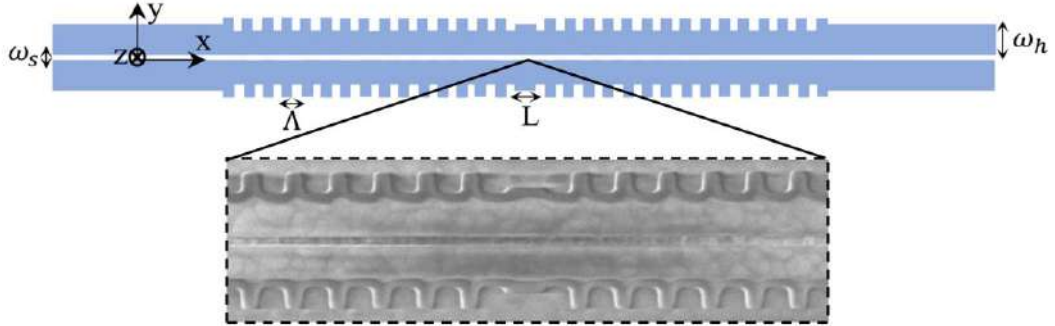


Figura 2. Esquema del diseño de partida de la cavidad de SiN basada en un patrón de cristal fotónico 1-D sobre una guía slot. El parámetro ω_h representa el valor de ancho de las guías, ω_s el ancho del slot, L la longitud del defecto central y Λ el periodo de las corrugaciones. Bajo el esquema se muestra una imagen SEM de la parte central de la estructura fabricada mediante litografía de haz de electrones para la demostración experimental de la viabilidad del diseño.

La estructura consiste en una red difractora de Bragg basada en una serie de corrugaciones en línea situadas a ambos lados de una guía slot de Si_3N_4 con anchura de guía ω_h y anchura de slot ω_s depositada en un sustrato de SiO_2 . En el centro de la estructura se implementa una perturbación del periodo de la red generando un defecto que confina el campo electromagnético en el eje x , funcionando como nano-cavidad óptica. Cada una de las dos regiones periódicas a ambos lados de la cavidad actúa como un espejo efectivo con reflectividad efectiva dependiente del número de períodos ($\#p$), creando un esquema Fabrit-Perot (FP). La longitud de la cavidad L se ajusta de forma que la λ de resonancia del modo fundamental FP de la cavidad coincide con la λ de emisión del EC objetivo. De igual forma el periodo Λ ajusta la λ central del bandgap fotónico a la λ objetivo. La distribución del perfil de campo eléctrico en la sección transversal de la guía muestra una extensa cola evanescente concentrada en el slot que se extiende hacia la parte superior de la guía en la región exterior al núcleo de Si_3N_4 . Esta distribución de campo proporciona ventajas en términos de β para EC integrados heterogéneamente sobre la parte superior de la guía. Al mismo tiempo, dado que la cavidad y la guía de salida comparten sección transversal, el modo fundamental de la FP posee un overlap perfecto con el modo TE_{10} de salida del dispositivo, lo que también repercute positivamente en β . El volumen modal estimado por las simulaciones FDTD está en el orden de $10^{-3}(\lambda/2n)^3$, por lo que se encuentra dentro del rango de V_{eff} adecuado para alcanzar el régimen de acoplamiento-fuerte.

En una primera fase, con el objetivo de obtener información acerca del comportamiento físico del dispositivo realizamos una evaluación general de su rendimiento en términos de I , β y P_f a partir de nuestro modelo teórico ajustando los parámetros para una longitud de onda objetivo de $\lambda = 801 \text{ nm}$ con un EC integrado en la parte central de la cavidad en la región del slot. El valor de I muestra una fuerte dependencia con los parámetros de $\#p$ y ω_s . A medida que ω_s aumenta el modo fundamental de la cavidad se esparce hacia los núcleos de las guías saliendo del slot y comienza a confinarse en cada guía lateral por separado.

Esto resulta en un decaimiento exponencial de la intensidad de campo en la región del slot, aumentando V_{eff} exponencialmente con ω_s . Dado que el acople $g \sim 1/V_{eff}$, g comienza a disminuir conduciendo al sistema fuera del régimen de acoplamiento-fuerte, induciendo un decaimiento exponencial de I . Para valores de $\omega_s < 10$ nm produce una I de 0.96, que empieza a decaer desde este valor con ω_s a un ratio de $5 \cdot 10^{-3}$ nm⁻¹. Por otro lado, el crecimiento de $\#p$ produce aumenta la reflectividad efectiva de la cavidad produciendo un aumento exponencial de Q . Como consecuencia, el parámetro κ disminuye exponencialmente con $\#p$ y el tiempo que el fotón emitido permanece en la cavidad aumenta con $\#p$. Llegado el punto en el que $\kappa < \gamma^*$ el fotón empieza a verse afectado por el dephasing del EC, y como resultado I decrece con $\#p$ reduciéndose a 0.4 para $\#p = 100$. En conclusión, el parámetro ω_s necesita ser ajustado para producir un V_{eff} mínimo para obtener acoplamiento-fuerte, y al mismo tiempo $\#p$ debe elegirse adecuadamente para mantener κ en el rango de valores adecuados para condición de alta I . El comportamiento de β en función de ω_s muestra un patrón similar al observado en I . Dado que β depende del overlap del dipolo del EC con el perfil de intensidad del modo fundamental de la cavidad, a medida que ω_s aumenta y el modo se esparce hacia las regiones exteriores al slot, el acoplamiento del EC con el modo guiado disminuye produciendo un decaimiento exponencial de β . Por otro lado, la dependencia de β con ω_h es análoga al caso del EC acoplado a guías de onda descrito en la subsección anterior. El valor de β se mantiene nulo hasta que ω_h alcanza el valor umbral de activación del modo fundamental y después comienza un crecimiento monótono hasta alcanzar un máximo de 0.75 cuando el modo se encuentra óptimamente confinado en el slot. A partir de este valor de ω_h , β decae asintóticamente conforme el modo se extiende a lo largo de los núcleos de las dos guías. La posición del EC en el interior de la cavidad juega un rol especialmente relevante. Dado que tanto el acoplamiento g como β dependen del overlap del EC con el modo fundamental, la desviación de la posición del EC con respecto al punto de máxima intensidad de campo tiene un impacto significativo. La sección transversal del modo fundamental de la cavidad tiene la forma de un modo típico de guía de slot, concentrando más de el 90% de la intensidad en la región del slot y con valores extremadamente bajos en la región de los núcleos de las guías. Así, con EC posicionados en la región del slot obtenemos tanto I como β máximas, y la mínima desviación de la posición hacia el exterior de la región del slot produce reducciones drásticas de ambos valores. En resumen, incluso para emisores fuertemente disipativos con $\gamma^* \sim 10^4 \gamma$ el diseño de la estructura puede ajustarse mediante los parámetros de ω_s y $\#p$ obtener valores de $I > 0.9$ y $\beta = 0.75$. Sin embargo, el requerimiento mínimo de $\omega_s < 10$ nm junto con la fuerte dependencia de las figuras de mérito con la posición del EC, imponen unos requerimientos extremos en términos de fabricación y precisión de posicionamiento que dificultan la realización experimental de la plataforma. La definición de anchos de slot de 10 nm es impracticable considerando el estado del arte de las tecnologías de fabricación, y la precisión de deposición en ese mismo rango se encuentra en el límite de la viabilidad.

Con el objetivo de la relajación de estos requerimientos, se procedió al entrenamiento del esquema híbrido de RNP-GA a partir de bancos de datos generados por el modelo teórico. En concreto, se propuso como límite el garantizar unos valores de $I > 0.9$ y $\beta > 0.75$ con una estructura con al menos $\omega_s = 20$ nm, un valor de mayor accesibilidad para las técnicas de fabricación y posicionamiento. Los grados de libertad del diseño para la optimización se muestran en la Figura 3:

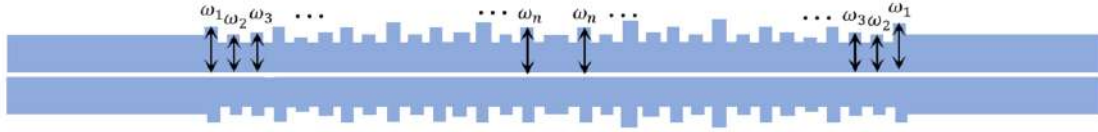


Figura 3. Esquema de los grados de libertad añadidos a la parametrización del diseño. Para el proceso de optimización se permite modificar las anchuras independientes de cada una de las corrugaciones de la red de difracción de Bragg.

El algoritmo de optimización dispone de la capacidad de alterar las anchuras independientes de cada una de las corrugaciones de la red de difracción de Bragg para encontrar una configuración que de alguna forma consiga reducir el valor de V_{eff} para alcanzar acoplamiento-fuerte, al mismo tiempo que ajustando Q al rango de alta I . Gracias a la reducción de recursos computacionales que proporciona nuestro esquema híbrido, cada evaluación del rendimiento de la plataforma realizada por la RNP se lleva a cabo en cuestión de microsegundos, en contraposición al cálculo a partir de simulaciones FDTD que puede llevar tiempos del orden de minutos o decenas de minutos. Esta reducción hace posible la optimización del dispositivo tomando un basto número de grados de libertad, como son cada una de las anchuras de las diferentes corrugaciones. Tras encontrar con éxito una arquitectura de RNP adecuada para le entrenamiento con el banco de datos del modelo teórico, se procedió a la optimización a través del AG. La estructura resultante se muestra en la Figura 4:

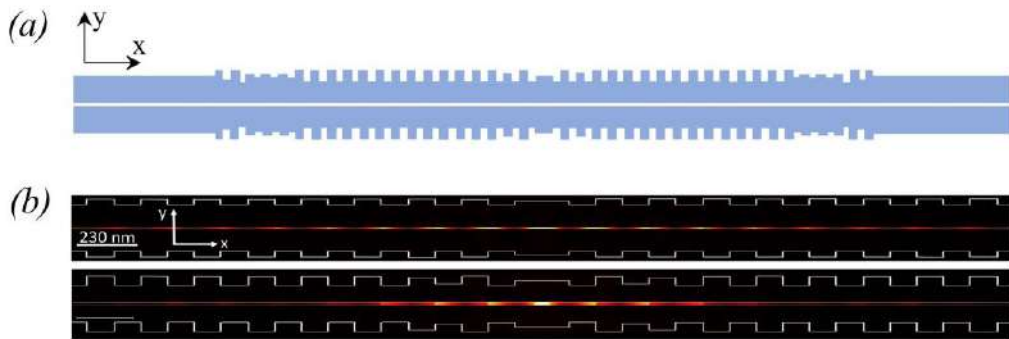


Figura 4. (a) Esquema de la configuración de la estructura optimizada a través del esquema híbrido RNP-AG. Las modificaciones de las corrugaciones se concentran especialmente en las regiones más próximas a las guías de entrada y salida del dispositivo, produciendo un efecto de confinamiento en el eje x capaz de disminuir el volumen modal. (b) Comparación del tamaño del volumen modal entre la estructura sin optimizar (arriba) y la estructura optimizada (abajo).

Sorprendentemente, el esquema RNP-AG encontró que es suficiente alterar las anchuras de las corrugaciones de los extremos de la cavidad dejando sin perturbar las centrales. Esta configuración proporciona el confinamiento óptimo del modo fundamental de la cavidad, reduciendo V_{eff} con respecto a la estructura sin optimizar en un factor de 2.8 (ver Figura 4 (b)) y manteniendo el valor de Q dentro del rango necesario para condición de alta I . Al mismo tiempo, la alteración de las corrugaciones externas genera una sección de acoplamiento que conecta la cavidad con las guías de entrada y salida del dispositivo de forma óptima aumentando el valor de β . Como resultado la estructura optimizada con un slot de $\omega_s = 20$ nm garantiza un valor de I de 0.91 manteniendo β por encima de 0.75.

En conclusión, la aplicación del modelo teórico desarrollado permitió establecer una conceptualización inicial de diseño adecuada para la maximización de I con emisores fuertemente disipativos, al mismo tiempo que funcionó para la evaluación del rendimiento de la estructura ayudándonos a identificar los parámetros críticos del diseño para el proceso de optimización. Seguidamente, los datos generados por el modelo teórico sirvieron para el entrenamiento de una arquitectura eficiente del esquema RNP-AG, que llevó a cabo la optimización de los grados de libertad necesarios para la mejora del rendimiento de la estructura. Como resultado, el diseño extraído del proceso de optimización garantiza condición de alta I y β con EC fuertemente disipativos relajando los requisitos técnicos a niveles asequibles para las técnicas establecidas de fabricación y deposición de EC.

Clústeres de emisores integrados en cavidades ópticas

En este trabajo se llevó a cabo el desarrollo de un modelo teórico puramente cuántico para el cálculo del grado de I en sistemas de EC fuertemente disipativos acoplados por interacción dipolar integrados en cavidades ópticas arbitrarias. En primer lugar se consiguió derivar una expresión analítica de I para un sistema de dos EC acoplados en una cavidad óptica por medio de la resolución de la ecuación de Lindblad del sistema abierto acoplado a varios reservorios, y el cálculo explícito de la función de correlación a dos tiempos del numerador de la expresión de I por medio de técnicas de funciones de Green fuera del equilibrio. La expresión analítica extraída del modelo relaciona el grado de I con los parámetros de los EC γ y γ^* , parámetros de la cavidad g y κ , y la distancia relativa d entre los dos emisores. A partir del análisis funcional de esta relación se puede interpretar el efecto de la separación entre los EC en la dinámica del sistema y su repercusión en los requisitos para los parámetros de g y κ para condición de alta I . Extendiendo las implicaciones del modelo, se desarrolló una teoría general para la obtención de expresiones analíticas de I con un número arbitrario de sistemas acoplados (i.e. mayor número de EC/mayor número de cavidades). Esta nueva metodología simplifica sustancialmente la obtención de fórmulas analíticas para I , ya que no necesita ni de la resolución de la ecuación de Lindblad ni el cálculo de funciones de Green fuera del equilibrio. En este marco el valor de I se obtiene de forma natural a partir de una reorganización de los coeficientes presentes en la ecuación de Lindblad, lo que permite extraer conclusiones de su comportamiento con sistemas de mayor número sistemas abiertos acoplados sin siquiera escribir la correspondiente ecuación de su evolución temporal. A partir de las conclusiones extraídas de este desarrollo, se procedió a la simulación y optimización de un sistema de cinco EC fuertemente disipativos acoplados por interacción dipolar integrados en una cavidad óptica. Para la optimización se empleó un método análogo de Machine Learning al presentado en la anterior subsección. A partir de los datos generados por el modelo teórico se entrenó una arquitectura de RNP que se empleó para la optimización a partir de un AG de las posiciones relativas entre los EC para garantizar $I = 1$. El sistema optimizado permite alcanzar I perfecta con EC fuertemente disipativos para cavidades con Q arbitrariamente bajo, ofreciendo unas ventajas sin precedentes para la relajación de los requerimientos técnicos sobre la plataforma para la cavidad.

Para el modelo de dos EC acoplados consideramos dos sistemas de dos niveles $\{|f\rangle, |e\rangle\}$ con mismos valores de γ y γ^* acoplados al modo fundamental de una cavidad óptica monomodal de estados de Fock

$\{|0\rangle, |1\rangle\}$ con parámetros g y κ . Los EC interactúan entre sí vía un acoplamiento dipolar con una fuerza de acoplo Ω_{12} inversa al cubo de la distancia relativa. En condiciones de acoplamiento dipolar fuerte ($kd \gg 1$) el sistema de dos emisores es equivalente a un único emisor efectivo con un ratio de decaimiento espontáneo 2γ , un acoplamiento a la cavidad de $\sqrt{2}g$ y un detuning (δ) entre su energía de transición y la frecuencia de resonancia de la cavidad $\delta = \Omega_{12}$ [116]. A partir de las soluciones de la ecuación de Lindblad y la función de Green fuera del equilibrio se obtuvieron las siguientes expresiones para la I y el ratio de transferencia de energía R entre los EC en el régimen incoherente ($g \ll \gamma + \gamma^* + \kappa$):

$$R = \frac{4g^2\Gamma}{\Gamma^2 + \frac{\gamma^2}{(kd)^6}}, \quad I = \frac{\gamma\kappa[\Gamma^3 + \Omega_{12}] + [4g^2(\gamma + 1) + \Omega_{12}\frac{\kappa\gamma}{\Gamma}]\cdot[\Gamma^2 + \Omega_{12}]}{[\Gamma^2 + \Omega_{12} + 8g^2]\cdot[\kappa\Gamma^2 + \Omega_{12} + 4g^2\Gamma]} \quad (10)$$

Donde $\Gamma = \gamma + \gamma^* + \kappa$. Estas expresiones analíticas fueron validadas vía resolución numérica de la ecuación de Lindblad mostrando una correspondencia perfecta entre el resultado del modelo y los datos de la simulación. En este régimen la cavidad se comporta como un emisor efectivo alimentado por el EC efectivo, y las condiciones de alta I son $\kappa < \gamma$ y $R < \gamma$. El efecto de la disminución de la distancia entre emisores d repercute directamente en una reducción de R , lo que implica que la condición de $R < \gamma$ de alta I modifica su requerimiento sobre el acoplo g , aumentando el rango de valores de g para los que se obtiene alta I . Sin embargo, la condición de $\kappa < \gamma$ no varía con d , por lo que el único efecto de la reducción de d es la ampliación del rango de valores adecuados de g . En otras palabras, el efecto de la implementación de un segundo EC en la cavidad simplemente posibilita la obtención de alta I con volúmenes modales más reducidos que en el caso de un solo EC, mientras que los requisitos de mínimo Q se mantienen sin modificar. Por lo tanto, el sistema de dos EC acoplados no proporciona ninguna ventaja práctica en términos de reducción de requisitos para la cavidad óptica. Sin embargo, la explotación del comportamiento cooperativo de sistemas optimizados de más emisores de dos emisores puede proporcionar beneficios en términos de I .

Para conjuntos de sistemas cuánticos de dos niveles acoplados entre sí en el régimen incoherente la dinámica del sistema total se reduce a un intercambio de poblaciones entre los subsistemas regulado por unos ratios de transferencia de energía R . Para el caso de un único EC acoplado a una cavidad monomodal (la cual también representa un sistema de dos niveles $\{|0\rangle, |1\rangle\}$) la ecuación de Lindblad para la matriz densidad del sistema compuesto en el régimen incoherente se reduce a [56]:

$$\begin{pmatrix} \dot{P}_{ec} \\ \dot{P}_C \end{pmatrix} = \begin{pmatrix} -(\gamma + R) & R \\ R & -(\kappa + R) \end{pmatrix} \begin{pmatrix} P_{ec} \\ P_C \end{pmatrix} \quad (11)$$

Donde P_{ec} es la población del EC, P_C la población en la cavidad y el ratio R se relaciona con los parámetros de ambos subsistemas $R = 4g^2/\Gamma$. A partir de la teoría general desarrollada en este trabajo, se puede determinar que el valor de I puede obtenerse a partir de una reorganización de los términos de la matriz en (11), viniendo dada por el siguiente cociente:

$$I = \frac{\bar{\Delta}}{\tau} = \frac{\gamma + \frac{\kappa R}{\kappa + R}}{\kappa + 2R + \gamma} \quad (12)$$

Donde Δ y τ son el determinante y la traza de la matriz respectivamente. Esta metodología ha sido testeada a partir de la comparación de las expresiones obtenidas para I con el método de funciones de Green fuera del equilibrio para sistemas más complejos: cavidades en cascada [117], parejas de EC acoplados a cavidades [118]. Los resultados obtenidos demuestran que esta nueva metodología es equivalente al formalismo de funciones de Green, con la ventaja añadida de que no es necesaria la resolución analítica de ninguna ecuación diferencial. Esta interpretación alternativa de I proporciona una orientación particular sobre cómo mantener alta I con valores mayores de κ (i.e. reducir los requisitos técnicos en términos de Q). Para el caso de un solo EC integrado en una cavidad la expresión (12) muestra que el decaimiento del grado de I con κ puede ajustarse a través de la modificación del ratio R . Si incorporamos subsistemas adicionales (como más EC o más cavidades) obtendremos un mayor número de ratios R_i que aparecerán en los términos no diagonales de la matriz y por lo tanto en el determinante y la traza del cálculo de I . Estos términos adicionales pueden potencialmente proporcionar vías alternativas de ajustar el decaimiento de I con κ a través del ajuste de los nuevos ratios R_i . Por lo tanto, añadiendo un mayor número de subsistemas podemos modificar los requerimientos en términos de Q para la condición de alta I .

De acuerdo con estas conclusiones, procedimos a explorar un sistema de cinco EC acoplados por interacción dipolar integrados en una cavidad. En este esquema existen diez ratios de transferencia R_{ij} que pueden ser ajustados a través de las distancias relativas entre los EC. En estas condiciones disponemos de un conjunto de parámetros lo bastante grande como para elaborar una optimización lo suficientemente compleja. El objetivo de la optimización es el de encontrar la disposición geométrica de los EC que proporcione el conjunto óptimo de ratios R_{ij} para mantener alta I con valores altos de κ . Este proceso envuelve un problema de optimización con 10 grados de libertad, y teniendo que para cada evaluación es necesario resolver la ecuación de Lindblad para una matriz de 10x10, el coste computacional puede hacer inviable su realización. Con el objetivo de la reducción del consumo de recursos computacionales, llevamos a cabo la aplicación del mismo sistema de Machine-Learning empleado para el caso de EC integrados en cavidades descrito en la subsección anterior. De tal forma, tras entrenar con éxito a partir de datos generados por el modelo teórico la arquitectura adecuada de RNP, procedimos a la optimización de las posiciones relativas de los EC a partir del AG. Repetimos este proceso para diferentes valores de κ para comprobar si el método consigue encontrar configuraciones de EC que proporcionen $I=I$ para cavidades con Q arbitrario. Las geometrías extraídas del proceso de optimización se muestran en la Figura 5:

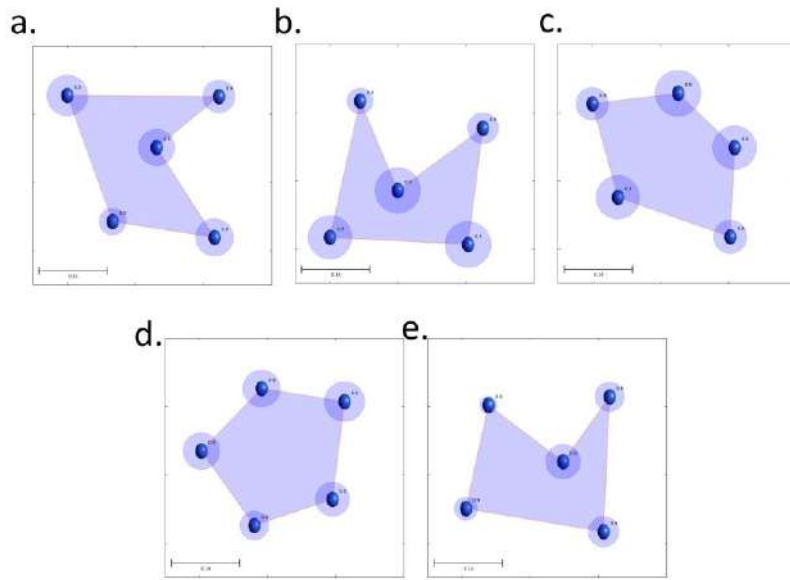


Figura 5. Geometrías obtenidas del proceso de optimización Machine Learning para las posiciones óptimas de los EC que garantizan alta I para diferentes valores de κ : (a) $\kappa = 10\gamma$, (b) $\kappa = 50\gamma$, (c) $\kappa = 100\gamma$, (d) $\kappa = 500\gamma$, (e) $\kappa = 1000\gamma$.

Las geometrías mostradas en la Figura 5 obtenidas tras el proceso de optimización proporcionan $I=1$ para los valores de $\kappa = 10\gamma, 50\gamma, 100\gamma, 500\gamma$ y 1000γ . Las mínimas distancias entre emisores obtenidas son del orden de $d_{ij} \sim 0.1\lambda$, valor compatible con la realización experimental [119-122]. Cada configuración da lugar a los ratios de transferencia R_{ij} entre los EC que mantienen alta I para cada situación específica determinada por el valor de κ . En la Figura 5 también se muestran las tolerancias de posicionamiento para cada EC para la obtención de $I > 0.9$, representadas por las regiones circulares en torno a cada EC. La plataforma propuesta permite la realización de FFI de alta I con EC fuertemente disipativos sin imponer restricciones técnicas a las figuras de mérito de la cavidad óptica.

En conclusión, el modelo desarrollado permite la obtención de expresiones analíticas para la estimación del valor de I en función de los parámetros del sistema para números arbitrarios de sistemas de dos niveles acoplados. Así mismo, se encontró la arquitectura adecuada para la RNP capaz de entrenarse con la base de datos creada por el modelo produciendo estimaciones fiables del valor de I . El resultado del proceso de optimización basado en el esquema híbrido RNP-AG determinó los parámetros necesarios para la obtención de alta I con valores de Q arbitrarios. El método propuesto proporciona una estrategia para la realización de una FFI con I perfecta con EC fuertemente disipativos.

Conclusiones

La fotónica cuántica integrada es un elemento indispensable para la miniaturización, estabilización y escalabilidad de las tecnologías cuánticas. El desarrollo de circuitos fotónicos integrados para aplicación en tecnologías cuánticas ayudará a traspasar el cuello de botella hacia niveles superiores de disponibilidad tecnológica y comercialización. La decoherencia cuántica supone uno de los retos técnicos a nivel fundamental con mayor relevancia para la realización de este desarrollo. En este contexto, el objetivo de este proyecto ha sido el de proporcionar herramientas teóricas para orientar la conceptualización y el diseño de los bloques fundamentales de los circuitos cuánticos integrados con vistas a la reducción de la decoherencia cuántica en estos sistemas. Los resultados obtenidos en forma de modelos teóricos, métodos numéricos de simulación y esquemas de optimización facilitan estas herramientas a través una serie de nuevos instrumentos matemáticos que sirven tanto para la caracterización de la decoherencia en diferentes componentes como para guías de diseño para su reducción:

- Expresiones analíticas que relacionan directamente los parámetros de diseño de estructuras fotónicas con el grado de decoherencia de la plataforma.
- Modelos para la simulación numérica de emisores cuánticos integrados en estructuras fotónicas que conectan la variación de los parámetros del diseño con el impacto en las figuras de mérito que caracterizan la decoherencia.
- Esquemas de optimización basados en métodos de Machine Learning para estructuras de fotónica cuántica integrada que ofrecen una reducción sin precedentes en términos de consumo de recursos computacionales.
- Interpretaciones físicas de las soluciones de los modelos desarrollados que contribuyen al avance del conocimiento del comportamiento de componentes de circuito en diferentes condiciones.

El aparato matemático desarrollado ha sido evaluado a través de su aplicación en diferentes casos prácticos validando su fiabilidad y demostrando resultados prometedores:

- Obtención de la diádica de Green para el problema de una fuente puntual en una guía de onda rectangular 3D con contornos no acotados.
- Descripción analítica de la relación entre el acople de un emisor cuántico a una guía de onda y los parámetros gométricos de la guía de onda.
- Identificación de los valores de los parámetros de diseño necesarios para la maximización de la indistinguibilidad y la eficiencia de extracción en emisores cuánticos acoplados a guías de onda dependiendo de las características del emisor, estimando incrementos en la indistinguibilidad de hasta un 30% para diseños optimizados.
- Desarrollo de un método numérico para la estimación de la indistinguibilidad en emisores disipativos acoplados a cavidades ópticas.

- Desarrollo de un esquema de optimización basado en métodos Machine Learning para la maximización de la indistinguibilidad de emisores cuánticos acoplados a cavidades ópticas.
- Optimización del diseño de una cavidad óptica para integración en chip de emisores cuánticos que garantiza valores de indistinguibilidad y eficiencia de extracción cercanos a la unidad con emisores fuertemente disipativos a temperatura ambiente.
- Desarrollo de un modelo analítico para la estimación de la indistinguibilidad en sistemas de parejas de emisores cuánticos acoplados a cavidades ópticas.
- Obtención de una ecuación general para indistinguibilidad en sistemas de emisores acoplados para un número arbitrario de emisores.
- Desarrollo de un esquema híbrido de redes neuronales y algoritmos genéticos para la estimación de la indistinguibilidad en sistemas de clústeres de emisores acoplados a cavidades ópticas.
- Relajación de los requisitos técnicos generales para cavidades ópticas a partir de una nueva plataforma propuesta basada en la integración de clústeres de emisores cuánticos acoplados que garantiza indistinguibilidad perfecta con emisores fuertemente disipativos a temperatura ambiente para las configuraciones óptimas.

Esperamos que los resultados obtenidos en esta disertación contribuyan al avance del conocimiento para el desarrollo de la fotónica cuántica integrada y sirvan de hoja de ruta para la realización de nuevas demostraciones experimentales que incrementen su impacto en el estado del arte de las tecnologías cuánticas.

Agradecimientos

Especial agradecimiento a mi director de tesis Pablo Aitor Postigo Resa por servir de guía constante a lo largo del desarrollo de este proyecto y proporcionar los medios y ayudas necesarios en todo momento para la consecución de los objetivos alcanzados. Agradecimientos a mis compañeros Lukas Weituschat, José Llorens y Lorenzo Sanchis por su colaboración indispensable en cada uno de los trabajos que se comprendían en esta tesis. Agradecimientos al programa de financiación europeo *Horizon 2020 Research & Innovation* que financió parcialmente este proyecto bajo el *grant agreement No.820423*. Agradecimientos también a mis padres Joaquín y Concepción por su apoyo incondicional que me permite desarrollar mi carrera profesional en la ciencia con seguridad y entusiasmo. Finalmente me gustaría dedicar un agradecimiento a mi viejo profesor de filosofía Sergio de Castro Sánchez, cuyas clases me sirvieron de inspiración para elegir la Física como profesión.

Referencias

- [1] Breuer, H. P., & Petruccione, F. (2002). *The theory of open quantum systems*. Oxford University Press on Demand.
- [2] Gudder, S. P. (2014). *Quantum probability*. Academic Press.
- [3] Von Neumann, J. (1955). *Mathematical Foundations of Quantum Mechanics: Translated from the German Ed. by Robert T. Beyer*. Princeton University Press.
- [4] Bell, J. S. (1964). On the einstein podolsky rosen paradox. *Physics Physique Fizika*, 1(3), 195.
- [5] Gordon, J. P. (1962). Quantum effects in communications systems. *Proceedings of the IRE*, 50(9), 1898-1908.
- [6] Helstrom, C. W. (1969). Quantum detection and estimation theory. *Journal of Statistical Physics*, 1(2), 231-252.
- [7] Holevo, A. S. (1973). Bounds for the quantity of information transmitted by a quantum communication channel. *Problemy Peredachi Informatsii*, 9(3), 3-11.
- [8] Fine, A. (1982). Hidden variables, joint probability, and the Bell inequalities. *Physical Review Letters*, 48(5), 291.
- [9] Clauser, J. F., Horne, M. A., Shimony, A., & Holt, R. A. (1969). Proposed experiment to test local hidden-variable theories. *Physical review letters*, 23(15), 880.
- [10] Fujikawa, K., & Ono, Y. A. (Eds.). (1996). *Quantum Coherence and Decoherence: Foundations of Quantum Mechanics in the Light of New Technology: Proceedings of the 5th International Symposium on Foundations of Quantum Mechanics in the Light of New Technology (ISQM-Tokyo'95) Advanced Research Laboratory, Hitachi, Ltd., Hatoyama, Saitama, Japan, August 21-24, 1995* (Vol. 5). North-Holland.
- [11] Rivas, A., & Huelga, S. F. (2012). *Open quantum systems* (Vol. 10, pp. 978-3). Berlin: Springer.
- [12] Beth, T., & Leuchs, G. (Eds.). (2005). *Quantum information processing*. Weinheim: Wiley-VCH.
- [13] Grover, L. K. (1996, July). A fast quantum mechanical algorithm for database search. In *Proceedings of the twenty-eighth annual ACM symposium on Theory of computing* (pp. 212-219).
- [14] Daniel R. Simon (1997) "On the Power of Quantum Computation" SIAM Journal on Computing, 26(5), 1474–1483
- [15] Shor, P. W. (1999). Polynomial-time algorithms for prime factorization and discrete logarithms on a quantum computer. *SIAM review*, 41(2), 303-332.
- [16] Cao, Y., Romero, J. & Aspuru-Guzik, J. Potential of quantum computing for drug discovery. *IBM J. Res. Dev.* 62, 6:1–6:20 (2018).

- [17] Batra, K. et al. Quantum machine learning for drug discovery. *J. Chem. Inf. Model.* 28, 2641–2647 (2021).
- [18] Li, J. et al. Drug discovery approaches using quantum machine learning. Preprint at arXiv <https://arxiv.org/abs/2104.00746> (2021).
- [19] Vikstål, P. et al. Applying the quantum approximate optimization algorithm to the tail-assignment problem. *Phys. Rev. Appl.* 14, 034009 (2020).
- [20] Alcazar, J., Cadarso, A., Katabarwa, A., Mauri, M., Peropadre, B., Wang, G., & Cao, Y. (2022). Quantum algorithm for credit valuation adjustments. *New Journal of Physics*, 24(2), 023036.
- [21] Orús, R., Mugel, S., & Lizaso, E. (2019). Quantum computing for finance: Overview and prospects. *Reviews in Physics*, 4, 100028.
- [22] Monroe, C.; Meekhof, D.M.; King, B.E.; Itano, W.M.; Wineland, D.J. Demonstration of a fundamental quantum logic gate. *Phys. Rev. Lett.* 1995, 75, 4714.
- [23] Makhlin, Y.; Scöhn, G.; Shnirman, A. Josephson-junction qubits with controlled couplings. *Nature* 1999, 398, 305–307.
- [24] Ahn, J., Kwon, H. Y., Ahn, B., Park, K., Kim, T., Lee, M. K., ... & Chung, J. (2022). Toward Quantum Secured Distributed Energy Resources: Adoption of Post-Quantum Cryptography (PQC) and Quantum Key Distribution (QKD). *Energies*, 15(3), 714.
- [25] Kok, P., & Lovett, B. W. (2010). *Introduction to optical quantum information processing*. Cambridge university press.
- [26] Cirac, J. I. & Zoller, P. Quantum computations with cold trapped ions. *Phys. Rev. Lett.* 74, 4091 (1995).
- [27] Holzgrafe, J., Sinclair, N., Zhu, D., Shams-Ansari, A., Colangelo, M., Hu, Y., ... & Lončar, M. (2020). Cavity electro-optics in thin-film lithium niobate for efficient microwave-to-optical transduction. *Optica*, 7(12), 1714-1720.
- [28] Drever, R. W. P., Hall, J. L., Kowalski, F. V., Hough, J., Ford, G. M., Munley, A. J., & Ward, H. (1983). Laser phase and frequency stabilization using an optical resonator. *Applied Physics B*, 31(2), 97-105.
- [29] Wang, J. et al. Multidimensional quantum entanglement with large-scale integrated optics. *Science* 360, 285–291 (2018).
- [30] Bogaerts, W. et al. Programmable photonic circuits. *Nature* 586, 207–216 (2020).
- [31] Politi, A., Cryan, M. J., Rarity, J. G., Yu, S. & O’Brien, J. L. Silica-on-silicon waveguide quantum circuits. *Science* 320, 646–649 (2008).

- [32] Pernice, W. H. P. et al. High-speed and high-efficiency travelling wave single-photon detectors embedded in nanophotonic circuits. *Nat. Commun.* 3, 1325 (2012).
- [33] Najafi, F. et al. On-chip detection of non-classical light by scalable integration of single-photon detectors. *Nat. Commun.* 6, 5873 (2015).
- [34] van Dijk, J. P. G., Charbon, E. & Sebastian, F. The electronic interface for quantum processors. *Microprocess. Microsyst.* 66, 90–101 (2019).
- [35] Politi, A.; Cryan, M.J.; Rarity, J.G.; Yu, S.; O'brien, J.L. Silica-on-silicon waveguide quantum circuits. *Science* 2008, 320, 646–649.
- [36] Zhou, Z., Yin, B., & Michel, J. (2015). On-chip light sources for silicon photonics. *Light: Science & Applications*, 4(11), e358-e358.
- [37] Gaeta, A. L., Lipson, M., & Kippenberg, T. J. (2019). Photonic-chip-based frequency combs. *nature photonics*, 13(3), 158-169.
- [38] Bogaerts, W., Pérez, D., Capmany, J., Miller, D. A., Poon, J., Englund, D., ... & Melloni, A. (2020). Programmable photonic circuits. *Nature*, 586(7828), 207-216.
- [39] Billaud, A., Agis, F. G., Saab, K., Meunier, M., Allioux, D., Pinel, O., & Labroille, G. (2022, April). On chip coherent phase and intensity control for atmospheric turbulence mitigation with multi-plane light conversion. In *Free-Space Laser Communications XXXIV* (p. PC1199303). SPIE.
- [40] Schmidgall, E. R., Chakravarthi, S., Gould, M., Christen, I. R., Hestroffer, K., Hatami, F., & Fu, K. M. C. (2018). Frequency control of single quantum emitters in integrated photonic circuits. *Nano letters*, 18(2), 1175-1179.
- [41] Du, H., Chau, F. S., & Zhou, G. (2016). Mechanically-tunable photonic devices with on-chip integrated MEMS/NEMS actuators. *Micromachines*, 7(4), 69.
- [42] Tanabe, T., Notomi, M., Mitsugi, S., Shinya, A., & Kuramochi, E. (2005). All-optical switches on a silicon chip realized using photonic crystal nanocavities. *Applied Physics Letters*, 87(15), 151112.
- [43] Barbier, R., Baudot, J., Chabanat, E., Depasse, P., Dulinski, W., Estre, N., ... & Winter, M. (2009). Performance study of a MegaPixel single photon position sensitive photodetector EBCMOS. *Nuclear Instruments and Methods in Physics Research Section A: Accelerators, Spectrometers, Detectors and Associated Equipment*, 610(1), 54-56.
- [44] Assefa, S., Xia, F., & Vlasov, Y. A. (2010). Reinventing germanium avalanche photodetector for nanophotonic on-chip optical interconnects. *Nature*, 464(7285), 80-84.
- [45] Dou, C., Jing, X., Li, S., Liu, Q., & Bian, J. (2016). A photonic crystal fiber polarized filter at 1.55 μm based on surface plasmon resonance. *Plasmonics*, 11(4), 1163-1168.
- [46] Akahane, Y., Asano, T., Song, B. S., & Noda, S. (2003). High-Q photonic nanocavity in a two-dimensional photonic crystal. *nature*, 425(6961), 944-947.

- [47] Bussières, F., Clausen, C., Tiranov, A., Korzh, B., Verma, V. B., Nam, S. W., ... & Gisin, N. (2014). Quantum teleportation from a telecom-wavelength photon to a solid-state quantum memory. *Nature Photonics*, 8(10), 775-778.
- [48] Sasani Ghamsari, M. (2021). Chip-scale quantum emitters. *Quantum Reports*, 3(4), 615-642.
- [49] Bartholomew, J. G., Rochman, J., Xie, T., Kindem, J. M., Ruskuc, A., Craiciu, I., ... & Faraon, A. (2020). On-chip coherent microwave-to-optical transduction mediated by ytterbium in YVO₄. *Nature communications*, 11(1), 1-6.
- [50] Burmeister, E. F., Mack, J. P., Poulsen, H. N., Mašanović, M. L., Stamenic, B., Blumenthal, D. J., & Bowers, J. E. (2009). Photonic integrated circuit optical buffer for packet-switched networks. *Optics Express*, 17(8), 6629-6635.
- [51] Bunandar, D.; Lentine, A.; Lee, C.; Cai, H.; Long, C.M.; Boynton, N.; Martinez, N.; DeRose, C.; Chen, C.; Grein, M. Metropolitan quantum key distribution with silicon photonics. *Phys. Rev. X* 2018, 8, 021009.
- [52] Lago-Rivera, D.; Grandi, S.; Rakonjac, J.V.; Seri, A.; de Riedmatten, H. Telecom-heralded entanglement between multimode solid-state quantum memories. *Nature* 2021, 594, 37–40.
- [53] Zhong, H.S.; Wang, H.; Deng, Y.H.; Chen, M.C.; Peng, L.C.; Luo, Y.H.; Qin, J.; Wu, D.; Ding, X.; Hu, Y. Quantum computational advantage using photons. *Science* 2020, 370, 1460–1463.
- [54] Peruzzo, A.; McClean, J.; Shadbolt, P.; Yung, M.H.; Zhou, X.Q.; Love, P.J.; Aspuru-Guzik, A.; O'brien, J.L. A variational eigenvalue solver on a photonic quantum processor. *Nat. Commun.* 2014, 5, 4213.
- [55] Acosta, V.M.; Bauch, E.; Ledbetter, M.P.; Santori, C.; Fu, K.M.; Barclay, P.E.; Beausoleil, R.G.; Linget, H.; Roch, J.F.; Treussart, F. Diamonds with a high density of nitrogen-vacancy centers for magnetometry applications. *Phys. Rev. B* 2009, 80, 115202.
- [56] Grange, T.; Hornecker, G.; Hunger, D.; Poizat, J. P.; Gérard, J. M.; Similar, P.; Affixes, A. Cavity-funneled generation of indistinguishable single photons from strongly dissipative quantum emitters. *Phys. Rev. Lett.* 2015, 114, No. 193601.
- [57] C.K. Hong, Z.Y. Ou, L. Mandel, *Phys. Rev. Lett.* 59, 2044 (1987)
- [58] Fox, A. M., & Fox, M. (2006). *Quantum optics: an introduction* (Vol. 15). Oxford university press.
- [59] Chen, Y., Zhang, J., Zopf, M., Jung, K., Zhang, Y., Keil, R., ... & Schmidt, O. G. (2016). Wavelength-tunable entangled photons from silicon-integrated III–V quantum dots. *Nature communications*, 7(1), 1-7.
- [60] Ishii, A., He, X., Hartmann, N. F., Machiya, H., Htoon, H., Doorn, S. K., & Kato, Y. K. (2018). Enhanced single-photon emission from carbon-nanotube dopant states coupled to silicon microcavities. *Nano Letters*, 18(6), 3873-3878.
- [61] Wu, C., Kumar, S., Kan, Y., Komisar, D., Wang, Z., Bozhevolnyi, S. I., & Ding, F. (2022). Room-temperature on-chip orbital angular momentum single-photon sources. *Science Advances*, 8(2), eabk3075.

- [62] Koch, M. K., Hoesche, M., Bharadwaj, V., Lang, J., Hadden, J. P., Ramponi, R., ... & Kubanek, A. (2021). On-chip single-photon subtraction by individual silicon vacancy centers in a laser-written diamond waveguide. *arXiv preprint arXiv:2111.01699*.
- [63] Peyskens, F., Chakraborty, C., Muneeb, M., Van Thourhout, D., & Englund, D. (2019). Integration of single photon emitters in 2D layered materials with a silicon nitride photonic chip. *Nature communications*, 10(1), 1-7.
- [64] Utzat, H., Sun, W., Kaplan, A. E., Krieg, F., Ginterseder, M., Spokoyny, B., ... & Bawendi, M. G. (2019). Coherent single-photon emission from colloidal lead halide perovskite quantum dots. *Science*, 363(6431), 1068-1072.
- [65] Ulanowski, A., Merkel, B., & Reiserer, A. (2022). Spectral multiplexing of telecom emitters with stable transition frequency. *Science Advances*, 8(43), eabo4538.
- [66] Juska, G.; Dimastrodonato, V.; Mereni, L.O.; Gocalinska, A.; Pelucchi, E. Towards quantum-dot arrays of entangled photon emitters. *Nat. Photonics* 2013, 7, 527–531.
- [67] Gérard, J.M.; Sermage, B.; Gayral, B.; Legrand, B.; Costard, E.; Thierry-Mieg, V. Enhanced spontaneous emission by quantum boxes in a monolithic optical microcavity. *Phys. Rev. Lett.* 1998, 81, 1110.
- [68] Hennessy, K.; Badolato, A.; Winger, M.; Gerace, D.; Atatüre, M.; Gulde, S.; Fält, S.; Hu, E.L.; Imamoglu, A. Quantum nature of a strongly coupled single quantum dot–cavity system. *Nature* 2007, 445, 896–899.
- [69] Wang, H.; Duan, Z.C.; Li, Y.H.; Chen, S.; Li, J.P.; He, Y.M.; Chen, M.C.; He, Y.; Ding, X.; Peng, C.Z.; et al. Near-transform-limited single photons from an efficient solid-state quantum emitter. *Phys. Rev. Lett.* 2016, 116, 213601.
- [70] He, Y.M.; He, Y.; Wei, Y.J.; Wu, D.; Atatüre, M.; Schneider, C.; Höfling, S.; Kamp, M.; Lu, C.Y.; Pan, J.W. On-demand semiconductor single-photon source with near-unity indistinguishability. *Nat. Nanotechnol.* 2013, 8, 213–217.
- [71] Somaschi, N.; Giesz, V.; De Santis, L.; Loredo, J.C.; Almeida, M.P.; Hornecker, G.; Portalupi, S.L.; Grange, T.; Anton, C.; Demory, J.; et al. Near-optimal single-photon sources in the solid state. *Nat. Photonics* 2016, 10, 340–345.
- [72] Mirin, R.P. Photon antibunching at high temperature from a single InGaAs/GaAs quantum dot. *Appl. Phys. Lett.* 2004, 84, 1260–1262.
- [73] Dusanowski, Ł.; Syperek, M.; Misiewicz, J.; Somers, A.; Hoefling, S.; Kamp, M.; Reithmaier, J.P.; Sęk, G. Single-photon emission of InAs/InP quantum dashes at 1.55 μm and temperatures up to 80 K. *Appl. Phys. Lett.* 2016, 108, 163108.

- [74] Yu, P.; Li, Z.; Wu, T.; Wang, Y.T.; Tong, X.; Li, C.F.; Wang, Z.; Wei, S.H.; Zhang, Y.; Liu, H.; et al. Nanowire quantum dot surface engineering for high temperature single photon emission. *ACS Nano* 2019, 13, 13492–13500.
- [75] Arakawa, Y.; Holmes, M.J. Progress in quantum-dot single photon sources for quantum information technologies: A broad spectrum overview. *Appl. Phys. Rev.* 2020, 7, 021309.
- [76] Bylander, J.; Robert-Philip, I.; Abram, I. Interference and correlation of two independent photons. *Eur. Phys. J. D-At. Mol. Opt. Plasma Phys.* 2003, 22, 295–301.
- [77] Chikara, R.; De Nibs, B.; Benz, F.; Barrow, S. J.; Sucherman, O. A.; Rosa, E.; Blumberg, J. J. Single-molecule strong coupling at room T in plasmonic nanocavities. *Nature* 2016, 535, 127–130.
- [78] Omri, M., Ouerghi, F., Abdelmalek, F., & Haxha, S. (2020). Highly sensitive photonic sensor based on V-shaped channel mediated gold nanowire. *IEEE sensors journal*, 20(15), 8505-8511.
- [79] Li, L., Fang Lim, S., Puretzky, A. A., Riehn, R., & Hallen, H. D. (2012). Near-field enhanced ultraviolet resonance Raman spectroscopy using aluminum bow-tie nano-antenna. *Applied physics letters*, 101(11), 113116.
- [80] Santhosh, K.; Button, O.; Chitonid, L.; Haran, G. Vacuum Rabi splitting in a plasmonic cavity at the single quantum emitter limit. *Nat. Commun.* 2016, 7, No. 11823.
- [81] Russell, K. J.; Hu, E. L. Gap-mode plasmonic nanocavity. *Appl. Phys. Lett.* 2010, 97, No. 163115.
- [82] Seo, M. K.; Kwon, S. H.; Ee, H. S.; Park, H. G. Full three-dimensional subwavelength high-Q surface-plasmon-polariton cavity. *Nano Lett.* 2009, 9, 4078–4082.
- [83] Kang, J. H.; No, Y. S.; Kwon, S. H.; Park, H. G. Ultrasmall subwavelength nanorod plasmonic cavity. *Opt. Lett.* 2011, 36, 2011– 2013.
- [84] Peng, P.; Liu, Y. C.; Xu, D.; Cao, Q. T.; Lu, G.; Gong, Q.; Xiao, Y. F. Enhancing coherent light-matter interactions through microcavity-engineered plasmonic resonances. *Phys. Rev. Lett.* 2017, 119, No. 233901.
- [85] Gurlek, B.; Sandoghdar, V.; Martín-Cano, D. Manipulation of quenching in nanoantenna–emitter systems enabled by external detuned cavities: a path to enhance strong-coupling. *ACS Photonics* 2018, 5, 456–461.
- [86] Hugall, J. T.; Singh, A.; van Hulst, N. F. Plasmonic cavity coupling. *ACS Photonics* 2018, 5, 43–53.
- [87] Cord, B. M. Achieving sub-10-nm Resolution Using Scanning Electron Beam Lithography. Doctoral Dissertation, Massachusetts Institute of Technology, 2009.
- [88] Zhang, H.; Zhang, J.; Chen, S.; Song, J.; Kee, J. S.; Yu, M.; Lo, G. Q. CMOS-compatible fabrication of silicon-based sub-100-nm slot waveguide with efficient channel-slot coupler. *IEEE Photonics Technol. Lett.* 2012, 24, 10–12.

- [89] McGuinness, H. J., Raymer, M. G., McKinstry, C. J., & Radic, S. (2010). Quantum frequency translation of single-photon states in a photonic crystal fiber. *Physical review letters*, 105(9), 093604.
- [90] Chang, W. H., Chen, W. Y., Chang, H. S., Hsieh, T. P., Chyi, J. I., & Hsu, T. M. (2006). Efficient single-photon sources based on low-density quantum dots in photonic-crystal nanocavities. *Physical review letters*, 96(11), 117401.
- [91] Englund, D., Faraon, A., Zhang, B., Yamamoto, Y., & Vučković, J. (2007). Generation and transfer of single photons on a photonic crystal chip. *Optics Express*, 15(9), 5550-5558.
- [92] Li, S., Chen, Y., Shang, X., Yu, Y., Yang, J., Huang, J., ... & Niu, Z. (2020). Boost of single-photon emission by perfect coupling of InAs/GaAs quantum dot and micropillar cavity mode. *Nanoscale research letters*, 15(1), 1-7.
- [93] Lee, C. M., Buyukkaya, M. A., Harper, S., Aghaeimeibodi, S., Richardson, C. J., & Waks, E. (2020). Bright telecom-wavelength single photons based on a tapered nanobeam. *Nano letters*, 21(1), 323-329.
- [94] Moczała-Dusanowska, M., Dusanowski, Ł., Iff, O., Huber, T., Kuhn, S., Czyszanowski, T., ... & Höfling, S. (2020). Strain-tunable single-photon source based on a circular Bragg grating cavity with embedded quantum dots. *ACS Photonics*, 7(12), 3474-3480.
- [95] Jöns, K. D., Rengstl, U., Oster, M., Hargart, F., Heldmaier, M., Bounouar, S., ... & Michler, P. (2015). Monolithic on-chip integration of semiconductor waveguides, beamsplitters and single-photon sources. *Journal of Physics D: Applied Physics*, 48(8), 085101.
- [96] Robinson, J. T.; Manolatou, C.; Chen, L.; Lipson, M. Ultrasmall mode volumes in dielectric optical microcavities. *Phys. Rev. Lett.* 2005, 95, No. 143901.
- [97] Seidler, P.; Lister, K.; Drechsler, U.; Hofrichter, J.; Stöferle, T. Slotted photonic crystal nanobeam cavity with an ultrahigh quality factor-to-mode volume ratio. *Opt. Express* 2013, 21, 32468–32483.
- [98] Ryckman, J. D.; Weiss, S. M. Low mode volume slotted photonic crystal single nanobeam cavity. *Appl. Phys. Lett.* 2012, 101, No. 071104.
- [99] Hu, S.; Weiss, S. M. Design of photonic crystal cavities for extreme light concentration. *ACS Photonics* 2016, 3, 1647–1653.
- [100] Choi, H.; Heuck, M.; Englund, D. Self-similar nanocavity design with ultrasmall mode volume for single-photon nonlinearities. *Phys. Rev. Lett.* 2017, 118, No. 223605.
- [101] Liu, S., Srinivasan, K., & Liu, J. (2021). Nanoscale Positioning Approaches for Integrating Single Solid-State Quantum Emitters with Photonic Nanostructures. *Laser & Photonics Reviews*, 15(10), 2100223.
- [102] Suemune, I., Nakajima, H., Liu, X., Odashima, S., Asano, T., Iijima, H., ... & Kumano, H. (2013). Metal-coated semiconductor nanostructures and simulation of photon extraction and coupling to optical fibers for a solid-state single-photon source. *Nanotechnology*, 24(45), 455205.

- [103] Katsumi, R., Ota, Y., Osada, A., Yamaguchi, T., Tajiri, T., Kakuda, M., ... & Arakawa, Y. (2019). Quantum-dot single-photon source on a CMOS silicon photonic chip integrated using transfer printing. *APL Photonics*, 4(3), 036105.
- [104] Geng, W., Manceau, M., Rahbany, N., Sallet, V., De Vittorio, M., Carbone, L., ... & Couteau, C. (2016). Localised excitation of a single photon source by a nanowaveguide. *Scientific reports*, 6(1), 1-9.
- [105] Chu, H. S., Ong, J. R., & Png, C. E. (2017, July). Efficiently coupling single photon source to plasmonic nanoslot waveguide by nanoantenna. In *2017 Opto-Electronics and Communications Conference (OECC) and Photonics Global Conference (PGC)* (pp. 1-2). IEEE.
- [106] Choi, H.; Zhu, D.; Yoon, Y.; Englund, D. Cascaded cavities boost the indistinguishability of imperfect quantum emitters. *Phys. Rev. Lett.* 2019, 122, 183602.
- [107] Saxena, A.; Chen, Y.; Ryou, A.; Sevilla, C.G.; Xu, P.; Majumdar, A. Improving indistinguishability of single photons from colloidal quantum dots using nanocavities. *ACS Photonics* 2019, 6, 3166–3173.
- [108] Guimba, J.; Sanchis, L.; Weituschat, L.; Manuel Llorens, J.; Song, M.; Cardenas, J.; Aitor Postigo, P. Numerical Optimization of a Nanophotonic Cavity by Machine Learning for Near-Unity Photon Indistinguishability at Room Temperature. *ACS Photonics* 2022, 9, 1926–1935.
- [109] Santosa, F., & Magnanini, R. (2001). Wave propagation in a 2-D optical waveguide. *SIAM Journal on Applied Mathematics*, 61(4), 1237-1252.
- [110] Brueck, S. R. J. (2000). Radiation from a dipole embedded in a dielectric slab. *IEEE Journal of Selected Topics in Quantum Electronics*, 6(6), 899-910.
- [111] L. Novotny and B. Hecht, “Principles of nano-optics,” (Cambridge University Press, 2012), pp 58.
- [112] D. Gammon, E. S. Snow, B. V. Shanabrook, D. S. Katzer, and D. Park, “Homogeneous linewidths in the optical spectrum of a single gallium arsenide quantum,” *Science* 273, 87–90 (1996).
- [113] J. M. Gérard, O. Cabrol, and B. Sermage, *Appl. Phys. Lett.* 68, 3123 (1996).
- [114] P. Borri, W. Langbein, S. Schneider, U. Woggen, R. L. Sellin, D. Ouyang, and D. Bimberg, “Ultralong dephasing time in InGaAs quantum dots,”
- [115] I. Aharonovich, D. Englund, and M. Toth, “Solid-state single-photon emitters,” *Nat. Photonics* 10, 631–641 (2016).
- [116] Shlesinger, I.; Senellart, P.; Lanco, L.; Greffet, J.J. Tunable bandwidth and nonlinearities in an atom-photon interface with subradiant states. *Phys. Rev. A* 2018, 98, 013813.
- [117] Choi, H.; Zhu, D.; Yoon, Y.; Englund, D. Cascaded cavities boost the indistinguishability of imperfect quantum emitters. *Phys. Rev. Lett.* 2019, 122, 183602.
- [118] Guimba, J., Sanchis, L., Weituschat, L. M., Llorens, J. M., & Postigo, P. A. (2022). Perfect photon indistinguishability from a set of dissipative quantum emitters. *Nanomaterials*, 12(16), 2800.

- [119] Hettich, C.; Schmitt, C.; Zitzmann, J.; Kühn, S.; Gerhardt, I.; Sandoghdar, V. Nanometer resolution and coherent optical dipole coupling of two individual molecules. *Science* 2002, 298, 385–389.
- [120] Vogl, T.; Campbell, G.; Buchler, B.C.; Lu, Y.; Lam, P.K. Fabrication and deterministic transfer of high-quality quantum emitters in hexagonal boron nitride. *ACS Photonics* 2018, 5, 2305–2312.
- [121] Schröder, T.; Trusheim, M.E.; Walsh, M.; Li, L.; Zheng, J.; Schukraft, M.; Sipahigil, A.; Evans, R.E.; Sukachev, D.D.; Nguyen, C.T.; et al. Scalable focused ion beam creation of nearly lifetime-limited single quantum emitters in diamond nanostructures. *Nat. Commun.* 2017, 8, 15376.
- [122] Hail, C.U.; Höller, C.; Matsuzaki, K.; Rohner, P.; Renger, J.; Sandoghdar, V.; Poulikakos, D.; Eghlidi, H. Nanoprinting organic molecules at the quantum level. *Nat. Commun.* 2019, 10, 1880.



Enhancement of the indistinguishability of single photon emitters coupled to photonic waveguides

J. GUIMBAO,^{*} L. M. WEITUSCHAT, J. M. LLORENS MONTOLIO, AND P. A. POSTIGO

Instituto de Micro y Nanotecnología, IMN-CNM, CSIC (CEI UAM+CSIC) Isaac Newton, 8, E-28760 Tres Cantos, Madrid, Spain

^{*}j.guimba@csic.es

Abstract: One of the main steps towards large-scale quantum photonics consists of the integration of single photon sources (SPS) with photonic integrated circuits (PICs). For that purpose, the PICs should offer an efficient light coupling and a high preservation of the indistinguishability of photons. Therefore, optimization of the indistinguishability through waveguide design is especially relevant. In this work we have developed an analytical model that uses the Green's Dyadic of a 3D unbounded rectangular waveguide to calculate the coupling and the indistinguishability of an ideal point-source quantum emitter coupled to a photonic waveguide depending on its orientation and position. The model has been numerically evaluated through finite-difference time-domain (FDTD) simulations showing consistent results. The maximum coupling is achieved when the emitter is embedded in the center of the waveguide but somewhat surprisingly the maximum indistinguishability appears when the emitter is placed at the edge of the waveguide where the electric field is stronger due to the surface discontinuity.

© 2021 Optical Society of America under the terms of the [OSA Open Access Publishing Agreement](#)

1. Introduction

Indistinguishability of single photons generated by point defects is the central topic of quantum photonic integrated circuits for quantum information applications like quantum simulation [1], quantum teleportation [2] or quantum networks [3]. Indistinguishable photons are usually generated by parametric down-conversion [4] or alternatively from a single two-level quantum emitter in a solid-state environment [5]. Over the last years several on-chip integration of different SPS material systems have been demonstrated: III-V quantum dots [6], carbon nanotubes [7], NV [8] or SiV centers in diamond [9] and 2D layered materials [10]. For most of those solid-state quantum emitters the intrinsic indistinguishability at room temperature is almost zero because pure dephasing rates are orders of magnitude larger than the population decay rate [11]. Improvement of the indistinguishability can be achieved by low temperature operation and by reducing the radiative lifetime of the SPS using an optical cavity that takes advantage of the Purcell effect [12]. The balance between dephasing and population decay rates varies significantly depending on the material system. Whereas for specific single self-assembled GaAs quantum dots the emission at low temperature can be radiative lifetime limited [13], defects in 2D materials can exhibit several orders of magnitude of difference between radiative decay and pure dephasing rates [14]. Purcell enhancement using photonic resonators permits on-chip control of light–matter interaction to enhance collection efficiency and generation of indistinguishable photons [15] that can be used for on-chip processing of quantum information [16–18]. Therefore, it is important to explore the coupling of SPS to PICs and its effect on the indistinguishability. In this work we use an analytical treatment of light radiation from a point source placed at an arbitrary location and with arbitrary orientation on a waveguide. The refractive indexes of the waveguide correspond to materials commonly used in silicon photonics (SiO_2 , Si_3N_4 , Si)

besides other high-index materials like WeS_2 or WO_3 [19]. It is worth to note that other specially designed nanomaterials with ultra high refractive index can be designed [20]. We explore how the position of the source and its orientation affects the coupling to the waveguide modes and the indistinguishability of the photons. We also explore how the dimensions of the waveguide impact the indistinguishability. We perform FDTD simulations to validate the analytical model and to calculate the Purcell effect. The results show remarkable differences depending on the orientation of the SPS and provide maximum indistinguishability when the source is placed at the edge of the waveguide, in contrast to the maximum coupling efficiency position at the center of the waveguide. The indistinguishability is expressed in terms of the pure dephasing value of the emitter, so that the effects of the waveguide can be compared between strong and weak dissipative emitters. Depending on the waveguide geometry and the position of the source the indistinguishability can either increase or decrease, showing non-negligible enhancements for weak dissipative emitters placed at optimum positions.

Several works deal with the radiation of a point source embedded in bounded dielectric slabs and square waveguides through Green's function methods [21–26]. Also, the problem of the unbounded dielectric slab is treated in [27] from a classical perspective and in [28] from a quantum perspective. However, in those cases the description of the source comes from the macroscopic expression of the dipole moment, without computing the Green's Dyadic. The Green's function of the unbounded 2D dielectric slab is covered in [29] and the same for the 3D cylindrical fiber in [30–32] through the development of a transform theory. As far as we know, the Green's Dyadic of a 3D unbounded rectangular waveguide has not been treated until this work. Here we develop a generalization of the transform theory from the 2D case [29] to obtain the solution of the 3D version of the problem for an unbounded rectangular waveguide. The obtention of the Green's Dyadic allows us to directly connect the value of the indistinguishability with the geometrical parameters of the waveguide, which also has not been covered neither in the previously mentioned works.

2. Methods, results and discussion

2.1. Indistinguishability for different SPS

In an isolated two-level system, the emission rate can be fully described by its population decay rate Γ_0 . However, a solid-state quantum emitter has an interaction with the mesoscopic environment. The two-level system is affected by random fluctuations of its energy that can be described by a stationary stochastic process characterized by a dephasing rate Γ^* [33]. In this situation the indistinguishability (I) is reduced to [34]:

$$I = \frac{\Gamma_0}{\Gamma_0 + \Gamma^*}, \quad (1)$$

In general, for any practical implementation in quantum information processing $I \geq 0.5$ [33]. The pure dephasing rates at room temperature of solid-state quantum emitters like color centers, quantum dots or organic molecules are about 3 to 6 orders of magnitude larger than their radiative decay rates [34]. Improvement of this efficiency can be achieved by working at cryogenic temperatures. For example, for excitons weakly confined in GaAs quantum dots the dot ground-state transition at low temperature is near radiative life-time limited [13] which would provide a balance of about $\Gamma^*/\Gamma_0 \approx 1$ and $I \approx 0.5$. There are recent reports of even better performance with strain free GaAs/AlGaAs quantum dots without the need of Purcell enhancement [35]. For those highly efficient emitters the ratio $\Gamma^*/\Gamma_0 \rightarrow 0$ and the intrinsic indistinguishability tends to the unity. As an example of an intermediate situation, InAs quantum dots have decay and pure dephasing rates $\Gamma^*/\Gamma_0 = 2.6$ [36,37] and the indistinguishability is only $I \approx 0.19$. On the opposite side, strain-induced defects in 2D materials have typical radiative lifetimes in the order of nanoseconds with dephasing lifetimes in the order of picoseconds [14]. For those emitters the

Γ^*/Γ_0 balance reaches 10^3 with almost zero indistinguishability. However, recent works related to defects created in transition metal dichalcogenides (like MoS₂) by local helium ion irradiation [38] show radiative lifetimes < 150 ps. Also, a lifetime < 100 ps has been observed recently in regular strain induced defects in WSe₂ layers deposited on metallic surfaces [39, 40]. More examples of quantum emission demonstrations in 2D materials can be found in [41]. Therefore, emitters with a certain Γ^*/Γ_0 ratio may enhance significantly their indistinguishability when properly integrated inside photonic waveguides due to the change in their radiative decay rate. We will show that for certain geometries and emitter positions I can be greatly reduced whereas optimal configurations can maintain or even enhance I significantly, especially for emitters with a certain Γ^*/Γ_0 ratio.

2.2. Analytic model for pure dephasing

We can assume that for a two-level emitter coupled to a waveguide the coupling (g) and the cavity decay rate (κ) are in the incoherent limit ($2g \ll \Gamma_0 + \Gamma^* + \kappa$) and “bad cavity” regime ($\kappa \gg \Gamma_0 + \Gamma^*$) [34]. In that limit the cavity can be adiabatically eliminated so the dynamics of the coupled system are described by an effective quantum emitter with decay rate ($\Gamma + R$) where R is the population transfer between the emitter and the cavity [34]:

$$I = \frac{(\Gamma_0 + R)}{(\Gamma_0 + R) + \Gamma^*} ; R = \frac{4g^2}{\Gamma_0 + \Gamma^* + \kappa} , \quad (2)$$

R is related to the Purcell enhancement (P_f) by $R = \Gamma_0 \cdot P_f$ [42]. Substituting in Eq. (2) we obtain:

$$I = \frac{(1 + P_f)}{(1 + P_f) + \frac{\Gamma^*}{\Gamma_0}} , \quad (3)$$

here the Purcell enhancement is defined as Γ/Γ_0 where Γ is the population decay rate in the inhomogeneous environment. This ratio is related to the power emitted by the source [43]:

$$\frac{\Gamma}{\Gamma_0} = \frac{P}{P_0} , \quad (4)$$

with P and P_0 the power emitted in the inhomogeneous and homogeneous environment, respectively. The radiative decay rate enhancement can be obtained by FDTD simulations integrating the power emitted by the source inside the waveguide (P) and normalizing it with respect to the power in a homogeneous surrounding (P_0). In order to extract the maximum amount of physical information from the interaction between the quantum emitter and the photonic waveguide, we develop an analytic model of the system. We use the relation between Γ and the Green dyadic of the equation governing the interaction between the source and the waveguide. From Eq. (4) one can obtain the dependence of the decay rate with the imaginary part of the Green dyadic evaluated at the position of the source [43]:

$$\Gamma = \frac{4\omega^2}{\pi c^2 \hbar \epsilon_0} \left[\vec{\mu} \cdot \text{Im} \left\{ \vec{G}(r_0, r_0) \right\} \cdot \vec{\mu} \right] , \quad (5)$$

where ω is the frequency of emission of the source, ϵ_0 is the vacuum dielectric constant, c the speed of light in vacuum, \hbar the reduced Planck constant, and μ the dipole moment of the source. Figure 1 shows a layout of a section of the waveguide used for our model. The waveguide (infinite in the z -axis) has a rectangular section filled with a linear homogeneous medium with refractive index n_1 . The surrounding environment has a refractive index $n_2 = 1$.

The calculation of the Green’s Dyadic is based on the development of a 3D transform theory applied to the unbounded Helmholtz equation. Details of the calculation and the explicit

dependence with the waveguide width and the position/orientation of the source (for each contributing guided mode) can be found in the [Supplement 1](#). Using the Green's dyadic we can obtain the Purcell enhancement as a function of the waveguide width for a point dipolar source that can be oriented parallel to the x -axis (s) or to the y -axis (p). The source is placed initially at the center of the waveguide cross-section ($x_0 = 0, y_0 = 0$). Initially, the waveguide thickness is arbitrarily fixed at $b = 200$ nm and we will change the width (a) and the refractive index of the waveguide (n_1) using $n_1 = 1.44, 2$ and 3.4 corresponding to SiO₂, SiN and Si respectively. This will provide some initial hints on how the system actually behaves.

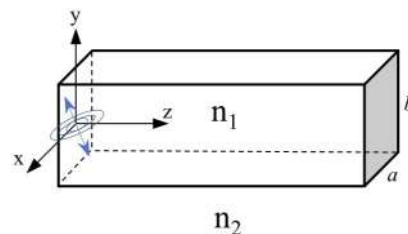


Fig. 1. Layout of the homogeneous infinite waveguide used for the analytical model.

Figure 2 shows the value of the Purcell enhancement, Γ/Γ_0 , as a function of the normalized waveguide width, a/λ , for the mentioned values of n_1 (1.44, 2, 3.4). Solid lines show the calculation of Γ/Γ_0 using Eq. (5) and open dots show the values obtained through FDTD simulations. Details of the FDTD simulations can be found in the [Supplement 1](#). Figure 2(a) shows the Purcell enhancement for the s -source. In general, it almost vanishes before the width reaches the cut-off of the TE₁₀ mode, which happens for $a/\lambda = 0.13, 0.1$ and 0.05 for $n_1 = 3.4, 2$ and 1.44 , respectively. Since the cut-off increases with n_1 , the vanishing threshold also increases with n_1 . After the cut-off, for increasing a/λ , The Purcell enhancement increases as the propagation constant decreases (with $1/a$) and the mode gets more confined. The maximum values for Γ/Γ_0 are 0.83, 1 and 1 when $a/\lambda = 0.23, 0.42$ and 0.64 respectively and the light confinement is maximum. If the waveguide becomes wider the modes spread out with lower intensity at the position of the source producing a decrease in Γ/Γ_0 that scales with $1/a$, until the cut-off with the second order mode is reached at $a/\lambda = 0.43, 0.8$ and 1.2 for the same values of n_1 . At this point, the same mechanism takes place showing the second maxima and second decay. The process is repeated for each contributing mode. We note that there is no contribution from the lowest TM₀₀ mode because the components of the Green dyadic vanish at the position of the source for this orientation. This is expected since the x -components of the fundamental modes are antisymmetric with respect to the source when it is placed at the center. For the p -source [Fig. 2(a)] the situation is somewhat opposite and the components do not vanish at the position of the source for the lowest order TM₀₀. Since $b = 200$ nm, in the case of $n_1 = 2$ and $n_1 = 1.44$ the cut-off condition is already reached at $a/\lambda = 0$. For $n_1 = 3.4$ the cut-off is reached at $a/\lambda = 0.05$. The Purcell enhancement for the s -source shows maximum values of $\Gamma/\Gamma_0 = 1.2, 0.51$ and 0.6 when $a/\lambda = 0.13, 0.27$ and 1 for the same values of n_1 than before. For both s and p orientations the Purcell enhancement decays asymptotically with the width, although in a different trend due to the different (m, n) values for each contributing mode. The maxima located at $a/\lambda = 0$ are accidentally generated by the model due to the unphysical divergence of the Green function at the origin. The maximum values of Γ/Γ_0 for the s -source are about 40% higher than for the p -source with $n_1 = 2$ and $n_1 = 1.44$. The reason is the transverse electric field component of the TE₁₀, which is higher than the TM₀₀ at the position of the source ($x_0 = 0, y_0 = 0$) [44]. Nevertheless, for $n_1 = 3.4$ the maximum Γ/Γ_0 is about 40% higher for the p -source. This happens because when $n_1 = 2$ and $n_1 = 1.44$ the TE₁₀ mode is well confined for $b = 200$ nm, but when $n_1 = 3.4$ the TE₁₀

mode is not optimally confined and the source has a better overlap with the TM_{00} . Therefore, high modal confinement and good spatial overlapping to waveguide modes are key ingredients for Purcell enhancement, as one could intuitively expect. The indistinguishability should show its maximum value when the Purcell enhancement is maximum, according to Eq. (3). We note that a deviation in the optimal width of about 20 nm can decrease the Purcell enhancement, and therefore the indistinguishability, about 10%.

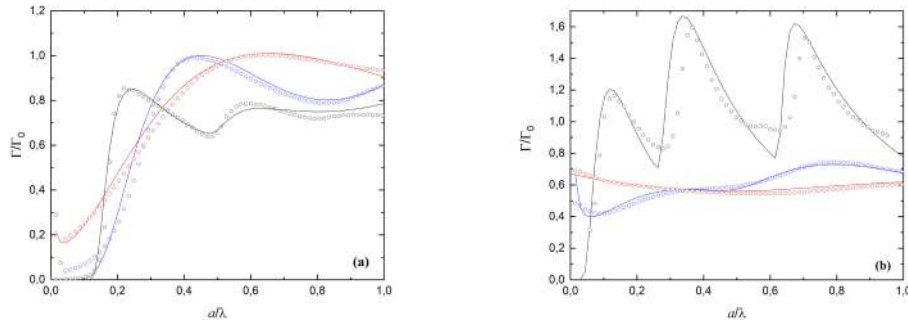


Fig. 2. Purcell enhancement of the radiative decay rate as a function of the wavelength-normalized waveguide width obtained from analytical calculations (lines) and FDTD simulations (open dots). $n_1 = 3.4$ (black), $n_1 = 2$ (blue), $n_1 = 1.44$ (red). (a) Source orientation parallel to x -axis (s); (b) Parallel to y -axis (p).

Since the position of the emitter is very relevant, we explore now its effect keeping fixed the waveguide widths in $a/\lambda=0.23$, 0.42 and 0.64 (respectively to the n_1 values as before) and for the s orientation. We change the position of the source along the x -axis, from the center of the waveguide ($x_0/a=0$) to far away from the edge ($x_0/a>\pm 1$).

First we focus on the region inside the waveguide core ($x_0/a<\pm 1$). Figure 3(a) shows the Purcell enhancement depending on the position of the s -source. As the s -source is separated from the center the overlapping to symmetric modes decreases and the enhancement decreases. The maximum enhancement happens at the center of the waveguide. A deviation from that optimal position of about $x_0/a=\pm 0.5$ leads to a decrease of the Purcell enhancement of about 20%. The opposite behavior is obtained for a p -source [Fig. 3(b)]. In this case the minimum overlapping is obtained at the center of the waveguide and the maximum enhancement is for about $x_0/a=\pm 0.75$, where the overlap with the antisymmetric modes is maximum. FDTD simulations provide a maximum value for the enhancement of 1.42 matching the analytical calculations within an error of 0.2% for the Purcell enhancement and 0.3% for x_0 .

The variation of the *coupling efficiency* with the position of the source inside the waveguide follows a similar trend than the Purcell enhancement. Details of coupling definition and its calculation can be found in the [Supplement 1](#). Figure 4 shows the coupling efficiency depending on the position of the source for both s and p orientations. At the center of the waveguide, the s -source achieves a maximum coupling of $P_c/P_0 = 0.88, 0.6$ and 0.25 for $n_1 = 3.4, 2$ and 1.44 respectively, where P_c is the emitted power coupled to guided modes. As expected, the coupling decreases with decreasing n_1 . When the s -source is separated from the center, the coupling to symmetric modes decreases. Again, the opposite behavior is obtained for the p -source, which shows minimum coupling at the center of the waveguide. Some discrepancies between analytic and FDTD results arise from the discretization of space in the FDTD simulations. Also, the slight asymmetries shown in the x_0/a dependence in Fig. 4(b) are due to small misalignments between the simulation cells and the dielectric waveguide.

Since there are recent experimental works that use heterogeneous integration of SPS and waveguides [45,46] it is worth to explore the dependence of the enhancement with the position of

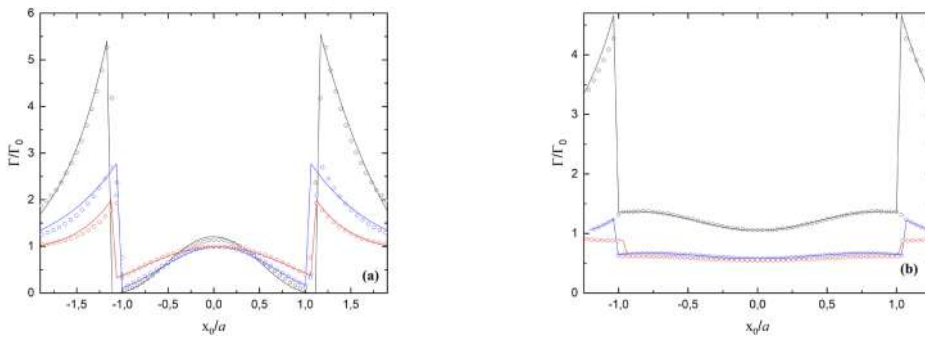


Fig. 3. Enhancement of the radiative decay rate as a function of the position of the point source (normalized with respect to the waveguide width, (a) obtained from the analytical model (lines) and from FDTD simulations (open dots). The origin in the x -axis corresponds to the center of the waveguide and the edges to $x_0/a=\pm 1$. $n_1 = 3.4$ (black), $n_1 = 2$ (blue), $n_1 = 1.44$ (red). (a) s -source (b); p -source.

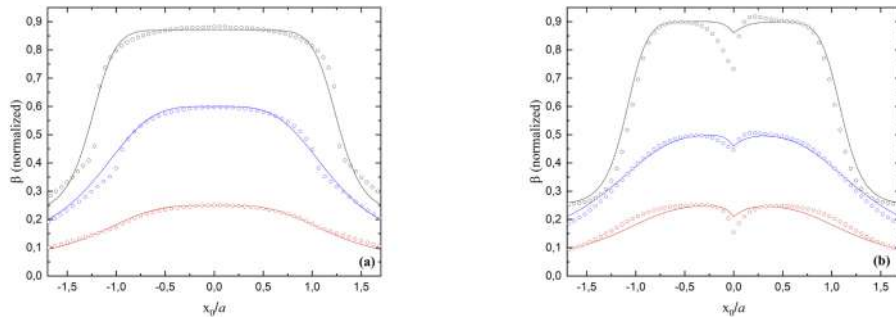


Fig. 4. Coupling efficiency versus normalized position of the source with respect to waveguide width a . The origin in the x -axis corresponds to the center of the waveguide. The edges of the waveguide correspond to $x_0/a=\pm 1$. Figure shows results from analytical model (lines) and from FDTD simulations (open dots). $n_1 = 3.4$ (black), $n_1 = 2$ (blue), $n_1 = 1.44$ (red). (a) s -source; (b) p -source.

the source in the region outside the waveguide but close to its edge ($x_0/a > \pm 1$). Due to the index contrast between air and waveguide the electric field shows a strong discontinuity at the interface with an amount comparable to the square of the index ratio at the interface [47]. This effect can lead to a dramatic alteration of the mode profile in the vicinity of the edge that drastically increments the Purcell enhancement. This effect has been used, for example, to achieve ultrasmall cavity mode volumes of the order of $7 \times 10^{-5} \lambda^3$ that enable ultra-strong Kerr nonlinearities at the single-photon level [48]. When the source is placed at the edge the enhancement is $\Gamma/\Gamma_0=4.2$, 2.6 and 1.9 for the s -source, and $\Gamma/\Gamma_0=4.6$, 1.2 and 0.87 for the p -source. The cost of the increase in the Purcell enhancement is a decrease in the coupling efficiency, which for the position at the edge is about $P_c/P_0 = 0.5$, 0.37 and 0.15 for the s -source and about $P_c/P_0 = 0.5$, 0.3 and 0.12 for the p -source. Details about this calculation can be seen in the [Supplement 1](#). At the points $x_0/a=\pm 1$ (i.e., the edges of the waveguide) the mode field shows its highest contrast according to $E_{\text{clad}} = (n_1/n_2)^2 E_{\text{core}}$ where E_{core} is the field inside the waveguide and E_{clad} is the field outside the waveguide. For that reason, the maximum value of the Purcell enhancement lies in the edges of the waveguide, especially for high n_1 . Since the Purcell enhancement is strictly dependent on the field value at the position of the source, its maximum value is achieved at the edge of the waveguide. On the other hand, the coupling is proportional to the guided-mode field value

divided by the non-guided modes field value. Despite the guided-mode field value is maximum at the edge, the value of non-guided modes is also maximum at the edge. In consequence, the coupling at the edge is weaker than in the center of the core (where the coupling to non-guided modes is smaller).

Now that we have a better understanding of the physical meaning of the model we can explore simultaneously both degrees of freedom (i.e., a and b) in order to find the optimal configurations in terms of the figures of merit. The source is placed initially at the center of the waveguide cross-section ($x_0 = 0$, $y_0 = 0$) in horizontal orientation (i.e., parallel to x -axis) but this time both a and b are varied from 0 to 0.7λ . The results are obtained for four different values of the refractive index of the waveguide $n_1 = 1.44, 2, 3.4$, and 4.

Figure 5 shows the value of Γ/Γ_0 as a function of the normalized waveguide width, a/λ , and normalized thickness, b/λ , calculated for the four different refractive indexes. The blue areas in the plots correspond to values of a and b below the first cut-off. The subsequent maxima and minima correspond to the activation of the TE_{mn} and TM_{mn} modes. For low refractive indexes (i.e., $n_1 = 1.44, 2$) the two first modes appear. As the refractive index increases the source starts to overlap effectively with the rest of higher order modes. The absolute maxima of Γ/Γ_0 increases with the refractive index, since the area of the spatial distribution of the modes decreases with n_1 , so the field intensity gets higher at the position of the source. We obtain maximum values of $\Gamma/\Gamma_0 = 1, 1.1, 1.6$ and 1.9 for $n_1 = 1.44, 2, 3.4$ and 4, respectively. Due to the symmetry of the system the plots for the vertical source show the same rotated 90 degrees (see Supplement 1).

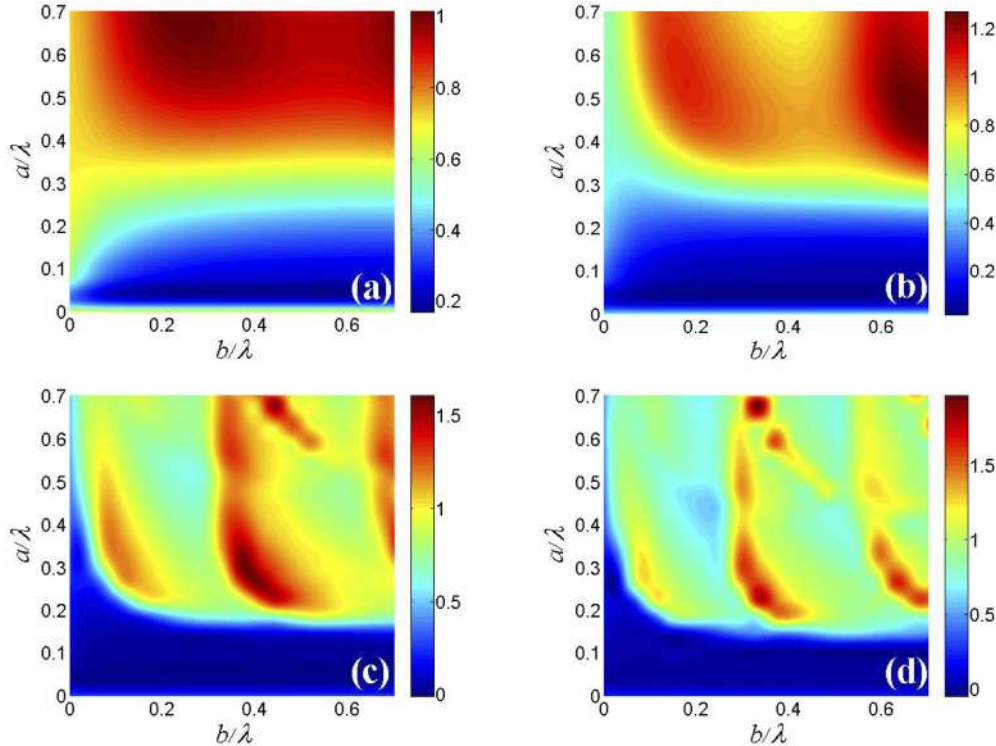


Fig. 5. Purcell enhancement as a function of the normalized width, a/λ , and thickness, b/λ , when the s -source is placed at the center of the waveguide calculated with the analytical model. (a) $n_1 = 1.44$; (b) $n_1 = 2$; (c) $n_1 = 3.4$; (d) $n_1 = 4$.

Next, we place the source outside the waveguide, 10 nm away from the edge and oriented horizontally (i.e., parallel to x -axis). Figure 6 shows the value of Γ/Γ_0 as a function of the

normalized waveguide width, a/λ , and normalized thickness, b/λ , for different n_1 . As we saw before, the field discontinuity generates a dramatic enhancement when the source is placed near the evanescent region of the mode. We observe that in all of the cases the maxima are located in the bottom left region, where both a and b have reached the cut-off but the first mode has not reached the maximum confinement. For that geometry, the mode is not optimally confined inside the core and the field gets accumulated at the edges of the waveguide so the overlap is more efficient. We obtain maximum values of $\Gamma/\Gamma_0 = 2, 3.5, 8$ and 10 for $n_1 = 1.44, 2, 3.4$ and 4 respectively. At this time the orientation of the source matters, since we can arrange two different configurations: (a) Parallel to the larger side of the waveguide (i.e., parallel to the x -axis if the source is placed on top of the core, or parallel to the y -axis if the source is placed on one side of the core); (b) Perpendicular to the larger side of the waveguide (i.e., parallel to the y -axis if the source is placed on top of the core, or parallel to the x -axis if the source is placed on one side of the core). The plots in Fig. 6 correspond to the second case. When the source is parallel we obtain lower values for the maximum enhancements: $\Gamma/\Gamma_0 = 0.9, 1.5, 6.8$ and 7.1 for the different values of n_1 . For emitters with orientations other than s or p one should decompose the projection of the orientation on the x -axis and the y -axis and treat the emitter as two separated emitters with corresponding s and p contributions. The total enhancement is given by the addition of those two contributions.

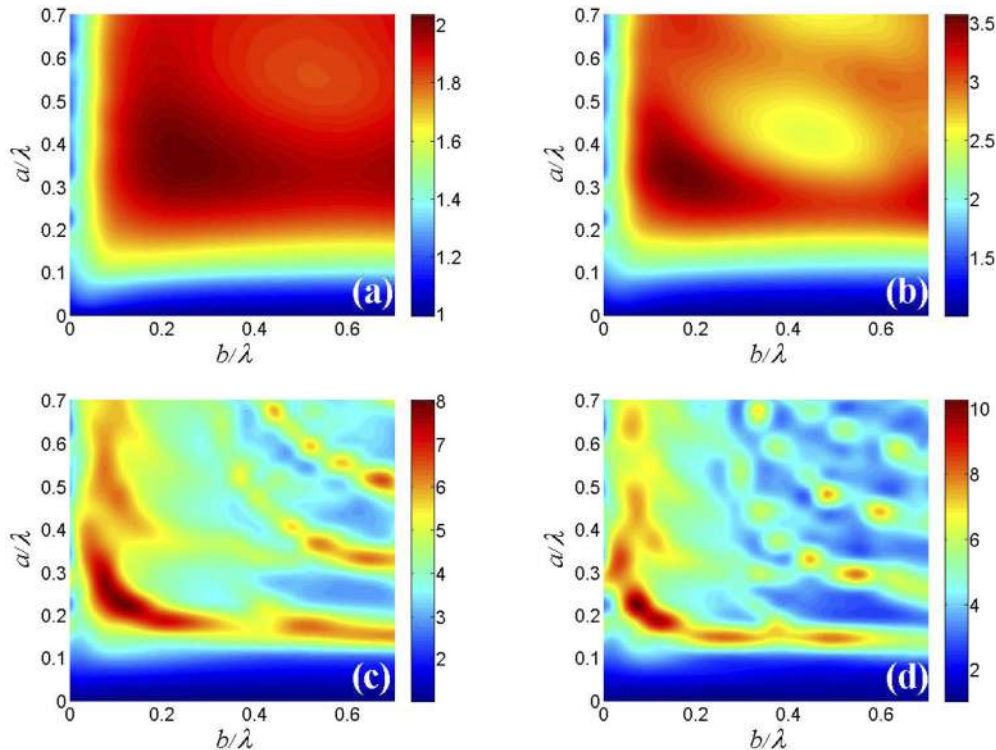


Fig. 6. Purcell enhancement as a function of a/λ and b/λ when the s -source is placed outside the core calculated with the analytical model. (a) $n_1 = 1.44$, (b) $n_1 = 2$, (c) $n_1 = 3.4$, (d) $n_1 = 4$.

The maximum enhancements obtained for the source at the edge can be used in Eq. (3) to obtain the maximum values for the indistinguishability. Figure 7 shows I for an s -emitter placed at the edge of the waveguide versus the intrinsic emitter normalized dephasing ratio, Γ^*/Γ_0 . Results for the p -source show an analogous behavior. From Fig. 7 we see that for low

dissipative emitters with $\Gamma^*/\Gamma_0 \sim 1$ (like weakly confined GaAs dots of Ref. [13]) the expected indistinguishability can reach a value up to 0.8 when $n_1 = 4$, which makes an enhancement of I of about 30% with respect to the same dots without coupling to a waveguide. For InAs quantum dots with $\Gamma^*/\Gamma_0 = 2.6$ [36,37] we obtain $I \approx 0.6$, an enhancement of 40%. As the pure dephasing rate increases the indistinguishability decays asymptotically reaching 0.2 when $\Gamma^*/\Gamma_0 = 50$. Therefore for strong dissipative systems with $\Gamma^*/\Gamma_0 > 50$ (like quantum emitters in 2D materials) the effect of the waveguide in the indistinguishability is very small. For emitters with lower dephasing ratio, $\Gamma^*/\Gamma_0 < 1$, and high intrinsic indistinguishability ($I >> 0.5$) the effect of the waveguide becomes again negligible since $I \rightarrow 1$ when $\Gamma^*/\Gamma_0 \rightarrow 0$. As n_1 increases the maximum Γ^*/Γ_0 for $I >> 0.5$ also increases reaching values up to 12 for $n_1 = 4$.

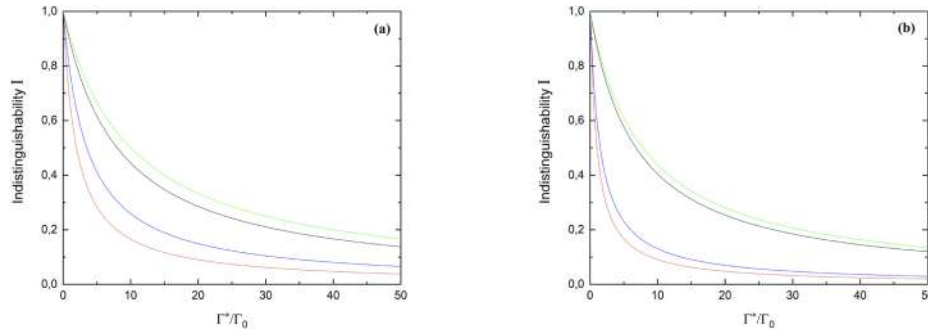


Fig. 7. Indistinguishability of an *s*-source quantum emitter placed at the edge of the waveguide versus its $\frac{\Gamma^*}{\Gamma_0}$ value. Green- $n_1 = 4$, Black- $n_1 = 3.4$, Blue- $n_1 = 2$, Red- $n_1 = 1.44$. (a) Perpendicular-source. (b) Parallel-source.

Despite a SPS can achieve much stronger Purcell enhancements inside optical cavities [49], it is often required small mode volumes or high quality factors, or both. Small mode volumes difficult the deposition of the emitter at the field maxima [50], and on the other hand, high quality factors reduce the extraction efficiency [34]. In the case of waveguide integration, deposition at the field maxima (i.e., edge of the waveguide) becomes trivial, and as it has been shown, high extraction efficiency can be achieved. However, our results also reveal that for strong dissipative SPS integrated in a waveguide the indistinguishability does not reach the standard requirements for quantum information applications. For those cases the use of an optical cavity is mandatory.

From a practical perspective, the heterogeneous integration of the emitter with a waveguide may be performed by placing the emitter inside a material with non-unity refractive index (i.e., $n_2 \neq 1$) [45], it is worth to explore how the Purcell enhancement is affected by different index contrasts. As we mentioned above, the field discontinuity at the edge of the waveguide is proportional to $(n_1/n_2)^2$, so we can expect a significant reduction of the enhancement depending on n_2 .

Figure 8(a) shows the dependence of the Purcell enhancement with n_2 for an *s*-source placed at the edge of the waveguide with optimal *(a,b)* geometry. Since the Purcell enhancement in the edge depends on the index contrast n_1/n_2 , it decreases asymptotically with n_2 . In the limit where $n_2 \sim 1$ the Purcell value approaches to that shown in Fig. 6, and when $n_2 \sim n_1$ we obtain the emitter decay rate corresponding to a homogeneous material (i.e., $P_f = 1$). For cladding materials like SiO₂ ($n_2 = 1.44$) the Purcell enhancement is reduced about 50% with respect to the value with $n_2 = 1$. On the other hand, Fig. 8(b) shows the reduction in the indistinguishability due to this lower Purcell enhancement for an emitter with $\Gamma^*/\Gamma_0 = 10$. Similarly to what happened to the Purcell enhancement, when $n_2 \sim 1$ the indistinguishability approaches to that shown in Fig. 7, and when $n_2 \sim n_1$ we obtain the value corresponding to the specific Γ^*/Γ_0 ratio in a homogeneous material (i.e., $I = 0.1$). Again, for $n_2 = n_{\text{SiO}_2}$ the indistinguishability is reduced about 15% with respect to $n_2 \sim 1$. Regarding the optimization sweep for finding the optimal waveguide height and

width for the case of n_2 in the range (1–1.6) the results are almost equivalent to that shown in Fig. 6 (case of $n_1 = 1.44$). Therefore Fig. 6 can be used as a guide for waveguide design when n_2 is inside that range.

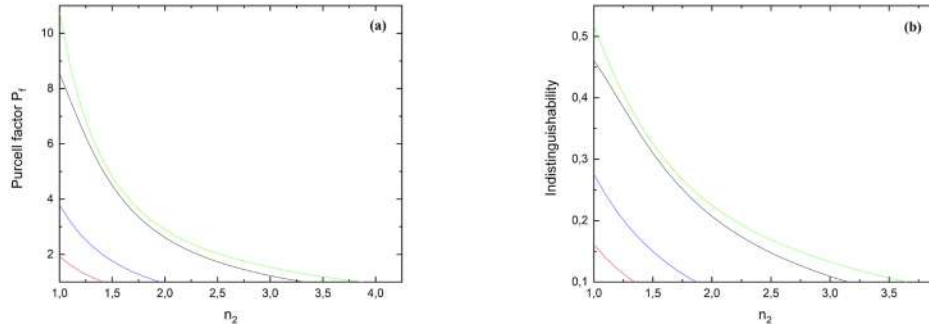


Fig. 8. (a) Purcell enhancement of an *s*-source at the edge of the waveguide as a function of n_2 . (b) Indistinguishability of an *s*-source at the edge of the waveguide as a function of n_2 .

It is important to highlight that the positions for maximum indistinguishability differ from those of maximum coupling efficiency. Indistinguishability depends strongly on Purcell enhancement, which for the case of a waveguide achieves its maximum value at the edge, where the field is strongest. On the other side, the coupling efficiency on the edge is not as high as in the center, but still may have a value useful for some experiments or even some applications. An interesting figure of merit for the geometrical optimization of the waveguide is the $I \cdot \beta$ product (with β the coupling efficiency) that can be explored as a function of a and b . In the same way we did for the optimization of the Purcell enhancement, a and b change from 0 to 0.7λ , and the emitter is placed at the edge of the waveguide. We set $n_2 = 1.44$ this time and we vary $n_1 = 2, 3.4, 4$ and 4.4 . For the estimation of the indistinguishability we set $\Gamma^*/\Gamma_0=10$ as before.

Figure 9 shows the $I \cdot \beta$ value as a function of the normalized waveguide width, a/λ , and normalized thickness, b/λ , calculated for $n_1 = 2, 3.4, 4$ and 4.4 . As expected, for the four refractive indexes the highest $I \cdot \beta$ happens for the geometry that maximizes the Purcell enhancement. Maximum $I \cdot \beta = 0.35$ is found for the highest waveguide index ($n_1 = 4.5$) and minimum $I \cdot \beta = 0.15$ for $n_1 = 2$. Also, in the four cases the $I \cdot \beta$ product is significantly higher than the obtained when the source is at the center of the waveguide (0.06 for $n_1 = 2$, 0.09 $n_1 = 3.4$, and 0.13 for $n_1 = 4$).

2.3. Analytic model for spectral diffusion

We have explored so far the effect of pure dephasing in the indistinguishability. In addition, the effect of spectral diffusion needs to be treated separately. Whereas the dynamics of pure dephasing evolve at shorter time scales than the emitter decay rate Γ_0 , spectral diffusion is related to processes with significantly larger time scales [51] so it is characterized by a statistical average over the different center frequencies associated with the emitter [52]. In this context, the spectral broadening of the emission is given by $\Gamma_2 = \Gamma_0 + \Gamma'$, where Γ' represents the FWHM of the distribution associated with spectral diffusion. The indistinguishability reads $I = \Gamma_0/\Gamma_2$ [51]. Being $\Delta\omega$ the intrinsic width of each center frequency, and $\Delta\delta$ the extrinsic width due to the entanglement with the extrinsic environment, for a Lorentzian distribution the ratio $\theta = \Delta\delta/\Delta\omega$ is equal to $2\Gamma'/\Gamma_0$ [52]. The indistinguishability can be written in terms of θ as:

$$I = \frac{\Gamma/\Gamma_0}{\Gamma/\Gamma_0 + \frac{\theta}{2}}, \quad (6)$$

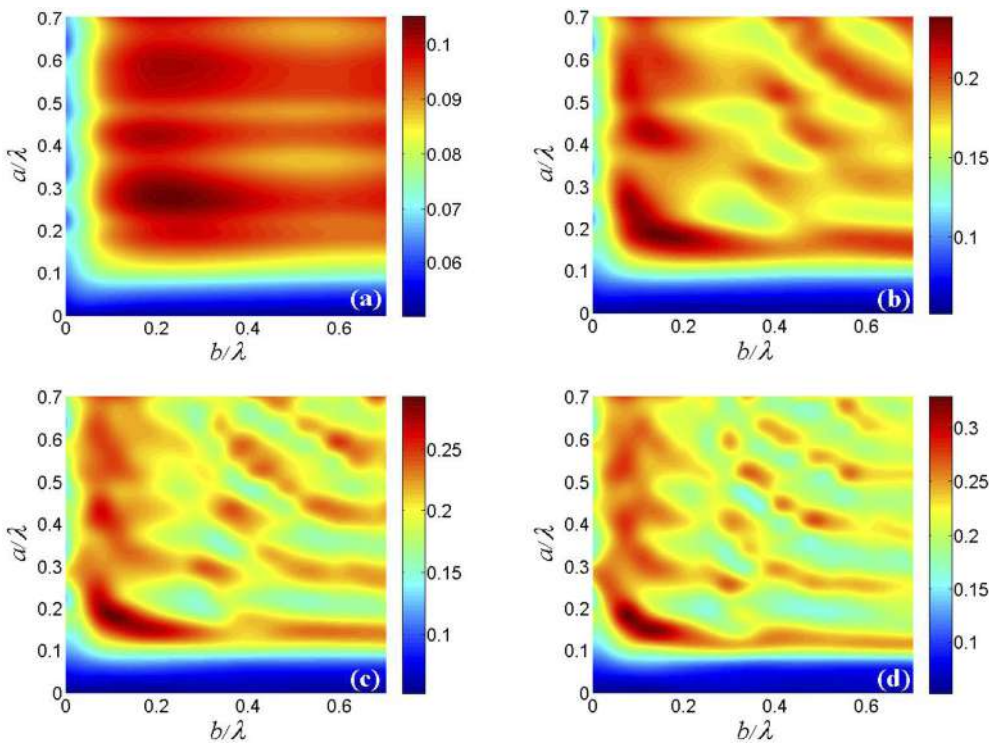


Fig. 9. $I\beta$ value as a function of the normalized width, a/λ , and thickness, b/λ , when the s -source is placed at the edge of the waveguide with $n_2 = 1.44$ calculated with the analytical model. (a) $n_1 = 2$, (b) $n_1 = 3.4$, (c) $n_1 = 4$, (d) $n_1 = 4.5$.

with Γ the enhanced decay rate due to Purcell effect. As we did in the previous section, we can use the maximum enhancements obtained for the source at the edge in Eq. (6) to obtain the maximum values for the indistinguishability.

Figure 10 shows I for s - and p -emitters placed at the edge of the waveguide versus the normalized ratio θ . From Fig. 1 we see that for emitters with $\theta \sim 1$ [13] the expected indistinguishability is above 0.9 for the four refractive indexes. As the extrinsic width of the

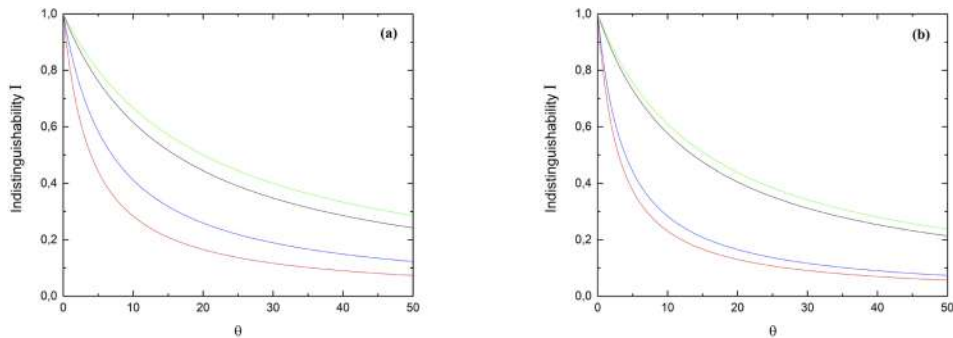


Fig. 10. Indistinguishability of an s -source quantum emitter placed at the edge of the waveguide versus its $\theta <$ value. Green- $n_1 = 4$, Black- $n_1 = 3.4$, Blue- $n_1 = 2$, Red- $n_1 = 1.44$. (a) Parallel-source. (b) Perpendicular-source.

emitter increases respect to the intrinsic width the indistinguishability decays asymptotically reaching 0.3 when $\theta = 50$ for $n_1 = 4$ and $\theta = 10$ for $n_1 = 1.44$. Therefore, for emitters with extrinsic width much larger than intrinsic width the effect of the waveguide in the indistinguishability is negligible. As n_1 increases the maximum θ for $I >> 0.5$ also increases reaching values up to 21 for $n_1 = 4$. We can say that in general we observe a similar behavior to pure dephasing although with a slower asymptotic decay of I .

3. Conclusions

We have calculated the indistinguishability of a point-source quantum emitter coupled to a waveguide because its technological implications in future quantum photonic integrated circuits. The emitter has arbitrary orientation and location with respect to the waveguide. We have obtained the results for different index of refraction of the waveguide (SiO_2 , Si_3N_4 , Si, and other high index materials like WeS_2 or WO_3). The analytical model used permits a fast computing of the indistinguishability from a set of simple expressions derived from the same solution of the dyadic Helmholtz equation. The model has been numerically evaluated through 3D-FDTD simulations with excellent agreement. Maximum indistinguishability for an optimal waveguide width is found for a source placed outside the core, at the edge of the waveguide, in contrast to maximum coupling efficiency position at the center of the waveguide. For strong dissipative emitters with $\Gamma^*/\Gamma_0 > 50$ (like transition metal dichalcogenides) the effects of the waveguide in the indistinguishability are negligible but for low dissipative emitters with $\Gamma^*/\Gamma_0 \approx 1$ (like GaAs quantum dots) the indistinguishability can be enhanced up to a 30% and reach values around $I \approx 0.8$ when dots are coupled to a waveguide. We hope this work can help for an optimized design of PIC waveguides in quantum photonic circuits.

Funding. Horizon 2020 Framework Programme (820423).

Acknowledgments. We gratefully acknowledge financial support from the European Union's Horizon 2020 research and innovation program under grant agreement No. 820423 (S2QUIP).

Disclosures. The authors declare that there are no conflicts of interest related to this article.

Data availability. All the data generated and analyzed in this work are available upon request.

Supplemental document. See [Supplement 1](#) for supporting content.

References

1. A. Aspuru-Guzik and P. Walther, "Photonic quantum simulators," *Nat. Phys.* **8**, 285–291 (2012).
2. D. Fattal, E. Diamanti, K. Inoue, and Y. Yamamoto, "Quantum teleportation with a quantum dot single photon source," *Phys. Rev. Lett.* **92**, 037904 (2004).
3. H. Kimble, "The quantum internet," *Nature (London)* **453**, 1023–1030 (2008).
4. M. Eisaman, J. Fan, A. Migdall, and S. Polyakov, "Invited Review Article: Single-photon sources and detectors," *Rev. Sci. Instrum.* **82**, 071101 (2011).
5. C. Santori, D. Fattal, J. Vučković, G. S. Solomon, and Y. Yamamoto, "Indistinguishable photons from a single-photon device," *Nature* **419**, 594–597 (2002).
6. Y. Chen, J. Zhang, M. Zopf, K. Jung, Y. Zhang, R. Keil, and O. G. Schmidt, "Wavelength-tunable entangled photons from silicon-integrated III–V quantum dots," *Nat. Commun.* **7**, 1–7 (2016).
7. S. Khasminskaya, F. Pyatkov, K. Słowik, S. Ferrari, O. Kahl, V. Kovalyuk, P. Rath, A. Vetter, F. Hennrich, M. M. Kappe, G. Gol'tsman, A. Korneev, C. Rockstuhl, R. Krupke, and W. H. P. Pernice, "Fully integrated quantum photonic circuit with an electrically driven light source," *Nat. Photonics* **10**, 727–732 (2016).
8. S. L. Mouradian, T. Schröder, C. B. Poitras, L. Li, J. Goldstein, E. H. Chen, and M. Lipson, "Scalable integration of long-lived quantum memories into a photonic circuit," *Phys. Rev. X* **5**, 031009 (2015).
9. A. Sipahigil, R. E. Evans, D. D. Sukachev, M. J. Burek, J. Borregaard, M. K. Bhaskar, and R. M. Camacho, "An integrated diamond nanophotonics platform for quantum-optical networks," *Science* **354**, 847–850 (2016).
10. F. Peyskens, C. Chakraborty, M. Muneeb, D. Van Thourhout, and D. Englund, "Integration of single photon emitters in 2D layered materials with a silicon nitride photonic chip," *Nat. Commun.* **10**, 4435–4437 (2019).
11. A. Kiraz, M. Ehrl, T. Hellerer, ÖE Müstecaplıoğlu, C. Bräuchle, and A. Zumbusch, "Indistinguishable photons from a single molecule," *Phys. Rev. Lett.* **94**, 223602 (2005).
12. J. M. Gérard, B. Sermage, B. Gayral, B. Legrand, E. Costard, and V. Thierry-Mieg, "Enhanced spontaneous emission by quantum boxes in a monolithic optical microcavity," *Phys. Rev. Lett.* **81**, 1110–1113 (1998).

13. D. Gammon, E. S. Snow, B. V. Shanabrook, D. S. Katzer, and D. Park, "Homogeneous linewidths in the optical spectrum of a single gallium arsenide quantum," *Science* **273**, 87–90 (1996).
14. I. Aharonovich, D. Englund, and M. Toth, "Solid-state single-photon emitters," *Nat. Photonics* **10**, 631–641 (2016).
15. L. Dusanowski, D. Köck, E. Shin, S. H. Kwon, C. Schneider, and S. Höfling, "Purcell enhanced and indistinguishable single-photon generation from quantum dots coupled to on-chip integrated ring resonators," *Nat. Photonics* **20**, 6357–6363 (2020).
16. X. Qiang, X. Zhou, J. Wang, C. M. Wilkes, T. Loke, S. O'Gara, and J. B. Wang, "Large-scale silicon quantum photonics implementing arbitrary two-qubit processing," *Nat. Photonics* **12**, 534–539 (2018).
17. J. Wang, F. Sciarrino, A. Laing, and M. G Thompson, (2019). "Integrated photonic quantum technologies," *Nat. Photonics* 1–12.
18. S. Slussarenko and G. J. Pryde, "Photonic quantum information processing: A concise review," *Appl. Phys. Rev.* **6**, 041303 (2019).
19. C. T. Chen, J. Pedrini, E. A. Gaulding, C. Kastl, G. Calafiole, S. Dhuey, and A. M. Schwartzberg, "Very high refractive index transition metal dichalcogenide photonic conformal coatings by conversion of ALD metal oxides," *Sci. Rep.* **9**, 1–9 (2019).
20. Y. He, S. He, J. Gao, and X. Yang, "Nanoscale metamaterial optical waveguides with ultrahigh refractive indices," *J. Opt. Soc. Am. B* **29**, 2559–2566 (2012).
21. W. Huang, A. B. Yakovlev, A. A. Kishk, and A. W. Glisson, (2006). *Dyadic Greens Function of the Hard Surface Rectangular Waveguide Verified Numerically by a Realistic Model*. In 2006 IEEE Antennas and Propagation Society International Symposium (pp. 2249–2252). IEEE.
22. W. Huang, A. B. Yakovlev, A. A. Kishk, A. W. Glisson, and I. A. Eshrah, "Green's function analysis of an ideal hard surface rectangular waveguide," *Radio Sci.* **40**, 1–12 (2005).
23. X. Zhang, C. Xu, and W. Song, "Calculating higher order mode characteristics of heteromorphic waveguide by operator theory," in 2000 Asia-Pacific Microwave Conference. Proceedings (Cat. No. 00TH8522) (2000). pp. 970–974
24. P. M. Slobodzian, "On the dyadic Green's function in the source region embedded in waveguides or cavities filled with a stratified medium," *Microwave and Optical Technology Letters* **35**, 93–97 (2002).
25. V. A. Klymko, A. B. Yakovlev, I. A. Eshrah, A. A. Kishk, and A. W. Glisson, "Dyadic Green's function of an ideal hard surface circular waveguide with application to excitation and scattering problems," *Radio Sci.* **40**, 1–15 (2005).
26. S. Liu, L. W. Li, M. S. Leong, and T. S. Yeo, "Rectangular conducting waveguide filled with uniaxial anisotropic media: A modal analysis and dyadic Green's function," *Prog. Electromagn. Res.* **25**, 111–129 (2000).
27. S. R. J. Brueck, "Radiation from a dipole embedded in a dielectric slab," *IEEE J. Sel. Top. Quantum Electron.* **6**, 899–910 (2000).
28. C. Creatore and L. C. Andreani, "Quantum theory of spontaneous emission in multilayer dielectric structures," *Phys. Rev. A* **78**, 063825 (2008).
29. F. Santosa and R. Magnanini, "Wave propagation in a 2-D optical waveguide," *SIAM J. Appl. Math.* **61**, 1237–1252 (2001).
30. O. Alexandrov and G. Ciraolo, "Wave propagation in a 3-D optical waveguide," *Math. Models Methods Appl. Sci.* **14**, 819–852 (2004).
31. G. Ciraolo, F. Gargano, and V. Sciacca, "A computational method for the Helmholtz equation in unbounded domains based on the minimization of an integral functional," *J. Comput. Phys.* **246**, 78–95 (2013).
32. O. Alexandrov, "The far-field expansion of the Green's function in a 3-D optical waveguide," *Asymptot. Anal.* **52**, 157–171 (2007).
33. J. Bylander, I. Robert-Philip, and I. Abram, "Interference and correlation of two independent photons," *Eur. Phys. J. D*, **22**, 295–301 (2003).
34. T. Grange, G. Hornecker, D. Hunger, J. P. Poizat, J. M. Gérard, P. Senellart, and A. Auffèves, "Cavity-funneled generation of indistinguishable single photons from strongly dissipative quantum emitters," *Phys. Rev. Lett.* **114**, 193601 (2015).
35. E. Schöll, L. Hanschke, L. Schweickert, K. D. Zeuner, M. Reindl, S. F. Covre da Silva, and A. Rastelli, "Resonance fluorescence of gaas quantum dots with near-unity photon indistinguishability," *Nano Lett.* **19**, 2404–2410 (2019).
36. J. M. Gérard, O. Cabrol, and B. Sermage, *Appl. Phys. Lett.* **68**, 3123 (1996).
37. P. Borri, W. Langbein, S. Schneider, U. Woggen, R. L. Sellin, D. Ouyang, and D. Bimberg, "Ultralong dephasing time in InGaAs quantum dots," *Phys. Rev. Lett.* **87**, 157401 (2001).
38. J. Klein, M. Lorke, M. Florian, F. Siggel, L. Sigl, S. Rey, and P. Zimmermann, "Site-selectively generated photon emitters in monolayer MoS 2 via local helium ion irradiation," *Nat. Commun.* **10**, 1–8 (2019).
39. C. Chakraborty, N. Vamivakas, and D. Englund, "Advances in quantum light emission from 2D materials," *Nanophotonics* **8**, 2017–2032 (2019).
40. L. N. Tripathi, O. Iff, S. Betzold, L. Dusanowski, M. Emmerling, K. Moon, and C. Schneider, "Spontaneous emission enhancement in strain-induced WSe₂ monolayer-based quantum light sources on metallic surfaces," *ACS Photonics* **5**, 1919–1926 (2018).
41. R. Chaudhary, V. Raghunathan, and K. Majumdar, "Origin of selective enhancement of sharp defect emission lines in monolayer WSe₂ on rough metal substrate," *J. Appl. Phys.* **127**, 073105 (2020).
42. S. Wein, N. Lauk, R. Ghobadi, and C. Simon, "Feasibility of efficient room-temperature solid-state sources of indistinguishable single photons using ultrasmall mode volume cavities," *Phys. Rev. B* **97**, 205418 (2018).

43. L. Novotny and B. Hecht, "Principles of nano-optics," (Cambridge University Press, 2012), pp 58.
44. S. L. Chuang, "Physics of Optoelectronic Devices," in Wiley Series in Pure and Applied Optics (Wiley, 1995), 22.
45. P. Lombardi, A. P. Ovyan, S. Pazzaglia, G. Mazzamuto, G. Kewes, O. Neitzke, and C. Toninelli, "Photostable molecules on chip: integrated sources of nonclassical light," *ACS Photonics* **5**(1), 126–132 (2018).
46. C. Errando-Herranz, E. Schöll, M. Laini, S. Gyger, A. W. Elshaari, A. Branny, and C. Bonato (2020). On-chip single photon emission from a waveguide-coupled two-dimensional semiconductor. arXiv preprint arXiv:2002.07657.
47. S. Majumder and R. Chakraborty, "Semianalytical method to study silicon slot waveguides for optical sensing application," *Opt. Eng.* **52**(10), 107102 (2013).
48. H. Choi, M. Heuck, and D. Englund, "Self-similar nanocavity design with ultrasmall mode volume for single-photon nonlinearities," *Phys. Rev. Lett.* **118**(22), 223605 (2017).
49. F. Pisanello, A. Qualtieri, T. Stomeo, L. Martiradonna, R. Cingolani, A. Bramati, and M. De Vittorio, "High-Purcell-factor dipolelike modes at visible wavelengths in H1 photonic crystal cavity," *Opt. Lett.* **35**(10), 1509–1511 (2010).
50. J. T. Hugall, A. Singh, and N. F. van Hulst, "Plasmonic cavity coupling," *Acs Photonics* **5**(1), 43–53 (2018).
51. H. Choi, D. Zhu, Y. Yoon, and D. Englund, "Cascaded cavities boost the indistinguishability of imperfect quantum emitters," *Phys. Rev. Lett.* **122**(18), 183602 (2019).
52. F. W. Sun and C. W. Wong, "Indistinguishability of independent single photons," *Phys. Rev. A: At., Mol., Opt. Phys.* **79**(1), 013824 (2009).

Numerical Optimization of a Nanophotonic Cavity by Machine Learning for Near-Unity Photon Indistinguishability at Room Temperature

J. Guimba,*, L. Sanchis, L. Weituschat, J. Manuel Llorens,*, M. Song, J. Cardenas, and P. Aitor Postigo



Cite This: *ACS Photonics* 2022, 9, 1926–1935



Read Online

ACCESS |

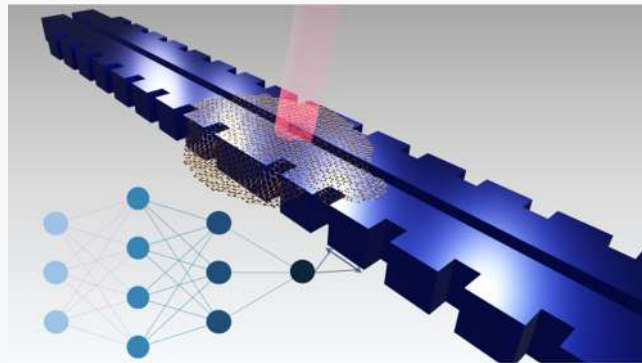
 Metrics & More

 Article Recommendations

 Supporting Information

ABSTRACT: Room-temperature (RT), on-chip deterministic generation of indistinguishable photons coupled to photonic integrated circuits is key for quantum photonic applications. Nevertheless, high indistinguishability (I) at RT is difficult to obtain due to the intrinsic dephasing of most deterministic single-photon sources (SPS). Here, we present a numerical demonstration of the design and optimization of a hybrid slot-Bragg nanophotonic cavity that achieves a theoretical near-unity I and a high coupling efficiency (β) at RT for a variety of single-photon emitters. Our numerical simulations predict modal volumes in the order of $10^{-3}(\lambda/2n)^3$, allowing for strong coupling of quantum photonic emitters that can be heterogeneously integrated. We show that high I and β should be possible by fine-tuning the quality factor (Q) depending on the intrinsic properties of the single-photon emitter. Furthermore, we perform a machine learning optimization based on the combination of a deep neural network and a genetic algorithm (GA) to further decrease the modal volume by almost 3 times while relaxing the tight dimensions of the slot width required for strong coupling. The optimized device has a slot width of 20 nm. The design requires fabrication resolution in the limit of the current state-of-the-art technology. Also, the condition for high I and β requires a positioning accuracy of the quantum emitter at the nanometer level. Although the proposal is not a scalable technology, it can be suitable for experimental demonstration of single-photon operation.

KEYWORDS: *single-photon, neural network, genetic algorithm, nanophotonics, nanocavity*



INTRODUCTION

Indistinguishable single photons are the leading candidates for quantum communication and quantum information processing technologies. They play a central role in a range of proposed schemes, including quantum simulation,¹ quantum walks,² boson sampling,³ quantum teleportation,⁴ and quantum networks.⁵ However, the complex mesoscopic environment of solid-state sources entails fundamental barriers that restrict the operation to cryogenic temperature (T).⁶ Trying to overcome the thermal restrictions of quantum devices remains a challenge for the development of on-chip, on-demand single-photon sources (SPS). A feasible approach for achieving efficient indistinguishable photon emission from a solid-state emitter consists of maximizing the emitter–field coupling (g) through the effective confinement of light in an ultrasmall cavity-mode volume (V_{eff}) and reaching the strong coupling regime.⁷ In this regime, the transfer rate between the emitter and the cavity field exceeds the dephasing rate of the emitter, and the emitted photons are able to leave the cavity before being affected by decoherence.⁷ Plasmonic cavities with subnanometer gaps between dimers like Au spheres,⁸ Ag nanowires,⁹ and surface plasmon-polariton systems¹⁰ or

metallic bowties with CdSe/ZnS quantum dots¹¹ produce the highest g value up to 200 meV¹¹ and the lowest quality factors ($Q \sim 10$).⁹ There are different proposals to improve Q and β in these systems, some of them involving dielectric-core/metal-shell schemes for Q ^{10,12} or hybrid FP-nanoantenna cavities for β .^{13,14} However, using plasmonic cavities faces two obstacles:¹⁵ (i) the placement of the emitter in the point with the strongest cavity field can be challenging and (ii) ohmic and quenching losses can be very high. The use of dielectric cavities can avoid the latter limitation, and strong coupling can happen using strategies to decrease the modal volume, like slotted photonic crystals. Discrete slotted nanobeams^{16,17} lead to volumes in the order of $10^{-3}(\lambda/2n)^3$ while keeping high Q . However, because introducing a finite slot causes a large

Received: October 27, 2021

Published: May 11, 2022



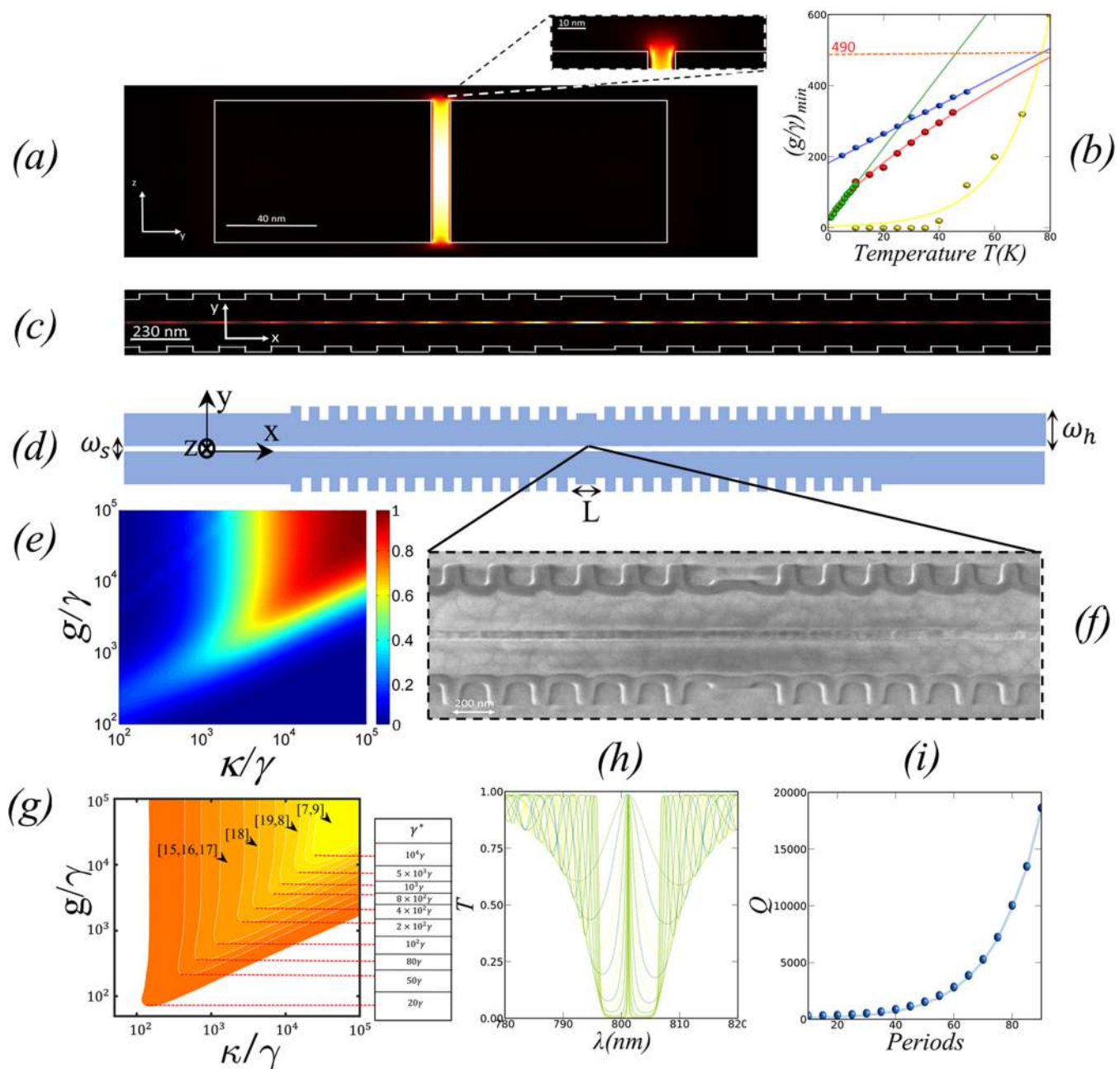


Figure 1. (a) $|E|^2$ field profile in the y - z plane. (b) Variation of the ratio $(g/\gamma)_{\min}$ with T for $I > 0.9$ and different SPS: GaAs (red), S.molecules (green), two-dimensional (blue), InAs (yellow). (c) $|E|^2$ field profile of the cavity mode in the x - y plane. (d) Layout of the proposed structure, where ω_h is the width of each waveguide, ω_s is the slot width, L is the cavity length, and Λ is the grating period. (e) Color map of I as a function of g/γ and κ/γ for photons emitted by a high dissipative QE with $\gamma^* = 10^4\gamma$. (f) SEM image of the center of the cavity. (g) Contour map of regions with $I > 0.9$ for different dephasing values ($\gamma^* = 20\gamma, 50\gamma, 80\gamma, 10^2\gamma, 2 \times 10^2\gamma, 4 \times 10^2\gamma, 8 \times 10^2\gamma, 10^3\gamma, 5 \times 10^3\gamma$, and $10^4\gamma$). (h) Transmission spectrum of the structure for a different number of periods, the full width at half maximum (FWHM) of the resonance scales exponentially with $\#p$. (i) Q versus number of periods.

perturbation to the optical mode, β values remain low. Continuous-slot designs improve β and Q ,¹⁸ and more recently, slot-antislot concatenations in 1D-PC^{19,20} have shown record Q/V_{eff} ratios with PC cavities. Also, designs based on cascaded cavities schemes have shown promising results with dielectric structures.²¹ According to those works, a slotted dielectric cavity can provide a sufficient small modal volume for strong coupling, thus a high I , avoiding at the same time the losses inherent to plasmonic cavities. However, for highly dissipative emitters, the dependence of I with g at RT is highly nontrivial.⁷ With high g , there is a high population

transfer rate between the emitter and the cavity field, so the emitted photons must leave the cavity before getting dephased by the emitter. This can be accomplished by setting the right Q . As we will show, this trade-off between different rates (i.e., dephasing rate, g , and Q) translates into a complex dependence of I with the cavity figures of merit.

In this work, we show that achieving a high I at RT requires tuning of Q together with a small modal volume. That does not translate to a high Q but a specific Q threshold depending on the emitter's intrinsic properties and the modal volume. From our calculations, none of the previously mentioned dielectric

cavities can provide a high I for strong dissipative emitters despite achieving small modal volumes. Furthermore, the implementation of machine learning algorithms for the geometrical optimization of the cavity modal volume and Q has shown promising results in recent works.^{22–25} Here, we present a numerical demonstration of a design strategy for high indistinguishable SPS at RT strongly coupled to a hybrid slot-Bragg waveguide cavity. We vary the geometrical parameters of the waveguide cavity (i.e., the waveguide width, slot width, number of periods), and we obtain a theoretical estimation of the cavity performance for I , β , and the Purcell enhancement. We explore different types of promising SPS (InGaAs²⁶ and GaAs²⁷ quantum dots, single molecules,²⁸ localized excitons in transition metal dichalcogenides transition-metal dichalcogenide (TMDC) monolayers,²⁹ and diamond color centers³⁰), and we obtain theoretical near-unity I and high β simultaneously by parameter optimization. Finally, we develop a hybrid deep neural network-genetic algorithm (GA) scheme that further reduces the modal volume for achieving near-unity I with a slot width of 20 nm. The optimized device presents strong challenges for current fabrication and quantum emitter (QE) positioning techniques. In this regard, we have developed a comparison of the design requirements with the state-of-the-art demonstrations.

METHODS

We can compute the value of I for a QE with radiative decay rate γ and pure dephasing rate γ^* coupled to a photonic cavity (with decay rate κ and electromagnetic coupling constant g) from the Lindblad equation and applying the quantum nonregression theorem. For each (g , κ , γ , γ^*), we have:⁷

$$I = \frac{\int \int_0^\infty dt d\tau | < \hat{a}^\dagger(t + \tau) \hat{a}(t) > |^2}{\int \int_0^\infty dt d\tau < \hat{a}^\dagger(t) \hat{a}(t) > < \hat{a}^\dagger(t + \tau) \hat{a}(t + \tau) >} \quad (1)$$

where \hat{a}^\dagger and \hat{a} are the creation and annihilation operators of the cavity mode, respectively. Details of the calculation can be found in the Supporting Information. The values of g and κ are linked to Q and V_{eff} by $\kappa \sim 1/Q$ and $g \sim 1/\sqrt{V_{\text{eff}}}$.

Figure 1e shows the value of I for photons emitted by a high dissipative QE with $\gamma^* = 10^4 \gamma$ as a function of g and κ normalized to γ in the coherent strong-coupling regime (i.e., $g > \gamma^* + \gamma$). In this regime, the rate of photon transfer from the emitter to the cavity is $R = 4g^2/\kappa$,⁷ which exceeds the pure dephasing rate ($R > \gamma^*$) for certain values of κ . For a high I , the photon must escape out of the cavity before the emitter dephases it. In other words, $\kappa > \gamma^*$, which means that a small Q is needed. Specifically, for a QE with $\gamma^* = 10^4 \gamma$, one needs a value of κ/γ above 2×10^4 for $I > 0.9$. The region of high I in Figure 1e has a shape and area that depend on T through γ^* . For a QE at RT, $\gamma^* \sim 10^4 \gamma$ ⁷ and the minimum value of g/γ to achieve $I > 0.9$ is $(g/\gamma)_{\min} \sim 10^4$. As γ^*/γ decreases, the area of high I grows and $(g/\gamma)_{\min}$ decreases.

Figure 1g shows the contour maps of the region with a high I ($I > 0.9$) as γ^* changes. For moderate dissipative emitters ($\gamma^* \sim 10^2 \gamma$), the minimum g/γ necessary for $I > 0.9$ is $(g/\gamma)_{\min} = 10^3$. As γ^* increases $(g/\gamma)_{\min}$ grows monotonously, reaching 10^4 for $\gamma^* \sim 10^4 \gamma$. Similarly, the minimum $(\kappa/\gamma)_{\min}$ increases from 10^3 for $\gamma^* \sim 10^2$, to 2×10^4 for $\gamma^* \sim 10^4 \gamma$. We can use this color map to plot the cavities mentioned before, according to its performance for I . Plasmonic cavities^{8–10} can achieve $I > 0.9$ even for high dissipative emitters with $\gamma^* \sim 10^4 \gamma$. On the

other hand, slotted dielectric cavities^{16–18} can achieve $I > 0.9$ for emitters with γ^* between $\sim 10^2$ to $\sim 2 \times 10^2 \gamma$ and slot-antislot concatenations in 1D-PC¹⁹ for emitters with $\gamma^* \sim 2 \times 10^2 \gamma$ to $\gamma^* \sim 4 \times 10^2 \gamma$. The cavity shown in ref 20 is the only one, in the group of dielectric structures, that can reach $I > 0.9$ when $\gamma^* > 2 \times 10^3 \gamma$. According to our calculations, those dielectric cavities can potentially achieve the region with $I > 0.9$ for high dissipative emitters (i.e., QE at RT) just by increasing its cavity decay rate κ (i.e., deteriorating its quality factor Q). Figure 1b shows the dependence of the value $(g/\gamma)_{\min}$ with T for $I > 0.9$, calculated for quantum dots of GaAs³¹ and InAs,³² organic molecules,^{33,34} and defects in 2D materials.³⁵ The evolution of $(g/\gamma)_{\min}$ with T shows a proportional increase with a different trend that depends on γ^* . We can obtain the $(g/\gamma)_{\min}$ needed for $I > 0.9$ for a QE at a specific T from Figure 1g. It is interesting to observe that for the technologically relevant T of liquid nitrogen (77 K), the same value $(g/\gamma)_{\min} = 490$ works for InAs and GaAs QDs and 2D materials.

Therefore, our goal is to keep the κ/g ratio inside the region with a high I by increasing g and adjusting Q . Moreover, we look for an on-chip cavity that can be CMOS-compatible with photonic integrated circuits (PICs) used in silicon photonics. Slotted one-dimensional dielectric photonic crystal cavities^{16–20} have been shown to fulfill most of our requirements in terms of compatibility and small modal volume. Nevertheless, to efficiently control Q , we choose a hybrid slot-Bragg cavity, where Q changes by the number of periods of the Bragg reflector section. Figure 1d shows a layout of our hybrid slot-Bragg photonic cavity aiming to achieve a near-unity I and a high β simultaneously; ω_h is the width of each waveguide, ω_s is the slot width, and $\#p$ is the number of periods. While this structure has been explored for sensing applications,^{36–38} it has never been proposed for SPS operation, as far as we know, nor its performance is calculated in terms of the figures of merit (I , β). It consists of a phase-shifted corrugated Bragg grating situated at the sides of a Si_3N_4 ($n_1 = 2$) deposited on top of a SiO_2 substrate ($n_2 = 1.4$). The cavity length L corresponds to the central section between the two periodic regions and matches the wavelength of the zero-order Fabry–Perot mode for the target wavelength λ . The Si_3N_4 thickness (t) is set for optimum field enhancement at the slot for the target λ . Each of the periodic regions behaves like a mirror with an effective reflectivity that depends on the number of periods ($\#p$), creating a Fabry–Perot structure. The grating period Λ matches the central frequency of the photonic bandgap at the target λ . To get information about the physical behavior of the device, we will set first $\lambda = 801$ nm to perform a general evaluation of the performance. After that, for each type of emitter, the geometrical parameters of the device (i.e., t , L , and Λ) are set to match the specific emission wavelength λ : $(\lambda, t, L, \Lambda) = (915, 900, 263, 263 \text{ nm})$ for InGaAs,²⁶ $(916, 900, 263, 263 \text{ nm})$ for GaAs,²⁷ $(728, 710, 210, 210 \text{ nm})$ for TMDC,²⁸ $(785, 770, 225, 225 \text{ nm})$ for S.molecules,²⁹ and $(685, 680, 195, 195 \text{ nm})$ for diamond color centers.³⁰ Figure 1a shows how the slotted cross section of the cavity enhances the field of the zero-order TE mode in the gap showing an evanescent tail in the top of the waveguide. This field distribution provides advantages related to the coupling of the source when it is heterogeneously integrated on top. The cavity provides strong coupling if the slot width is sufficiently small, and it also provides advantages in extraction efficiency (β) since (i) cavity and output waveguide share the same cross section, so the

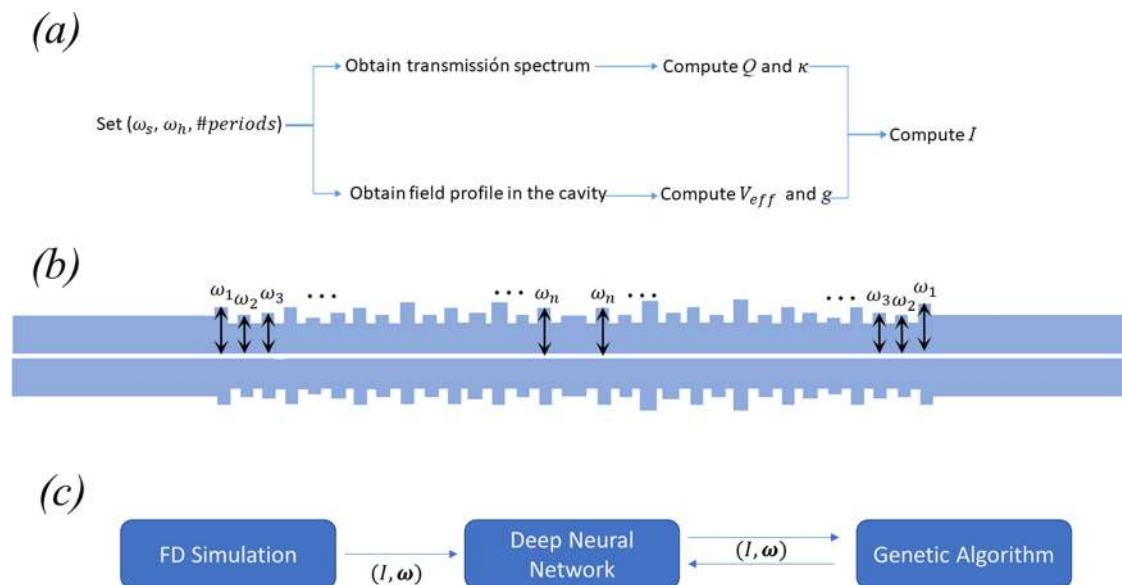


Figure 2. (a) Outline of the computation algorithm for the calculation of I . (b) Parametrization of the Bragg corrugations for machine learning optimization. Each ω_i represents the width of the corresponding Bragg corrugation. (c) Routine for the hybrid NN-GA optimization of the Bragg corrugations.

modes are perfectly matched; (ii) the integration of the QE (for example colloidal QDs) can be done by direct deposition on top of the cavity, which avoids interferences by total internal reflection and enhances β ; and (iii) the slot mode has the field maxima at the edges of the slot, which matches well with the region of maximum probability of having SPS in 2D materials deposited on top of waveguides.³⁹ Finally, the cavity modal volumes are in the order of $10^{-3}(\lambda/2n)^3$ along with the whole slot, increasing the probability of having one or several QE strongly coupled to the cavity mode. As a proof of concept, we have fabricated a specific design valid for diamond color center requirements. We selected $(\omega_s, \#p) = (38 \text{ nm}, 50)$ and added vertical grating couplers to the structure to collect the input and output light beams. Figure 1f shows an SEM image of the cavity fabricated by e-beam lithography (EBL) and reactive-ion etching on a layer of 130 nm thick Si₃N₄ deposited on top of a SiO₂ layer (1 μm thick) by plasma-enhanced chemical vapor deposition (PECVD). The obtained slot width is $\omega_s = 54 \text{ nm}$, and the grating period is 204 nm, with less than 5% of the error to the initial design for the grating period and 30% for ω_s . According to our simulations, the wider slot translates into a modal volume increase, $V_{eff} \sim 6 \times 10^{-2}(\lambda/2n)^3$, which slightly reduces the indistinguishability to $I = 0.81$. This issue can be solved by further optimization by machine learning, as we will show later. We can obtain the transmission spectrum $T(\lambda)$ shown in Figure 1h and the field profile (Figure 1c) of the cavity mode for a set $(\omega_s, \omega_h, \#p)$ using a fully vectorial, bidirectional, frequency-domain model for solving Maxwell's equation (3D-FD).⁴⁰ We obtain Q from $T(\lambda)$ by $Q = \frac{\lambda_0}{FWHM}$ and the cavity decay rate from $\kappa = \omega/2Q$. Details of the model appear in the Supporting Information. There is a different effective index for each set $(\omega_s, \omega_h, \#p)$, so the values of Λ and L are changed to keep the cavity resonance at 801 nm. The volume of the cavity-mode V_{eff} is⁴¹

$$V_{eff} = \frac{\oint \epsilon(\vec{r}) |\vec{E}(\vec{r})|^2 d^3r}{\max\{\epsilon |\vec{E}(\vec{r})|^2\}} \quad (2)$$

The value of g , when the QE is placed at the maximum cavity field and perfectly matches the polarization, is⁴²

$$g = \frac{\mu_{eg}}{\hbar} \sqrt{\frac{\hbar\omega}{2\epsilon_M V_{eff}}} ; \quad \mu_{eg} = \frac{3\hbar e^2 f}{2m_{eff}\omega} \quad (3)$$

where μ_{eg} is the electric dipole moment of the excitonic transition, ω is the frequency of the transition, e is the electron charge, ϵ_M is the dielectric constant in the source region, \hbar is the reduced Planck constant, m_{eff} is the exciton effective mass, and f is the oscillator strength. Once we have g and κ , we obtain I according to the procedure outlined in Figure 2a. For the computation of the Purcell enhancement (Γ_p) and the coupling efficiency β , we perform three-dimensional-finite difference time domain (3D-FDTD) simulations⁴⁰ by placing a dipole point source emitting at 801 nm with position x_0, y_0 at the center of the slot and $z_0 = 4 \text{ nm}$ above the top of the waveguides. We obtain Γ_p by integrating the power P emitted by the source and normalizing it to the power inside a homogeneous environment P_0 .⁴³ Finally, we calculate β by measuring the fraction of light coupled to guided modes at the output waveguide. Details of the simulations appear in the Supporting Information.

Our design strategy can be further enhanced using machine learning techniques, especially to keep critical fabrication parameters, like the slot width ω_s , experimentally accessible and far from too narrow and unrealistic values. Recently, the optimization of nanophotonic structures by deep learning techniques has been reported.^{22–25} The two main advantages are: (i) further improved performance beyond the time-consuming method of sweeping the $(\omega_s, \omega_h, \#p)$ parameters and (ii) we can introduce a vast number of new parameters for the optimization, such as the width of each of the Bragg corrugations, as shown in Figure 2b.

For that purpose, we can use a vector $\omega = (\omega_1, \omega_2, \omega_3, \dots, \omega_n)$, where each entry ω_i with $i = 1, \dots, 20$ represents the width of each Bragg corrugation. For each configuration ω , we obtain I using the two-step method described in Figure 2c. We use a GA to create a random vector ω and the fitness function

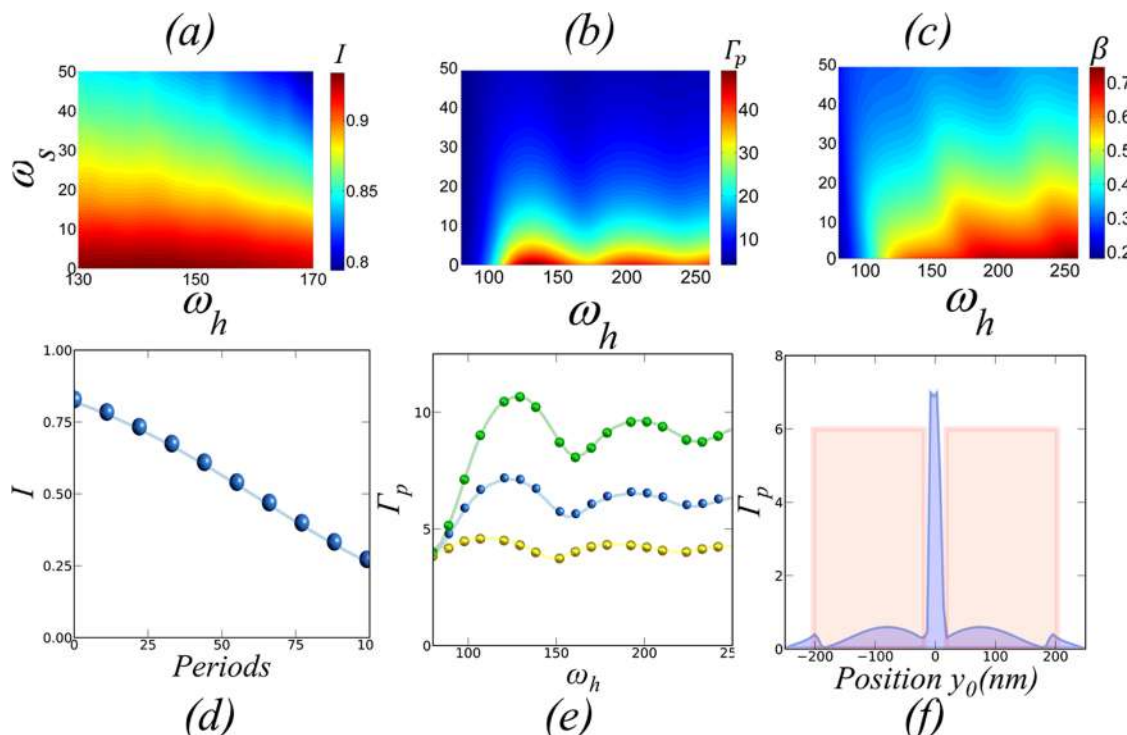


Figure 3. (a) Cavity-induced I when $\gamma/\gamma^* = 10^4$ versus waveguide width (ω_h) and slot width (ω_s) for $\#p = 10$. (b) Purcell enhancement (Γ_p) versus waveguide width (ω_h) and slot width (ω_s). (c) Coupling efficiency (β) versus waveguide width (ω_h) and slot width (ω_s) for $\#p = 10$. (d) I versus number of grating periods ($\#p$) for $(\omega_s, \omega_h) = (5 \text{ nm}, 140 \text{ nm})$. (e) Γ_p versus ω_h for three ω_s (green, $\omega_s = 15 \text{ nm}$; blue, $\omega_s = 20 \text{ nm}$; yellow, $\omega_s = 25 \text{ nm}$). (f) Γ_p versus source position y_0 along the y -axis.

obtains I from the 3D-FD simulation (Figure 2a). Through the iteration of crossover and mutation, the GA should find the optimal configuration for maximizing I after a certain number of generations. Details of the code appear in the Supporting Information. However, this procedure faces a critical issue. Typically, in a GA optimization, one needs to generate about 10^5 pairs $(\boldsymbol{\omega}, I)$ and the generation of each pair $(\boldsymbol{\omega}, I)$ involves a 3D-FD simulation that may take several minutes, making the whole optimization process unfeasible in terms of time and computational resources. To solve this issue, we take a different approach: (i) we generate 5000 pairs $(\boldsymbol{\omega}, I)$ through 3D-FD simulations; (ii) with these data, we train a deep neural network (NN) which learns to estimate the outcome of I for any possible $\boldsymbol{\omega}$. Now we can use the NN to calculate I for the fitness function of the GA optimization. In this way, the calculation of the fitness function for each $\boldsymbol{\omega}$ takes just a few seconds; (iii) We perform the GA optimization by calculating the fitness function for each individual of the population through the NN. With this scheme, we reduce by 2 orders of magnitude the number of actual numerical simulations for the dataset from 10^5 to 10^3 with the aid of the NN.

RESULTS AND DISCUSSION

We first assess the performance of the cavity by sweeping the main geometrical parameters and setting a target $\lambda = 801 \text{ nm}$; t , L , and Λ are set to $(t, L, \Lambda) = (800, 230, 230 \text{ nm})$, respectively. Figure 3 shows how I changes with (ω_s, ω_h) and $\#p$ when $\gamma^* = 10^4 \gamma$ (a typical ratio for many QE at RT as we have seen before). Figure 3a shows I versus ω_h and ω_s for $\#p = 10$ with ω_s varying between 10–50 nm and ω_h between 150–220 nm (required for single-mode operation). With $\#p$ fixed, Q remains constant ($Q = 50$), while the field profile of the cavity

mode varies for each (ω_h, ω_s) . Therefore, the variation of I follows the variation of g with ω_h and ω_s . As ω_s increase, the cavity mode spreads out from the slot and gets confined at each waveguide core separately. That results in an exponential decay of the field intensity in the slot region,⁴⁴ increasing V_{eff} exponentially with ω_s . Since $g \sim 1/\sqrt{V_{\text{eff}}}$, g decreases, driving the system to the weak coupling regime (i.e., going downward in Figure 1a) and inducing an exponential decay of I . For a small enough ω_s ($< 20 \text{ nm}$), the system remains in the strong-coupling regime and I becomes independent of g .⁷ Therefore, we can observe that for $\omega_s < 20 \text{ nm}$, I shows a weak variation with ω_h . When $\omega_s > 20 \text{ nm}$, the cavity starts to perform away from the strong coupling regime and I shows an evident change with ω_h , which we will further analyze later. A slot width $\omega_s < 10 \text{ nm}$ produces a maximum value of $I = 0.96$, decaying with ω_s at a rate of $5 \times 10^{-3} \text{ nm}^{-1}$. Figure 3d shows the dependence of I with $\#p$, with $\#p$ in the range of 10–100 and fixed $\omega_h = 140 \text{ nm}$ and $\omega_s = 15 \text{ nm}$ so we keep the strong coupling regime. As $\#p$ increases, the effective reflectivity also increases and the Q factor grows exponentially (see Figure 1i). Consequently, κ decreases exponentially with $\#p$. Therefore, the time that the photon stays in the cavity increases exponentially with $\#p$, and when $\kappa < \gamma^*$, the photon is dephased by the emitter (i.e., going in the left direction in Figure 1a). The result is that I decreases with $\#p$ giving $I = 0.4$ for $\#p = 100$. Figure 3b shows Γ_p versus (ω_s, ω_h) when $\#p = 10$, ω_s in the range 10–100 nm, and ω_h between 110 and 600 nm. Since $\Gamma_p \sim 1/V_{\text{eff}}$, Γ_p changes with ω_s in a similar way to I . As the slot mode spreads over the waveguide cores, the field's intensity at the source's position decreases and Γ_p shows an exponential decay. The change with ω_h displays a more complex structure, shown more clearly in Figure 3e. For $\omega_s =$

15 nm and $\omega_h = 80$, Γ_p increases monotonically as the zero-order cosine/even⁴⁵ slot mode gets more efficiently confined in the waveguide. Γ_p is maximum ($\Gamma_p = 11$) when $\omega_h = 125$ nm, and the strongest light confinement in the waveguide happens. For a higher ω_h , the mode spreads over the structure producing a decay of the overlapping with the source that scales with $1/\omega_h$. The decay interrupts abruptly when the zero-order sin-type/odd mode cutoff is reached at $\omega_h = 155$ nm. From there, the same pattern reproduces until the activation of the subsequent mode, and so on. The same behavior happens for ω_s . However, as ω_s increase the dependence of Γ_p with ω_h shifts to lower values of ω_h . This is because the ω_h cutoff value of the zero-order sine mode/odd decreases monotonically with ω_s .⁴⁵ Therefore, the activation of the second mode shifts to lower values of ω_h as ω_s increases.

Figure 3c shows β versus ω_s and ω_h for the same values of $\#p$, ω_s and ω_h used in Figure 3b. While Γ_p is a measure of the field enhancement due to the overlapping of all available modes, β accounts just for the overlapping with guided modes. Therefore, we expect a similar dependence and, in fact, β shows an exponential decay with ω_s similarly to I and Γ_p . The dependence with ω_h shows the same “mode jumps” found for Γ_p , giving a maximum $\beta = 75\%$ at $\omega_h = 128$ nm. In this case, the regions of high β become bigger for higher values of ω_h , as the number of available modes increases with ω_h .

The position of the QE inside the cavity plays a relevant role.⁴⁶ To explore the effect of the position of the QE in Γ_p , we have performed 3D-FDTD simulations changing the position (y_0) of the QE along the cavity cross section (y -axis) at $z_0 = 4$ nm above the top of the cavity. Figure 3f shows Γ_p versus y_0 varying from -225 to +225 nm when $\omega_h = 200$ nm, $\omega_s = 30$ nm, and $\#p = 10$. Since Γ_p is proportional to the field of the available modes for each spatial position, the plot reproduces the field profile of the zero-order mode of the slot waveguide. The maximum Γ_p happens in the region inside the slot, with maxima at the edges of the waveguides. The enhancement falls abruptly inside the waveguide, with values reduced by 1 order of magnitude. For a QE located away from the outer edges of the waveguide cores, the evanescent coupling increases the enhancement slightly. In summary, even for a strong dissipative emitter with $\gamma^* = 10^4\gamma$, we can achieve $I > 0.9$ by adjusting the number of periods and reducing the slot width ω_s below 10 nm. At the same time, a high Purcell enhancement ($\Gamma_p = 45$) and a good extraction efficiency ($\beta = 0.7$) can be obtained for the same ω_s . On the other hand, we need an accurate positioning of the emitter inside the slot region.

We further explore the performance of the device and the design requirements for different types of QE with different dephasing rates. For each type of emitter, the geometrical parameters of the device (i.e., t , L , and Λ) are set to match the specific emission wavelength λ . Table 1 shows the values of the pairs (ω_s , $\#p$) needed for $I > 0.9$ for five different γ^*/γ values

Table 1. Maximum (ω_s (nm), $\#p$) for $I > 0.9$ Using InGaAs QD, GaAs QD, TMDCs, and Single Molecules as QE

	$\gamma^* = 10^2\gamma$	$\gamma^* = 10^3\gamma$	$\gamma^* = 10^4\gamma$
InGaAs	(43,100)	(36,50)	(15,10)
GaAs	(41,100)	(30,50)	(9,10)
TMDC	(36,120)	(25,60)	(5,12)
S.molecules	(40,120)	(28,60)	(8,12)
Diamond	(45,100)	(38,50)	(15,10)

corresponding to each emitter. The values of the oscillation strengths are extracted from InGaAs,⁴⁷ GaAs,⁴⁸ TMDC,^{49,50} single molecules,^{28,51} and diamond.⁵² We observe that as γ^* increases (i.e., T increases), the cavity demands smaller ω_s (i.e., narrower slot). For the highest oscillator strength (~5 in InGaAs QD and diamond color centers), $(g/\gamma)_{\min}$ is easily reached when $\omega_s < 44$ nm and $\gamma^* = 10^2\gamma$. A TMDC QE with oscillator strength ~ 0.1 demands $\omega_s < 38$ nm on the opposite side. In an intermediate situation, the oscillation strength of the GaAs QD (~1) gives $\omega_s < 42$ nm. From this, we can find the optimal design for each emitter at a high T . InGaAs at 300 K has a pure dephasing of 600γ ,⁵³ so $(\omega_s, \#p) = (36 \text{ nm}, 50)$ are needed for $I > 0.9$. GaAs at 300 K has 1450γ ,⁵⁴ and needs the same values $(\omega_s, \#p) = (36, 50)$. High dissipative emitters with dephasing of $\sim 10^4\gamma$ at 300 K, like TMDC⁵⁵ and single molecules, demand narrower slot widths $(\omega_s, \#p) = (5 \text{ nm}, 10)$. For color centers in diamond, with $\gamma^* = 10^3\gamma$ at room T,⁵⁶ the optimal configuration is $(\omega_s, \#p) = (38 \text{ nm}, 50)$.

As we have shown, for high dissipative emitters with $\gamma^* = 10^4\gamma$, the width of the cavity slot must be $\omega_s < 10$ nm for $I > 0.9$. Similarly, $\omega_s < 10$ nm is needed for $\beta > 0.7$. At the same time, the emitter's position plays a critical role, giving very low coupling when the emitter is outside the slot region. These requirements make complex both the fabrication and the emitter integration. Achieving slot widths below 10 nm is beyond the state of the art of almost any fabrication technology, and deterministic deposition of a QD with that accuracy can be complicated. To reduce those limitations, we need to optimize the geometry of the cavity further. We have performed a hybrid GA-NN optimization of the Bragg corrugation geometry. The GA-NN optimization must deal with the trade-off between reducing the cavity modal volume (to increase g) and maintaining the appropriate Q to achieve $I > 0.9$ with $\gamma^* = 10^4\gamma$. With this aim, we set $\omega_s = 20$ nm and the number of periods to $\#p = 20$. The structure without optimization has a modal volume of about $10^{-2}(\lambda/2n)^3$, which gives $I = 0.82$ with $\gamma^* = 10^4\gamma$. Figure 4a shows the GA-NN optimized geometry. Somehow surprisingly to us, the GA-NN found that it is enough to change the widths of the most external Bragg corrugations, leaving the others unperturbed. This geometry provides the best confinement of the cavity mode in the center of the structure, significantly reducing the modal volume while maintaining the correct Q .

Figure 4b-d shows the cavity-mode profile and the transmission spectrum for the structure with and without optimization. It is easy to appreciate how the cavity mode is significantly more confined in the central region of the optimized cavity. The modification of the widths of the external Bragg corrugations creates a tapered section that connects the cavity with the input/output slot waveguides and increases the confinement of the cavity mode. The modal volume is reduced from $7 \times 10^{-3}(\lambda/2n)^3$ to $2.5 \times 10^{-3}(\lambda/2n)^3$, a factor of 2.8. At the same time, FWHM has been increased to $Q = 50$, keeping the system in the region of high I . The reduction in the modal volume and the Q adjustment improve the indistinguishability from $I = 0.82$ to 0.91. In conclusion, we obtain that for the optimized structure, we can achieve $I > 0.9$ for $\gamma^* = 10^4\gamma$ with a slot width of $\omega_s = 20$ nm, relaxing the tight requirements for the fabrication of the slot to more realistic values. The resulting transmission spectra of the optimized device reveal that there is a 7 nm shift of the resonance wavelength. This results from the discontinuous alteration of the periodicity of the Bragg reflectors. The λ -Bragg condition

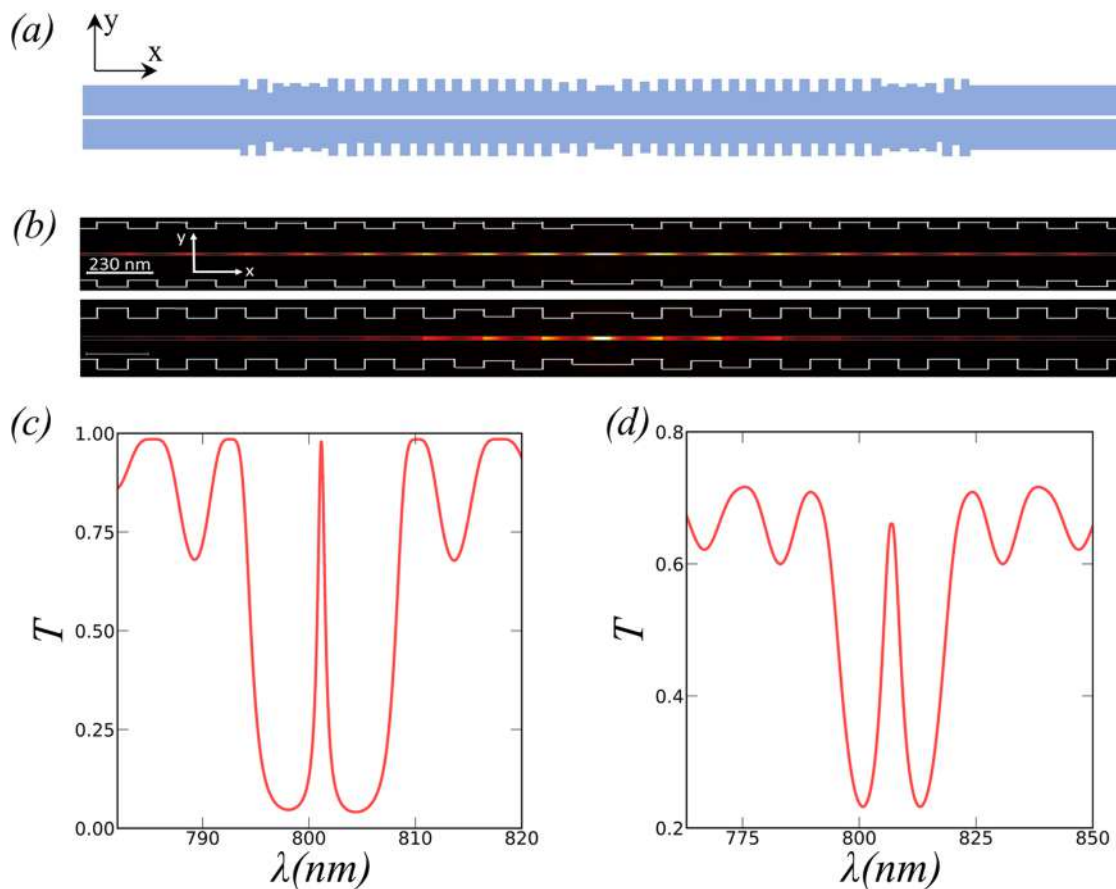


Figure 4. (a) Optimized structure for fixed $(\omega_s, \#p) = (20, 20)$. Cavity-mode field profile in the XY plane inside the cavity region for (b) cavity mode profiles of the nonoptimized structure (top) and optimized structure (bottom). Transmission spectra for (c) structure without optimization and (d) GA-NN optimized structure.

for total reflection changes along the corrugations, giving rise to a small modification of the spectra. This resonance displacement could be reduced through a second optimization process involving the maximization of I together with the minimization of the λ -shift, which will be covered in future works.

Although simulation results show a promising device performance, potential difficulties related to fabrication have to be considered according to CMOS-compatible processes. Realization of vertical slot widths below 80 nm can be difficult with standard lithography techniques. For emitters with $\gamma^* = 10^2\gamma$, slots between 36 and 45 nm are needed (see Table 1). Despite that achieving these widths can be challenging, there are many experimental demonstrations reporting the fabrication of sub-100 nm slots (between 30 and 80 nm) using e-beam lithography (EBL).^{57–64} On the other hand, strong dissipative emitters with $\gamma^* = 10^4\gamma$ require slot widths between 5 and 15 nm. Defining sub-10 nm structures with EBL is a great challenge, requiring simultaneous control of several factors like resist contrast, beam diameter, resist development mechanics, and limitations in metrology.⁶⁵ A novel fabrication procedure with EBL was reported,⁶⁵ which allows us to achieve slot widths down to 8 nm in Si substrates. Also, recent works⁶⁶ experimentally demonstrate a different fabrication approach achieving slots with 10 nm width in Si waveguides. In this context, the relaxation up to 20 nm width achieved through the ML optimization is especially relevant since it reduces the fabrication requirements from the limit of the technology (5

nm) to a more accessible value (20 nm). Still, we must emphasize that achieving such ultranarrow slots presents a significant challenge, which requires top-state-of-the-art resolution technology.

Another key aspect to consider for the experimental realization is the nanoscale positioning approach for the deposition of the QE in the 20 nm slot region of the cavity. Recently, several nanoscale positioning techniques compatible with nanofabrication processes have shown promising results, achieving positioning accuracy at the nanometer level.⁶⁷ Atomic force microscopy-based positioning approaches with 30 nm positioning accuracy have been reported with GaAs QDs strongly coupled to a nanocavity.⁶⁸ Confocal microphotoluminescence techniques also showed 10 nm positioning accuracy with GaAs QDs inside a photonic structure.⁶⁹ Bichromatic photoluminescence approaches with 5 nm position accuracy were recently achieved through a novel image analysis software implementation in the positioning setup.⁷⁰ Also, in situ lithographic techniques, where the QD position extraction and the nanostructure definition are developed in the same setup, have improved position accuracy down to 30 nm.⁷¹ Pick-and-place techniques, which are the most suitable approach for our specific structure, have also shown significant progress.⁷² Recently, Si vacancy centers were transferred to AlN waveguides achieving 98% coupling efficiency,⁷³ the placement mean error was about 38 nm. According to this, for a pick-and-place deposition, assuming a normal distribution, we would have a standard deviation of 38

nm with a target of 20 nm, which leads to 34% probability of successful deposition. Therefore, the positioning accuracy required for our structure lies close to the limit of the technology depending on the positioning approach. An experimental realization of a QE coupling requires fabricating many devices and looking for good candidates one by one. This approach allows the experimental demonstration of certain quantum effects for quantum information applications, but is still far from a scalable technology.

CONCLUSIONS

We explored a hybrid slot-Bragg nanophotonic cavity for the generation of indistinguishable photons at RT from various quantum emitters through a combination of numerical methods. We obtain the values of the theoretical indistinguishability, efficiency, and Purcell enhancement for each configuration (i.e., waveguide width, slot width, number of periods). We obtained theoretical near-unity indistinguishability and high efficiency simultaneously by parameter sweep optimization. To relax the fabrication requirements (slot width) for near-unity indistinguishability, we have developed a machine learning algorithm that provides the optimal geometry of the cavity. According to our simulations, the optimized structure shows high indistinguishability ($I > 0.9$) with slot widths of about 20 nm. The geometrical features of the optimized design present significant challenges from the perspective of fabrication process. Although the device may be far from a real scalable technology, it can be suitable for experimental demonstration of single-photon operation. Also, the developed ML approach may provide insights for the optimization of different photonic structures for quantum information applications.

ASSOCIATED CONTENT

Supporting Information

The Supporting Information is available free of charge at <https://pubs.acs.org/doi/10.1021/acsphtronics.1c01651>.

Computation of the indistinguishability; numerical simulation; machine learning algorithm; and fabrication process ([PDF](#))

AUTHOR INFORMATION

Corresponding Authors

J. Guimbao — *Instituto de Micro y Nanotecnología, IMN-CNM, CSIC (CEI UAM+CSIC), Madrid E-28760, Spain;*  [0000-0003-0895-1989](https://orcid.org/0000-0003-0895-1989); Email: j.guimbao@csic.es

J. Manuel Llorens — *Instituto de Micro y Nanotecnología, IMN-CNM, CSIC (CEI UAM+CSIC), Madrid E-28760, Spain;*  [0000-0002-6155-6462](https://orcid.org/0000-0002-6155-6462); Email: jose.llorens@csic.es

Authors

L. Sanchis — *Instituto de Micro y Nanotecnología, IMN-CNM, CSIC (CEI UAM+CSIC), Madrid E-28760, Spain*

L. Weituschat — *Instituto de Micro y Nanotecnología, IMN-CNM, CSIC (CEI UAM+CSIC), Madrid E-28760, Spain*

M. Song — *The Institute of Optics, University of Rochester, Rochester, New York 14627, United States*

J. Cardenas — *The Institute of Optics, University of Rochester, Rochester, New York 14627, United States;*  [0000-0002-6232-0275](https://orcid.org/0000-0002-6232-0275)

P. Aitor Postigo — *Instituto de Micro y Nanotecnología, IMN-CNM, CSIC (CEI UAM+CSIC), Madrid E-28760, Spain; The Institute of Optics, University of Rochester, Rochester, New York 14627, United States*

Complete contact information is available at:
<https://pubs.acs.org/10.1021/acsphtronics.1c01651>

Funding

This work was funded by the European Union's Horizon 2020 research and innovation program under grant agreement no. 820423 (S2QUIP).

Notes

The authors declare no competing financial interest. Details underlying the results presented in this paper are available in the Supplement 1 file.

ACKNOWLEDGMENTS

The authors gratefully acknowledge financial support from the European Union's Horizon 2020 research and innovation program under grant agreement no. 820423 (S2QUIP) and CSIC Quantum Technology Platform PT-001. J.M.L. acknowledges the Agencia Estatal de Investigación (AEI) grant PID2019-106088RB-C31.

REFERENCES

- (1) Aspuru-Guzik, A.; Walther, P. Photonic quantum simulators. *Nat. Phys.* **2012**, *8*, 285–291.
- (2) Aharonov, D.; Ambainis, A.; Kempe, J.; Vazirani, U. In *Quantum Walks on Graphs*; Proceedings of the 33rd ACM Symposium on Theory of Computing 2001.
- (3) Broome, M. A.; Fedrizzi, A.; Rahimi-Keshari, S.; Dove, J.; Aaronson, S.; Ralph, T. C.; White, A. G. Photonic boson sampling in a tunable circuit. *Science* **2013**, *339*, 794–798.
- (4) Fattal, D.; Diamanti, E.; Inoue, K.; Yamamoto, Y. Quantum teleportation with a quantum dot single photon source. *Phys. Rev. Lett.* **2004**, *92*, No. 037904.
- (5) Kimble, H. J. The quantum internet. *Nature* **2008**, *453*, 1023–1030.
- (6) Aharonovich, I.; Englund, D.; Toth, M. Solid-state single-photon emitters. *Nat. Photonics* **2016**, *10*, 631–641.
- (7) Grange, T.; Hornecker, G.; Hunger, D.; Poizat, J. P.; Gérard, J. M.; Similar, P.; Affixes, A. Cavity-funneled generation of indistinguishable single photons from strongly dissipative quantum emitters. *Phys. Rev. Lett.* **2015**, *114*, No. 193601.
- (8) Chikara, R.; De Nibis, B.; Benz, F.; Barrow, S. J.; Sucherman, O. A.; Rosa, E.; Blumberg, J. J. Single-molecule strong coupling at room T in plasmonic nanocavities. *Nature* **2016**, *535*, 127–130.
- (9) Russell, K. J.; Hu, E. L. Gap-mode plasmonic nanocavity. *Appl. Phys. Lett.* **2010**, *97*, No. 163115.
- (10) Seo, M. K.; Kwon, S. H.; Ee, H. S.; Park, H. G. Full three-dimensional subwavelength high-Q surface-plasmon-polariton cavity. *Nano Lett.* **2009**, *9*, 4078–4082.
- (11) Santhosh, K.; Button, O.; Chitonid, L.; Haran, G. Vacuum Rabi splitting in a plasmonic cavity at the single quantum emitter limit. *Nat. Commun.* **2016**, *7*, No. 11823.
- (12) Kang, J. H.; No, Y. S.; Kwon, S. H.; Park, H. G. Ultrasmall subwavelength nanorod plasmonic cavity. *Opt. Lett.* **2011**, *36*, 2011–2013.
- (13) Peng, P.; Liu, Y. C.; Xu, D.; Cao, Q. T.; Lu, G.; Gong, Q.; Xiao, Y. F. Enhancing coherent light-matter interactions through microcavity-engineered plasmonic resonances. *Phys. Rev. Lett.* **2017**, *119*, No. 233901.
- (14) Gurlek, B.; Sandoghdar, V.; Martín-Cano, D. Manipulation of quenching in nanoantenna–emitter systems enabled by external detuned cavities: a path to enhance strong-coupling. *ACS Photonics* **2018**, *5*, 456–461.

- (15) Hugall, J. T.; Singh, A.; van Hulst, N. F. Plasmonic cavity coupling. *ACS Photonics* **2018**, *5*, 43–53.
- (16) Robinson, J. T.; Manolatou, C.; Chen, L.; Lipson, M. Ultrasmall mode volumes in dielectric optical microcavities. *Phys. Rev. Lett.* **2005**, *95*, No. 143901.
- (17) Seidler, P.; Lister, K.; Drechsler, U.; Hofrichter, J.; Stöferle, T. Slotted photonic crystal nanobeam cavity with an ultrahigh quality factor-to-mode volume ratio. *Opt. Express* **2013**, *21*, 32468–32483.
- (18) Ryckman, J. D.; Weiss, S. M. Low mode volume slotted photonic crystal single nanobeam cavity. *Appl. Phys. Lett.* **2012**, *101*, No. 071104.
- (19) Hu, S.; Weiss, S. M. Design of photonic crystal cavities for extreme light concentration. *ACS Photonics* **2016**, *3*, 1647–1653.
- (20) Choi, H.; Heuck, M.; Englund, D. Self-similar nanocavity design with ultrasmall mode volume for single-photon nonlinearities. *Phys. Rev. Lett.* **2017**, *118*, No. 223605.
- (21) Saxena, A.; Chen, Y.; Ryou, A.; Sevilla, C. G.; Xu, P.; Majumdar, A. Improving indistinguishability of single photons from colloidal quantum dots using nanocavities. *ACS Photonics* **2019**, *6*, 3166–3173.
- (22) Sanchis, L.; Cryan, M. J.; Pozo, J.; Craddock, I. J.; Rarity, J. G. Ultrahigh Purcell factor in photonic crystal slab microcavities. *Phys. Rev. B* **2007**, *76*, No. 045118.
- (23) Sanchis, L.; Häkansson, A.; López-Zanón, D.; Bravo-Abad, J.; Sánchez-Dehesa, J. Integrated optical devices design by genetic algorithm. *Appl. Phys. Lett.* **2004**, *84*, 4460–4462.
- (24) Morgado-León, A.; Escuín, A.; Guerrero, E.; Yáñez, A.; Galindo, P. L.; Sanchis, L. Genetic Algorithms Applied to the Design of 3D Photonic Crystals. In *International Work-Conference on Artificial Neural Networks*; Springer: Berlin, Heidelberg, 2011; pp 291–298.
- (25) Marqués-Hueso, J.; Sanchis, L.; Cluzel, B.; de Fornel, F.; Martínez-Pastor, J. P. Genetic algorithm designed silicon integrated photonic lens operating at 1550 nm. *Appl. Phys. Lett.* **2010**, *97*, No. 071115.
- (26) Tomm, N.; Javadi, A.; Antoniadis, N. O.; Najer, D.; Löbl, M. C.; Korsch, A. R.; Warburton, R. J.; et al. A bright and fast source of coherent single photons. *Nat. Nanotechnol.* **2021**, *16*, 399–403.
- (27) Schnauber, P.; Singh, A.; Schall, J.; Park, S. I.; Song, J. D.; Rodt, S.; Davanco, M.; et al. Indistinguishable photons from deterministically integrated single quantum dots in heterogeneous GaAs/Si3N4 quantum photonic circuits. *Nano Lett.* **2019**, *19*, 7164–7172.
- (28) Iff, O.; Buchinger, Q.; Moczala-Dusanowska, M.; Kamp, M.; Betzold, S.; Davanco, M.; Schneider, C.; et al. Purcell-enhanced single photon source based on a deterministically placed WSe₂ monolayer quantum dot in a circular Bragg grating cavity. *Nano Lett.* **2021**, *21*, 4715–4720.
- (29) Toninelli, C.; Gerhardt, I.; Clark, A. S.; Reserbat-Plantey, A.; Götzinger, S.; Ristanovic, Z.; Orrit, M. A. J. G.; et al. Single organic molecules for photonic quantum technologies. *Nat. Mater.* **2021**, *20*, 1615–1628.
- (30) Dolan, P. R.; Adekanye, S.; Trichet, A. A. P.; Johnson, S.; Flatten, L. C.; Chen, Y. C.; Smith, J. M.; et al. Robust, tunable, and high purity triggered single photon source at room temperature using a nitrogen-vacancy defect in diamond in an open microcavity. *Opt. Express* **2018**, *26*, 7056–7065.
- (31) Fan, X.; Takagahara, T.; Cunningham, J. E.; Wang, H. Pure dephasing induced by exciton–phonon interactions in narrow GaAs quantum wells. *Solid State Commun.* **1998**, *108*, 857–861.
- (32) Jakubczyk, T.; Delmonte, V.; Fischbach, S.; Wigger, D.; Reiter, D. E.; Mermilliod, Q.; Rodt, S.; et al. Impact of phonons on dephasing of individual excitons in deterministic quantum dot microlenses. *ACS Photonics* **2016**, *3*, 2461–2466.
- (33) Kummer, S.; Basche, T. Measurement of optical dephasing of a single terrylene molecule with nanosecond time resolution. *J. Phys. Chem. A* **1995**, *99*, 17078–17081.
- (34) Hesselink, W. H.; Wiersma, D. A. Optical dephasing and vibronic relaxation in molecular mixed crystals: A picosecond photon echo and optical study of pentacene in naphthalene and p-terphenyl. *J. Chem. Phys.* **1980**, *73*, 648–663.
- (35) Moody, G.; Dass, C. K.; Hao, K.; Chen, C. H.; Li, L. J.; Singh, A.; Li, X.; et al. Intrinsic homogeneous linewidth and broadening mechanisms of excitons in monolayer transition metal dichalcogenides. *Nat. Commun.* **2015**, *6*, No. 8315.
- (36) Wang, X.; Grist, S.; Flueckiger, J.; Jaeger, N. A.; Chrostowski, L. Silicon photonic slot waveguide Bragg gratings and resonators. *Opt. Express* **2013**, *21*, 19029–19039.
- (37) Bera, A.; Kuittinen, M.; Honkanen, S.; Roussey, M. Silicon slot waveguide Fano resonator. *Opt. Lett.* **2018**, *43*, 3489–3492.
- (38) Wang, X.; Flueckiger, J.; Schmidt, S.; Grist, S.; Fard, S. T.; Kirk, J.; Chrostowski, L.; et al. A silicon photonic biosensor using phase-shifted Bragg gratings in slot waveguide. *J. Biophotonics* **2013**, *6*, 821–828.
- (39) Errando-Herranz, C.; Schöll, E.; Picard, R.; Laini, M.; Gyger, S.; Elshaari, A. W.; Jöns, K. D. On-Chip Single Photon Emission from a Waveguide-Coupled Two-Dimensional Semiconductor. In *Quantum Nanophotonic Materials, Devices, and Systems 2020*; International Society for Optics and Photonics, 2020; Vol. 11471, p 1147105.
- (40) Lumerical Inc. <https://www.lumerical.com/products/> (accessed February 21, 2022).
- (41) Kristensen, T.; Van Vlack, C.; Hughes, S. Effective mode volumes and purcell factors for leaky optical cavities. 2011-7-22. *Opt. Lett.* **2011**, *37*, 1649–1651.
- (42) Vuckovic, J. Quantum Optics and Cavity QED with Quantum Dots in Photonic Crystals. In *Quantum Optics and Nanophotonics*; Oxford University Press, 2017.
- (43) Novotny, L.; Hecht, B. *Principles of Nano-Optics*; Cambridge University Press, 2012.
- (44) Almeida, V. R.; Xu, Q.; Barrios, C. A.; Lipson, M. Guiding and confining light in void nanostructure. *Opt. Lett.* **2004**, *29*, 1209–1211.
- (45) Liu, Y.; Kong, M.; Jiang, Y. Transverse magnetic modes in planar slot waveguides. *J. Opt. Soc. Am. B* **2015**, *32*, 2052–2060.
- (46) Guimbao, J.; Weituschat, L. M.; Montolio, J. L.; Postigo, P. A. Enhancement of the indistinguishability of single photon emitters coupled to photonic waveguides. *Opt. Express* **2021**, *29*, 21160–21173.
- (47) Stoleru, V. G.; Towe, E. Oscillator strength for intraband transitions in (In, Ga) As/GaAs quantum dots. *Appl. Phys. Lett.* **2003**, *83*, S026–S028.
- (48) Hatami, F.; Grundmann, M.; Ledentsov, N. N.; Heinrichsdorff, F.; Heitz, R.; Böhrer, J.; Kop'ev, P. S.; et al. Carrier dynamics in type-II GaSb/GaAs quantum dots. *Phys. Rev. B* **1998**, *57*, No. 4635.
- (49) Schneider, C.; Glazov, M. M.; Korn, T.; Höfling, S.; Urbaszek, B. Two-dimensional semiconductors in the regime of strong light-matter coupling. *Nat. Commun.* **2018**, *9*, No. 2695.
- (50) Lundt, N.; Marynski, A.; Cherotchenko, E.; Pant, A.; Fan, X.; Tongay, S.; Schneider, C. Monolayered MoSe₂: a candidate for room T polaritonics. *2D Mater.* **2016**, *4*, No. 015006.
- (51) Zhao, H.; Zhao, Y.; Song, Y.; Zhou, M.; Lv, W.; Tao, L.; Wang, X.; et al. Strong optical response and light emission from a monolayer molecular crystal. *Nat. Commun.* **2019**, *10*, No. 5589.
- (52) Heidari Saani, M.; Vesaghi, M. A.; Esfarjani, K. Oscillator strength calculations in color centers of diamond and the role of spin. *Eur. Phys. J. B* **2004**, *39*, 441–446.
- (53) Borri, P.; Langbein, W.; Schneider, S.; Woggon, U.; Sellin, R. L.; Ouyang, D.; Bimberg, D. Ultralong dephasing time in InGaAs quantum dots. *Phys. Rev. Lett.* **2001**, *87*, No. 157401.
- (54) Bayer, M.; Forchel, A. Temperature dependence of the exciton homogeneous linewidth in In 0.60 Ga 0.40 As/GaAs self-assembled quantum dots. *Phys. Rev. B* **2002**, *65*, No. 041308.
- (55) Huang, L.; Krasnok, A.; Alu, A.; Yu, Y.; Neshev, D.; Miroshnichenko, A. Enhanced Light-Matter Interaction in Two-Dimensional Transition Metal Dichalcogenides. *Rep. Prog. Phys.* **2022**, *85*, No. 046401.
- (56) Albrecht, R.; Bommer, A.; Deutsch, C.; Reichel, J.; Becher, C. Coupling of a single nitrogen-vacancy center in diamond to a fiber-based microcavity. *Phys. Rev. Lett.* **2013**, *110*, No. 243602.

- (57) Häyrinen, M.; Roussey, M.; Säynätjoki, A.; Kuittinen, M.; Honkanen, S. Titanium dioxide slot waveguides for visible wavelengths. *Appl. Opt.* **2015**, *54*, 2653–2657.
- (58) Raza, A.; Van Daele, M.; Wuytens, P.; Dendooven, J.; Detavernier, C.; Clemmen, S.; Baets, R. E-beam-Lithography Free Plasmonic Slot Waveguides for On-Chip Raman Spectroscopy. In *CLEO: Science and Innovations*; Optical Society of America, 2018; p SW3L-6.
- (59) Wang, Y.; He, S.; Gao, X.; Ye, P.; Lei, L.; Dong, W.; Zhang, X.; Xu, P. Enhanced optical nonlinearity in a silicon–organic hybrid slot waveguide for all-optical signal processing. *Photonics Res.* **2022**, *10*, 50–58.
- (60) Lin, S.; Hu, J.; Crozier, K. B. Ultracompact, broadband slot waveguide polarization splitter. *Appl. Phys. Lett.* **2011**, *98*, No. 151101.
- (61) Hochberg, M.; Baehr-Jones, T.; Wang, G.; Huang, J.; Sullivan, P.; Dalton, L.; Scherer, A. Towards a millivolt optical modulator with nano-slot waveguides. *Opt. Express* **2007**, *15*, 8401–8410.
- (62) Wang, J.; Cheng, Z.; Chen, Z.; Wan, X.; Zhu, B.; Tsang, H. K.; Shu, C.; Xu, J. High-responsivity graphene-on-silicon slot waveguide photodetectors. *Nanoscale* **2016**, *8*, 13206–13211.
- (63) Lin, C. Y.; Wang, X.; Chakravarty, S.; Lee, B. S.; Lai, W.; Luo, J.; Jen, A. Y.; Chen, R. T. Electro-optic polymer infiltrated silicon photonic crystal slot waveguide modulator with 23 dB slow light enhancement. *Appl. Phys. Lett.* **2010**, *97*, No. 194.
- (64) Zhang, H.; Zhang, J.; Chen, S.; Song, J.; Kee, J. S.; Yu, M.; Lo, G. Q. CMOS-compatible fabrication of silicon-based sub-100-nm slot waveguide with efficient channel-slot coupler. *IEEE Photonics Technol. Lett.* **2012**, *24*, 10–12.
- (65) Cord, B. M. Achieving sub-10-nm Resolution Using Scanning Electron Beam Lithography. Doctoral Dissertation, Massachusetts Institute of Technology, 2009.
- (66) Debnath, K.; Khokhar, A. Z.; Reed, G. T.; Saito, S. Fabrication of arbitrarily narrow vertical dielectric slots in silicon waveguides. *IEEE Photonics Technol. Lett.* **2017**, *29*, 1269–1272.
- (67) Liu, S.; Srinivasan, K.; Liu, J. Nanoscale Positioning Approaches for Integrating Single Solid-State Quantum Emitters with Photonic Nanostructures. *Laser Photonics Rev.* **2021**, *15*, No. 2100223.
- (68) Hennessy, K.; Badolato, A.; Winger, M.; Gerace, D.; Atature, M.; Gulde, S.; Imamoglu, A.; et al. et al. Quantum nature of a strongly coupled single quantum dot–cavity system. *Nature* **2007**, *445*, 896–899.
- (69) Thon, S. M.; Rakher, M. T.; Kim, H.; Gudat, J.; Irvine, W. T.; Petroff, P. M.; Bouwmeester, D. Strong coupling through optical positioning of a quantum dot in a photonic crystal cavity. *Appl. Phys. Lett.* **2009**, *94*, No. 111115.
- (70) Liu, J.; Davanco, M. I.; Sapienza, L.; Konthasinghe, K.; De Miranda Cardoso, J. V.; Song, J. D.; Badolato, A.; Srinivasan, K. Cryogenic photoluminescence imaging system for nanoscale positioning of single quantum emitters. *Rev. Sci. Instrum.* **2017**, *88*, No. 023116.
- (71) Gschrey, M.; Schmidt, R.; Schulze, J. H.; Strittmatter, A.; Rodt, S.; Reitenstein, S. Resolution and alignment accuracy of low-temperature in situ electron beam lithography for nanophotonic device fabrication. *J. Vac. Sci. Technol., B: Nanotechnol. Microelectron.: Mater., Process., Meas., Phenom.* **2015**, *33*, No. 021603.
- (72) Elshaari, A. W.; Pernice, W.; Srinivasan, K.; Benson, O.; Zwiller, V. Hybrid integrated quantum photonic circuits. *Nat. Photonics* **2020**, *14*, 285–298.
- (73) Wang, J.; Sciarrino, F.; Laing, A.; Thompson, M. G. Integrated photonic quantum technologies. *Nat. Photonics* **2020**, *14*, 273–284.

□ Recommended by ACS

Strain Tuning Self-Assembled Quantum Dots for Energy-Tunable Entangled-Photon Sources Using a Photolithographically Fabricated Microelectromechanical...

Weiwen Ou, Jiaxiang Zhang, et al.

SEPTEMBER 23, 2022

ACS PHOTONICS

READ ▶

High-Performance Single-Photon Sources at Telecom Wavelength Based on Broadband Hybrid Circular Bragg Gratings

Andrea Barbiero, Andrew J. Shields, et al.

AUGUST 11, 2022

ACS PHOTONICS

READ ▶

Double-Pulse Generation of Indistinguishable Single Photons with Optically Controlled Polarization

Junyong Yan, Feng Liu, et al.

FEBRUARY 11, 2022

NANO LETTERS

READ ▶

Silicon Nitride Waveguides with Intrinsic Single-Photon Emitters for Integrated Quantum Photonics

Alexander Senichev, Vladimir M. Shalaev, et al.

SEPTEMBER 13, 2022

ACS PHOTONICS

READ ▶

Get More Suggestions >

Article

Perfect Photon Indistinguishability from a Set of Dissipative Quantum Emitters

Joaquin Guimba 1,*^{ID}, Lorenzo Sanchis 1, Lukas M. Weituschat 1^{ID}, Jose M. Llorens 1^{ID} and Pablo A. Postigo 1,2,*^{ID}¹ Instituto de Micro y Nanotecnología, INM-CNM, CSIC (CEI UAM+CSIC), Isaac Newton 8, Tres Cantos, E-28760 Madrid, Spain² The Institute of Optics, University of Rochester, Rochester, NY 14627, USA

* Correspondence: j.guimba@csic.es (J.G.); pabloaitor.postigo@imn.cnm.csic.es (P.A.P.)

Abstract: Single photon sources (SPS) based on semiconductor quantum dot (QD) platforms are restricted to low temperature (T) operation due to the presence of strong dephasing processes. Although the integration of QD in optical cavities provides an enhancement of its emission properties, the technical requirements for maintaining high indistinguishability (I) at high T are still beyond the state of the art. Recently, new theoretical approaches have shown promising results by implementing two-dipole-coupled-emitter systems. Here, we propose a platform based on an optimized five-dipole-coupled-emitter system coupled to a cavity which enables perfect I at high T . Within our scheme the realization of perfect I single photon emission with dissipative QDs is possible using well established photonic platforms. For the optimization procedure we have developed a novel machine-learning approach which provides a significant computational-time reduction for high demanding optimization algorithms. Our strategy opens up interesting possibilities for the optimization of different photonic structures for quantum information applications, such as the reduction of quantum decoherence in clusters of coupled two-level quantum systems.



Citation: Guimba, J.; Sanchis, L.; Weituschat, L.M.; Llorens, J.M.; Postigo, P.A. Perfect Photon Indistinguishability from a Set of Dissipative Quantum Emitters. *Nanomaterials* **2022**, *12*, 2800.
<https://doi.org/10.3390/nano12162800>

Academic Editor: Fedor Jelezko

Received: 17 July 2022

Accepted: 12 August 2022

Published: 15 August 2022

Publisher's Note: MDPI stays neutral with regard to jurisdictional claims in published maps and institutional affiliations.



Copyright: © 2022 by the authors. Licensee MDPI, Basel, Switzerland. This article is an open access article distributed under the terms and conditions of the Creative Commons Attribution (CC BY) license (<https://creativecommons.org/licenses/by/4.0/>).

Keywords: single-photon; quantum optics; photonic integrated circuits; quantum decoherence

1. Introduction

Over the last decade, milestones achieved in integrated quantum photonics (IQP) have led to promising results. While other quantum technologies (QT) such as ion trapping or superconducting systems were used to demonstrate their first logical operations in the 1990s [1,2], the first functioning IQP gate was only developed in 2008 [3]. Yet, despite its immaturity, IQP has become established in a wide range of proposed schemes: (Quantum Communications) Si-based chip to chip quantum key distribution (QKD) over 43 km dark fiber was demonstrated in 2018 [4]; network operation for distributed quantum computation (i.e., quantum internet) was reported in 2021 [5]; (Quantum Computation) Gaussian boson sampling scheme with 50 photons for specific quantum computing demonstrated quantum advantage for the first time in 2020 [6]; (Quantum simulation) A IQP based variational eigensolver for calculation of the ground state energy of H₂ molecules was developed in 2013 [7]; (Quantum Metrology) A IQP platform based on defects in diamond was used for extremely efficient detectors of magnetic fields with unprecedent sensitivity [8]. In contrast to other QT platforms, IQP leverage commercially available systems from the integrated photonics industry, which provide reliable devices for on-chip integration [9] and metamaterial systems for broadband operation [10,11]. In this context, IQP shows a new leading candidate for the future q-bit in QT: the indistinguishable single photon.

Integrated photonics offer different approaches for the modulation of photon emission [12,13]. Suitable platforms for indistinguishable SPS are epitaxially grown semiconductor QDs. QDs enable site control during growth [14] and the possibility of monolithic integration into photonic nanocavities [15,16], providing enhanced quantum emission. As

a result, many recent experimental demonstrations have reported record I with cavity-integrated QDs at cryogenic T: $g^{(2)}(0) = 7 \times 10^{-3}$ and $I = 0.96$ was reported with InAs/GaAs QDs embedded in a micropillar cavity at 4.3 K [17]; $g^{(2)}(0) = 1.2 \times 10^{-2}$ and $I = 0.97$ with InAs/GaAs QDs integrated in a DBR microcavity at 4.2 K [18]; $g^{(2)}(0) = 2.8 \times 10^{-3}$ and $I = 0.99$ with InGaAs/GaAs QDs inside DBR micropillars at 4 K [19]. However, for T above the cryogenic regime, QDs are subject to pure dephasing mechanisms which reduce the coherence of the emission [20–22]: $g^{(2)}(0) = 0.47$ with InGaAs/GaAs QDs at 120 K [23]; $g^{(2)}(0) = 0.34$ with InAs/InP QDs at 80 K [24]; $g^{(2)}(0) = 0.48$ with GaAs/GaAsP QDs at 160 K [25]. For T > 200 K the best reported value is $g^{(2)}(0) = 0.34$ [26]. As a consequence, I is reduced to non-practical values for quantum information tasks: $I > 0.79$ for most quantum information processing schemes and $I > 0.5$ for QKD protocols [27]. In this regard, QDs for SPS operation are restricted to low T. In an attempt to overcome this limitation, a variety of cavity-engineering approaches have been conducted [28,29]. However, several theoretical works [30–32] indicate that cavity quality factors (Q) above 4×10^7 are required for QDs to function at room T, while, to date, the highest reported Q coupled to a quantum emitter is about $Q = 55,000$ [33]. In this regard, the theoretical exploration over new strategies for enhancing I in the presence of dephasing processes is especially relevant.

Recently, theoretical studies [34–38] have shown that the enhancement and tunability of single photon emission are possible through interfaces based on two-emitter systems coupled to a cavity mode. In their scheme, tunable bandwidth and Purcell enhancement are achieved by dynamical control of the collective states of the two emitters coupled by dipolar interaction. The results open up interesting possibilities for application in single photon generation for quantum information processing. At the same time, deterministic positioning required for dipole–dipole coupling between emitters has been experimentally demonstrated on several SPS platforms: organic molecules [39], color centers in h-BN [40] and diamond [41], terylene molecules [42] and QDs [43–46]. The potential applications of these cluster systems for the enhancement of I have not been studied neither theoretically nor experimentally. As we will show, the cooperative dynamics of these cluster systems can be exploited to maintain high I with arbitrary low Q cavities by tuning the energy transfer rates between the emitters.

In this work, we present a theory for estimating I in a two-emitter system with strong dephasing coupled to a single-mode cavity. We derived an analytical expression of I as a function of the distance between the emitters, cavity decay rate, and pure dephasing rate. The results show how the requirements of the cavity for high I change with the strength of the dipolar interaction. Taking the model further, we propose a new interpretation of the I value, which allows us to estimate its behavior with larger systems (i.e., systems with more than two emitters). We performed numerical simulations of a system of five dipole-coupled emitters to find the optimal configuration for maximum I . For the optimization process, we developed a novel machine-learning (ML) scheme based on a hybrid neural network (NN)-genetic algorithm (GA) to find the position of each emitter to maximize I . The optimization procedure provides perfect I (i.e., $I = 1$) in arbitrary low Q cavities, offering unprecedent advantages for relaxing the cavity requirements and favoring the use of QDs as SPS at room T.

2. Materials and Methods

2.1. Dipole-Dipole Coupling Model

After rotating the wave approximation, the Hamiltonian for the two-QE system shown in Figure 1a coupled to the single-mode cavity reads [35]:

$$H = \Omega_{12} \left(\hat{a}_1^\dagger \sigma_2 + \sigma_1 \hat{a}_2^\dagger \right) + i g \left(\hat{a}^\dagger (\sigma_1 + \sigma_2) - a (\sigma_1^\dagger + \sigma_2^\dagger) \right), \quad (1)$$

where $\sigma_i / \sigma_i^\dagger$ are the lowering/rising operators of the QEs and a / a^\dagger the annihilation/creation operators of the cavity field. The terms associated with γ, γ^* and κ are described under

Born–Markov approximation, so the evolution of the density matrix follows the Lindblad equation [34]:

$$\begin{aligned} \frac{\partial \rho}{\partial t} = & -i[H, \rho] + \sum_n (D_n \rho D_n^\dagger - \frac{1}{2}(D_n^\dagger D_n \rho + \rho D_n^\dagger D_n)) \\ & + 2\gamma \sum_{i \neq j} (\sigma_i \rho \sigma_j^\dagger - \frac{1}{2}(\sigma_j^\dagger \sigma_i \rho + \rho \sigma_j^\dagger \sigma_i)) \end{aligned} \quad (2)$$

where the D_n denotes the collapse operators: $\sqrt{\kappa}a$, and $\sqrt{\gamma^*}\sigma_i^\dagger\sigma_i$. We have assumed $kd \ll 1$ so the modified radiative decay rate is 2γ and $\Omega_{12} = \frac{3\gamma}{4(kd)^3}$. Without detuning between the QEs there is no coherent coupling between any state but the $\{|gg\rangle, |+\rangle\}$ set, so the Hamiltonian and Lindblad equation can be written as:

$$\begin{aligned} H = & \Omega_{12}|+\rangle\langle+| + i\sqrt{2g}(a^\dagger\sigma_+ - a\sigma_+^\dagger) \\ \frac{\partial \rho}{\partial t} = & -i[H, \rho] + \sum_n (D_n \rho D_n^\dagger - \frac{1}{2}(D_n^\dagger D_n \rho + \rho D_n^\dagger D_n)) \end{aligned} \quad (3)$$

where $\sigma_+ = \frac{\sigma_1 + \sigma_2}{\sqrt{2}}$ and now the D_n denotes the collapse operators: $\sqrt{\kappa}a$, $\sqrt{2\gamma}\sigma_+$ and $\sqrt{\gamma^*}\sigma_+^\dagger\sigma_+$ [34]. The equations in (14) corresponds to the evolution of a system with a single effective QE with decay rate 2γ coupled to a single-mode cavity field with $\sqrt{2g}$. The degree of I is defined as [30]:

$$I = \frac{\iint_0^\infty dt d\tau \langle a^\dagger(t+\tau)a(t) \rangle^2}{\iint_0^\infty dt d\tau \langle a^\dagger(t)a(t) \rangle \langle a^\dagger(t+\tau)a(t+\tau) \rangle} \quad (4)$$

Which can be computed numerically via the quantum regression theorem (QRT). Alternatively, to derivate an explicit formula for I we start from the following expressions of the master equation:

$$\begin{aligned} \frac{\partial \rho_{ee}}{\partial t} &= ig(\rho_{ec} - \rho_{ce}) - \gamma\rho_{ee} \\ \frac{\partial \rho_{cc}}{\partial t} &= ig(\rho_{ce} - \rho_{ec}) - \kappa\rho_{cc} \\ \frac{\partial \rho_{ec}}{\partial t} &= ig(\rho_{ee} - \rho_{cc}) - (\frac{\Gamma}{2} + \frac{3\gamma}{4(kd)^3})\rho_{ec} \end{aligned} \quad (5)$$

In the incoherent regime we can apply adiabatic elimination of the coherences by setting $\frac{\partial \rho_{ec}}{\partial t} = 0$ [30]. Substituting in (5) we obtain the rate Equation (14) with the corresponding transfer rate R shown in (13). We can now obtain the numerator of (8) by calculating the ne-G of the system from the equations of motion:

$$i\frac{\partial}{\partial t}\hat{G}^R(\tau) = i\delta(\tau)\hat{I} + \left[\hat{H} - i\hat{\Sigma}^R(0)\right]\hat{G}^R(\tau), \quad \hat{\Sigma}^R = \begin{pmatrix} \left(\frac{\Gamma}{2} + \frac{\gamma^*}{2}\right) & 0 \\ 0 & \kappa/2 \end{pmatrix} \quad (6)$$

where $\hat{G}^R(\tau)$ is the retarded $\hat{G}^R(\tau)$ and $\hat{\Sigma}^R$ the retarded self-energy. Following a similar procedure as in [30], the numerator in (4) can be substituted by:

$$\left\langle a^\dagger(t+\tau)a(t) \right\rangle^2 = P_c^2(t)e^{-\tau(\kappa+4g^2\Gamma/(\Gamma^2+\frac{\gamma^2}{(kd)^6}))} \quad (7)$$

Solving Equation (14) for P_C we can analytically solve (4), which gives the expression shown in (13).

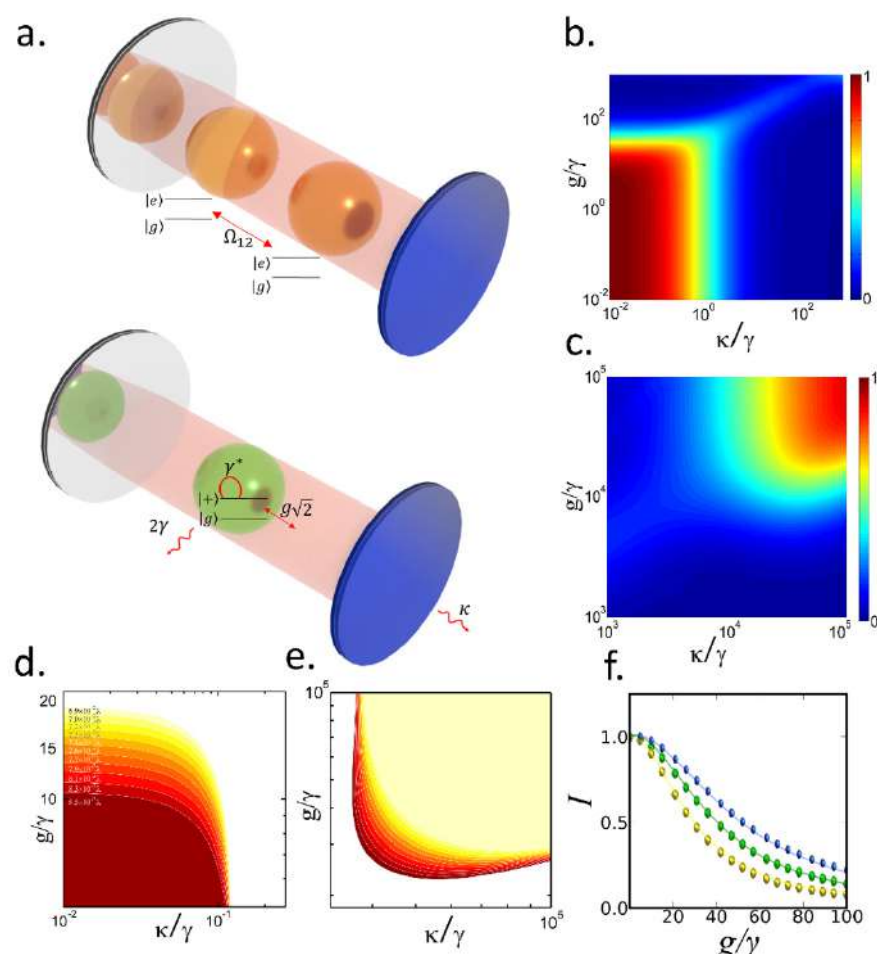


Figure 1. (a) The two interacting QEs with γ coupled to the cavity field with g are equivalent to a single QE with 2γ coupled to the cavity with $\sqrt{2}g$, each sphere represents a single two-level-system. (b) Indistinguishability of the effective QE versus the normalized κ and g in the (b) incoherent regime and (c) coherent regime. Contour map of regions with $I > 0.9$ for different distances between the regimens (d) incoherent regime (red) and (e) coherent regime (green). (f) Indistinguishability versus normalized g/γ calculated in (b) incoherent regime and (c) coherent regime. The effective indistinguishability versus the normalized κ/γ (d) incoherent regime (red), (e) coherent regime (green) (f) Indistinguishability versus (b) normalized g/γ calculated in (b) incoherent regime (red), (d) incoherent regime (green) and from $d = 6.9 \cdot 10^{-2}$ (blue); solid lines calculated using Equation (1); colored dots obtained from numerical integration of the Lindblad equation with two QEs.

2.2. Larger Systems

2.2. Larger Systems We first obtain the characteristic polynomial of (14): $P(\lambda) = \lambda^2 + (\kappa + 2R + 1)\lambda + W R$. We first obtain the characteristic polynomial of (14) by iterative process (2R+1)λ P(λ_n) (κR + from R), where n checks the stability. Then we start iterative process (2R+1)λ P(λ_n) (from parameter check the stability of P(λ) for a fixed R). Black Figure 2a shows the complex plane parameters corresponding to values whose iteration stays bounded and does not diverge to infinity. White colors correspond to values whose iteration diverges to infinity at a maximum speed. Gradient colors correspond to values whose iteration diverges to infinity at different speeds. Our region of interest is the positive real line $\kappa \in \mathbb{R}^+$. In this region the iteration diverges to infinity for all R . We want to measure the speed of the divergence θ for each κ and R (i.e., the number of iterations that takes the process to infinity). A good candidate to characterize this value is the slope of $P(\lambda)$ at $\lambda = 0$ (i.e., $P'(0)$). Since $P'(\lambda)$ grows monotonically with λ , $P'(0)$ uniquely determines θ . In Figure 2b we show the value of $P'(0)$ (blue line) for specific (κ, R) . The arrows indicate consecutive λ_n values of the iteration process. In order to express θ in the decay rate units (λ units), we draw the tangent line to $P(\lambda)$ at $\lambda = 0$ (red line in Figure 2b) and take the cut with the x-axis, which gives $\frac{P(0)}{P'(0)}$. With this definition θ reads:

$$\theta = \frac{P(0)}{P'(0)} = \frac{\kappa R + \kappa + R}{\kappa + 2R + 1} \quad (8)$$

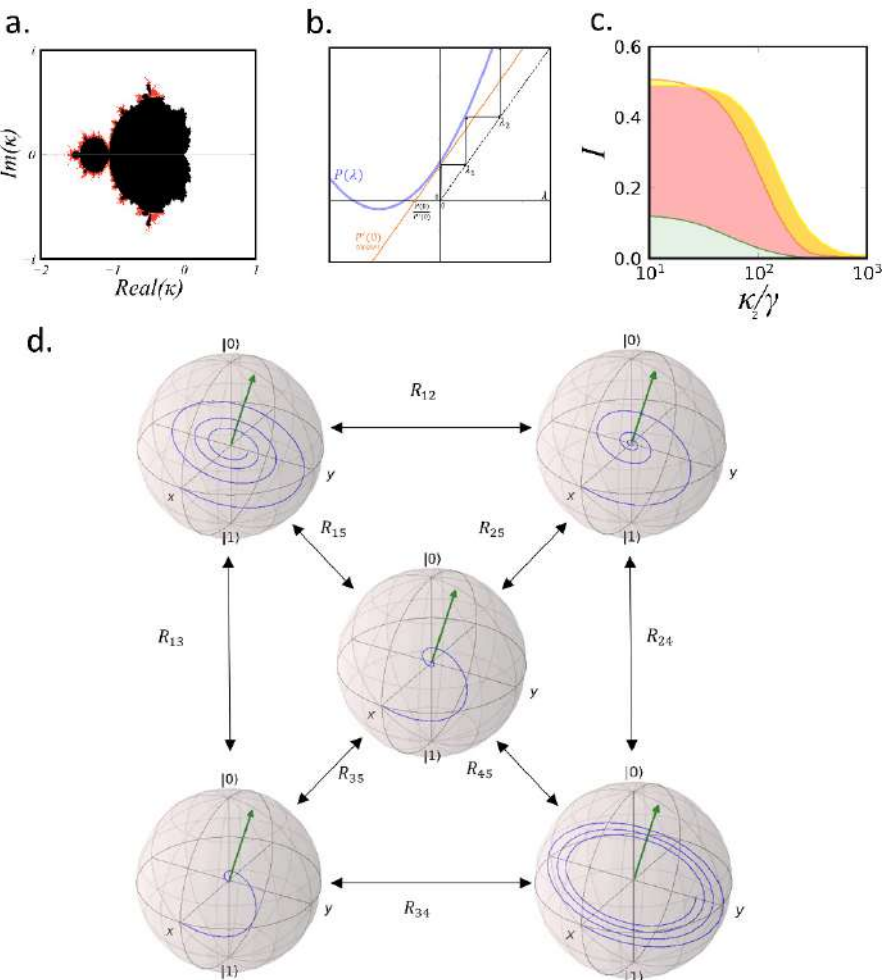


Figure 2. (a) κ -parameter space of the stability of rate equations of a single QE system coupled to a cavity. Black dots correspond to bounded points while the gradient colors represent the degree of stability. (b) Characteristic equation of (2) (blue line); tangent line with slope $P'(0)$. The cut of the tangent line with the x -axis is given by $\frac{P(0)}{P'(0)}$. The arrows indicate consecutive λ_n values of cavity. Black dots correspond to bounded points while the gradient colors represent the degree of stability. (c) Indistinguishability versus normalized κ_2 for $g_1\bar{\gamma}$ (green), $2\bar{\gamma}$ (red) and $3\bar{\gamma}$ (yellow). (d) Bloch-spheres of the five-QE system with population rate transfers R_{ij} between each subsystem. The Hamiltonian for the 5-QEs system is given by Equation (8) by its maximum value θ_{max} is given by:

2.3. Machine Learning Scheme

The Hamiltonian for the 5-QEs system coupled to a single-mode cavity field can be (9) written as:

$$\sum_{i=1}^5 \Omega_i (\sigma_i^\dagger \sigma_i + \sigma_i^\dagger \sigma_j^\dagger + i g \sum_{i \neq j} (\sigma_i^\dagger (\sigma_i + \sigma_j) - \sigma_i (\sigma_i + \sigma_j^\dagger))) \quad (11)$$

which matches the expression for I [30]. If we apply the same definition of $\bar{\theta}$ for the cascaded cavity system (Equation (13)) we obtain:

$$\kappa_1/2 + \frac{\kappa_2 R_2}{2(x_1 + R_2)}$$

with $i, j = (1, \dots, 5)$. The modified radiative decay rates $\gamma_{ij} I$ and the dipolar interaction strengths Ω_{ij} can be obtained from the Green's tensor of the system leading to [38]:

which again matches the expression of $k d_i$ [31] after applying the same approximations.

In the same way, for the two-emitter system $\bar{\theta}$ matches the I value shown in (13). Note that for general θ we have $\theta = \frac{P(0)}{P'(0)} \cos(k d_i) / \tau$ where $\cos(k d_i) / \tau$ is the determinant and τ is the trace of

the rate equations matrix. Therefore, with this method we are able to obtain the analytic expression of I for any system from trivial operations in the rate equations, without the need of calculating the ne-G.

2.3. Machine Learning Scheme

The Hamiltonian for the 5-QEs system coupled to a single-mode cavity field can be written as:

$$H = \sum_{i \neq j} \Omega_{ij} \left(\hat{q}_i^\dagger \sigma_j + \sigma_i \hat{q}_j^\dagger \right) + ig \sum_{i \neq j} \left(\hat{q}_i^\dagger (\hat{q}_i + \sigma_j) - a (\sigma_i^\dagger + \sigma_j^\dagger) \right) \quad (11)$$

with $i, j = (1, \dots, 5)$. The modified radiative decay rates γ_{ij} and the dipolar interaction strengths Ω_{ij} can be obtained from the Green's tensor of the system leading to [38]:

$$\begin{aligned} \gamma_{ij} &= \frac{3}{2} \left\{ \sin(kd_{ij}) / (kd_{ij}) - 2(\cos(kd_{ij}) / (kd_{ij})^2) - \sin(kd_{ij}) / (kd_{ij})^2 \right\} \\ \Omega_{ij} &= \frac{3}{4} \left\{ -\cos(kd_{ij}) / (kd_{ij}) - 2(\sin(kd_{ij}) / (kd_{ij})^2) - \cos(kd_{ij}) / (kd_{ij})^2 \right\} \end{aligned} \quad (12)$$

The evolution of the density matrix follows the Lindblad Equation (2) substituting γ by γ_{ij} and adding the corresponding $\sqrt{\gamma^*} \sigma_i^\dagger \sigma_i$ operators. For each iteration the value of I is calculated by solving (2) numerically and computing (8) by QRT. As in each iteration a 12×12 matrix is diagonalized, the total time of each function evaluation can take several minutes. At the same time, a GA optimization may require 10^5 evaluations of the fitness function. If we directly use QRT for each evaluation, the optimization would require excessive computational times. Instead, in our approach we first generate a data set (ω, I) with the results obtained from 2000 iterations. With these data, we train a deep NN which learns to estimate the outcome of I for any possible set of random positions $\vec{\omega}$. Now, each time the GA creates a random vector ω , the evaluation of the fitness function obtains I from the estimation of the NN. This way, each evaluation takes just a few seconds. Through the iteration of cross-over and mutation, the GA finds the optimal configuration for maximizing I after a certain number of generations. Therefore, with our NN-GA scheme we reduce the number of actual numerical simulations for the dataset by two orders of magnitude.

The NN consists of a sequential layer model implemented in Keras module with the corresponding settings: number of layers = 4; neurons per layer = 200; input-dimension = 10; output dimension = 1; loss = mean square error; Epochs = 200; learning rate = 0.001; Batch size = 100; Number of samples = 2000. After the training with 2000 samples both loss and validation-loss converged to 10^{-3} , giving enough accuracy for the estimation of I and the optimization model. The genetic algorithm uses decimal representation for the genes, one-point crossover and uniform mutation. The total initial population was set to 5000, the number of parents matings = 2500, number of weights = 1000. Using these values, we needed over 216 generations to find each optimal geometry.

3. Results

3.1. Indistinguishability of Dipole Coupled Emitters

We consider a system of two quantum emitters (QE) coupled to a single-mode cavity field. Each QE is described by a two-level-system $\{|g\rangle, |e\rangle\}$ with a decay rate γ and a pure dephasing rate γ^* . The QEs interact with each other by direct dipole–dipole coupling with a strength $\Omega_{12} = \frac{3\gamma}{4(kd)^3}$, where k is the wave vector of the emission and d is the distance between the QEs [34]. The cavity field in the Fock basis $\{|0\rangle, |1\rangle\}$ has a decay rate κ and is coupled to the QEs with a coupling constant g . Assuming $kd \ll 1$ and no detuning between the QEs this system is equivalent to a single effective QE $\{|gg\rangle, |+\rangle\}$ (e-QE) with a decay rate 2γ [34]. Figure 1a (top) shows a layout of the proposed system where Figure 1a (top) shows the two interacting QEs with γ coupled to the cavity field with g , and Figure 1a (bottom) shows the equivalent single effective QE system coupled to the same cavity. Here $|+\rangle$ represents the superradiant state $|+\rangle = \frac{|eg\rangle - |ge\rangle}{\sqrt{2}}$. The e-QE is coupled to the cavity field with $\sqrt{2}g$ and a cavity detuning $\delta = \Omega_{12}$ [35]. In Figure 1b,c we report the

numerical calculation of I for the e-QE as a function of the cavity parameters (g and κ) for fixed d , γ and $\gamma^* = 10^4\gamma$. Figure 1b shows the region of high I in the incoherent regime (i.e., $g \ll \kappa + \gamma + \gamma^*$) while Figure 1c corresponds to the region in the coherent regime ($g \gg \kappa + \gamma + \gamma^*$). The plots shows a color map with the indistinguishability of the effective QE versus the normalized parameters of the cavity κ and g .

Within the incoherent regime the dynamics can be approximated to a population transfer between the e-QE and the cavity field with an effective transfer rate R [30]. From the non-equilibrium Green's function (ne-G) of the system we obtain (see methods):

$$R = \frac{4g^2\Gamma}{\Gamma^2 + \frac{\gamma^2}{(kd)^6}}, I = \frac{\gamma\kappa[\Gamma^3 + \Omega_{12}] + [4g^2(\gamma + 1) + \Omega_{12}\frac{\kappa\gamma}{\Gamma}]\cdot[\Gamma^2 + \Omega_{12}]}{[\Gamma^2 + \Omega_{12} + 8g^2]\cdot[\kappa\Gamma^2 + \Omega_{12} + 4g^2\Gamma]} \quad (13)$$

where $\Gamma = \gamma + \gamma^* + \kappa$. In this regime the cavity behaves as an effective emitter pumped by the e-QE, and the conditions for high I are $\kappa < \gamma$ and $R < \gamma$ [30], as shown in Figure 1b. As the distance between the QEs decreases the R of the e-QE reduces, so I remains high for higher g values. This effect is easily visualized in Figure 1d, where we plot the iso-contours of $I = 0.9$ versus the normalized parameters of the cavity κ and g for different values of d . Each color region in Figure 1d shows the $I > 0.9$ area for a specific value of d , which ranges from $d = 6.9 \times 10^{-2}\lambda$ to $d = 8.5 \times 10^{-2}\lambda$. Whereas the maximum g for $I > 0.9$ is about $g = 10\gamma$ when $d = 8.5 \times 10^{-2}\lambda$, this value increases to $g = 20\gamma$ when $d = 6.9 \times 10^{-2}\lambda$. In other words, the requirement for Q (i.e., $\kappa < \gamma$) remains unchanged and the R -reduction effect just enables high I for higher g values, which is not particularly interesting. Therefore, the implementation of the two-QE system does not provide any practical advantages (in terms of Q and g) with respect to the single-QE. For the three distances, Figure 1f confirms the excellent agreement for I values obtained from Equation (1) and from numerical simulations of the two-QE system (see methods).

In the coherent regime the conclusions are roughly similar. Within the range where g is close to the strong coupling condition, the (e-QE)-cavity system is equivalent to an effective emitter [30] with decay rate $2\gamma + R$. Here the condition for high I is $R > \gamma^*$ [30], as shown in Figure 1c. Same as before, reducing d decreases R , requiring higher g for high I . Figure 1e shows the same iso-contours as Figure 1d in the coherent regime. The $I > 0.9$ region narrows upwards as d decreases due to the same R reduction effect. Thus, in the coherent regime the two-QE system impose stronger restrictions than the single QE, since it demands higher g values for obtaining high I . Therefore, the two-QE interface does not provide any advantage for high I in terms of cavity requirements, in the incoherent or coherent regimes. However, an extended exploration over systems with larger number of coupled emitters can be relevant. As we will show next, exploiting the cooperative behavior of optimized systems with more than 2 emitters can provide benefits in terms of I .

3.2. Larger Systems

We showed before that for a set of interacting two-level quantum systems in the incoherent regime the dynamics are described by a population transfer between the subsystems with effective transfer rates R . As an example, for a single QE coupled to a single-mode cavity field the evolution of the system reduces to the following rate equations [30]:

$$\begin{pmatrix} \dot{P}_{QE} \\ \dot{P}_C \end{pmatrix} = \begin{pmatrix} (\gamma + R) & R \\ R & -(\kappa + R) \end{pmatrix} \begin{pmatrix} P_{QE} \\ P_C \end{pmatrix} \quad (14)$$

where P_{QE} is the population of the QE, P_C is the population of the cavity and $R = \frac{4g^2}{\Gamma}$. As it is described in the Methods section, I is obtained from the solution of (14) via the QRT. Since QRT computation is an iterative process, it may be useful to study the dynamic stability of the characteristic equation of (14) to find any kind of relation with I . For this purpose, we have defined the degree of stability ($\bar{\theta}$) by measuring the speed of divergence of the characteristic equation of (14) (see Methods). After some algebra, we have found a direct relationship between $\bar{\theta}$ and I (see Equations (9) and (10) in the Methods section).

This means that we can derive analytic expressions of I for arbitrary large system without having to compute the ne-G. Instead, we obtain I from the determinant Δ and the trace τ of (14), which significantly simplifies the problem, especially for more complicated systems (such as the ones with more than two emitters). This finding can be expressed as:

$$\bar{\theta} = I = \frac{\bar{\Delta}}{\tau} = \frac{\gamma + \frac{\kappa R}{\kappa + R}}{\kappa + 2R + \gamma} \quad (15)$$

where $\bar{\Delta}$ is the normalized determinant (see Methods). In the same way as I , if κ increases, $\bar{\theta}$ decays at different rates depending on R . The alternative interpretation of I shown in Equation (15) provides some hints to find a way of keeping high I with higher κ values (i.e., to reduce the Q of the cavity). For the case of a single QE-cavity system the decay of $\bar{\theta}$ with κ can be tuned by changing R . If we include more QEs (or, in general, more subsystems) we have additional transfer rates that may help even more to reduce the cavity Q . The additional transfer rates will show up in the off-diagonal terms of the rate equations, giving additional terms in Δ which can lead to new paths to improve the reduction of $\bar{\theta}$ with κ . This approach can be illustrated with the cascaded-cavities scheme [31]. This system considers a single QE coupled to a cavity which at the same time is coupled to a second cavity. In the incoherent regime the dynamics follows the rate equations [31]:

$$\begin{pmatrix} P_{QE} \\ P_{C1} \\ P_{C2} \end{pmatrix} = \begin{pmatrix} -(\gamma + R_1) & R_1 & 0 \\ R_1 & -(\kappa_1 + R_1 + R_2) & R_2 \\ 0 & R_2 & -(\kappa_2 + R_2) \end{pmatrix} \begin{pmatrix} P_{QE} \\ P_{C1} \\ P_{C2} \end{pmatrix} \quad (16)$$

where P_{C1} is the population of the first cavity, P_{C2} is the population of the second cavity, κ_1 is the decay rate of the first cavity, κ_2 is the decay rate of the second cavity, R_1 is the transfer rate between the QE and the first cavity and R_2 is the transfer rate between the first and second cavity. In this case we have one more degree of freedom (R_2) than in the single QE-cavity system. Therefore, by adjusting R_1 and R_2 we can tune the decay of the stability with κ in a more efficient way. Figure 2c shows a quantitative example of this improvement. The plot shows the indistinguishability versus the normalized second-cavity parameter κ_2 for three different values of normalized first-cavity parameter g_1 = (green), 2γ (red) and 3γ (yellow). While with the single QE-cavity system I decreases below 0.5 for $\kappa = \gamma$, the cascaded-cavities scheme can maintain $I > 0.5$ up to $\kappa_2 = 100\gamma$ when setting the right R_1 and R_2 values (i.e., setting the cavity mode volume, V_{eff} , and Q).

Therefore, adding more subsystems (emitters and/or cavities) provides additional paths to maintain the stability and, therefore, relax the cavity requirements for high I . Accordingly, we study now the case of a cluster of five QEs coupled to a single-mode cavity field. With this scheme, we have 10 transfer rates (R_{ij}) that can be tuned by setting the relative distances between the QEs, so we have enough parameters to perform a sufficiently complex optimization. Figure 2d shows a layout of the system where each Bloch-sphere represents the time evolution of each QE_i , and each arrow represents the specific transfer rate between the QE_i and QE_j . Our aim now is to find the geometrical configuration of the QEs that provides the optimal set of R_{ij} that keep high I for high κ values. This goal involves an optimization task with 10 degrees of freedom, which is a highly non-trivial problem and computationally very time-consuming. Nevertheless, similar optimization problems have been recently solved using machine-learning methods [28,47–50]. Employing a similar approach, we developed a machine-learning scheme based on a hybrid NN-GA algorithm which is able to solve the optimization problem in very short computational times providing the best geometrical configuration for the emitters.

3.3. Machine Learning Optimization

We consider five QEs with γ^* randomly positioned in a 2D-grid. All of them are coupled to a single-mode cavity field with the same coupling constant g and cavity decay rate κ . Each relative distance d_{ij} ($i, j = 1, \dots, 5$) between QEs leads to a dipolar interaction

strength Ω_{ij} and modified decay rate γ_{ij} . Since this scheme requires solving a system of 144 coupled differential equations, we are not able to derive an analytic expression for I such as in the two-QE case. Instead, we numerically solve the Lindblad equation of the system and compute I via QRT. At each iteration we generate a vector ω with five random positions of the QEs and we calculate I via QRT for a fixed g and κ . The data set (ω, I) is then used to train the NN-GA algorithm which finds the optimal positions for maximum I for that g and κ . In Figure 3a–e we report the obtained optimal geometries for $g = \gamma$ and $\kappa = 10\gamma, 50\gamma, 100\gamma, 500\gamma$ and 1000γ , respectively. All these geometries provide perfect I ($I = 1$) with realizations [34–41]. Each geometry leads to the right transfer rates R_{ij} between the subsystems for keeping the stability at the specific rates g and κ . For a fixed geometry, small changes in g and κ drastically reduce I . This is displayed in Figure 3f, which shows I versus normalized g/γ versus normalized κ/γ for the optimal geometry obtained for $g = \gamma, \kappa = 10\gamma$. The plot shows a small ‘bubble’ of high I at the $(g/\gamma, \kappa/\gamma) = (1, 10)$ point, while in the neighbor regions of the bubble I reduces to 0. Figure 3a–e also shows the positioning tolerances for each QE for obtaining $I > 0.9$. The tolerances for the accuracy in the position depend on the specific QE and the (g, κ) values.

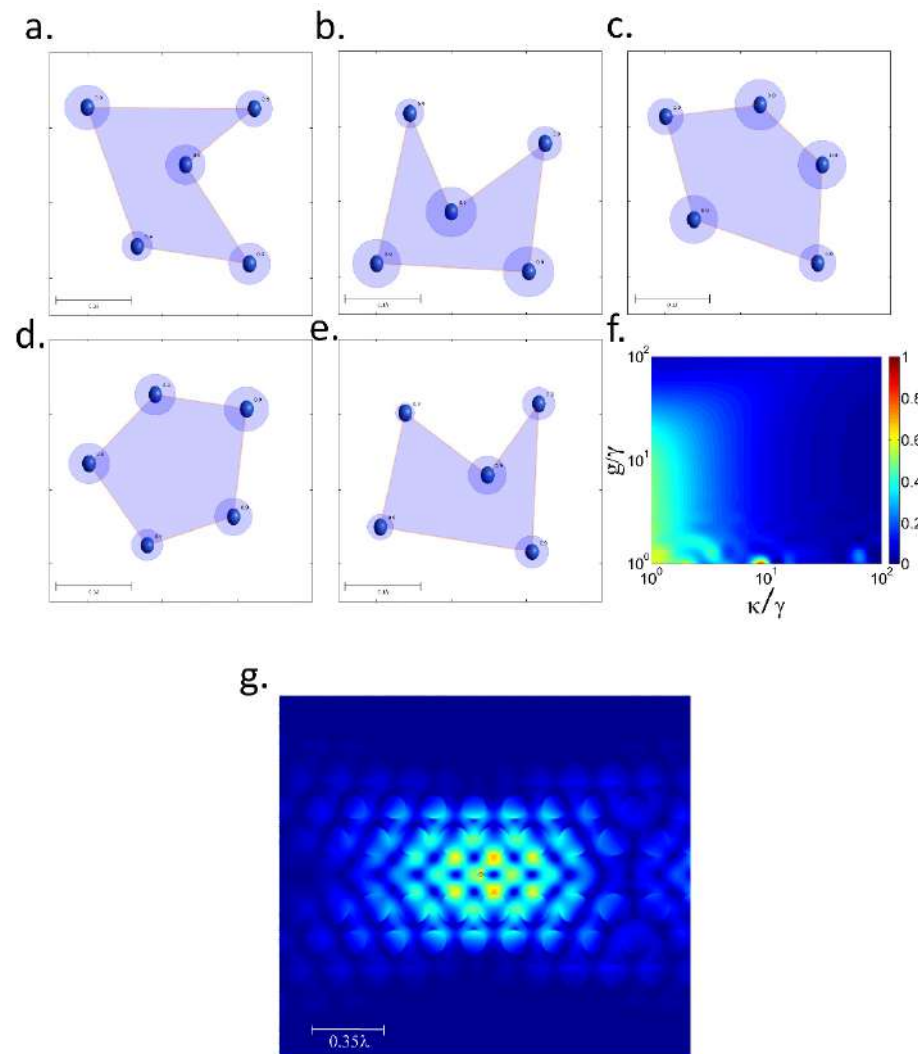


Figure 3. (a) Optimal configuration of the 5-QEs system in a 2D plane for (a) $\kappa = 10\gamma$, (b) $\kappa = 50\gamma$, (c) $\kappa = 100\gamma$, (d) $\kappa = 500\gamma$ and (e) $\kappa = 1000\gamma$. The circles around each QE position corresponds to the positioning tolerance for having $I > 0.9$. (f) Indistinguishability versus normalized κ and g for the optimized configuration of the 5-QE system. (g) Field profile of the first hexagonal PC cavity mode corresponding to the point source placed at the antinode.

Within our scheme the realization of perfect I SPS with strong dissipative QEs is possible using well established photonic platforms. To verify this claim we performed 3D-

Within our scheme the realization of perfect I SPS with strong dissipative QEs is possible using well established photonic platforms. To verify this claim we performed 3D-FDTD simulations [51] of a point source placed at the antinode of a cavity-mode in a standard 2D-hexagonal SiN photonic crystal cavity (PCc). The V_{eff} and Q were obtained from the field profile (see Figure 3g) and frequency analysis of the resonance. For a QE with $(\gamma, \gamma^*, \omega) = (160 \text{ MHz}, 400 \text{ GHz} \text{ and } 400 \text{ THz})$ such as color centers in diamond [52] we obtained $(g, \kappa) \approx (1, 100)$. The radius and distances between the holes of the PCc were set to 120 nm and 50 nm, respectively, which is compatible with most fabrication techniques [53–55]. To highlight the benefits of our strategy we have contrasted the obtained performance with standard single-emitter-cavity systems [30] for different QEs at high T. Diamond color centers, InGaAs QDs, GaAs QDs and single molecules at 300 K has a pure dephasing of 1000 γ , 600 γ , 1450 γ and $10^4 \gamma$, respectively [20,21,52,56]. Considering the same standard PCc with $(g, \kappa) \approx (1, 100)$, a single-emitter-cavity system leads to $I \sim 0.01$ for all these emitters, whereas the five-QEs optimized platform provides $I = 1$. For these emitters, obtaining $I = 1$ with a single-emitter-cavity at room T would require at least a cavity with Q above 4×10^7 , which is beyond the state of the art for most current fabrication technologies.

4. Discussion

A key point to evaluate for the experimental realization of our scheme is the nanoscale positioning approach for the deposition of the cluster of QDs. Novel positioning technologies have recently shown positioning accuracy at the nanometer level [57]. A 30 nm positioning accuracy with GaAs QDs has been reported using atomic force microscopy [16]. Confocal micro-photoluminescence can provide 10 nm positioning accuracy also with GaAs QDs as it has been shown in [58]. A 5 nm position accuracy has been achieved recently with Bi-chromatic photoluminescence through a new image analysis software implementation [59]. In situ lithography approaches have also shown promising results improving its position accuracy down to 30 nm [60]. Pick-and-place approaches have shown 38 nm positioning accuracy for Si vacancy centers transference to aluminum nitride waveguides, achieving 98% coupling efficiency [61,62]. Therefore, according to tolerances shown in Figure 3b, for the case of point defects in diamond, using pick-and-place positioning we would have a standard deviation of 38 nm with a target of about 30 nm. This leads to 81% probability of successful deposition for a single QD. Successful deposition of the five QDs in place would have a probability of 32%. An experimental realization should require the fabrication of a large number of devices and checking for suitable candidates one by one. According to this, although our scheme could enable the experimental demonstration of certain quantum phenomena, it is still far from a high-scalable technology.

So far, we have explored the theoretical performance of our scheme considering identical QDs without detuning Δ between the emitters. However, a more realistic analysis involves the evaluation of the effect of mismatching between the emission frequencies of the QDs. With this aim, we have incorporated a statistical detuning distribution to the system of five QDs in the configuration shown in Figure 3b. We consider a normal distribution setting the mean equal to 0 and standard deviation $\sigma_n = n\gamma$, as shown in Figure 4a. The Δ of each QD is set randomly according to the normal distribution. We start with the distribution $\sigma_1 = \gamma$, we set five random Δ for the QDs and compute I . Then we reset the random Δ according to the same distribution and compute again I , repeating this process 200 times and computing the average of all obtained values of I . We obtained the average value of I for the 20 different probability distributions $\sigma_n = n\gamma$ with $n = 1 \dots 20$, as shown in Figure 4b.

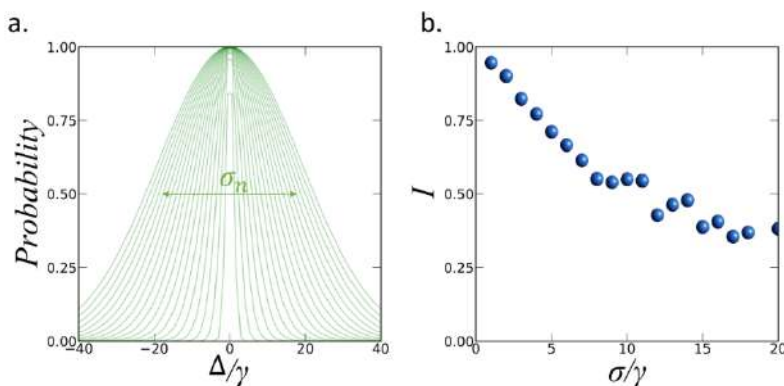


Figure 4. (a) Probability distributions with standard deviation σ_n for $n = 1 \dots 20$ for the normalized detuning values Δ/γ . At each iteration we set a random Δ value for each QD according to the corresponding distribution. (b) Average value of the indistinguishability obtained for each of the 20 probability distributions.

As expected, the value of I reduces as the standard deviation of the distribution increases. For the distribution $\sigma_1 = \gamma$ the possible values for the Δ between the QDs range from -5γ to 5γ , leading to a negligible reduction of I . On the opposite side, with $\sigma_{20} = 20\gamma$ the possible values of Δ range from -60γ to 60γ , giving a reduction of I of about 70%, of about 70%. According to these results, our scheme is able to maintain high $I > 0.75$ for normal distributions of emitters with standard deviation below 5γ , which includes frequency mismatching between the QEs of about 20γ . Therefore, the proposed system is a relatively robust platform for distributions of non-identical QDs according to recent experimental demonstrations [26].

5. Conclusions

5. Conclusions

We have developed an analytical model for estimation of the indistinguishability with two QE interfaces with dephasing integrated in optical cavities. The model provides an analytical expression that relates the indistinguishability to the distance between the two QEs and the parameters of the cavity. Through an alternative interpretation of the indistinguishability, we can estimate the behavior of the QEs system coupled to a single cavity by performing a learning algorithm. This is of great interest for systems including more QEs. Finally, by mismatching the QEs in a cavity, the results predict the probability of indistinguishability is strongly dissipative when it is somehow feasible. The proposed single-photon strategy for the realization of specific indistinguishabilities in the heterogeneity of QD properties is promising. The strategy presents significant challenges for its implementation but is feasible. The proposed strategy is a promising approach for the optimization of the heterogeneity of QD properties in a single-photon source. Although the required factor for experiments is not yet available, it is still feasible to implement operation with high indistinguishability. Experimental demonstration provides insights for optimizing with slight indistinguishabilities for many applications, such as the reduction of quantum decoherence in clusters of coupled two-level quantum systems.

Author Contributions: Conceptualization, J.G.; methodology, J.G.; software, J.G. and L.S.; validation, P.A.P. and J.M.W.; formal analysis, L.G. and J.M.W.; investigation, J.G.; resources, P.A.P.; data curation, J.G.; writing—original draft preparation, J.G. and J.M.W.; review and editing, J.G. and P.A.P.; supervision, J.G.; project administration, P.A.P.; funding acquisition, P.A.P. All authors have read and agreed to the published version of the manuscript. **P.A.P.**: funding acquisition, P.A.P. All authors have read and agreed to the published version of the manuscript.

Funding: European Union's Horizon 2020 research and innovation program under grant agreement No 820423 (SEQUUME), CSIC Interdisciplinary Thematic Platform (PTI-QTEP+), Agencia Estatal de Investigación N6AE2018-02420 (SEQUUME-100188R681), Interdisciplinary Metaphysics Project 2011 (Agencia Estatal de Investigación ga2016-05195) and CSIC Interdisciplinary Thematic Platform (PTI-QTEP+); PTI-QTEP+ Innovation and Research: 20FUN05 SEQUUME and CSIC Interdisciplinary Thematic Platform (PTI+); PTI-QTEP+.

Data Availability Statement: Data underlying the results of this paper are available from the corresponding author upon request.

Acknowledgments: We gratefully acknowledge Ian Shlesinger for his contribution in the development of this work.

Conflicts of Interest: The authors declare no conflict of interest.

References

- Monroe, C.; Meekhof, D.M.; King, B.E.; Itano, W.M.; Wineland, D.J. Demonstration of a fundamental quantum logic gate. *Phys. Rev. Lett.* **1995**, *75*, 4714. [[CrossRef](#)] [[PubMed](#)]
- Makhlin, Y.; Scöhn, G.; Shnirman, A. Josephson-junction qubits with controlled couplings. *Nature* **1999**, *398*, 305–307. [[CrossRef](#)]
- Politi, A.; Cryan, M.J.; Rarity, J.G.; Yu, S.; O'brien, J.L. Silica-on-silicon waveguide quantum circuits. *Science* **2008**, *320*, 646–649. [[CrossRef](#)] [[PubMed](#)]
- Bunandar, D.; Lentine, A.; Lee, C.; Cai, H.; Long, C.M.; Boynton, N.; Martinez, N.; DeRose, C.; Chen, C.; Grein, M. Metropolitan quantum key distribution with silicon photonics. *Phys. Rev. X* **2018**, *8*, 021009. [[CrossRef](#)]
- Lago-Rivera, D.; Grandi, S.; Rakonjac, J.V.; Seri, A.; de Riedmatten, H. Telecom-heralded entanglement between multimode solid-state quantum memories. *Nature* **2021**, *594*, 37–40. [[CrossRef](#)] [[PubMed](#)]
- Zhong, H.S.; Wang, H.; Deng, Y.H.; Chen, M.C.; Peng, L.C.; Luo, Y.H.; Qin, J.; Wu, D.; Ding, X.; Hu, Y. Quantum computational advantage using photons. *Science* **2020**, *370*, 1460–1463. [[CrossRef](#)] [[PubMed](#)]
- Peruzzo, A.; McClean, J.; Shadbolt, P.; Yung, M.H.; Zhou, X.Q.; Love, P.J.; Aspuru-Guzik, A.; O'brien, J.L. A variational eigenvalue solver on a photonic quantum processor. *Nat. Commun.* **2014**, *5*, 4213. [[CrossRef](#)] [[PubMed](#)]
- Acosta, V.M.; Bauch, E.; Ledbetter, M.P.; Santori, C.; Fu, K.M.; Barclay, P.E.; Beausoleil, R.G.; Linget, H.; Roch, J.F.; Treussart, F. Diamonds with a high density of nitrogen-vacancy centers for magnetometry applications. *Phys. Rev. B* **2009**, *80*, 115202. [[CrossRef](#)]
- Pelucchi, E.; Fagas, G.; Aharonovich, I.; Englund, D.; Figueroa, E.; Gong, Q.; Hannes, H.; Liu, J.; Lu, C.Y.; Matsuda, N. The potential and global outlook of integrated photonics for quantum technologies. *Nat. Rev. Phys.* **2022**, *4*, 194–208. [[CrossRef](#)]
- Zhang, H.; Zhang, H.F.; Liu, G.B.; Li, H.M. Ultra-broadband multilayer absorber with the lumped resistors and solid-state plasma. *Results Phys.* **2019**, *12*, 917–924. [[CrossRef](#)]
- Cheben, P.; Halir, R.; Schmid, J.H.; Atwater, H.A.; Smith, D.R. Subwavelength integrated photonics. *Nature* **2018**, *560*, 565–572. [[CrossRef](#)] [[PubMed](#)]
- Zhang, Y.; Wang, Z.; Su, Y.; Zheng, Y.; Tang, W.; Yang, C.; Tang, H.; Qu, L.; Li, Y.; Zhao, Y. Simple vanilla derivatives for long-lived room-temperature polymer phosphorescence as invisible security inks. *Research* **2021**, *2021*, 8096263. [[CrossRef](#)] [[PubMed](#)]
- Wu, S.; Xia, H.; Xu, J.; Sun, X.; Liu, X. Manipulating luminescence of light emitters by photonic crystals. *Adv. Mater.* **2018**, *30*, 1803362. [[CrossRef](#)] [[PubMed](#)]
- Juska, G.; Dimastrodonato, V.; Mereni, L.O.; Gocalinska, A.; Pelucchi, E. Towards quantum-dot arrays of entangled photon emitters. *Nat. Photonics* **2013**, *7*, 527–531. [[CrossRef](#)]
- Gérard, J.M.; Sermage, B.; Gayral, B.; Legrand, B.; Costard, E.; Thierry-Mieg, V. Enhanced spontaneous emission by quantum boxes in a monolithic optical microcavity. *Phys. Rev. Lett.* **1998**, *81*, 1110. [[CrossRef](#)]
- Hennessy, K.; Badolato, A.; Winger, M.; Gerace, D.; Atatüre, M.; Gulde, S.; Fält, S.; Hu, E.L.; Imamoglu, A. Quantum nature of a strongly coupled single quantum dot–cavity system. *Nature* **2007**, *445*, 896–899. [[CrossRef](#)]
- Wang, H.; Duan, Z.C.; Li, Y.H.; Chen, S.; Li, J.P.; He, Y.M.; Chen, M.C.; He, Y.; Ding, X.; Peng, C.Z.; et al. Near-transform-limited single photons from an efficient solid-state quantum emitter. *Phys. Rev. Lett.* **2016**, *116*, 213601. [[CrossRef](#)]
- He, Y.M.; He, Y.; Wei, Y.J.; Wu, D.; Atatüre, M.; Schneider, C.; Höfling, S.; Kamp, M.; Lu, C.Y.; Pan, J.W. On-demand semiconductor single-photon source with near-unity indistinguishability. *Nat. Nanotechnol.* **2013**, *8*, 213–217. [[CrossRef](#)]
- Somaschi, N.; Giesz, V.; De Santis, L.; Loredo, J.C.; Almeida, M.P.; Hornecker, G.; Portalupi, S.L.; Grange, T.; Anton, C.; Demory, J.; et al. Near-optimal single-photon sources in the solid state. *Nat. Photonics* **2016**, *10*, 340–345. [[CrossRef](#)]
- Borri, P.; Langbein, W.; Schneider, S.; Woggon, U.; Sellin, R.L.; Ouyang, D.; Bimberg, D. Ultralong dephasing time in InGaAs quantum dots. *Phys. Rev. Lett.* **2001**, *87*, 157401. [[CrossRef](#)]
- Bayer, M.; Forchel, A. Temperature dependence of the exciton homogeneous linewidth in In 0.60 Ga 0.40 As/GaAs self-assembled quantum dots. *Phys. Rev. B* **2002**, *65*, 041308. [[CrossRef](#)]
- Berthelot, A.; Favero, I.; Cassabois, G.; Voisin, C.; Delalande, C.; Roussignol, P.; Ferreira, R.; Gérard, J.M. Unconventional motional narrowing in the optical spectrum of a semiconductor quantum dot. *Nat. Phys.* **2006**, *2*, 759–764. [[CrossRef](#)]
- Mirin, R.P. Photon antibunching at high temperature from a single InGaAs/GaAs quantum dot. *Appl. Phys. Lett.* **2004**, *84*, 1260–1262. [[CrossRef](#)]
- Dusanowski, Ł.; Syperek, M.; Misiewicz, J.; Somers, A.; Hoefling, S.; Kamp, M.; Reithmaier, J.P.; Sek, G. Single-photon emission of InAs/InP quantum dashes at 1.55 μm and temperatures up to 80 K. *Appl. Phys. Lett.* **2016**, *108*, 163108. [[CrossRef](#)]
- Yu, P.; Li, Z.; Wu, T.; Wang, Y.T.; Tong, X.; Li, C.F.; Wang, Z.; Wei, S.H.; Zhang, Y.; Liu, H.; et al. Nanowire quantum dot surface engineering for high temperature single photon emission. *ACS Nano* **2019**, *13*, 13492–13500. [[CrossRef](#)] [[PubMed](#)]

26. Arakawa, Y.; Holmes, M.J. Progress in quantum-dot single photon sources for quantum information technologies: A broad spectrum overview. *Appl. Phys. Rev.* **2020**, *7*, 021309. [[CrossRef](#)]
27. Bylander, J.; Robert-Philip, I.; Abram, I. Interference and correlation of two independent photons. *Eur. Phys. J. D-At. Mol. Opt. Plasma Phys.* **2003**, *22*, 295–301. [[CrossRef](#)]
28. Guimba, J.; Sanchis, L.; Weituschat, L.; Manuel Llorens, J.; Song, M.; Cardenas, J.; Aitor Postigo, P. Numerical Optimization of a Nanophotonic Cavity by Machine Learning for Near-Unity Photon Indistinguishability at Room Temperature. *ACS Photonics* **2022**, *9*, 1926–1935. [[CrossRef](#)]
29. Guimba, J.; Weituschat, L.M.; Montolio, J.L.; Postigo, P.A. Enhancement of the indistinguishability of single photon emitters coupled to photonic waveguides. *Opt. Express* **2021**, *29*, 21160–21173. [[CrossRef](#)]
30. Grange, T.; Hornecker, G.; Hunger, D.; Poizat, J.P.; Gérard, J.M.; Senellart, P.; Auffèves, A. Cavity-funneled generation of indistinguishable single photons from strongly dissipative quantum emitters. *Phys. Rev. Lett.* **2015**, *114*, 193601. [[CrossRef](#)]
31. Choi, H.; Zhu, D.; Yoon, Y.; Englund, D. Cascaded cavities boost the indistinguishability of imperfect quantum emitters. *Phys. Rev. Lett.* **2019**, *122*, 183602. [[CrossRef](#)] [[PubMed](#)]
32. Saxena, A.; Chen, Y.; Ryou, A.; Sevilla, C.G.; Xu, P.; Majumdar, A. Improving indistinguishability of single photons from colloidal quantum dots using nanocavities. *ACS Photonics* **2019**, *6*, 3166–3173. [[CrossRef](#)]
33. Ota, Y.; Iwamoto, S.; Kumagai, N.; Arakawa, Y. Spontaneous two-photon emission from a single quantum dot. *Phys. Rev. Lett.* **2011**, *107*, 233602. [[CrossRef](#)] [[PubMed](#)]
34. Shlesinger, I.; Senellart, P.; Lanco, L.; Greffet, J.J. Time-frequency encoded single-photon generation and broadband single-photon storage with a tunable subradiant state. *Optica* **2021**, *8*, 95–105. [[CrossRef](#)]
35. Shlesinger, I.; Senellart, P.; Lanco, L.; Greffet, J.J. Tunable bandwidth and nonlinearities in an atom-photon interface with subradiant states. *Phys. Rev. A* **2018**, *98*, 013813. [[CrossRef](#)]
36. Schilder, N.J.; Sauvan, C.; Sortais, Y.R.P.; Browaeys, A.; Greffet, J.J. Near-resonant light scattering by a subwavelength ensemble of identical atoms. *Phys. Rev. Lett.* **2020**, *124*, 073403. [[CrossRef](#)] [[PubMed](#)]
37. Ficek, Z.; Tanas, R.; Kielich, S. Cooperative effects in the spontaneous emission from two non-identical atoms. *Opt. Acta* **1986**, *33*, 1149–1160.
38. Lehmberg, R.H. Radiation from an N-atom system. I. General formalism. *Phys. Rev. A* **1970**, *2*, 883. [[CrossRef](#)]
39. Hettich, C.; Schmitt, C.; Zitzmann, J.; Kühn, S.; Gerhardt, I.; Sandoghdar, V. Nanometer resolution and coherent optical dipole coupling of two individual molecules. *Science* **2002**, *298*, 385–389. [[CrossRef](#)]
40. Vogl, T.; Campbell, G.; Buchler, B.C.; Lu, Y.; Lam, P.K. Fabrication and deterministic transfer of high-quality quantum emitters in hexagonal boron nitride. *ACS Photonics* **2018**, *5*, 2305–2312. [[CrossRef](#)]
41. Schröder, T.; Trusheim, M.E.; Walsh, M.; Li, L.; Zheng, J.; Schukraft, M.; Sipahigil, A.; Evans, R.E.; Sukachev, D.D.; Nguyen, C.T.; et al. Scalable focused ion beam creation of nearly lifetime-limited single quantum emitters in diamond nanostructures. *Nat. Commun.* **2017**, *8*, 15376. [[CrossRef](#)]
42. Hail, C.U.; Höller, C.; Matsuzaki, K.; Rohner, P.; Renger, J.; Sandoghdar, V.; Poulikakos, D.; Eghlidi, H. Nanoprinting organic molecules at the quantum level. *Nat. Commun.* **2019**, *10*, 1880. [[CrossRef](#)] [[PubMed](#)]
43. Bayer, M.; Hawrylak, P.; Hirzer, K.; Fafard, S.; Korkusinski, M.; Wasilewski, Z.R.; Stern, O.; Forchel, A. Coupling and entangling of quantum states in quantum dot molecules. *Science* **2001**, *291*, 451–453. [[CrossRef](#)]
44. Kim, H.; Kyhm, K.; Taylor, R.A.; Kim, J.S.; Song, J.D.; Park, S. Optical shaping of the polarization anisotropy in a laterally coupled quantum dot dimer. *Light Sci. Appl.* **2020**, *9*, 100. [[CrossRef](#)]
45. Takagahara, T. Excitonic Structures and Optical Properties of Quantum Dots. In *Semiconductor Quantum Dots*; Springer: Berlin/Heidelberg, Germany, 2002; pp. 59–114.
46. Senellart, P.; Solomon, G.; White, A. High-performance semiconductor quantum-dot single-photon sources. *Nat. Nanotechnol.* **2017**, *12*, 1026–1039. [[CrossRef](#)] [[PubMed](#)]
47. Sanchis, L.; Cryan, M.J.; Pozo, J.; Craddock, I.J.; Rarity, J.G. Ultrahigh Purcell factor in photonic crystal slab microcavities. *Phys. Rev. B* **2007**, *76*, 045118. [[CrossRef](#)]
48. Sanchis, L.; Häkansson, A.; López-Zanón, D.; Bravo-Abad, J.; Sánchez-Dehesa, J. Integrated optical devices design by genetic algorithm. *Appl. Phys. Lett.* **2004**, *84*, 4460–4462. [[CrossRef](#)]
49. Morgado-León, A.; Escuín, A.; Guerrero, E.; Yáñez, A.; Galindo, P.L.; Sanchis, L. Genetic Algorithms Applied to the Design of 3D Photonic Crystals. In Proceedings of the International Work-Conference on Artificial Neural Networks, Torremolinos, Spain, 8–10 June 2011; Springer: Berlin/Heidelberg, Germany, 2011; pp. 291–298.
50. Marques-Hueso, J.; Sanchis, L.; Cluzel, B.; de Fornel, F.; Martínez-Pastor, J.P. Genetic algorithm designed silicon integrated photonic lens operating at 1550 nm. *Appl. Phys. Lett.* **2010**, *97*, 071115. [[CrossRef](#)]
51. *3D Electromagnetic Simulator*; Lumerical Inc.: Vancouver, BC, Canada, 2022.
52. Neu, E.; Hepp, C.; Hauschild, M.; Gsell, S.; Fischer, M.; Sternschulte, H.; Steinmüller-Nethl, D.; Schreck, M.; Becher, C. Low-temperature investigations of single silicon vacancy colour centres in diamond. *New J. Phys.* **2013**, *15*, 043005. [[CrossRef](#)]
53. Englund, D.; Faraon, A.; Zhang, B.; Yamamoto, Y.; Vučković, J. Generation and transfer of single photons on a photonic crystal chip. *Opt. Express* **2007**, *15*, 5550–5558. [[CrossRef](#)] [[PubMed](#)]
54. Chang, W.H.; Chen, W.Y.; Chang, H.S.; Hsieh, T.P.; Chyi, J.I.; Hsu, T.M. Efficient single-photon sources based on low-density quantum dots in photonic-crystal nanocavities. *Phys. Rev. Lett.* **2006**, *96*, 117401. [[CrossRef](#)] [[PubMed](#)]

55. Clark, A.S.; Husko, C.; Collins, M.J.; Lehoucq, G.; Xavier, S.; De Rossi, A.; Combrié, S.; Xiong, C.; Eggleton, B.J. Heralded single-photon source in a III–V photonic crystal. *Opt. Lett.* **2013**, *38*, 649–651. [[CrossRef](#)] [[PubMed](#)]
56. Huang, L.; Krasnok, A.; Alu, A.; Yu, Y.; Neshev, D.; Miroshnichenko, A. Enhanced Light-Matter Interaction in Two Dimensional Transition Metal Dichalcogenides. *Rep. Prog. Phys.* **2022**, *85*, 046401. [[CrossRef](#)]
57. Liu, S.; Srinivasan, K.; Liu, J. Nanoscale Positioning Approaches for Integrating Single Solid-State Quantum Emitters with Photonic Nanostructures. *Laser Photonics Rev.* **2021**, *15*, 2100223. [[CrossRef](#)]
58. Thon, S.M.; Rakher, M.T.; Kim, H.; Gudat, J.; Irvine, W.T.; Petroff, P.M.; Bouwmeester, D. Strong coupling through optical positioning of a quantum dot in a photonic crystal cavity. *Appl. Phys. Lett.* **2009**, *94*, 111115. [[CrossRef](#)]
59. Liu, J.; Davanço, M.I.; Sapienza, L.; Konthasinghe, K.; De Miranda Cardoso, J.V.; Song, J.D.; Badolato, A.; Srinivasan, K. Cryogenic photoluminescence imaging system for nanoscale positioning of single quantum emitters. *Rev. Sci. Instrum.* **2017**, *88*, 023116. [[CrossRef](#)] [[PubMed](#)]
60. Gschrey, M.; Schmidt, R.; Schulze, J.H.; Strittmatter, A.; Rodt, S.; Reitzenstein, S. Resolution and alignment accuracy of low-temperature in situ electron beam lithography for nanophotonic device fabrication. *J. Vac. Sci. Technol. B* **2015**, *33*, 021603. [[CrossRef](#)]
61. Elshaari, A.W.; Pernice, W.; Srinivasan, K.; Benson, O.; Zwiller, V. Hybrid integrated quantum photonic circuits. *Nat. Photonics* **2020**, *14*, 285–298. [[CrossRef](#)]
62. Wan, N.H.; Lu, T.J.; Chen, K.C.; Walsh, M.P.; Trusheim, M.E.; De Santis, L.; Bersin, E.A.; Harris, I.B.; Mouradian, S.L.; Christen, I.R.; et al. Large-scale integration of near-indistinguishable artificial atoms in hybrid photonic circuits. *arXiv* **2019**. Available online: <https://arxiv.org/abs/1911.05265> (accessed on 16 July 2022).